A large-deformation thermo-mechanically coupled elastic-viscoplastic theory for amorphous polymers: modeling of micro-scale forming and the shape memory phenomenon

by

Vikas Srivastava

B. Tech., Indian Institute of Technology, Kanpur (1998)
S.M., University of Rhode Island, Kingston (1999)

Submitted to the Department of Mechanical Engineering
in partial fulfillment of the requirements for the degree of

Doctor of Philosophy

at the

Massachusetts Institute of Technology

February 2010

Author .....
Department of Mechanical Engineering
December 28, 2009

Certified by .....
Lallit Anand
Rohsenow Professor of Mechanical Engineering
Thesis Supervisor

Accepted by .....
David E. Hardt
Chairman, Department Committee on Graduate Students

A large-deformation thermo-mechanically coupled elastic-viscoplastic theory for amorphous polymers: modeling of micro-scale forming and the shape memory phenomenon

by
Vikas Srivastava

Submitted to the Department of Mechanical Engineering
on December 28, 2009, in partial fulfillment of the
requirements for the degree of
Doctor of Philosophy

Abstract

Amorphous polymers are important engineering materials; however, their nonlinear, strongly temperature- and rate-dependent elastic-viscoplastic behavior is still not very well understood, and is modeled by existing constitutive theories with varying degrees of success. There is no generally agreed upon theory to model the large-deformation, thermo-mechanically coupled response of these materials in a temperature range which *spans* their glass transition temperature. Such a theory is crucial for the development of a numerical capability for the simulation and design of important polymer processing operations, and also for predicting the relationship between processing methods and the subsequent mechanical properties of polymeric products.

We have developed a large-deformation thermo-mechanically coupled elastic-viscoplastic theory for thermoplastic amorphous polymers and shape memory polymers which spans their glass transition temperature. The theory has been specialized to represent the major features of the thermo-mechanical response of three technologically important thermoplastic amorphous polymers — a cyclo-olefin polymer (Zeonex-690R), polycarbonate, poly(methyl methacrylate) and a representative thermoset shape memory polymer — in a temperature range from room temperature to approximately 40 °C above the glass transition temperature of each material, in a strain-rate range of $\approx 10^{-4}$ to $10^{-1}\,\mathrm{s}^{-1}$, and compressive true strains exceeding 100%. Our theory has been implemented in the finite element program ABAQUS. In order to validate the predictive capability of our constitutive theory, we have performed a variety of macro- and micro-scale validation experiments involving complex inhomogeneous deformations and thermal processing cycles. By comparing some key features, such as the experimentally-measured deformed shapes and the load-displacement curves from various validation experiments against corresponding results from numerical simulations, we show that our theory is capable of reasonably accurately reproducing the results obtained in the validation experiments.

Thesis Supervisor: Lallit Anand
Title: Rohsenow Professor of Mechanical Engineering

Acknowledgments

First and foremost, I would like to express my sincere gratitude to Professor Lallit Anand for his support and guidance over the last four years. His encouragement to conduct outstanding research in the area of mechanics and materials, think creatively, and to pursue impeccable standards will continue to inspire me throughout my research career. I would also like to thank my thesis committee members, Professor Mary Boyce, Professor David Hardt, and Professor Gareth McKinley for their invaluable suggestions during my Ph.D. research.

Many thanks to Ray Hardin, Leslie Regan, and Pierce Hayward for their support, which always far exceeded administrative details.

I would like to thank my labmates Nicoli Ames, Shawn Chester, David Henann, Kaspar Loeffel, Mary Cookson, Claudio Di Leo, and Emily Houston for being great colleagues and friends. I would particularly like to thank Shawn and David for many fruitful discussions and their inputs on various matters. Furthermore, I would like to convey my special thanks to Shawn for his collaboration on several important aspects of my research.

I am thankful to the extended Mechanics and Materials group, especially Meredith Silberstein, Brian Greviskes and Allison Beese for their friendship and support during my stay at MIT.

Finally, I would like to thank my family in India and in New England, particularly my parents for their constant encouragement and support throughout my academic endeavors. I would like to thank Anita Shukla for being a wonderful wife and for her ability to bring out the best in life.

Financial support for this research was provided by grants from the Singapore-MIT Alliance (MST) and the NSF (DMI-0517966).

Contents

List of Figures

List of Tables

Chapter 1

Introduction

Amorphous thermoplastic polymers are important engineering materials that are widely used in a variety of applications because of their light weight and excellent physical, optical (light transparency) and mechanical properties. However, their nonlinear, strongly temperature- and rate-dependent elastic-viscoplastic behavior is still not very well understood, and is modeled by existing constitutive theories with varying degrees of success. Polymer processing operations, such as micro-hot-embossing for the manufacture of microfluidic devices, hot drawing of fibers and films, thermoforming, and blow-molding of various thin walled containers take place at temperatures approximately 10 to 40 °Cabove the glass transition temperature, ϑ_g of the polymer where it is easy to flow but has some "solid"-like characteristics, and not yet a viscoelastic fluid. During hot processing, the polymer undergoes large deformation and is subsequently cooled to a temperature below its glass transition to lock-in the deformed shape. In the process of cooling, the polymer transitions from a soft "rubbery-state"[1] to a solid "glassy-state" during which, the polymer's initial stiffness, flow stress and strain hardening rate change by several orders of magnitudes. There is no generally agreed upon theory to model the large-deformation, thermo-mechanically coupled, elastic-viscoplastic response of these materials in a temperature range which *spans their glass transition temperature.* Such a theory is crucial for the development of a numerical capability for the simulation and design of important polymer processing operations, and also for predicting the relationship between processing methods and the subsequent mechanical properties of polymeric products. A numerical simulation capability based on an accurate theoretical model offers an excellent opportunity to cut cost by predicting material response over a large range of conditions which could be very expensive to examine experimentally. It

[1] At temperatures above the glass transition, the polymer is easy to flow and behaves like an elastic-viscoplastic "soft" solid with some "rubber"-like characteristics. Due to a lack of better terminology, at temperatures above ϑ_g, we refer polymers to be in a "rubbery-state" which is the terminology commonly used in the literature. At temperatures below ϑ_g, the polymer behaves like an elastic-viscoplastic solid where its elastic response and flow stress values are a few orders of magnitude higher than those above ϑ_g. For temperature below ϑ_g, we refer polymers to be in solid a "glassy-state."

is the main objective of this thesis to develop a constitutive theory for amorphous polymers that fulfills this need. Apart from its intrinsic theoretical importance from the viewpoint of mechanics and physics of materials, we shall show that our new theory is practically useful for modeling important polymer processing operations, such as micro-hot-embossing for the manufacture of microfluidic devices and blow-molding of thin-walled containers. Furthermore, for applications where amorphous polymers are used as structural materials to resist impact (e.g. helmets and body armors), our theory may be used to predict thermo-mechanically coupled large-deformation response of these structures under high strain-rate loading conditions.

In addition, this thesis includes an important extension of our work on amorphous thermoplastic polymers by specializing the theory to model and numerically simulate the shape memory response of thermally-actuated amorphous shape memory polymers. Shape memory polymers can be subjected to large deformations at a temperature above their ϑ_g; the deformed shape can be fixed by cooling the deformed body to a temperature below ϑ_g under active kinematical constraints; and the original shape is recovered when the material is heated back to a temperature above ϑ_g without the kinematical constraints.[2] This phenomenon is known as the *shape-memory effect*. If the shape recovery is partially constrained, the material exerts a recovery force and the phenomenon is known as force- or constrained-recovery. Although many novel applications for shape memory polymers ranging from self-deploying stents for treatment of arterial disease (Wache et al., 2003; Yakacki et al., 2007; Baer et al., 2007b), nanoscale-patterned surfaces for information storage and recovery (Vettiger et al., 2002; Wornyo et al., 2007), and self-deployable reflectors for space applications (Campbell et al., 2005) have been envisioned and demonstrated in the published literature, the practical use of shape memory polymers and devices made from these materials is still quite limited. The major reason for this is that an accurate thermo-mechanically-coupled constitutive theory for shape memory behavior in polymers, and an attendant numerical implementation for simulation-based design does not exist. To fill this need we have developed a constitutive theory and numerical simulation capability to model the shape recovery behavior of amorphous shape memory polymers.

[2]The amorphous shape memory polymers preserve heavy cross-linking and respond as viscoelastic rubber-like materials above ϑ_g. After loading and unloading at a temperature above ϑ_g, these polymers show negligible permanent set, which is an important characteristic for the shape memory behavior. On the contrary, thermoplastic amorphous polymers such as Zeonex-690R, PC and PMMA show significant slippage of mechanical cross-links (due to physical entanglements) when deformed above their glass transition temperature. Such polymers when deformed above ϑ_g, cooled under kinematical constraint to a temperature below ϑ_g, and then heated back without constraints to a temperature above ϑ_g, do not show complete recovery to their original shape.

1.1 Background

1.1.1 Amorphous polymers

Over the past twenty-five years considerable effort has been devoted to develop constitutive models to represent the large-deformation elastic-viscoplastic behavior of amorphous polymers. One of the early seminal work was a simple one-dimensional rheological model by Haward and Thackray (1968). In their paper, Haward and Thackray (1968) proposed the essence of the large strain behavior of glassy polymers in a one-dimensional setting by combining the features of both glass-like behavior and nonlinear rubber-like behavior. They used a linear spring to represent the elastic intermolecular interactions, a viscous dashpot with yield/flow based on Eyring (1936) theory to model rate-dependent macro-yielding, and a nonlinear spring, the so-called rubber-elastic Langevin spring, to describe the subsequent strain hardening due to the alignment of the macromolecular network built of entangled polymer molecules. The alignment of the network chains gives rise to an entropic (rubbery) restorative stress or a "back stress" in the material.

The simple one-dimensional model by Haward and Thackray (1968) has had substantial influence on the construction of constitutive models for amorphous polymers. Their approach was extended to three-dimensions by Bagepalli (1984), Parks et al. (1985), Boyce et al. (1988), Wu and Van der Giessen (1993a), Govaert et al. (2000) and Anand and Gurtin (2003a). Although differing in details, these models were able to reproduce the large deformation elastic-viscoplastic response of the glassy amorphous polymers in a reasonably acceptable manner; however, these models were developed to primarily describe the *isothermal* deformation of polymers below their glass transition temperature.

A great deal of attention has been given to modeling the rate- and temperature-dependent yield stress of polymers. There are many models for the yield strength of polymers in the literature which consider plastic flow as a thermally-activated process (cf., e.g., Eyring, 1936; Robertson, 1966; Argon, 1973). Most of these models rely on a single micromechanism for the yield stress and give a reasonably acceptable representation of the variation of the yield strength with temperature and strain rate over limited ranges of these variables. Mulliken and Boyce (2006), have proposed an alternate model to describe the variation of the yield strength of amorphous polymers over a wide range of strain rates and temperatures for temperatures below the glass transition. Their model is a generalization of the model(s) proposed by Bauwens, Bauwens-Crowet and co-workers (cf., e.g., Bauwens et al., 1969; Bauwens-Crowet et al., 1969; Bauwens, 1972; Bauwens-Crowet, 1973) in which they introduced two rheological micro-mechanisms — designated as primary or α and secondary or β — which contribute to the yield strength of the material. The primary α-mechanism represents the rotations of the main-chain segments of the polymer, and the secondary β-mechanism represents the rotations of the side groups. These two mechanisms are rate-limiting in different regimes of strain rates and/or temperatures; the α-mechanism is the dominant rate-limiting mechanism at low rates (or high temperatures), and the β-mechanism is the dominant rate-limiting mechanism at high strain rates (or low temperatures). On the other hand, Richeton

et al. (2005a, 2006, 2007) have based their yield flow function on the so-called "cooperative"-model of Fotheringham et al. (1976), Fotheringham and Cherry (1978), Povolo and Hermida (1995) and Povolo et al. (1996). Richeton et al. have shown that instead of using two different micromechanisms — α and β for the yield strength, a flow function based on a single micromechanism and following the "cooperative"-model may be used to satisfactorily represent the variation of the yield strength of amorphous polymers over a wide range of strain rates and temperatures.

Thermo-mechanical coupling effects have also been studied for temperatures below the glass transition temperature. Arruda et al. (1995) and Ames (2007) modeled and experimentally verified the phenomenon of stress softening due to the internal heat generation from the plastic dissipation for strain rates $\gtrapprox 0.01\,\mathrm{s}^{-1}$ under nominally homogeneous deformations; while Garg et al. (2008) measured temperature rise in polycarbonate due to adiabatic heating at strain rates of the order of $\approx 5000\,\mathrm{s}^{-1}$. Van der Giessen and coworkers (e.g. Basu and Van der Giessen, 2002; Estevez et al., 2005; Estevez and Basu, 2008) have studied the effects of adiabatic heating in the context of temperature changes on the fracture response at cracks and notches under high-rate mode-I loading.

Theories to model the large-deformation response of amorphous polymers in a temperature range which spans their glass transition temperature are still in their infancy. Constitutive theories for this class of applications have been proposed by Boyce and coworkers (Dupaix, 2003; Dupaix and Boyce, 2007), Buckley and coworkers (Buckley and Jones, 1995; Dooling et al., 2002), and Richeton and coworkers (Richeton et al., 2007). Ames (2007) in her recent thesis developed a model for PMMA for a strain level upto 100% and at temperatures ranging from room temperature to temperatures $\approx 50\,^{\circ}$Cabove ϑ_g. These theories though differing in details rely on two basic micromechanisms, one due to intermolecular resistance and the other due to molecular network resistance to model the macroscopic polymer response. Although most of these theories are able to predict the major rate- and temperature-dependent trends under homogeneous deformation conditions, their predictive capabilities are either limited to a certain range of strain and temperature or to a specific polymer. Further, there exists no single theory that has been demonstrated to accurately simulate a complete thermal-forming cycle (involving large, deformation above ϑ_g and subsequent cooling to a temperature below ϑ_g) for a variety of amorphous polymers under complex inhomogeneous deformation situations.

Following the multimechanism approach of Buckley and Jones (1995), Dooling et al. (2002), Dupaix (2003), Dupaix and Boyce (2007), Richeton et al. (2007) and Ames (2007), we have developed a reasonably accurate theory for a wide variety of amorphous polymers which spans their glass transition temperature. Our theory uses internal state variables to macroscopically represent the important aspects of the microstructural resistance to the plastic flow. Some of the important new features that are proposed in our theory are:

- The number of microscopic relaxation mechanisms increase as the temperature increases from below ϑ_g to above ϑ_g, therefore, we employ three micromechanisms to reasonably accurately model the rate- and temperature-dependent response of amorphous polymers in a temperature range which spans their glass transition temperature.

The first micromechanism ($\alpha = 1$) represents the intermolecular resistance and the second and third micromechanisms ($\alpha = 2, 3$) represent the molecular network resistance.

- For temperatures below ϑ_g, our model reduces to a simpler two-micromechanism model similar to the models proposed by Buckley and Jones (1995), Dooling et al. (2002), Dupaix (2003), Dupaix and Boyce (2007), Richeton et al. (2007) and Ames (2007). As in Ames (2007), one major difference here is that we employ a tensorial backstress which is used to phenomenologically capture the unloading and cyclic loading phenomenon. In addition, it allows us to properly account for the energy dissipation and temperature rise during plastic flow.

- In almost all the existing literature on amorphous polymers, the rapid nonlinear increase in stress levels at large deformations for temperatures below ϑ_g has been attributed entirely to elastic effects associated with the stretching of polymer chains. However, our experience with experiments that involve both loading to large strains and subsequent *unloading*, indicate that if in a corresponding theoretical model, the rapid increase in stress levels during loading is attributed entirely to the elastic effects, then the unloading response is incorrectly predicted — there is too much "elastic recovery" upon unloading. In our theory, we have introduced a macroscopic stress-like internal variable to model a *dissipative* resistance to plastic flow which arises at large strains as the chains are pulled taut between entanglements and there is increasing interaction between long chains and pendant side-groups. This dissipative resistance is in addition to any nonlinear elastic contribution from network chain stretching and is effective at temperatures both below and above ϑ_g.

- Based on the "cooperative"-model of Fotheringham et al. (1976), Fotheringham and Cherry (1978), Povolo and Hermida (1995), Povolo et al. (1996) and the works of Richeton et al. (2005a, 2006, 2007) for the yield strength, we have proposed a physically motivated thermally-activated flow function for the plastic shear strain rate which accounts for the increase in concentration of "flow-defects" and decrease in activation energy as the temperature is increased through ϑ_g. This flow function satisfactorily represents the variation of the yield strength of amorphous polymers over a wide range of strain rates and temperatures.

1.1.2 Shape memory polymers

In the past decade, several efforts at experimental characterization of the thermo-mechanical response of a wide variety of shape memory polymers have been published in the literature. Some of the notable studies characterized thermo-mechanical properties (Tobushi et al., 1996; Baer et al., 2007a), effect of process parameters on shape recovery behavior (Gall et al., 2005), and fundamental trends between network chemical structure and mechanical response (Yakacki et al., 2007; Safranski and Gall, 2008). Although these experimental studies provide substantial understanding of the phenomenology of shape memory behavior, a relatively

complete set of experimental data which characterizes the large-deformation, strain-rate and temperature-dependent stress-strain response for any given shape memory polymer, currently does not exist. Recently Qi et al. (2008) have reported a set of rate- and temperature-dependent large-deformation stress-strain data for a thermoset shape memory polymer, but even this study lacks published details regarding the significant nonlinear hardening observed at large strains and unloading response of these materials, which are crucial to properly model the details of the recovery response.

In a typical thermo-mechanical shape memory cycle, the polymer transitions from a viscoelastic rubber-like material into an elastic-viscoplastic glassy solid during the fixation of the deformed shape, and again into a viscoelastic rubber-like material when the shape-recovery is actuated. Modeling this complex change in material behavior poses major challenges. Significant modeling efforts have been carried out in the past several years. A few of the notable published modeling studies are those of Liu et al. (2006), Chen and Lagoudas (2008), Qi et al. (2008), and Nguyen et al. (2008). Liu et al. (2006) proposed a three-dimensional constitutive model in the small strain limit with the phenomenological concept of coexisting soft (rubbery) and frozen (glassy) phases within the glass transition regime where the evolution of the frozen state solely depended on the temperature. Based on this concept Chen and Lagoudas (2008), and Qi et al. (2008) developed large deformation three-dimensional constitutive models for shape memory polymers. The major drawback of these theories lies in the fact that no physical evidence exists to support the arguments upon which these theories are formulated. In our view, the recent thermo-viscoelastic model by Nguyen et al. (2008) is a better approach to model shape memory behavior. However, this model relies on the limited set of experimental data from the earlier study by Qi et al. (2008), and therefore lacks the necessary details to accurately model the shape-recovery response of these materials.

Research on modeling the thermo-mechanical response of shape memory polymers is still in its infancy, and a significant amount of experimental, theoretical, and computational work needs to be conducted. Therefore, we have specialized our theory for amorphous polymers to model the thermo-mechanically coupled large-deformation response of amorphous shape memory polymers.

1.2 Contributions of this thesis

- Amorphous polymers show a large number of similar characteristics irrespective of their chemical composition. Consequently, a primary goal of this thesis is to develop constitutive theories that are general enough to reasonably accurately model a variety of amorphous polymers. Towards this goal, the thermo-mechanically coupled large-deformation elastic-viscoplastic framework presented in Chapter 2 has been specialized to develop the following thermo-mechanically coupled, large-deformation constitutive theories: (i) a constitutive theory for amorphous polymers below their glass transition temperature for a wide range of strain-rates; (ii) a constitutive theory for amorphous polymers in a temperature range which spans their glass transition; and (iii) a constitutive theory to model the shape memory response of shape memory polymers.

- We have generated a relatively complete set of stress-strain data for a technologically important amorphous thermoplastic cyclo-olefin copolymer Zeonex-690R[3] by conducting a suite of simple compression experiments on Zeonex-690R to large strains exceeding 130%, including loading and unloading; at strain rates of $3 \times 10^{-4}\,s^{-1}$, $3 \times 10^{-3}\,s^{-1}$, $3 \times 10^{-2}\,s^{-1}$, and $3 \times 10^{-1}\,s^{-1}$, in a temperature range from room temperature to $\approx 40\,^{\circ}C$ above the glass transition temperature of the material. The nominal glass transition temperature of Zeonex-690R is $135\,^{\circ}C$.

- Stress-strain data for a chemically cross-linked shape memory polymer was generated by conducting a suite of simple compression experiments to strains $\sim 100\%$, including loading and unloading; at strain rates of $10^{-3}\,s^{-1}$, and $10^{-1}\,s^{-1}$, in a temperature range from room temperature to $\approx 30\,^{\circ}C$above the glass transition temperature of the material. The polymer was fabricated via photopolymerization of a tert-butyl acrylate (tBA) monomer with the cross-linking agent poly(ethylene glycol) dimethacrylate (PEGDMA). The nominal glass transition temperature of this tBA/PEGDMA shape memory polymer is $37\,^{\circ}C$.

- We have presented calibration procedures for the material parameters that appear in our theories and following these procedures, we have obtained material parameter values for (i) three technologically important thermoplastic amorphous polymers Zeonex-690R, PC and PMMA, and (ii) a tBA/PEGDMA thermoset shape memory polymer.

  Theories of the type considered in this thesis, even in the linear-viscoelasticity regime, typically require a large number of Maxwell-elements (or Kelvin-Voigt/Zener-elements) M, with an associated large number of spring-constants and viscosities, to fit experimentally observed stress-relaxation, creep and other mechanical response characteristics of polymers in the small strain regime. For the large deformation theory considered here, our goal was to choose the minimum number of micro-mechanisms M, and thereby the associated number of material parameters, which can replicate the experimentally-observed stress-strain curves in the strain, strain-rate, and temperature range of interest with reasonable accuracy. Nevertheless, the number of material parameters for the polymers considered in this thesis is still quite large. Unfortunately, this is a limitation of this class of phenomenological continuum-level theories. However, once the material parameters are calibrated, we show in this thesis that the theory is able to predict the response of the material in complex three-dimensional geometries which are subjected to a variety of thermo-mechanical histories.

[3]From Zeon Chemicals. Relative to conventional amorphous polymers such as PC and PMMA, Zeonex-690R, a cyclo-olefin polymer is biocompatible, has lower moisture uptake, has better light transmittance characteristics, and it is also chemical resistant to a wide variety of solvents. These characteristics make Zeonex-690R an attractive material for several applications such as microfluidic devices and therefore a focus of our study.

- An implicit time-integration procedure for our thermo-mechanically coupled theory was developed and implemented by my colleague Shawn A. Chester to create a numerical simulation capability for the finite element program ABAQUS/Standard (2009). Using this simulation capability, polymer processing operations such as micro-hot-embossing, thermoforming, and blow-molding as well as thermo-mechanical shape-recovery response of shape memory polymers have been successfully simulated.

- We have presented results for the following macro-scale validation experiments in this thesis which involved inhomogeneous deformations: (i) isothermal fixed-end reversed torsion test on PC; (ii) high-speed normal-impact of a circular plate of PC; (iii) isothermal plane-strain cold- and hot-forming operations on PC; (iv) isothermal, axi-symmetric hot-forming operations on Zeonex-690R; (v) blow-forming of thin-walled semi-spherical shapes in PC; (vi) force-recovery in a tBA/PEGDMA shape memory polymer ring subjected to kinematical constraints; and (vii) unconstrained shape-recovery in a diamond-shaped lattice geometry of tBA/PEGDMA shape memory polymer. In addition to validating the accuracy of our models and their numerical implementations, experimental results presented in this thesis could also serve the purpose of verifying the predictive capability of other models. Most of these validation experiments were conducted in collaboration with Shawn A. Chester of our laboratory.

- We have used numerical simulations to successfully determine suitable temperature, pressure and hold-time process conditions for micro-hot-embossing of various features in Zeonex-690R. We have conducted corresponding micro-hot-embossing experiments on Zeonex-690R to verify the predictive capability of our theory and its numerical simulation capability. Numerical simulation approaches such as the ones demonstrated in this thesis can be used to determine optimum processing conditions for micro-hot-embossing without a need for costly experimentation.

1.3 List of publications related to this thesis

- Anand, L., Ames, N. M., Srivastava, V., and Chester, S. A., 2009. A thermo-mechanically coupled theory for large deformations of amorphous polymers. Part I: formulation, *International Journal of Plasticity* 25, 1474–1494.

- Ames, N. M., Srivastava, V., Chester, S. A., and Anand, L., 2009. A thermo-mechanically coupled theory for large deformations of amorphous polymers. Part II: applications, *International Journal of Plasticity* 25, 1495–1539.

- Srivastava, V., Chester, S. A., Ames, N. M., and Anand, L., 2009. A thermo-mechanically coupled large-deformation theory for amorphous polymers which spans their glass transition, *International Journal of Plasticity*, submitted.

- Srivastava, V., Chester, S. A., and Anand, L., 2009. Thermally-actuated shape memory polymers: experiments, theory, and numerical simulations, *Journal of the Mechanics and Physics of Solids*, submitted.

- Srivastava, V., and Anand, L., Nov. 2008. On modeling the mechanical behavior of amorphous polymers for the micro-hot-embossing of microfluidic devices, *Proceedings of ASME International Mechanical Engineering Congress & Exposition*, Boston, MA.

- Henann, D., Srivastava, V., Taylor, H. K., Hale, M. H., Hardt, D. E., and Anand, L., 2009. Metallic glasses: viable tool materials for production of surface microstructures in amorphous polymers by micro-hot-embossing, *Journal of Micromechanics and Microengineering* 19, 115030 (10 pp).

1.4 Structure of thesis

The structure of this thesis is as follows. In Chapter 2, we present a large-deformation, thermo-mechanically coupled elastic-viscoplastic theory. A specialization of this theoretical framework to model the response of amorphous polymers below the glass transition temperature is presented in Chapter 3. A material parameter calibration procedure that was used to fit the experimental stress-strain data for Zeonex-690R, PC, and PMMA for the theory presented in Chapter 3 is described in detail in Appendix A. Chapter 4 presents a specialized constitutive theory to model the polymer response through the glass transition. A material parameter calibration procedure used to fit the experimental stress-strain data for Zeonex-690R, PC, and PMMA for the theory presented in Chapter 4 is described in detail in Appendix B. The theory presented in Chapter 4 was specialized in Chapter 5 to model the shape memory polymers. We close in Chapter 6 with some final remarks and a discussion on future research directions.

Chapter 2

Anand's thermo-mechanically coupled large-deformation theory for isotropic elastic-viscoplastic materials

2.1 Introduction

Amorphous thermoplastics are important engineering materials which are widely used in a variety of applications. Over the past twenty-five years considerable effort has been devoted to develop constitutive models to represent the large deformation elastic-viscoplastic behavior of these materials (e.g., Parks et al., 1985; Boyce et al., 1988; Govaert et al., 2000; Anand and Gurtin, 2003a; Anand and Ames, 2006; Anand et al., 2009). These models have been primarily used to describe the *isothermal* deformation of polymers below their glass transition temperature, ϑ_g. There exists a major need to develop a large-deformation thermo-mechanically coupled theory for amorphous polymers which spans their glass transition temperature. Such a theory would be useful for modeling important polymer processing operations such as micro-hot-embossing for the manufacture of microfluidic devices, hot-drawing, and blow-molding for manufacture of various thin walled container. Constitutive theories aimed at this class of applications have been proposed by Boyce and co-workers (e.g., Boyce et al., 2000; Dupaix, 2003; Dupaix and Boyce, 2007), as well as Buckley and co-workers (e.g., Buckley and Jones, 1995; Dooling et al., 2002). Guided by the work of Boyce, Buckley and their co-workers, a thermo-mechanically coupled large-deformation theoretical framework for isotropic elastic-viscoplastic materials was recently developed by L. Anand. It is the purpose of this chapter to present the unpublished theory of L. Anand which was first presented in his plenary Khan International Medal lecture at the 2007 Plasticity conference in Alaska. The reasonably general theoretical framework presented in this chapter is specialized in Chapter 3 to model the salient features of thermo-mechanically-coupled strain rate and temperature dependent response of amorphous polymers in the glassy region. A

constitutive theory for amorphous polymers which spans their glass transition temperature is then presented in Chapter 4. Further this theory is specialized in Chapter 5 to model the shape memory response of shape memory polymers.

2.2 Kinematics

Consider a homogeneous body B identified with the region of space it occupies in a fixed *reference configuration*, and denote by $\mathbf{X}$ an arbitrary material point of B. A *motion* of B is then a smooth one-to-one mapping $\mathbf{x} = \boldsymbol{\chi}(\mathbf{X}, t)$ with *deformation gradient*, *velocity*, and *velocity gradient* given by[1]

$$\mathbf{F} = \nabla\boldsymbol{\chi}, \qquad \mathbf{v} = \dot{\boldsymbol{\chi}}, \qquad \mathbf{L} = \operatorname{grad}\mathbf{v} = \dot{\mathbf{F}}\mathbf{F}^{-1}. \tag{2.1}$$

An essential kinematical ingredient of elastic-viscoplastic constitutive theories for amorphous polymers *below* their glass transition temperatures, is the classical Kröner (1960)- Lee (1969) multiplicative decomposition

$$\mathbf{F} = \mathbf{F}^e\mathbf{F}^p \tag{2.2}$$

of the deformation gradient $\mathbf{F}$ into elastic and plastic parts $\mathbf{F}^e$ and $\mathbf{F}^p$ (e.g., Parks et al., 1985; Boyce et al., 1988; Govaert et al., 2000; Anand and Gurtin, 2003a; Anand and Ames, 2006; Anand et al., 2009). We wish to model the behavior of glassy polymers in the technologically important range temperature range which *spans their glass transition temperatures.* Thus since the number of microscopic relaxation mechanisms in these polymers increase as the temperature is increased, the theory is based on "multi-mechanism" generalization of the decomposition (2.2),

$$\mathbf{F} = \mathbf{F}^{e\,(\alpha)}\mathbf{F}^{p\,(\alpha)}, \qquad \alpha = 1, \ldots, M, \tag{2.3}$$

where each α denotes a local micromechanism of deformation. Such a multimechanism generalization forms the basis of the recent work of Anand, Buckley, Boyce, and their coworkers (Buckley and Jones, 1995; Boyce et al., 2000; Dooling et al., 2002; Dupaix, 2003; Dupaix and Boyce, 2007; Ames, 2007). For each micromechanism indexed by α, we refer to

[1]We use standard notation of modern continuum mechanics (e.g., Gurtin et al., 2009). Specifically: ∇ and Div denote the gradient and divergence with respect to the material point $\mathbf{X}$ in the *reference configuration*; grad and div denote these operators with respect to the point $\mathbf{x} = \boldsymbol{\chi}(\mathbf{X}, t)$ in the *deformed body*; a superposed dot denotes the material time-derivative. Throughout, we write $\mathbf{F}^{e-1} = (\mathbf{F}^e)^{-1}$, $\mathbf{F}^{p-\mathsf{T}} = (\mathbf{F}^p)^{-\mathsf{T}}$, etc. We write $\operatorname{tr}\mathbf{A}$, $\operatorname{sym}\mathbf{A}$, $\operatorname{skw}\mathbf{A}$, $\mathbf{A}_0$, and $\operatorname{sym}_0\mathbf{A}$ respectively, for the trace, symmetric, skew, deviatoric, and symmetric-deviatoric parts of a tensor $\mathbf{A}$. Also, the inner product of tensors $\mathbf{A}$ and $\mathbf{B}$ is denoted by $\mathbf{A}:\mathbf{B}$, and the magnitude of $\mathbf{A}$ by $|\mathbf{A}| = \sqrt{\mathbf{A}:\mathbf{A}}$.

$\mathbf{F}^{p\,(\alpha)}$ and $\mathbf{F}^{e\,(\alpha)}$ as the *plastic and elastic parts* of $\mathbf{F}$.[2] As is standard, we assume that

$$J = \det \mathbf{F} > 0,$$

and consistent with this we assume that

$$J^{e\,(\alpha)} \stackrel{\text{def}}{=} \det \mathbf{F}^{e\,(\alpha)} > 0, \qquad J^{p\,(\alpha)} \stackrel{\text{def}}{=} \det \mathbf{F}^{p\,(\alpha)} > 0, \tag{2.4}$$

so that $\mathbf{F}^{e\,(\alpha)}$ and $\mathbf{F}^{p\,(\alpha)}$ are invertible.

Restrict attention to a prescribed *material point* $\mathbf{X}$, and let $\mathbf{x}$ denote its place in the deformed configuration at a fixed time t. Then, bearing in mind that (for $\mathbf{X}$ fixed) the linear transformations $\mathbf{F}^{e\,(\alpha)}(\mathbf{X})$ and $\mathbf{F}^{p\,(\alpha)}(\mathbf{X})$ at $\mathbf{X}$ are invertible, we let

$$\mathcal{M}_{\mathbf{X}}{}^{(\alpha)} \stackrel{\text{def}}{=} \text{range of } \mathbf{F}^{p\,(\alpha)}(\mathbf{X}) = \text{domain of } \mathbf{F}^{e\,(\alpha)}(\mathbf{X}), \tag{2.5}$$

and refer to $\mathcal{M}_{\mathbf{X}}{}^{(\alpha)}$ as the *intermediate space* at $\mathbf{X}$ for the α-th micromechanism. Even though we use this terminology, *there is no actual physical space* that may be associated with an "intermediate structural space" — such spaces are purely mathematical constructs.

For each micromechanism indexed by α, we refer to $\mathbf{F}^{p\,(\alpha)}$ and $\mathbf{F}^{e\,(\alpha)}$ as the *plastic and elastic parts* of $\mathbf{F}$. Physically, for each α,

- $\mathbf{F}^{p\,(\alpha)}(\mathbf{X})$ represents the local inelastic distortion of the material at $\mathbf{X}$ due to a "plastic mechanism" such as the relative chain slippage of the long-chain polymer molecules, or the cumulative effects of destruction of temporary mechanical cross-links. This local deformation carries the material into — and ultimately "pins" the material to — a *coherent structure* that resides in the *intermediate space* at $\mathbf{X}$ for each α (as represented by the range of $\mathbf{F}^{p\,(\alpha)}(\mathbf{X})$);

- $\mathbf{F}^{e\,(\alpha)}(\mathbf{X})$ represents the subsequent stretching and rotation of this coherent structure, and thereby represents the corresponding "elastic distortion," such as stretching and rotation of the intermolecular bonds and the long-chain polymer molecules.

Also, it is important to note from the outset, that each $\mathbf{F}^{p\,(\alpha)}$ is to be regarded as an internal variable of the theory which is defined as the solution of the differential equation (flow rule to be discussed later)

$$\dot{\mathbf{F}}^{p\,(\alpha)} = \mathbf{L}^{p\,(\alpha)}\mathbf{F}^{p\,(\alpha)} \text{ with } \det \mathbf{F}^{p\,(\alpha)} = 1, \text{ and with the initial condition } \mathbf{F}^{p\,(\alpha)}(\mathbf{X}, 0) = \mathbf{1}. \tag{2.6}$$

[2] In a one-dimensional theory of linear viscoelasticity, which is based on a widely-used mechanical analog of M Maxwell-elements assembled in parallel, the one-dimensioinal strain ϵ is decomposed as

$$\epsilon = \epsilon^{e(\alpha)} + \epsilon^{p(\alpha)}, \qquad \alpha = 1, \ldots, M;$$

the decomposition (2.3) is a three-dimensional, large-deformation, generalization of such a decomposition.

The corresponding $\mathbf{F}^{e\,(\alpha)}$ is the defined by $\mathbf{F}^{e\,(\alpha)} \stackrel{\text{def}}{=} \mathbf{F}\mathbf{F}^{p\,(\alpha)-1}$. Hence the decomposition (2.3) are not purely kinematical in nature as they are not defined independently of constitutive equations; they are to be viewed as *kinematical constitutive equations.*

By $(2.1)_3$ and (2.3),

$$\mathbf{L} = \operatorname{grad}\mathbf{v} = \mathbf{L}^{e\,(\alpha)} + \mathbf{F}^{e\,(\alpha)}\mathbf{L}^{p\,(\alpha)}\mathbf{F}^{e\,(\alpha)-1}, \tag{2.7}$$

with

$$\mathbf{L}^{e} = \dot{\mathbf{F}}^{e(\alpha)}\mathbf{F}^{e\,(\alpha)-1}, \qquad \mathbf{L}^{p\,(\alpha)} = \dot{\mathbf{F}}^{p(\alpha)}\mathbf{F}^{p\,(\alpha)-1}. \tag{2.8}$$

As is standard, the total elastic and plastic stretching, and spin tensors are defined through

$$\left.\begin{aligned} &\mathbf{D} = \operatorname{sym}\mathbf{L}, && \mathbf{W} = \operatorname{skw}\mathbf{L}, \\ &\mathbf{D}^{e\,(\alpha)} = \operatorname{sym}\mathbf{L}^{e\,(\alpha)}, && \mathbf{W}^{e\,(\alpha)} = \operatorname{skw}\mathbf{L}^{e\,(\alpha)}, \\ &\mathbf{D}^{p\,(\alpha)} = \operatorname{sym}\mathbf{L}^{p\,(\alpha)}, && \mathbf{W}^{p\,(\alpha)} = \operatorname{skw}\mathbf{L}^{p\,(\alpha)}, \end{aligned}\right\} \tag{2.9}$$

so that $\mathbf{L} = \mathbf{D} + \mathbf{W}$, $\mathbf{L}^{e\,(\alpha)} = \mathbf{D}^{e\,(\alpha)} + \mathbf{W}^{e\,(\alpha)}$, and $\mathbf{L}^{p\,(\alpha)} = \mathbf{D}^{p\,(\alpha)} + \mathbf{W}^{p\,(\alpha)}$.

The right and left and polar decompositions of $\mathbf{F}^{e\,(\alpha)}$ are given by

$$\mathbf{F}^{e\,(\alpha)} = \mathbf{R}^{e\,(\alpha)}\mathbf{U}^{e\,(\alpha)} = \mathbf{V}^{e\,(\alpha)}\mathbf{R}^{e\,(\alpha)}, \tag{2.10}$$

where $\mathbf{R}^{e\,(\alpha)}$ is a rotation (proper orthogonal tensor), while $\mathbf{U}^{e\,(\alpha)}$ and $\mathbf{V}^{e\,(\alpha)}$ are symmetric, positive-definite tensors with

$$\mathbf{U}^{e\,(\alpha)} = \sqrt{\mathbf{F}^{e\,(\alpha)\top}\,\mathbf{F}^{e\,(\alpha)}}, \qquad \mathbf{V}^{e\,(\alpha)} = \sqrt{\mathbf{F}^{e\,(\alpha)}\,\mathbf{F}^{e\,(\alpha)\top}}\,. \tag{2.11}$$

Also, the right and left elastic Cauchy-Green tensors are given by

$$\mathbf{C}^{e\,(\alpha)} = \mathbf{U}^{e\,(\alpha)2} = \mathbf{F}^{e\,(\alpha)\top}\,\mathbf{F}^{e\,(\alpha)}, \qquad \mathbf{B}^{e\,(\alpha)} = \mathbf{V}^{e\,(\alpha)2} = \mathbf{F}^{e\,(\alpha)}\mathbf{F}^{e\,(\alpha)\top}, \tag{2.12}$$

and the right and left inelastic Cauchy-Green tensors by

$$\mathbf{C}^{p\,(\alpha)} = \mathbf{U}^{p\,(\alpha)2} = \mathbf{F}^{p\,(\alpha)\top}\,\mathbf{F}^{p\,(\alpha)}, \qquad \mathbf{B}^{p\,(\alpha)} = \mathbf{V}^{p\,(\alpha)2} = \mathbf{F}^{p\,(\alpha)}\mathbf{F}^{p\,(\alpha)\top}. \tag{2.13}$$

2.2.1 Incompressible, irrorational plastic flow

We assume that the *plastic flow is incompressible* so that

$$J^{p\,(\alpha)} = 1, \tag{2.14}$$

and

$$\operatorname{tr}\mathbf{L}^{p\,(\alpha)} = \operatorname{tr}\mathbf{D}^{p\,(\alpha)} = 0\,. \tag{2.15}$$

Hence

$$J^{e\,(\alpha)} = J \quad \text{for all } \alpha\,. \tag{2.16}$$

Further, from the outset, we constrain the theory by limiting our discussion to circumstances under which the material may be idealized as isotropic (see later). For isotropic elastic-viscoplastic theories utilizing the multiplicative decomposition (2.3) it is widely assumed that the plastic flow is irrotational in the sense that[3]

$$\mathbf{W}^{p\,(\alpha)} = \mathbf{0}. \tag{2.17}$$

Then, $\mathbf{L}^{p\,(\alpha)} = \mathbf{D}^{p\,(\alpha)}$, and

$$\dot{\mathbf{F}}^{p(\alpha)} = \mathbf{D}^{p\,(\alpha)}\mathbf{F}^{p\,(\alpha)}. \tag{2.18}$$

Thus, using (2.1), (2.7), (2.8), and (2.18), we may rewrite (2.7) for future use as

$$(\nabla\dot{\boldsymbol{\chi}})\mathbf{F}^{-1} = \dot{\mathbf{F}}^{e\,(\alpha)}\mathbf{F}^{e\,(\alpha)-1} + \mathbf{F}^{e\,(\alpha)}\mathbf{D}^{p\,(\alpha)}\mathbf{F}^{e\,(\alpha)-1}. \tag{2.19}$$

2.3 Frame-indifference

Changes in frame (observer) are smooth time-dependent rigid transformations of the Euclidean space through which the body moves. The theory needs to be invariant under such transformations, and hence under transformations of the form

$$\boldsymbol{\chi}(\mathbf{X}, t) \to \mathbf{Q}(t)(\boldsymbol{\chi}(\mathbf{X}, t) - \mathbf{o}) + \mathbf{y}(t) \tag{2.20}$$

with $\mathbf{Q}(t)$ a rotation (proper-orthogonal tensor), $\mathbf{y}(t)$ a point at each t, and $\mathbf{o}$ a fixed origin. Then, under a change in observer, the deformation gradient transforms according to

$$\mathbf{F} \to \mathbf{Q}\mathbf{F}. \tag{2.21}$$

Thus, $\dot{\mathbf{F}} \to \mathbf{Q}\dot{\mathbf{F}} + \dot{\mathbf{Q}}\mathbf{F}$, and by $(2.1)_3$,

$$\mathbf{L} \to \mathbf{Q}\mathbf{L}\mathbf{Q}^{\top} + \dot{\mathbf{Q}}\mathbf{Q}^{\top}. \tag{2.22}$$

Hence,

$$\mathbf{D} \to \mathbf{Q}\mathbf{D}\mathbf{Q}^{\top}, \qquad \mathbf{W} \to \mathbf{Q}\mathbf{W}\mathbf{Q}^{\top} + \dot{\mathbf{Q}}\mathbf{Q}^{\top}\,. \tag{2.23}$$

Moreover, $\mathbf{F}^{e\,(\alpha)}\mathbf{F}^{p\,(\alpha)} \to \mathbf{Q}\mathbf{F}^{e\,(\alpha)}\mathbf{F}^{p\,(\alpha)}$, and therefore, since *observers view only the deformed configuration*,

$$\mathbf{F}^{e\,(\alpha)} \to \mathbf{Q}\mathbf{F}^{e\,(\alpha)}, \qquad \mathbf{F}^{p\,(\alpha)} \text{ are invariant}, \tag{2.24}$$

[3]This assumption is based solely on pragmatic grounds: when discussing finite deformations a theory without plastic spin is far simpler than with plastic spin. However, in the context of the single micromechanism decomposition $\mathbf{F} = \mathbf{F}^e\mathbf{F}^p$, see Boyce et al. (1989) and Gurtin and Anand (2005) for a detailed discussion concerning irrotationality of plastic flow for isotropic materials.

and, by (2.8),

$$\mathbf{L}^{e\,(\alpha)} \to \mathbf{Q}\mathbf{L}^{e\,(\alpha)}\mathbf{Q}^{\top} + \dot{\mathbf{Q}}\mathbf{Q}^{\top}, \tag{2.25}$$

and

$$\mathbf{L}^{p\,(\alpha)},\ \mathbf{D}^{p\,(\alpha)},\ \text{and}\ \mathbf{W}^{p\,(\alpha)}\ \text{are invariant.} \tag{2.26}$$

Further, by (2.10),

$$\mathbf{F}^{e\,(\alpha)} = \mathbf{R}^{e\,(\alpha)}\mathbf{U}^{e\,(\alpha)} \to \mathbf{Q}\mathbf{F}^{e\,(\alpha)} = \underline{\mathbf{Q}\mathbf{R}^{e\,(\alpha)}}\mathbf{U}^{e\,(\alpha)},$$
$$\mathbf{F}^{e\,(\alpha)} = \mathbf{V}^{e\,(\alpha)}\mathbf{R}^{e\,(\alpha)} \to \mathbf{Q}\mathbf{F}^{e\,(\alpha)} = \underline{\mathbf{Q}\mathbf{V}^{e\,(\alpha)}\mathbf{Q}^{\top}}\ \mathbf{Q}\mathbf{R}^{e\,(\alpha)},$$

and it can be concluded from the uniqueness of the polar decomposition that

$$\mathbf{R}^{e\,(\alpha)} \to \mathbf{Q}\mathbf{R}^{e\,(\alpha)}, \qquad \mathbf{V}^{e\,(\alpha)} \to \mathbf{Q}\mathbf{V}^{e\,(\alpha)}\mathbf{Q}^{\top}, \qquad \mathbf{U}^{e\,(\alpha)}\ \text{are invariant.} \tag{2.27}$$

Hence, from (2.12), $\mathbf{B}^{e\,(\alpha)}$ and $\mathbf{C}^{e\,(\alpha)}$ transform as

$$\mathbf{B}^{e\,(\alpha)} \to \mathbf{Q}\mathbf{B}^{e\,(\alpha)}\mathbf{Q}^{\top}, \qquad \text{and} \qquad \mathbf{C}^{e\,(\alpha)}\ \text{are invariant.} \tag{2.28}$$

2.4 Development of the theory based on the principle of virtual power

Following the pioneering approach of Gurtin (2002), and previous work on modeling polymeric materials (Anand and Gurtin, 2003a; Anand and Ames, 2006), the theory is developed based on the principle of virtual power.

Denote by P an arbitrary *part* of the reference body B with $\mathbf{n}_{\mathrm{R}}$ the outward unit normal on the boundary ∂P of P. The power expended on P by material or bodies exterior to P results from a *macroscopic surface traction* $\mathbf{s}(\mathbf{n}_{\mathrm{R}})$, measured per unit area in the reference body, and a *macroscopic body force* $\mathbf{b}_{\mathrm{R}}$, measured per unit volume in the reference body, each of whose working accompanies the macroscopic motion of the body. The body force $\mathbf{b}_{\mathrm{R}}$ is assumed to include inertial forces; that is, granted that the underlying frame is inertial,

$$\mathbf{b}_{\mathrm{R}} = \mathbf{b}_{0\mathrm{R}} - \rho_{\mathrm{R}}\ddot{\boldsymbol{\chi}}, \tag{2.29}$$

with $\mathbf{b}_{0\mathrm{R}}$ the noninertial body force, and $\rho_{\mathrm{R}} > 0$ the mass density in the reference body. We therefore write the *external power* as

$$\mathcal{W}_{\mathrm{ext}}(\mathrm{P}) = \int_{\partial \mathrm{P}} \mathbf{s}(\mathbf{n}_{\mathrm{R}}) \cdot \dot{\boldsymbol{\chi}}\, dA_{\mathrm{R}} + \int_{P} \mathbf{b}_{\mathrm{R}} \cdot \dot{\boldsymbol{\chi}}\, dV_{\mathrm{R}}, \tag{2.30}$$

with $\mathbf{s}(\mathbf{n}_{\mathrm{R}})$ (for each unit vector $\mathbf{n}_{\mathrm{R}}$) and $\mathbf{b}_{\mathrm{R}}$ defined over the body for all time.

We assume that power is expended internally by *elastic stresses* $\mathbf{T}^{e\,(\alpha)}$ power-conjugate to $\dot{\mathbf{F}}^{e\,(\alpha)}$, *plastic stresses* $\mathbf{T}^{p\,(\alpha)}$ power-conjugate to $\mathbf{D}^{p\,(\alpha)}$, and we write the *internal power*

as

$$\mathcal{W}_{\text{int}}(\mathrm{P}) = \int_{\mathrm{P}} \sum_{\alpha=1}^{M} \left(\mathbf{T}^{e\,(\alpha)} : \dot{\mathbf{F}}^{e\,(\alpha)} + \mathbf{T}^{p\,(\alpha)} : \mathbf{D}^{p\,(\alpha)} \right) dV_{\mathrm{R}} \,. \tag{2.31}$$

Here $\mathbf{T}^{e\,(\alpha)}$ and $\mathbf{T}^{p\,(\alpha)}$ are defined over the body for all time. We assume that $\mathbf{T}^{p\,(\alpha)}$ are *symmetric deviatoric*, since $\mathbf{D}^{p\,(\alpha)}$ are symmetric deviatoric.

2.4.1 Principle of virtual power

Assume that, at some arbitrarily chosen but *fixed time*, the fields $\boldsymbol{\chi}$, $\mathbf{F}^{e\,(\alpha)}$ (and hence $\mathbf{F}$ and $\mathbf{F}^{p\,(\alpha)}$) are known, and consider the fields $\dot{\boldsymbol{\chi}}$, $\dot{\mathbf{F}}^{e\,(\alpha)}$, and $\mathbf{D}^{p\,(\alpha)}$ as virtual velocities to be specified independently in a manner consistent with (2.19); that is, denoting the virtual fields by $\tilde{\dot{\boldsymbol{\chi}}}$, , $\tilde{\dot{\mathbf{F}}}^{e(\alpha)}$, and $\tilde{\mathbf{D}}^{p(\alpha)}$ to differentiate them from fields associated with the actual evolution of the body. We require that

$$(\nabla \tilde{\dot{\boldsymbol{\chi}}})\mathbf{F}^{-1} = \tilde{\dot{\mathbf{F}}}^{e(\alpha)}\mathbf{F}^{e\,(\alpha)-1} + \mathbf{F}^{e\,(\alpha)}\tilde{\mathbf{D}}^{p(\alpha)}\mathbf{F}^{e\,(\alpha)-1} \quad \text{for each } \alpha \,. \tag{2.32}$$

More specifically, we define a *generalized virtual velocity* to be a list

$$\mathcal{V} = (\tilde{\dot{\boldsymbol{\chi}}}, \tilde{\dot{\mathbf{F}}}^{e(\alpha)}, \tilde{\mathbf{D}}^{p(\alpha)})$$

consistent with (2.32). We write

$$\left.\begin{aligned} \mathcal{W}_{\text{ext}}(\mathrm{P}, \mathcal{V}) &= \int_{\partial \mathrm{P}} \mathbf{s}(\mathbf{n}) \cdot \tilde{\dot{\boldsymbol{\chi}}} \, dA_{\mathrm{R}} + \int_{\mathrm{P}} \mathbf{b}_{\mathrm{R}} \cdot \tilde{\dot{\boldsymbol{\chi}}} \, dV_{\mathrm{R}}, \\ \mathcal{W}_{\text{int}}(\mathrm{P}, \mathcal{V}) &= \int_{\mathrm{P}} \sum_{\alpha=1}^{M} \left(\mathbf{T}^{e\,(\alpha)} : \tilde{\dot{\mathbf{F}}}^{e(\alpha)} + \mathbf{T}^{p\,(\alpha)} : \tilde{\mathbf{D}}^{p(\alpha)} \right) dV_{\mathrm{R}}, \end{aligned}\right\} \tag{2.33}$$

respectively, for the external and internal expenditures of *virtual power*, the *principle of virtual power* consists of two basic requirements:

(i) (Power Balance) Given any part P,

$$\mathcal{W}_{\text{ext}}(\mathrm{P}, \mathcal{V}) = \mathcal{W}_{\text{int}}(\mathrm{P}, \mathcal{V}) \quad \textit{for all generalized virtual velocities } \mathcal{V}. \tag{2.34}$$

(ii) (Frame-Indifference) Given any part P and any generalized virtual velocity ,$\mathcal{V}$,

$$\mathcal{W}_{\text{int}}(\mathrm{P}, \mathcal{V}) \quad \textit{is invariant under all changes in frame.} \tag{2.35}$$

Consequences of frame-indifference

It is required that the internal power be invariant under a change in frame. Thus, consider the internal power $\mathcal{W}_{\text{int}}(\mathrm{P})$ under an arbitrary change in frame, and we require that

$$\mathcal{W}^*_{\text{int}}(\mathrm{P}, \mathcal{V}^*) = \mathcal{W}_{\text{int}}(\mathrm{P}, \mathcal{V}), \tag{2.36}$$

where $\mathcal{V}^*$ is the generalized virtual velocity in the new frame. In the new frame the stresses $\mathbf{T}^{e\,(\alpha)}$, and $\mathbf{T}^{p\,(\alpha)}$ transform to $\mathbf{T}^{e\,(\alpha)*}$, and $\mathbf{T}^{p\,(\alpha)*}$, while $\nabla\tilde{\boldsymbol{\chi}}$ and $\tilde{\dot{\mathbf{F}}}^{e(\alpha)}$ transform according to

$$(\nabla\tilde{\dot{\boldsymbol{\chi}}})^* = \mathbf{Q}\nabla\tilde{\dot{\boldsymbol{\chi}}} + \dot{\mathbf{Q}}\nabla\boldsymbol{\chi}, \quad (\tilde{\dot{\mathbf{F}}}^{e(\alpha)})^* = \mathbf{Q}\tilde{\dot{\mathbf{F}}}^{e(\alpha)} + \dot{\mathbf{Q}}\mathbf{F}^{e\,(\alpha)},$$

and $\tilde{\mathbf{D}}^{p(\alpha)}$ are invariant. Therefore, under a change in frame $\mathcal{W}_{\text{int}}(\mathrm{P}, \mathcal{V})$ transforms to

$$\begin{aligned}\mathcal{W}^*_{\text{int}}(\mathrm{P}, \mathcal{V}^*) &= \int_{\mathrm{P}} \sum_{\alpha=1}^{M} \left\{ \mathbf{T}^{e\,(\alpha)*} : \left(\mathbf{Q}\tilde{\dot{\mathbf{F}}}^{e(\alpha)} + \dot{\mathbf{Q}}\mathbf{F}^{e\,(\alpha)} \right) + \mathbf{T}^{p\,(\alpha)*} : \tilde{\mathbf{D}}^{p(\alpha)} \right\} dV_{\mathrm{R}}, \\ &= \int_{\mathrm{P}} \sum_{\alpha=1}^{M} \left\{ \mathbf{Q}^{\top}\mathbf{T}^{e\,(\alpha)*} : (\tilde{\dot{\mathbf{F}}}^{e(\alpha)} + \mathbf{Q}^{\top}\dot{\mathbf{Q}}\mathbf{F}^{e\,(\alpha)}) + \mathbf{T}^{p\,(\alpha)*} : \tilde{\mathbf{D}}^{p(\alpha)} \right\} dV_{\mathrm{R}}.\end{aligned}$$

Then (2.36) implies that

$$\begin{aligned}\int_{\mathrm{P}} \sum_{\alpha=1}^{M} &\left\{ \mathbf{Q}^{\top}\mathbf{T}^{e\,(\alpha)*} : (\tilde{\dot{\mathbf{F}}}^{e(\alpha)} + \mathbf{Q}^{\top}\dot{\mathbf{Q}}\mathbf{F}^{e\,(\alpha)}) + \mathbf{T}^{p\,(\alpha)*} : \tilde{\mathbf{D}}^{p(\alpha)} \right\} dV_{\mathrm{R}} \\ &= \int_{\mathrm{P}} \sum_{\alpha=1}^{M} \left(\mathbf{T}^{e\,(\alpha)} : \tilde{\dot{\mathbf{F}}}^{e(\alpha)} + \mathbf{T}^{p\,(\alpha)} : \tilde{\mathbf{D}}^{p(\alpha)} \right) dV_{\mathrm{R}}, \end{aligned} \tag{2.37}$$

and since the part P is arbitrary,

$$\mathbf{Q}^{\top}\mathbf{T}^{e\,(\alpha)*} : (\tilde{\dot{\mathbf{F}}}^{e(\alpha)} + \mathbf{Q}^{\top}\dot{\mathbf{Q}}\mathbf{F}^{e\,(\alpha)}) + \mathbf{T}^{p\,(\alpha)*} : \tilde{\mathbf{D}}^{p(\alpha)} = \mathbf{T}^{e\,(\alpha)} : \tilde{\dot{\mathbf{F}}}^{e(\alpha)} + \mathbf{T}^{p\,(\alpha)} : \tilde{\mathbf{D}}^{p(\alpha)}, \tag{2.38}$$

for each α. The change in frame is arbitrary; if we choose it such that $\mathbf{Q}$ is an arbitrary *time-independent* rotation, so that $\dot{\mathbf{Q}} = \mathbf{0}$, we find that

$$(\mathbf{Q}^{\top}\mathbf{T}^{e\,(\alpha)*} - \mathbf{T}^{e\,(\alpha)}) : \tilde{\dot{\mathbf{F}}}^{e(\alpha)} + (\mathbf{T}^{p\,(\alpha)*} - \mathbf{T}^{p\,(\alpha)}) : \tilde{\mathbf{D}}^{p(\alpha)} = 0.$$

Since this must hold for all $\tilde{\dot{\mathbf{F}}}^{e(\alpha)}$, and $\tilde{\mathbf{D}}^{p(\alpha)}$ we find that the stresses $\mathbf{T}^{e\,(\alpha)}$ transform according to

$$\mathbf{T}^{e\,(\alpha)*} = \mathbf{Q}\mathbf{T}^{e\,(\alpha)}, \tag{2.39}$$

while $\mathbf{T}^{p\,(\alpha)}$ are invariant

$$\mathbf{T}^{p\,(\alpha)*} = \mathbf{T}^{p\,(\alpha)}. \tag{2.40}$$

Next, if we assume that $\mathbf{Q} = \mathbf{1}$ at the time in question, so that $\dot{\mathbf{Q}}$ is an arbitrary skew tensor, using (2.39) and (2.40), we find that

$$\mathbf{T}^{e\,(\alpha)}\mathbf{F}^{e\,(\alpha)\top} : \dot{\mathbf{Q}} = 0, \tag{2.41}$$

or that the tensors $\mathbf{T}^{e\,(\alpha)}\mathbf{F}^{e\,(\alpha)\top}$ are *symmetric*,

$$\mathbf{T}^{e\,(\alpha)}\mathbf{F}^{e\,(\alpha)\top} = \mathbf{F}^{e\,(\alpha)}\mathbf{T}^{e\,(\alpha)\top}. \tag{2.42}$$

Macroscopic force balance

In applying the virtual balance (2.34) we are at liberty to chose any $\mathcal{V}$ consistent with the constraint (2.32). First consider a generalized virtual velocity which is strictly elastic in the sense that

$$\tilde{\mathbf{D}}^{p(\alpha)} \equiv \mathbf{0}, \quad \text{so that by (2.32)} \quad \dot{\tilde{\mathbf{F}}}^{e(\alpha)} = (\nabla\tilde{\boldsymbol{\chi}})\mathbf{F}^{p\,(\alpha)-1}. \tag{2.43}$$

For this choice of $\mathcal{V}$, (2.34) yields

$$\int_{\partial \mathrm{P}} \mathbf{s}(\mathbf{n}_{\mathrm{R}}) \cdot \tilde{\boldsymbol{\chi}}\, dA_{\mathrm{R}} + \int_{\mathrm{P}} \mathbf{b}_{\mathrm{R}} \cdot \tilde{\boldsymbol{\chi}}\, dV_{\mathrm{R}} = \int_{\mathrm{P}} \Big(\sum_{\alpha=1}^{M} \mathbf{T}^{e\,(\alpha)}\mathbf{F}^{p\,(\alpha)-\top}\Big) : \nabla\tilde{\boldsymbol{\chi}}\, dV_{\mathrm{R}} = \int_{\mathrm{P}} \mathbf{T}_{\mathrm{R}} : \nabla\tilde{\boldsymbol{\chi}}\, dV_{\mathrm{R}}\,,$$

where we have written

$$\mathbf{T}_{\mathrm{R}} \stackrel{\text{def}}{=} \sum_{\alpha=1}^{M} \mathbf{T}^{e\,(\alpha)}\mathbf{F}^{p\,(\alpha)-\top}\,, \tag{2.44}$$

and note that on account of (2.42),

$$\mathbf{T}_{\mathrm{R}}\mathbf{F}^{\top} = \mathbf{F}\mathbf{T}_{\mathrm{R}}^{\top}. \tag{2.45}$$

Then, using the divergence theorem,

$$\int_{\partial \mathrm{P}} \big(\mathbf{s}(\mathbf{n}_{\mathrm{R}}) - \mathbf{T}_{\mathrm{R}}\mathbf{n}_{\mathrm{R}}\big) \cdot \tilde{\boldsymbol{\chi}}\, dA_{\mathrm{R}} + \int_{\mathrm{P}} (\mathrm{Div}\,\mathbf{T}_{\mathrm{R}} + \mathbf{b}_{\mathrm{R}})\tilde{\boldsymbol{\chi}}\, dV_{\mathrm{R}} = 0.$$

Since this relation must hold for all P and all $\tilde{\boldsymbol{\chi}}$, standard variational arguments yield the traction condition

$$\mathbf{s}(\mathbf{n}_{\mathrm{R}}) = \mathbf{T}_{\mathrm{R}}\mathbf{n}_{\mathrm{R}}, \tag{2.46}$$

and the local force balance

$$\mathrm{Div}\,\mathbf{T}_{\mathrm{R}} + \mathbf{b}_{\mathrm{R}} = \mathbf{0}. \tag{2.47}$$

Recall that it was assumed that $\mathbf{b}_{\mathrm{R}}$ includes inertial body forces. Thus, recalling (2.29), the local force balance (2.47) becomes

$$\mathrm{Div}\,\mathbf{T}_{\mathrm{R}} + \mathbf{b}_{0\mathrm{R}} = \rho_{\mathrm{R}}\ddot{\boldsymbol{\chi}}, \tag{2.48}$$

with $\mathbf{b}_{0\mathrm{R}}$ the noninertial body force. Therefore, the stress $\mathbf{T}_{\mathrm{R}}$ plays the role of the macroscopic *Piola stress*, and (2.48) and (2.45) represent the classical *macroscopic force and moment balances* in the reference body.

Further, as is standard, the Piola stress is related to the symmetric Cauchy stress $\mathbf{T}$ in the deformed body by

$$\mathbf{T}_{\mathrm{R}} = J\mathbf{T}\mathbf{F}^{-\top}, \tag{2.49}$$

thus

$$\mathbf{T} = J^{-1}\mathbf{T}_{\mathrm{R}}\mathbf{F}^{\top}. \tag{2.50}$$

Then, using $\mathbf{F}^{e\,(\alpha)\top} = \mathbf{F}^{p\,(\alpha)-\top}\mathbf{F}^{\top}$ in (2.44) yields that the Cauchy stress admits the additive decomposition

$$\mathbf{T} = \sum_{\alpha=1}^{M} \mathbf{T}^{(\alpha)}, \tag{2.51}$$

where each contribution

$$\mathbf{T}^{(\alpha)} = J^{-1}\mathbf{T}^{e\,(\alpha)}\mathbf{F}^{e\,(\alpha)\top}, \tag{2.52}$$

to the total stress $\mathbf{T}$ on account of (2.42) is symmetric.

Microscopic force balances

Next, we choose a generalized virtual velocity field $\mathcal{V}$ for which

$$\tilde{\boldsymbol{\chi}} \equiv \mathbf{0}, \quad \text{so that by (2.32)} \quad \tilde{\dot{\mathbf{F}}}^{e(\alpha)} = -\mathbf{F}^{e\,(\alpha)}\tilde{\mathbf{D}}^{p(\alpha)}. \tag{2.53}$$

Then, the external power vanishes identically, so that, by (2.34), the internal power must also vanish, and satisfy

$$\mathcal{W}_{\mathrm{int}}(\mathrm{P},\mathcal{V}) = \int_{\mathrm{P}} \sum_{\alpha=1}^{M} \left(\mathbf{T}^{p\,(\alpha)} - \mathbf{F}^{e\,(\alpha)\top}\mathbf{T}^{e\,(\alpha)}\right) : \tilde{\mathbf{D}}^{p(\alpha)}\, dV_{\mathrm{R}} = 0.$$

Since this must be satisfied for all P and all deviatoric tensors $\mathbf{T}^{p\,(\alpha)}$, a standard argument yields the *microforce balance*

$$\mathbf{M}_0^{e\,(\alpha)} = \mathbf{T}^{p\,(\alpha)}, \tag{2.54}$$

where

$$\mathbf{M}^{e\,(\alpha)} \stackrel{\mathrm{def}}{=} \mathbf{F}^{e\,(\alpha)\top}\mathbf{T}^{e\,(\alpha)} \tag{2.55}$$

defines a *Mandel stress* for each α. *The microscopic force balances* (2.54) *characterize the interaction between internal forces associated with the elastic and plastic response of the material for each micromechanism* α.

2.5 Balance of energy. Entropy imbalance. Local dissipation inequality

Let

- $\vartheta > 0$ denote the absolute temperature,
- ε_{R} and η_{R} represent the *internal energy* and *entropy* densities, measured per unit volume in the reference body,
- $\mathbf{q}_{\mathrm{R}}$ denote the *heat flux*, measured per unit area in the reference body, and
- q_{R} denote the scalar heat supply, measured per unit volume in the reference body.

Then, *balance of energy* is the requirement that

$$\dot{\overline{\int_{\mathrm{P}} \varepsilon_{\mathrm{R}}\, dV_{\mathrm{R}}}} = -\int_{\partial \mathrm{P}} \mathbf{q}_{\mathrm{R}} \cdot \mathbf{n}_{\mathrm{R}}\, dA_{\mathrm{R}} + \int_{\mathrm{P}} q_{\mathrm{R}}\, dV_{\mathrm{R}} + \mathcal{W}_{\mathrm{ext}}(\mathrm{P}), \tag{2.56}$$

while the *second law* takes the form of an *entropy imbalance*

$$\dot{\overline{\int_{\mathrm{P}} \eta_{\mathrm{R}}\, dV_{\mathrm{R}}}} \geq -\int_{\partial \mathrm{P}} \frac{\mathbf{q}_{\mathrm{R}} \cdot \mathbf{n}_{\mathrm{R}}}{\vartheta}\, dA_{\mathrm{R}} + \int_{\mathrm{P}} \frac{q_{\mathrm{R}}}{\vartheta}\, dV_{\mathrm{R}}. \tag{2.57}$$

Thus, since $\mathcal{W}_{\mathrm{ext}}(\mathrm{P}) = \mathcal{W}_{\mathrm{int}}(\mathrm{P})$ and since P is arbitrary, we may use (2.31) to obtain local forms of (2.56) and (2.57):

$$\left.\begin{aligned} \dot{\varepsilon}_{\mathrm{R}} &= -\mathrm{Div}\, \mathbf{q}_{\mathrm{R}} + q_{\mathrm{R}} + \sum_{\alpha=1}^{M} \mathbf{T}^{e\,(\alpha)} : \dot{\mathbf{F}}^{e\,(\alpha)} + \sum_{\alpha=1}^{M} \mathbf{T}^{p\,(\alpha)} : \mathbf{D}^{p\,(\alpha)}, \\ \dot{\eta}_{\mathrm{R}} &\geq -\frac{1}{\vartheta}\mathrm{Div}\, \mathbf{q}_{\mathrm{R}} + \frac{1}{\vartheta^2}\mathbf{q}_{\mathrm{R}} \cdot \nabla\vartheta + \frac{q_{\mathrm{R}}}{\vartheta}\,. \end{aligned}\right\} \tag{2.58}$$

Let

$$\psi_{\mathrm{R}} \stackrel{\mathrm{def}}{=} \varepsilon_{\mathrm{R}} - \vartheta\eta_{\mathrm{R}} \tag{2.59}$$

denote the *specific (Helmholtz) free energy*. Then (2.58) yields the *local dissipation inequality*

$$\dot{\psi}_{\mathrm{R}} + \eta_{\mathrm{R}}\dot{\vartheta} + \frac{1}{\vartheta}\,\mathbf{q}_{\mathrm{R}} \cdot \nabla\vartheta - \sum_{\alpha=1}^{M} \mathbf{T}^{e\,(\alpha)} : \dot{\mathbf{F}}^{e\,(\alpha)} - \sum_{\alpha=1}^{M} \mathbf{T}^{p\,(\alpha)} : \mathbf{D}^{p\,(\alpha)} \leq 0\,. \tag{2.60}$$

Note that from (2.52),

$$\mathbf{T}^{e\,(\alpha)} = J\mathbf{T}^{(\alpha)}\mathbf{F}^{e\,(\alpha)-\mathrm{T}}, \tag{2.61}$$

and each $\mathbf{T}^{e\,(\alpha)}$ represents a non-symmetric first Piola stress with respect to its local structural space.

Let

$$\mathbf{S}^{e\,(\alpha)} = \mathbf{F}^{e\,(\alpha)-1}\mathbf{T}^{e\,(\alpha)} = J\mathbf{F}^{e\,(\alpha)-1}\mathbf{T}^{(\alpha)}\mathbf{F}^{e\,(\alpha)-\top}, \tag{2.62}$$

represent a second Piola stress with respect to the α-th structural space; these stress measures are symmetric since $\mathbf{T}^{(\alpha)}$ are symmetric. The Mandel stresses defined in (2.55) are then related to $\mathbf{S}^{e\,(\alpha)}$ by

$$\mathbf{M}^{e\,(\alpha)} = \mathbf{C}^{e\,(\alpha)}\mathbf{S}^{e\,(\alpha)}. \tag{2.63}$$

Next differentiating $(2.12)_1$ results in the following expression for the rate of change of $\mathbf{C}^{e\,(\alpha)}$

$$\dot{\mathbf{C}}^{e\,(\alpha)} = \mathbf{F}^{e\,(\alpha)\top}\dot{\mathbf{F}}^{e\,(\alpha)} + \dot{\mathbf{F}}^{e\,(\alpha)\top}\mathbf{F}^{e\,(\alpha)}, \tag{2.64}$$

hence since $\mathbf{S}^{e\,(\alpha)}$ are symmetric

$$\mathbf{S}^{e\,(\alpha)} : \dot{\mathbf{C}}^{e\,(\alpha)} = 2\mathbf{S}^{e\,(\alpha)} : \mathbf{F}^{e\,(\alpha)\top}\dot{\mathbf{F}}^{e\,(\alpha)} = 2(\mathbf{F}^{e\,(\alpha)}\mathbf{S}^{e\,(\alpha)}) : \dot{\mathbf{F}}^{e\,(\alpha)}, \tag{2.65}$$

or using (2.62), we obtain

$$\mathbf{T}^{e\,(\alpha)} : \dot{\mathbf{F}}^{e\,(\alpha)} = \frac{1}{2}\mathbf{S}^{e\,(\alpha)} : \dot{\mathbf{C}}^{e\,(\alpha)}. \tag{2.66}$$

Then from (2.31) and (2.66), we note that the internal power per unit reference volume is

$$\frac{1}{2}\mathbf{S}^{e\,(\alpha)} : \dot{\mathbf{C}}^{e\,(\alpha)} + \mathbf{T}^{p\,(\alpha)} : \mathbf{D}^{p\,(\alpha)}. \tag{2.67}$$

Thus the energy balance $(2.58)_1$ becomes

$$\dot{\varepsilon}_{\mathrm{R}} = -\mathrm{Div}\,\mathbf{q}_{\mathrm{R}} + q_{\mathrm{R}} + \frac{1}{2}\sum_{\alpha=1}^{M} \mathbf{S}^{e\,(\alpha)} : \dot{\mathbf{C}}^{e\,(\alpha)} + \sum_{\alpha=1}^{M} \mathbf{T}^{p\,(\alpha)} : \mathbf{D}^{p\,(\alpha)}, \tag{2.68}$$

while the free-energy imbalance (2.60) becomes

$$\dot{\psi}_{\mathrm{R}} + \eta_{\mathrm{R}}\dot{\vartheta} + \frac{1}{\vartheta}\,\mathbf{q}_{\mathrm{R}} \cdot \nabla\vartheta - \frac{1}{2}\sum_{\alpha=1}^{M} \mathbf{S}^{e\,(\alpha)} : \dot{\mathbf{C}}^{e\,(\alpha)} - \sum_{\alpha=1}^{M} \mathbf{T}^{p\,(\alpha)} : \mathbf{D}^{p\,(\alpha)} \leq 0\,. \tag{2.69}$$

Finally, we note that ψ_{R}, η_{R}, and ϑ are invariant under a change in frame since they are scalar fields, and on account of the transformation rules discussed in Section 2.3, the transformation rules (2.39), (2.40), and the definitions (2.55) and (2.62), the fields

$$\mathbf{B}^{p\,(\alpha)}, \quad \mathbf{C}^{e\,(\alpha)}, \quad \mathbf{D}^{p\,(\alpha)}, \quad \mathbf{S}^{e\,(\alpha)}, \quad \mathbf{M}^{e\,(\alpha)}, \quad \mathbf{T}^{p\,(\alpha)} \tag{2.70}$$

are also invariant, as are the fields,

$$\mathbf{q}_{\mathrm{R}}, \quad \nabla\vartheta \tag{2.71}$$

since they are referential vector fields.

2.6 Constitutive theory

To account for the major strain-hardening characteristics of materials observed during plastic deformation, we introduce **internal state variables** which represent important aspects of the microstructural resistance to plastic flow. Specifically we introduce

- A list of m scalar *internal state-variables*

$$\boldsymbol{\xi}^{(\alpha)} = (\xi_1^{(\alpha)}, \xi_2^{(\alpha)}, \ldots, \xi_m^{(\alpha)})$$

  for each α. Since $\boldsymbol{\xi}^{(\alpha)}$ are scalar fields they are invariant under a change in frame.

- A list of *symmetric and unimodular* tensor fields

$$\mathbf{A}^{(\alpha)}(\mathbf{X}, t), \quad \mathbf{A}^{(\alpha)} = \mathbf{A}^{(\alpha)\top}, \quad \det \mathbf{A}^{(\alpha)} = 1.$$

  Each such tensor field represents a dimensionless *squared stretch-like* quantity, which as a linear transformation, maps vectors in the intermediate space for each α, into vectors in the same space. Thus, $\mathbf{A}^{(\alpha)}$ is a *structural tensor field*[4], and therefore invariant under a change in frame.

Guided by the dissipation inequality (2.69), and previous work by Anand and Gurtin (2003a) and Anand and Ames (2006), we assume the following *special* set of constitutive equations:

$$\left.\begin{aligned}
\psi_{\mathrm{R}} &= \sum_{\alpha=1}^{M} \bar{\psi}^{(\alpha)}(\mathbf{C}^{e\,(\alpha)}, \mathbf{A}^{(\alpha)}, \vartheta), \\
\eta_{\mathrm{R}} &= \sum_{\alpha=1}^{M} \bar{\eta}^{(\alpha)}(\mathbf{C}^{e\,(\alpha)}, \mathbf{A}^{(\alpha)}, \vartheta), \\
\mathbf{S}^{e\,(\alpha)} &= \bar{\mathbf{S}}^{e\,(\alpha)}(\mathbf{C}^{e\,(\alpha)}, \vartheta), \\
\mathbf{T}^{p\,(\alpha)} &= \bar{\mathbf{T}}^{p(\alpha)}(\mathbf{D}^{p\,(\alpha)}, \boldsymbol{\Lambda}^{(\alpha)}), \\
\dot{\xi}_i^{(\alpha)} &= \underbrace{h_i^{(\alpha)}(\mathbf{D}^{p\,(\alpha)}, \boldsymbol{\Lambda}^{(\alpha)})}_{\text{dynamic evolution}} - \underbrace{\mathcal{R}_i^{(\alpha)}(\boldsymbol{\Lambda}^{(\alpha)})}_{\text{static recovery}}, \\
\overset{\cdot}{\mathbf{A}^{(\alpha)}} &= \underbrace{\mathbf{D}^{p\,(\alpha)}\mathbf{A}^{(\alpha)} + \mathbf{A}^{(\alpha)}\mathbf{D}^{p\,(\alpha)} - \mathbf{G}^{(\alpha)}(\boldsymbol{\Lambda}^{(\alpha)})\, d^{p\,(\alpha)}}_{\text{dynamic evolution}} - \underbrace{\mathbf{G}^{(\alpha)}_{\text{static}}(\boldsymbol{\Lambda}^{(\alpha)})}_{\text{static recovery}},
\end{aligned}\right\} \tag{2.72}$$

where $\boldsymbol{\Lambda}^{(\alpha)}$ denotes the list

$$\boldsymbol{\Lambda}^{(\alpha)} = (\mathbf{C}^{e\,(\alpha)}, \mathbf{B}^{p\,(\alpha)}, \mathbf{A}^{(\alpha)}, \boldsymbol{\xi}^{(\alpha)}, \vartheta), \tag{2.73}$$

[4]That is, a tensor defined in the intermediate structural space for each α.

and

$$d^{p\,(\alpha)} \stackrel{\text{def}}{=} |\mathbf{D}^{p\,(\alpha)}| \tag{2.74}$$

denotes a *scalar flow rate* for each α. To the constitutive equations (2.72), we append a simple Fourier's relation for the heat flux,

$$\mathbf{q}_{\mathrm{R}} = -\mathbf{K}(\vartheta)\,\nabla\vartheta\,, \tag{2.75}$$

where $\mathbf{K}$ is a positive definite thermal conductivity tensor. Note that on account of the transformation rules listed in Section 2.3, along with the paragraph containing (2.70) and (2.71), and since $(\boldsymbol{\xi}^{(\alpha)}, \mathbf{A}^{(\alpha)})$ are also invariant, *the constitutive equations* (2.72) *and* (2.75) *are frame-indifferent.*

In the evolution equation (2.140) for the internal variables $\xi_i^{(\alpha)}$ and $\mathbf{A}^{(\alpha)}$, the terms $\mathcal{R}_i^{(\alpha)}(\boldsymbol{\Lambda}^{(\alpha)})$ and $\mathbf{G}^{(\alpha)}_{\text{static}}(\boldsymbol{\Lambda}^{(\alpha)})$ represent *static recovery* (or time recovery, or thermal recovery), since they do not depend on $\mathbf{D}^{p\,(\alpha)}$. Also, in $(2.140)_2$, the term $\mathbf{G}^{(\alpha)}(\boldsymbol{\Lambda}^{(\alpha)})\,\nu^{p\,(\alpha)}$ represents a *dynamic recovery* term. If both the dynamic and static recovery terms were to vanish, then we may associate each $\mathbf{A}^{(\alpha)}$ with the corresponding left Cauchy-Green tensor $\mathbf{B}^{p\,(\alpha)} = \mathbf{F}^{p\,(\alpha)}\mathbf{F}^{p\,(\alpha)\top}$, since then, for a constitutive theory with $\mathbf{W}^{p\,(\alpha)} = \mathbf{0}$,

$$\dot{\mathbf{B}}^{p(\alpha)} = \mathbf{D}^{p\,(\alpha)}\mathbf{B}^{p\,(\alpha)} + \mathbf{B}^{p\,(\alpha)}\mathbf{D}^{p\,(\alpha)}. \tag{2.76}$$

In the theory considered here, as in the classical small deformation theory of metal plasticity with non-linear kinematic-hardening (e.g., Chaboche, 2008), we allow for *recovery*, that is we allow for $\mathbf{G}^{(\alpha)}(\boldsymbol{\Lambda}^{(\alpha)})\,\nu^{p\,(\alpha)} \neq \mathbf{0}$ as well as $\mathbf{G}^{(\alpha)}_{\text{static}}(\boldsymbol{\Lambda}^{(\alpha)}) \neq \mathbf{0}$, and thus, in general, the internal variables $\mathbf{A}^{(\alpha)}$ are not the same as $\mathbf{B}^{p\,(\alpha)}$.

2.6.1 Thermodynamic restrictions

Since

$$\dot{\bar{\psi}}^{(\alpha)}_{\mathrm{R}}(\mathbf{C}^{e\,(\alpha)}, \mathbf{A}^{(\alpha)}, \vartheta) = \frac{\partial \bar{\psi}^{(\alpha)}_{\mathrm{R}}}{\partial \mathbf{C}^{e\,(\alpha)}} : \dot{\overline{\mathbf{C}^{e\,(\alpha)}}} \quad + \frac{\partial \bar{\psi}^{(\alpha)}_{\mathrm{R}}}{\partial \mathbf{A}^{(\alpha)}} : \dot{\overline{\mathbf{A}^{(\alpha)}}} + \frac{\partial \bar{\psi}^{(\alpha)}_{\mathrm{R}}}{\partial \vartheta}\,\dot{\vartheta},$$

and, using $(2.72)_6$,

$$\begin{aligned} \frac{\partial \bar{\psi}^{(\alpha)}_{\mathrm{R}}}{\partial \mathbf{A}^{(\alpha)}} : \dot{\overline{\mathbf{A}^{(\alpha)}}} &= \frac{\partial \bar{\psi}^{(\alpha)}_{\mathrm{R}}}{\partial \mathbf{A}^{(\alpha)}} : \left(\mathbf{D}^{p\,(\alpha)}\mathbf{A}^{(\alpha)} + \mathbf{A}^{(\alpha)}\mathbf{D}^{p\,(\alpha)} - \mathbf{G}^{(\alpha)} d^{p\,(\alpha)} - \mathbf{G}^{(\alpha)}_{\text{static}}\right), \\ &= \left(2\frac{\partial \bar{\psi}^{(\alpha)}_{\mathrm{R}}}{\partial \mathbf{A}^{(\alpha)}}\mathbf{A}^{(\alpha)}\right)_0 : \mathbf{D}^{p\,(\alpha)} - \left(\frac{\partial \bar{\psi}^{(\alpha)}_{\mathrm{R}}}{\partial \mathbf{A}^{(\alpha)}} : \mathbf{G}^{(\alpha)}\right) d^{p\,(\alpha)} - \frac{\partial \bar{\psi}^{(\alpha)}_{\mathrm{R}}}{\partial \mathbf{A}^{(\alpha)}} : \mathbf{G}^{(\alpha)}_{\text{static}}, \end{aligned} \tag{2.77}$$

the free-energy imbalance (2.69) requires that the constitutive equations (2.72) and (2.75) satisfy

$$\begin{aligned}
&\sum_{\alpha=1}^{M}\left[\frac{1}{2}\bar{\mathbf{S}}^{e\,(\alpha)}(\mathbf{C}^{e\,(\alpha)},\mathbf{A}^{(\alpha)},\vartheta)-\frac{\partial\bar{\psi}_{\mathrm{R}}^{(\alpha)}(\mathbf{C}^{e\,(\alpha)},\mathbf{A}^{(\alpha)},\vartheta)}{\partial\mathbf{C}^{e\,(\alpha)}}\right]:\dot{\mathbf{C}^{e\,(\alpha)}}\\
&-\sum_{\alpha=1}^{M}\left[\bar{\eta}_{\mathrm{R}}^{(\alpha)}(\mathbf{C}^{e\,(\alpha)},\mathbf{A}^{(\alpha)},\vartheta)+\frac{\partial\bar{\psi}_{\mathrm{R}}^{(\alpha)}(\mathbf{C}^{e\,(\alpha)},\mathbf{A}^{(\alpha)},\vartheta)}{\partial\vartheta}\right]\dot{\vartheta}\\
&+\sum_{\alpha=1}^{M}\left[\bar{\mathbf{T}}^{p(\alpha)}(\mathbf{D}^{p\,(\alpha)},\mathbf{\Lambda}^{(\alpha)})-\left(2\,\frac{\partial\bar{\psi}^{(\alpha)}(\mathbf{C}^{e\,(\alpha)},\mathbf{A}^{(\alpha)},\vartheta)}{\partial\mathbf{A}^{(\alpha)}}\mathbf{A}^{(\alpha)}\right)_{0}\right]:\mathbf{D}^{p\,(\alpha)}\\
&+\sum_{\alpha=1}^{M}\left(\frac{\partial\bar{\psi}^{(\alpha)}(\mathbf{C}^{e\,(\alpha)},\mathbf{A}^{(\alpha)},\vartheta)}{\partial\mathbf{A}^{(\alpha)}}:\mathbf{G}^{(\alpha)}(\mathbf{\Lambda}^{(\alpha)})\right)d^{p\,(\alpha)}+\sum_{\alpha=1}^{M}\frac{\partial\bar{\psi}^{(\alpha)}(\mathbf{C}^{e\,(\alpha)},\mathbf{A}^{(\alpha)},\vartheta)}{\partial\mathbf{A}^{(\alpha)}}:\mathbf{G}_{\mathrm{static}}^{(\alpha)}(\mathbf{\Lambda}^{(\alpha)})\\
&+\frac{1}{\vartheta}\nabla\vartheta\cdot\mathbf{K}(\vartheta)\nabla\vartheta\geq 0,
\end{aligned}\tag{2.78}$$

and hold for all arguments in the domains of the constitutive functions, and in all motions of the body. Thus, *sufficient* conditions that the constitutive equations satisfy the free-energy imbalance are

(i) *the free energy determines the stress and the entropy via the* **stress relations** and **entropy relations:**

$$\bar{\mathbf{S}}^{e\,(\alpha)}(\mathbf{C}^{e\,(\alpha)},\mathbf{A}^{(\alpha)},\vartheta)=2\,\frac{\partial\bar{\psi}_{\mathrm{R}}^{(\alpha)}(\mathbf{C}^{e\,(\alpha)},\mathbf{A}^{(\alpha)},\vartheta)}{\partial\mathbf{C}^{e\,(\alpha)}},\tag{2.79}$$

$$\bar{\eta}_{\mathrm{R}}^{(\alpha)}(\mathbf{C}^{e\,(\alpha)},\mathbf{A}^{(\alpha)},\vartheta)=-\frac{\partial\bar{\psi}_{\mathrm{R}}^{(\alpha)}(\mathbf{C}^{e\,(\alpha)},\mathbf{A}^{(\alpha)},\vartheta)}{\partial\vartheta}.\tag{2.80}$$

(ii) *the plastic distortion-rates* $\mathbf{D}^{p\,(\alpha)}$ *and the temperature gradient* $\nabla\vartheta$ *satisfy the* **reduced dissipation inequality**

$$\begin{aligned}
&\sum_{\alpha=1}^{M}\left[\bar{\mathbf{T}}^{p(\alpha)}(\mathbf{D}^{p\,(\alpha)},\mathbf{\Lambda}^{(\alpha)})-\left(2\,\frac{\partial\bar{\psi}^{(\alpha)}(\mathbf{C}^{e\,(\alpha)},\mathbf{A}^{(\alpha)},\vartheta)}{\partial\mathbf{A}^{(\alpha)}}\mathbf{A}^{(\alpha)}\right)_{0}\right]:\mathbf{D}^{p\,(\alpha)}\\
&+\sum_{\alpha=1}^{M}\left(\frac{\partial\bar{\psi}^{(\alpha)}(\mathbf{C}^{e\,(\alpha)},\mathbf{A}^{(\alpha)},\vartheta)}{\partial\mathbf{A}^{(\alpha)}}:\mathbf{G}^{(\alpha)}(\mathbf{\Lambda}^{(\alpha)})\right)d^{p\,(\alpha)}+\sum_{\alpha=1}^{M}\frac{\partial\bar{\psi}^{(\alpha)}(\mathbf{C}^{e\,(\alpha)},\mathbf{A}^{(\alpha)},\vartheta)}{\partial\mathbf{A}^{(\alpha)}}:\mathbf{G}_{\mathrm{static}}^{(\alpha)}(\mathbf{\Lambda}^{(\alpha)})\\
&+\frac{1}{\vartheta}\nabla\vartheta\cdot\mathbf{K}(\vartheta)\nabla\vartheta\geq 0.
\end{aligned}\tag{2.81}$$

We assume henceforth that (2.79) and (2.80) hold in all motions of the body, and that the material is **strictly dissipative** in the sense that it satisfies

(i) the **mechanical dissipation inequality**

$$\mathbf{Y}^{p\,(\alpha)}(\mathbf{D}^{p\,(\alpha)}, \boldsymbol{\Lambda}^{(\alpha)}) : \mathbf{D}^{p\,(\alpha)} + \Big(\frac{\partial \bar{\psi}^{(\alpha)}(\mathbf{C}^{e\,(\alpha)}, \mathbf{A}^{(\alpha)}, \vartheta)}{\partial \mathbf{A}^{(\alpha)}} : \mathbf{G}^{(\alpha)}(\boldsymbol{\Lambda}^{(\alpha)}) \Big) d^{p\,(\alpha)} > 0 \qquad (2.82)$$

whenever $\mathbf{D}^{p\,(\alpha)} \neq \mathbf{0}$ for each α, where we have introduced *symmetric deviatoric flow stresses* $\mathbf{Y}^{p\,(\alpha)}$ defined by

$$\mathbf{Y}^{p\,(\alpha)}(\mathbf{D}^{p\,(\alpha)}, \boldsymbol{\Lambda}^{(\alpha)}) \stackrel{\text{def}}{=} \bar{\mathbf{T}}^{p(\alpha)}(\mathbf{D}^{p\,(\alpha)}, \boldsymbol{\Lambda}^{(\alpha)}) - 2 \left(\frac{\partial \bar{\psi}^{(\alpha)}(\mathbf{C}^{e\,(\alpha)}, \mathbf{A}^{(\alpha)}, \vartheta)}{\partial \mathbf{A}^{(\alpha)}} \mathbf{A}^{(\alpha)} \right)_0 ; \qquad (2.83)$$

(ii) the **static recovery dissipation inequality**

$$\sum_{\alpha=1}^{M} \frac{\partial \bar{\psi}^{(\alpha)}(\mathbf{C}^{e\,(\alpha)}, \mathbf{A}^{(\alpha)}, \vartheta)}{\partial \mathbf{A}^{(\alpha)}} : \mathbf{G}^{(\alpha)}_{\text{static}}(\boldsymbol{\Lambda}^{(\alpha)}) > 0, \qquad (2.84)$$

as long as $\mathbf{G}^{(\alpha)}_{\text{static}}(\boldsymbol{\Lambda}^{(\alpha)}) \neq 0$;

(ii) and that the material seriately satisfies the **heat conduction inequality**

$$\frac{1}{\vartheta} \nabla\vartheta \cdot \mathbf{K}(\vartheta) \nabla\vartheta > 0 \quad \text{whenever} \quad \nabla\vartheta \neq \mathbf{0}. \qquad (2.85)$$

The last inequality implies that the thermal conductivity tensor is positive definite.

From (2.82) we note that the stresses $\mathbf{T}^{p\,(\alpha)}$, which are conjugate to $\mathbf{D}^{p\,(\alpha)}$, may be split into a dissipative part and an energetic part as follows:

$$\mathbf{T}^{p\,(\alpha)} = \bar{\mathbf{T}}^{p(\alpha)}(\mathbf{D}^{p\,(\alpha)}, \boldsymbol{\Lambda}^{(\alpha)}) = \underbrace{\mathbf{Y}^{p\,(\alpha)}(\mathbf{D}^{p\,(\alpha)}, \boldsymbol{\Lambda}^{(\alpha)})}_{\text{dissipative}} + \underbrace{2 \left(\frac{\partial \bar{\psi}^{(\alpha)}(\mathbf{C}^{e\,(\alpha)}, \mathbf{A}^{(\alpha)}, \vartheta)}{\partial \mathbf{A}^{(\alpha)}} \mathbf{A}^{(\alpha)} \right)_0}_{\text{energetic}} . \qquad (2.86)$$

Further consequences of thermodynamics

In view of (2.72), (2.79) and (2.80), we have the *first Gibbs relation*,

$$\begin{aligned} \dot{\psi}_{\text{R}} = \frac{1}{2} \sum_{\alpha=1}^{M} \mathbf{S}^{e\,(\alpha)} : \overset{\cdot}{\overline{\mathbf{C}^{e\,(\alpha)}}} - \eta_{\text{R}} \dot{\vartheta} + 2 \sum_{\alpha=1}^{M} \left(\frac{\partial \bar{\psi}^{(\alpha)}}{\partial \mathbf{A}^{(\alpha)}} \mathbf{A}^{(\alpha)} \right)_0 : \mathbf{D}^{p\,(\alpha)} \\ - \sum_{\alpha=1}^{M} \Big(\frac{\partial \bar{\psi}^{(\alpha)}}{\partial \mathbf{A}^{(\alpha)}} : \mathbf{G}^{(\alpha)}(\boldsymbol{\Lambda}^{(\alpha)}) \Big) d^{p\,(\alpha)} - \sum_{\alpha=1}^{M} \frac{\partial \bar{\psi}^{(\alpha)}}{\partial \mathbf{A}^{(\alpha)}} : \mathbf{G}^{(\alpha)}_{\text{static}}, \end{aligned} \qquad (2.87)$$

which, with (2.59), yields the *second Gibbs relation*

$$\dot{\varepsilon}_{\mathrm{R}} = \vartheta\dot{\eta}_{\mathrm{R}} + \frac{1}{2}\sum_{\alpha=1}^{M} \mathbf{S}^{e\,(\alpha)} : \overset{\cdot}{\overline{\mathbf{C}^{e\,(\alpha)}}} + 2\sum_{\alpha=1}^{M} \Big(\frac{\partial\bar{\psi}^{(\alpha)}}{\partial\mathbf{A}^{(\alpha)}}\mathbf{A}^{(\alpha)}\Big)_0 : \mathbf{D}^{p\,(\alpha)}$$
$$- \sum_{\alpha=1}^{M} \Big(\frac{\partial\bar{\psi}^{(\alpha)}}{\partial\mathbf{A}^{(\alpha)}} : \mathbf{G}^{(\alpha)}(\boldsymbol{\Lambda}^{(\alpha)})\Big)\, d^{p\,(\alpha)} - \sum_{\alpha=1}^{M} \frac{\partial\bar{\psi}^{(\alpha)}}{\partial\mathbf{A}^{(\alpha)}} : \mathbf{G}^{(\alpha)}_{\mathrm{static}}, \tag{2.88}$$

where ε_{R} is the internal energy density per unit reference volume.

Using the second Gibbs relation, the balance of energy (2.68) may be written as an *entropy balance*

$$\vartheta\dot{\eta}_{\mathrm{R}} = -\mathrm{Div}\,\mathbf{q}_{\mathrm{R}} + q_{\mathrm{R}} + \sum_{\alpha=1}^{M} \big(\mathbf{Y}^{p\,(\alpha)} : \mathbf{D}^{p\,(\alpha)}\big) + \sum_{\alpha=1}^{M} \Big(\frac{\partial\bar{\psi}^{(\alpha)}}{\partial\mathbf{A}^{(\alpha)}} : \mathbf{G}^{(\alpha)}(\boldsymbol{\Lambda}^{(\alpha)})\Big) d^{p\,(\alpha)} + \sum_{\alpha=1}^{M} \frac{\partial\bar{\psi}^{(\alpha)}}{\partial\mathbf{A}^{(\alpha)}} : \mathbf{G}^{(\alpha)}_{\mathrm{static}}\,. \tag{2.89}$$

Granted the thermodynamically restricted constitutive relations (2.79) and (2.80), this entropy relation is equivalent to balance of energy.

Next, the internal energy density for each α is given by

$$\bar{\varepsilon}^{(\alpha)}(\mathbf{C}^{e\,(\alpha)}, \mathbf{A}^{(\alpha)}, \vartheta) \overset{\mathrm{def}}{=} \bar{\psi}^{(\alpha)}(\mathbf{C}^{e\,(\alpha)}, \mathbf{A}^{(\alpha)}, \vartheta) + \vartheta\,\bar{\eta}^{(\alpha)}(\mathbf{C}^{e\,(\alpha)}, \mathbf{A}^{(\alpha)}, \vartheta), \tag{2.90}$$

so that the total internal energy is

$$\varepsilon_{\mathrm{R}} = \sum_{\alpha=1}^{M} \bar{\varepsilon}^{(\alpha)}(\mathbf{C}^{e\,(\alpha)}, \mathbf{A}^{(\alpha)}, \vartheta)\,. \tag{2.91}$$

Then, the *specific heat* is defined by

$$c \overset{\mathrm{def}}{=} \sum_{\alpha=1}^{M} \frac{\partial\bar{\varepsilon}^{(\alpha)}(\mathbf{C}^{e\,(\alpha)}, \mathbf{A}^{(\alpha)}, \vartheta)}{\partial\vartheta}\,. \tag{2.92}$$

Hence, from (2.90)

$$c \overset{\mathrm{def}}{=} \sum_{\alpha=1}^{M} \Big[\frac{\partial\bar{\psi}^{(\alpha)}}{\partial\vartheta} + \bar{\eta}^{(\alpha)} + \vartheta\,\frac{\partial\bar{\eta}^{(\alpha)}}{\partial\vartheta}\Big]\,, \tag{2.93}$$

and use of (2.80) gives

$$c \overset{\mathrm{def}}{=} -\vartheta \sum_{\alpha=1}^{M} \frac{\partial^2\bar{\psi}^{(\alpha)}}{\partial\vartheta^2}\,. \tag{2.94}$$

Next, from (2.80),

$$\dot{\eta}_r = -\sum_{\alpha=1}^{M} \frac{\partial^2 \bar{\psi}^{(\alpha)}}{\partial\vartheta\,\partial \mathbf{C}^{e\,(\alpha)}} : \dot{\mathbf{C}}^{e\,(\alpha)} - \sum_{\alpha=1}^{M} \frac{\partial^2 \bar{\psi}^{(\alpha)}}{\partial\vartheta\,\partial \mathbf{A}^{(\alpha)}} : \dot{\mathbf{A}}^{(\alpha)} - \sum_{\alpha=1}^{M} \frac{\partial^2 \bar{\psi}^{(\alpha)}}{\partial\vartheta^2}\,\dot{\vartheta}\,. \tag{2.95}$$

Then, using (2.94) and (2.95) in (2.89) gives the following partial differential equation for the temperature

$$\begin{aligned} c\dot{\vartheta} = &-\mathrm{Div}\,\mathbf{q}_{\mathrm{R}} + q_{\mathrm{R}} + \sum_{\alpha=1}^{M} \left(\mathbf{Y}^{p\,(\alpha)} : \mathbf{D}^{p\,(\alpha)}\right) + \sum_{\alpha=1}^{M} \left(\frac{\partial \bar{\psi}^{(\alpha)}}{\partial \mathbf{A}^{(\alpha)}} : \mathbf{G}^{(\alpha)}\right) d^{p\,(\alpha)} \\ &+ \sum_{\alpha=1}^{M} \frac{\partial \bar{\psi}^{(\alpha)}}{\partial \mathbf{A}^{(\alpha)}} : \mathbf{G}^{(\alpha)}_{\mathrm{static}} + \vartheta \sum_{\alpha=1}^{M} \frac{\partial^2 \bar{\psi}^{(\alpha)}}{\partial\vartheta\,\partial \mathbf{A}^{(\alpha)}} : \dot{\mathbf{A}}^{(\alpha)} + \vartheta \sum_{\alpha=1}^{M} \frac{\partial^2 \bar{\psi}^{(\alpha)}}{\partial\vartheta\,\partial \mathbf{C}^{e\,(\alpha)}} : \dot{\mathbf{C}}^{e\,(\alpha)}. \end{aligned} \tag{2.96}$$

2.6.2 Isotropy

The following definitions help to make precise our notion of an isotropic material:

(i) Orth^{+} = the group of all rotations (the proper orthogonal group);

(ii) the *symmetry group* $\mathcal{G}_{\mathrm{R}}$, is the group of all rotations of the *reference* configuration that leaves the response of the material unaltered;

(iii) the *symmetry group* $\mathcal{G}_{\mathrm{I}}^{(\alpha)}$ at each time t, is the group of all rotations of the *intermediate* structural space for each α that leaves the response of the material unaltered.

We now discuss the manner in which the basic fields transform under such transformations, granted the physically natural requirement of invariance of the internal power (2.31), or equivalently, the requirement that

$$\mathbf{S}^{e\,(\alpha)} : \dot{\mathbf{C}}^{e\,(\alpha)} \quad \text{and} \quad \mathbf{T}^{p\,(\alpha)} : \mathbf{D}^{p\,(\alpha)} \quad \text{be invariant.} \tag{2.97}$$

Isotropy of the reference space

Fix attention on a given micromechanism α, and let $\mathbf{Q}$ be a *time-independent rotation of the reference configuration.* Then $\mathbf{F} \to \mathbf{F}\mathbf{Q}$, and hence

$$\mathbf{F}^{p\,(\alpha)} \to \mathbf{F}^{p\,(\alpha)}\mathbf{Q} \quad \text{and} \quad \mathbf{F}^{e\,(\alpha)} \text{ are invariant,} \tag{2.98}$$

so that, by (2.8) and (2.12), $\mathbf{D}^{p\,(\alpha)}$ and $\dot{\mathbf{C}}^{e\,(\alpha)}$ are invariant. We may therefore use (2.97) to conclude that $\mathbf{S}^{e\,(\alpha)}$ and $\mathbf{T}^{p\,(\alpha)}$ are invariant. Also, by (2.12) and (2.13)

$$\mathbf{C}^{e\,(\alpha)}, \quad \text{and} \quad \mathbf{B}^{p\,(\alpha)} \quad \text{are invariant.} \tag{2.99}$$

Further, since the tensor $\mathbf{A}^{(\alpha)}$ maps vectors in the intermediate space into vectors in the same space, $\mathbf{A}^{(\alpha)}$ is invariant, and since $\boldsymbol{\xi}^{(\alpha)}$ are scalars, they too are invariant.

Turning our attention next to the constitutive equation (2.75) for the heat flux, a standard result from the theory of finite thermoelasticity is that under a symmetry transformation $\mathbf{Q}$ for the reference configuration, the temperature gradient $\nabla\vartheta$ and the heat flux $\mathbf{q}_{\mathrm{R}}$ transform as

$$\nabla\vartheta \to \mathbf{Q}^{\top}\nabla\vartheta, \qquad \mathbf{q}_{\mathrm{R}} \to \mathbf{Q}^{\top}\mathbf{q}_{\mathrm{R}}.$$

Hence, from (2.75) the thermal conductivity tensor must obey

$$\mathbf{K}(\vartheta) = \mathbf{Q}^{\top}\mathbf{K}(\vartheta)\mathbf{Q} \tag{2.100}$$

for all rotations $\mathbf{Q} \in \mathcal{G}_{\mathrm{R}}$.

We refer to the material as *initially isotropic* if

$$\mathcal{G}_{\mathrm{R}} = \mathrm{Orth}^{+}, \tag{2.101}$$

so that the response of the material is invariant under arbitrary rotations of the reference space for each α at each time t.

Isotropy of the intermediate structural space

Next, fix attention on a given micromechanism α, and let $\mathbf{Q}$, a *time-independent rotation of the corresponding intermediate space*, be a symmetry transformation. Then $\mathbf{F}$ is unaltered by such a rotation, and hence

$$\mathbf{F}^{e\,(\alpha)} \to \mathbf{F}^{e\,(\alpha)}\mathbf{Q} \quad \text{and} \quad \mathbf{F}^{p\,(\alpha)} \to \mathbf{Q}^{\top}\mathbf{F}^{p\,(\alpha)}, \tag{2.102}$$

and also

$$\mathbf{B}^{p\,(\alpha)} \to \mathbf{Q}^{\top}\mathbf{B}^{p\,(\alpha)}\mathbf{Q}, \quad \mathbf{C}^{e\,(\alpha)} \to \mathbf{Q}^{\top}\mathbf{C}^{e\,(\alpha)}\mathbf{Q}, \qquad \dot{\mathbf{C}}^{e\,(\alpha)} \to \mathbf{Q}^{\top}\dot{\mathbf{C}}^{e\,(\alpha)}\mathbf{Q}, \qquad \mathbf{D}^{p\,(\alpha)} \to \mathbf{Q}^{\top}\mathbf{D}^{p\,(\alpha)}\mathbf{Q}. \tag{2.103}$$

Further, since the tensor $\mathbf{A}^{(\alpha)}$ maps vectors in the intermediate space into vectors in the same space, we assume that $\mathbf{A}^{(\alpha)}$ transforms as

$$\mathbf{A}^{(\alpha)} \to \mathbf{Q}^{\top}\mathbf{A}^{(\alpha)}\mathbf{Q},$$

and hence

$$\dot{\mathbf{A}}^{(\alpha)} \to \mathbf{Q}^{\top}\dot{\mathbf{A}}^{(\alpha)}\mathbf{Q}.$$

Then (2.103) and (2.97) yield the transformation laws

$$\mathbf{S}^{e\,(\alpha)} \to \mathbf{Q}^{\top}\mathbf{S}^{e\,(\alpha)}\mathbf{Q}, \qquad \mathbf{T}^{p\,(\alpha)} \to \mathbf{Q}^{\top}\mathbf{T}^{p\,(\alpha)}\mathbf{Q}. \tag{2.104}$$

Thus, with reference to the constitutive equations (2.72) we conclude that

$$\left.\begin{aligned}
\bar{\psi}^{(\alpha)}(\mathbf{C}^{e\,(\alpha)}, \mathbf{A}^{(\alpha)}, \vartheta) &= \bar{\psi}^{(\alpha)}(\mathbf{Q}^{\top}\mathbf{C}^{e\,(\alpha)}\mathbf{Q}, \mathbf{Q}^{\top}\mathbf{A}^{(\alpha)}\mathbf{Q}, \vartheta),\\
\bar{\eta}^{(\alpha)}(\mathbf{C}^{e\,(\alpha)}, \mathbf{A}^{(\alpha)}, \vartheta) &= \bar{\eta}^{(\alpha)}(\mathbf{Q}^{\top}\mathbf{C}^{e\,(\alpha)}\mathbf{Q}, \mathbf{Q}^{\top}\mathbf{A}^{(\alpha)}\mathbf{Q}, \vartheta),\\
\mathbf{Q}^{\top}\bar{\mathbf{S}}^{e\,(\alpha)}(\mathbf{C}^{e\,(\alpha)}, \mathbf{A}^{(\alpha)}, \vartheta)\mathbf{Q} &= \bar{\mathbf{S}}^{e\,(\alpha)}(\mathbf{Q}^{\top}\mathbf{C}^{e\,(\alpha)}\mathbf{Q}, \mathbf{Q}^{\top}\mathbf{A}^{(\alpha)}\mathbf{Q}, \vartheta),\\
\mathbf{Q}^{\top}\bar{\mathbf{T}}^{p\,(\alpha)}(\mathbf{D}^{p\,(\alpha)}, \mathbf{\Lambda}^{(\alpha)})\mathbf{Q} &= \bar{\mathbf{T}}^{p\,(\alpha)}(\mathbf{Q}^{\top}\mathbf{D}^{p\,(\alpha)}\mathbf{Q}, \mathbf{Q}^{\top}\mathbf{\Lambda}^{(\alpha)}\mathbf{Q},),\\
h_i^{(\alpha)}(\mathbf{D}^{p\,(\alpha)}, \mathbf{\Lambda}^{(\alpha)}) &= h_i^{(\alpha)}(\mathbf{Q}^{\top}\mathbf{D}^{p\,(\alpha)}\mathbf{Q}, \mathbf{Q}^{\top}\mathbf{\Lambda}^{(\alpha)}\mathbf{Q}),\\
\mathcal{R}_i^{(\alpha)}(\mathbf{\Lambda}^{(\alpha)}) &= \mathcal{R}_i^{(\alpha)}(\mathbf{Q}^{\top}\mathbf{\Lambda}^{(\alpha)}\mathbf{Q}),\\
\mathbf{Q}^{\top}\mathbf{G}^{(\alpha)}(\mathbf{\Lambda}^{(\alpha)})\mathbf{Q} &= \mathbf{G}^{(\alpha)}(\mathbf{Q}^{\top}\mathbf{\Lambda}^{(\alpha)}\mathbf{Q}),\\
\mathbf{Q}^{\top}\mathbf{G}^{(\alpha)}_{\text{static}}(\mathbf{\Lambda}^{(\alpha)})\mathbf{Q} &= \mathbf{G}^{(\alpha)}_{\text{static}}(\mathbf{Q}^{\top}\mathbf{\Lambda}^{(\alpha)}\mathbf{Q})
\end{aligned}\right\} \tag{2.105}$$

with

$$\mathbf{Q}^{\top}\mathbf{\Lambda}^{(\alpha)}\mathbf{Q} = (\mathbf{Q}^{\top}\mathbf{C}^{e\,(\alpha)}\mathbf{Q}, \mathbf{Q}^{\top}\mathbf{B}^{p\,(\alpha)}\mathbf{Q}, \mathbf{Q}^{\top}\mathbf{A}^{(\alpha)}\mathbf{Q}, \boldsymbol{\xi}^{(\alpha)}, \vartheta), \tag{2.106}$$

must hold for all rotations $\mathbf{Q}$ in the *symmetry group* $\mathcal{G}_{\text{I}}^{(\alpha)}$ at each time t.

We refer to the material as *continually isotropic* (and to the reference configuration and intermediate spaces as undistorted) if

$$\mathcal{G}_{\text{I}}^{(\alpha)} = \text{Orth}^{+}, \tag{2.107}$$

so that the response of the material is invariant under arbitrary rotations of the reference and intermediate space for each α at each time t.[5] Henceforth

- *we restrict attention to materials that are* **isotropic**, *initially, and continually.*

In this case,

- the response functions $\bar{\psi}^{(\alpha)}$, $\bar{\eta}^{(\alpha)}$, $\bar{\mathbf{S}}^{e\,(\alpha)}$, $\bar{\mathbf{T}}^{p\,(\alpha)}$, $h_i^{(\alpha)}$, $\mathcal{R}_i^{(\alpha)}$, $\mathbf{G}^{(\alpha)}$, and $\mathbf{G}^{(\alpha)}_{\text{static}}$ must each be *isotropic*,

and that the thermal conductivity has the representation

$$\mathbf{K}(\vartheta) = \kappa(\vartheta)\mathbf{1}, \qquad \text{with} \qquad \kappa(\vartheta) > 0, \tag{2.108}$$

a scalar thermal conductivity.

[5]For polymer glasses this notion attempts to characterize situations in which the material has a completely disordered molecular structure.

2.6.3 Separability hypothesis for the free energy

We assume that the free energy has the separable form

$$\psi_{\mathrm{R}} = \sum_{\alpha=1}^{M} \bar{\psi}^{e\,(\alpha)}(\mathbf{C}^{e\,(\alpha)}, \vartheta) + \sum_{\alpha=1}^{M} \bar{\psi}^{p\,(\alpha)}(\mathbf{A}^{(\alpha)}, \vartheta) \tag{2.109}$$

with $\bar{\psi}^{e\,(\alpha)}$ an elastic energy, and $\bar{\psi}^{p\,(\alpha)}$ a defect energy associated with plastic flow, for each α.

Consequences of isotropy of the elastic energy

Since $\bar{\psi}^{e\,(\alpha)}(\mathbf{C}^{e\,(\alpha)}, \vartheta)$ is an isotropic function of $\mathbf{C}^{e\,(\alpha)}$, it has the representation

$$\bar{\psi}^{e\,(\alpha)}(\mathbf{C}^{e\,(\alpha)}, \vartheta) = \tilde{\psi}^{e\,(\alpha)}(\mathcal{I}_{\mathbf{C}^e}, \vartheta), \tag{2.110}$$

where

$$\mathcal{I}_{\mathbf{C}^{e\,(\alpha)}} = \Big(I_1(\mathbf{C}^{e\,(\alpha)}), I_2(\mathbf{C}^{e\,(\alpha)}), I_3(\mathbf{C}^{e\,(\alpha)})\Big)$$

is the list of principal invariants of $\mathbf{C}^{e\,(\alpha)}$. Thus, from (2.79)

$$\mathbf{S}^{e\,(\alpha)} = 2\frac{\partial \tilde{\psi}^{e\,(\alpha)}(\mathcal{I}_{\mathbf{C}^{e\,(\alpha)}})}{\partial \mathbf{C}^{e\,(\alpha)}}, \tag{2.111}$$

and we note that $\mathbf{S}^{e\,(\alpha)}$ are *isotropic functions of* $\mathbf{C}^{e\,(\alpha)}$. Then since (cf. (2.63))

$$\mathbf{M}^{e\,(\alpha)} = \mathbf{C}^{e\,(\alpha)}\mathbf{S}^{e\,(\alpha)},$$

and $\mathbf{S}^{e\,(\alpha)}$ are isotropic, we find that $\mathbf{S}^{e\,(\alpha)}$ and $\mathbf{C}^{e\,(\alpha)}$ commute,

$$\mathbf{C}^{e\,(\alpha)}\mathbf{S}^{e\,(\alpha)} = \mathbf{S}^{e\,(\alpha)}\mathbf{C}^{e\,(\alpha)}, \tag{2.112}$$

and hence that

- *the Mandel stress* $\mathbf{M}^{e\,(\alpha)}$ *for each* α *is* **symmetric.**

Consequences of isotropy of the defect energy

Let

$$\mathcal{I}_{\mathbf{A}^{(\alpha)}} = \Big(I_1(\mathbf{A}^{(\alpha)}), I_2(\mathbf{A}^{(\alpha)}), I_3(\mathbf{A}^{(\alpha)}), \vartheta\Big)$$

denote the list of principal invariants of $\mathbf{A}^{(\alpha)}$, then the defect free energy has a representation

$$\bar{\psi}^{p\,(\alpha)} = \tilde{\psi}^{p\,(\alpha)}(\mathcal{I}_{\mathbf{A}^{(\alpha)}}, \vartheta), \tag{2.113}$$

and this yields that

$$\frac{\partial \bar{\psi}^{p(\alpha)}(\mathcal{I}_{\mathbf{A}^{(\alpha)}}, \vartheta)}{\partial \mathbf{A}^{(\alpha)}} \mathbf{A}^{(\alpha)}, \tag{2.114}$$

are symmetric tensors.

2.7 Flow rule

Recall from (2.86) that the constitutive equation for $\mathbf{T}^{p(\alpha)}$ is

$$\mathbf{T}^{p(\alpha)} = \bar{\mathbf{T}}^{p(\alpha)}(\mathbf{D}^{p(\alpha)}, \mathbf{\Lambda}^{(\alpha)}) = \underbrace{\mathbf{Y}^{p(\alpha)}(\mathbf{D}^{p(\alpha)}, \mathbf{\Lambda}^{(\alpha)})}_{\text{dissipative}} + \underbrace{2\left(\frac{\partial \bar{\psi}^{p(\alpha)}(\mathcal{I}_{\mathbf{A}^{(\alpha)}}, \vartheta)}{\partial \mathbf{A}^{(\alpha)}} \mathbf{A}^{(\alpha)}\right)_0}_{\text{energetic}}. \tag{2.115}$$

We denote the energetic part of $\mathbf{T}^{p(\alpha)}$ by

$$\mathbf{M}^{(\alpha)}_{\text{back}} \stackrel{\text{def}}{=} 2\left(\frac{\partial \bar{\psi}^{p(\alpha)}(\mathcal{I}_{\mathbf{A}^{(\alpha)}}, \vartheta)}{\partial \mathbf{A}^{(\alpha)}} \mathbf{A}^{(\alpha)}\right)_0, \tag{2.116}$$

and call them *back-stresses*, and denote *effective Mandel stresses* by

$$\mathbf{M}^{e(\alpha)}_{\text{eff}} \stackrel{\text{def}}{=} \mathbf{M}^{e(\alpha)} - \mathbf{M}^{(\alpha)}_{\text{back}}. \tag{2.117}$$

Then, upon using the constitutive relation (2.115) and the microforce balance (2.54), together with the symmetry of the Mandel stresses, a central result of the theory are the *flow rules*

$$(\mathbf{M}^{e(\alpha)}_{\text{eff}})_0 = \mathbf{Y}^{p(\alpha)}(\mathbf{D}^{p(\alpha)}, \mathbf{\Lambda}^{(\alpha)}). \tag{2.118}$$

We now make two major assumptions concerning the plastic flow of isotropic materials:

(i) Let

$$\mathbf{N}^{p(\alpha)} \stackrel{\text{def}}{=} \frac{\mathbf{D}^{p(\alpha)}}{d^{p(\alpha)}} \tag{2.119}$$

denote the direction of plastic flow for each α whenever $\mathbf{D}^{p(\alpha)} \neq \mathbf{0}$. Then the mechanical dissipation inequality may be written as

$$\left[\mathbf{Y}^{p(\alpha)}(d^{p(\alpha)}, \mathbf{N}^{p(\alpha)}, \mathbf{\Lambda}^{(\alpha)}) : \mathbf{N}^{p(\alpha)} + \left(\frac{\partial \bar{\psi}^{p(\alpha)}(\mathcal{I}_{\mathbf{A}^{(\alpha)}}, \vartheta)}{\partial \mathbf{A}^{(\alpha)}}\right) : \mathbf{G}^{(\alpha)}(\mathbf{\Lambda}^{(\alpha)})\right] d^{p(\alpha)} > 0 \tag{2.120}$$

when $\mathbf{D}^{p(\alpha)} \neq \mathbf{0}$. Guided by (2.120), we assume henceforth that the dissipative flow stresses $\mathbf{Y}^{p(\alpha)}$ are parallel and point in the same direction as the $\mathbf{N}^{p(\alpha)}$, so that[6]

$$\mathbf{Y}^{p(\alpha)}(d^{p(\alpha)}, \mathbf{N}^{p(\alpha)}, \mathbf{\Lambda}^{(\alpha)}) = Y^{(\alpha)}(d^{p(\alpha)}, \mathbf{N}^{p(\alpha)}, \mathbf{\Lambda}^{(\alpha)})\mathbf{N}^{p(\alpha)}, \tag{2.121}$$

[6]This assumption leads to the classical notion of *maximal dissipation*.

where

$$Y^{(\alpha)}(d^{p\,(\alpha)}, \mathbf{N}^{p\,(\alpha)}, \mathbf{\Lambda}^{(\alpha)}) = \mathbf{Y}^{p\,(\alpha)}(d^{p\,(\alpha)}, \mathbf{N}^{p\,(\alpha)}, \mathbf{\Lambda}^{(\alpha)}) : \mathbf{N}^{p\,(\alpha)} \tag{2.122}$$

represents a scalar *flow strength* of the material for each α.

(ii) We also assume that the scalar flow strength $Y^{(\alpha)}(d^{p\,(\alpha)}, \mathbf{N}^{p\,(\alpha)}, \mathbf{\Lambda}^{(\alpha)})$ and the function $h_i^{(\alpha)}(d^{p\,(\alpha)}, \mathbf{N}^{p\,(\alpha)}, \mathbf{\Lambda}^{(\alpha)})$ characterizing the evolution of the scalar internal variables $\boldsymbol{\xi}^{(\alpha)}$ are independent of the flow directions $\mathbf{N}^{p\,(\alpha)}$ so that,

$$Y^{(\alpha)}(d^{p\,(\alpha)}, \mathbf{\Lambda}^{(\alpha)}), \quad h_i^{(\alpha)}(d^{p\,(\alpha)}, \mathbf{\Lambda}^{(\alpha)}). \tag{2.123}$$

Thus using (2.123) and (2.121), the flow rules reduce to

$$(\mathbf{M}_{\text{eff}}^{e\,(\alpha)})_0 = Y^{(\alpha)}(d^{p\,(\alpha)}, \mathbf{\Lambda}^{(\alpha)})\mathbf{N}^{p\,(\alpha)} \tag{2.124}$$

which immediately gives

$$\mathbf{N}^{p\,(\alpha)} = \frac{(\mathbf{M}_{\text{eff}}^{e\,(\alpha)})_0}{\left|(\mathbf{M}_{\text{eff}}^{e\,(\alpha)})_0\right|}, \tag{2.125}$$

and

$$\left|(\mathbf{M}_{\text{eff}}^{e\,(\alpha)})_0\right| = Y^{(\alpha)}(d^{p\,(\alpha)}, \mathbf{\Lambda}^{(\alpha)}). \tag{2.126}$$

When $\mathbf{M}_{\text{eff}}^{e\,(\alpha)}$, and $\mathbf{\Lambda}^{(\alpha)}$ are known (2.126) serve as implicit equations for the scalar flow rates $d^{p\,(\alpha)}$. Finally, using (2.121), $(2.123)_1$, and (2.126), the mechanical dissipation inequality (2.120) reduces to

$$\left[\left|(\mathbf{M}_{\text{eff}}^{e\,(\alpha)})_0\right| + \left(\frac{\partial \bar{\psi}^{p(\alpha)}(\mathcal{I}_{\mathbf{A}^{(\alpha)}}, \vartheta)}{\partial \mathbf{A}^{(\alpha)}}\right) : \mathbf{G}^{(\alpha)}(\mathbf{\Lambda}^{(\alpha)})\right] d^{p\,(\alpha)} > 0 \quad \text{when} \quad d^{p\,(\alpha)} \neq 0, \tag{2.127}$$

for each α.

2.8 Summary of the constitutive theory for isotropic materials

Although no real material is composed of springs and dashpots, as a visual aid, Fig. 2-1 shows a schematic "spring-dashpot"-representation of the generalized micromechanism based model. The underlying constitutive equations relate the following basic fields:

$\mathbf{x} = \boldsymbol{\chi}(\mathbf{X}, t)$,	motion;
$\mathbf{F} = \nabla\boldsymbol{\chi}, \quad J = \det \mathbf{F} > 0$,	deformation gradient;
$\mathbf{F} = \mathbf{F}^{e\,(\alpha)}\mathbf{F}^{p\,(\alpha)}, \quad \alpha = 1, \ldots, M$,	elastic-plastic decomposition of $\mathbf{F}$;
$\mathbf{F}^{e\,(\alpha)}, \quad J^{e\,(\alpha)} = \det \mathbf{F}^{e\,(\alpha)} = J > 0$,	elastic distortions;

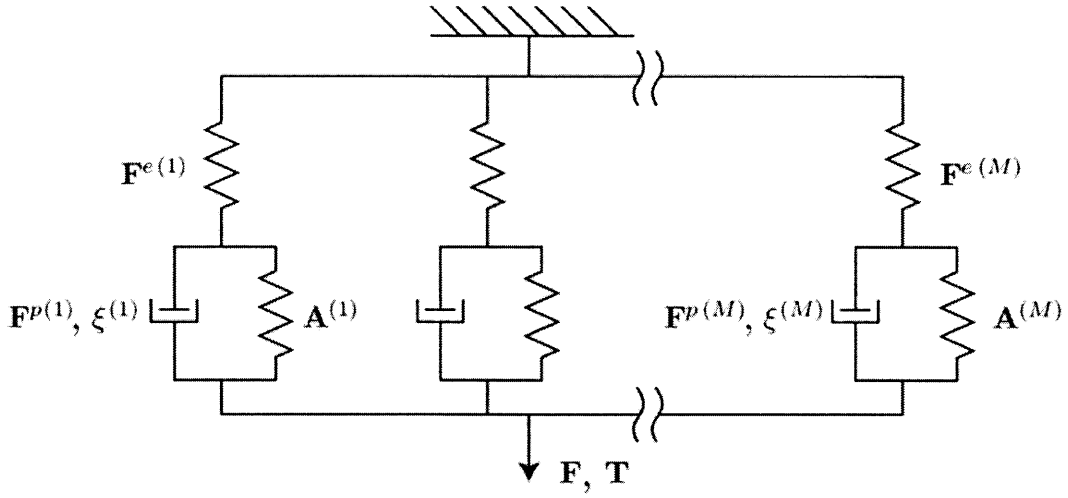

Figure 2-1: A schematic "spring-dashpot"-representation of the general multi-mechanism based theory (generalization of the Zener model).

$\mathbf{F}^{p\,(\alpha)}$, $J^{p\,(\alpha)} = \det \mathbf{F}^{p\,(\alpha)} = 1$,	inelastic distortions;
$\mathbf{F}^{e\,(\alpha)} = \mathbf{R}^{e\,(\alpha)}\mathbf{U}^{e\,(\alpha)}$,	polar decomposition of $\mathbf{F}^{e\,(\alpha)}$;
$\mathbf{C}^{e\,(\alpha)} = \mathbf{F}^{e\,(\alpha)\top}\mathbf{F}^{e\,(\alpha)}$,	elastic right Cauchy-Green tensors;
$\mathbf{B}^{p\,(\alpha)} = \mathbf{F}^{p\,(\alpha)}\mathbf{F}^{p\,(\alpha)\top}$,	plastic left Cauchy-Green tensors;
$\mathbf{T} = \sum_{\alpha=1}^{M} \mathbf{T}^{(\alpha)}$, $\quad \mathbf{T}^{(\alpha)} = \mathbf{T}^{(\alpha)\top}$,	Cauchy stress;
$\mathbf{T}_{\mathrm{R}} = J\mathbf{T}\mathbf{F}^{-\top}$,	Piola stress;
$\psi_{\mathrm{R}} = \sum_{\alpha=1}^{M} \bar{\psi}^{(\alpha)}$,	free energy density per unit reference volume;
$\eta_{\mathrm{R}} = \sum_{\alpha=1}^{M} \bar{\eta}^{(\alpha)}$,	entropy density per unit reference volume;
$\vartheta > 0$,	absolute temperature;
$\nabla\vartheta$,	referential temperature gradient;
$\mathbf{q}_{\mathrm{R}}$,	referential heat flux vector;
q_{R},	scalar heat supply.

2.8.1 Constitutive equations

1. **Free energy:**

   We assume that the free energy has the separable form

$$\psi_{\mathrm{R}} = \sum_{\alpha=1}^{M} \bar{\psi}^{e\,(\alpha)}(\mathcal{I}_{\mathbf{C}^{e\,(\alpha)}}, \vartheta) + \sum_{\alpha=1}^{M} \bar{\psi}^{p\,(\alpha)}(\mathcal{I}_{\mathbf{A}^{(\alpha)}}, \vartheta), \tag{2.128}$$

with $\bar{\psi}^{e\,(\alpha)}$ an elastic energy, and $\bar{\psi}^{p\,(\alpha)}$ a defect energy associated with plastic flow, for each α. Also, $\mathcal{I}_{\mathbf{C}^{e\,(\alpha)}}$ and $\mathcal{I}_{\mathbf{A}^{(\alpha)}}$ represent lists of the principal invariants of $\mathbf{C}^{e\,(\alpha)}$ and $\mathbf{A}^{(\alpha)}$, respectively.

2. **Cauchy stress:**

The Cauchy stress in the deformed body is the sum of the contributions from each micromechanism,

$$\mathbf{T} = \sum_{\alpha=1}^{M} \mathbf{T}^{(\alpha)}, \tag{2.129}$$

with

$$\mathbf{T}^{(\alpha)} \stackrel{\text{def}}{=} J^{-1}\left(\mathbf{F}^{e\,(\alpha)}\mathbf{S}^{e\,(\alpha)}\mathbf{F}^{e\,(\alpha)\top}\right), \qquad \mathbf{T}^{(\alpha)} = \mathbf{T}^{(\alpha)\top}, \tag{2.130}$$

where

$$\mathbf{S}^{e\,(\alpha)} = 2\frac{\partial\bar{\psi}^{e\,(\alpha)}(\mathcal{I}_{\mathbf{C}^{e\,(\alpha)}}, \vartheta)}{\partial\mathbf{C}^{e\,(\alpha)}}. \tag{2.131}$$

is a symmetric second Piola stress defined with respect to the local intermediate structural space for each α.

3. **Driving stresses for plastic flow:**

With

$$\mathbf{M}^{e\,(\alpha)} = \mathbf{C}^{e\,(\alpha)}\mathbf{S}^{e\,(\alpha)} \tag{2.132}$$

denoting the *symmetric* Mandel stress,

$$\mathbf{M}^{(\alpha)}_{\text{back}} = 2\left(\frac{\partial\bar{\psi}^{p\,(\alpha)}(\mathcal{I}_{\mathbf{A}^{(\alpha)}}, \vartheta)}{\partial\mathbf{A}^{(\alpha)}}\,\mathbf{A}^{(\alpha)}\right)_0 \tag{2.133}$$

a *symmetric deviatoric* back stress, and

$$\mathbf{M}^{e\,(\alpha)}_{\text{eff}} \stackrel{\text{def}}{=} \mathbf{M}^{e\,(\alpha)} - \mathbf{M}^{(\alpha)}_{\text{back}}, \tag{2.134}$$

an *effective Mandel stress*, the driving stress for plastic flow for each α is taken as

$$(\mathbf{M}^{e\,(\alpha)}_{\text{eff}})_0 = \mathbf{M}^{e\,(\alpha)}_0 - \mathbf{M}^{(\alpha)}_{\text{back}}, \tag{2.135}$$

which is symmetric and deviatoric.

4. **Flow rules:**

The evolution equation for each $\mathbf{F}^{p\,(\alpha)}$, with $\mathbf{W}^{p\,(\alpha)} = \mathbf{0}$,[7] is

$$\dot{\mathbf{F}}^{p\,(\alpha)} = \mathbf{D}^{p\,(\alpha)}\,\mathbf{F}^{p\,(\alpha)}, \tag{2.136}$$

[7]For a detailed discussion and justification of the $\mathbf{W}^p = \mathbf{0}$ assumption in a single micro-mechanism isotropic theory see Gurtin and Anand (2005); we adopt it here as well.

with the plastic stretching given by

$$\mathbf{D}^{p\,(\alpha)} = d^{p\,(\alpha)}\,\mathbf{N}^{p\,(\alpha)}, \qquad \mathbf{N}^{p\,(\alpha)} = \frac{(\mathbf{M}^{e\,(\alpha)}_{\text{eff}})_0}{|(\mathbf{M}^{e\,(\alpha)}_{\text{eff}})_0|}, \tag{2.137}$$

where, with

$$\boldsymbol{\Lambda}^{(\alpha)} = (\mathbf{C}^{e\,(\alpha)}, \mathbf{B}^{p\,(\alpha)}, \mathbf{A}^{(\alpha)}, \boldsymbol{\xi}^{(\alpha)}, \vartheta), \tag{2.138}$$

denoting a list of constitutive variables, the scalar flow rates $d^{p\,(\alpha)}$ are obtained by solving the scalar strength relations

$$|(\mathbf{M}^{e\,(\alpha)}_{\text{eff}})_0| = Y^{(\alpha)}(\boldsymbol{\Lambda}^{(\alpha)}, d^{p\,(\alpha)}), \tag{2.139}$$

for given $\mathbf{M}^{e\,(\alpha)}_{\text{eff}}$ and $\boldsymbol{\Lambda}^{(\alpha)}$, with the strength function $Y^{(\alpha)}(\boldsymbol{\Lambda}^{(\alpha)}, d^{p\,(\alpha)})$ is an isotropic function of its arguments.

5. Evolution equations for internal variables:

The internal variables $\boldsymbol{\xi}^{(\alpha)}$ and $\mathbf{A}^{(\alpha)}$ are presumed to evolve according to the differential equations

$$\left.\begin{aligned} \dot{\xi}^{(\alpha)}_i &= \underbrace{h^{(\alpha)}_i(\boldsymbol{\Lambda}^{(\alpha)}, \mathbf{D}^{p\,(\alpha)})}_{\text{dynamic evolution}} - \underbrace{\mathcal{R}^{(\alpha)}_i(\boldsymbol{\Lambda}^{(\alpha)})}_{\text{static recovery}}, \\ \overset{\cdot}{\mathbf{A}^{(\alpha)}} &= \underbrace{\mathbf{D}^{p\,(\alpha)}\mathbf{A}^{(\alpha)} + \mathbf{A}^{(\alpha)}\mathbf{D}^{p\,(\alpha)} - \mathbf{G}^{(\alpha)}(\boldsymbol{\Lambda}^{(\alpha)})\,\nu^{p\,(\alpha)}}_{\text{dynamic evolution}} - \underbrace{\mathbf{G}^{(\alpha)}_{\text{static}}(\boldsymbol{\Lambda}^{(\alpha)})}_{\text{static recovery}}, \end{aligned}\right\} \tag{2.140}$$

with the functions $h^{(\alpha)}_i$, $\mathcal{R}^{(\alpha)}_i$, $\mathbf{G}^{(\alpha)}$, and $\mathbf{G}^{(\alpha)}_{\text{static}}$ isotropic functions of their arguments.

The evolution equations for $\mathbf{F}^{p\,(\alpha)}$, $\boldsymbol{\xi}^{(\alpha)}$ and $\mathbf{A}^{(\alpha)}$ need to be accompanied by initial conditions. Typical initial conditions presume that the body is initially (at time $t = 0$, say) in a **virgin state** in the sense that

$$\mathbf{F}(\mathbf{X}, 0) = \mathbf{F}^{p\,(\alpha)}(\mathbf{X}, 0) = \mathbf{A}^{(\alpha)}(\mathbf{X}, 0) = \mathbf{1}, \qquad \xi^{(\alpha)}_i(\mathbf{X}, 0) = \xi^{(\alpha)}_{i,0}\ (= \text{constant}), \tag{2.141}$$

so that by $\mathbf{F} = \mathbf{F}^{e\,(\alpha)}\mathbf{F}^{p\,(\alpha)}$ we also have $\mathbf{F}^{e\,(\alpha)}(\mathbf{X}, 0) = \mathbf{1}$.

6. Entropy relation. Fourier's Law:

Finally, we have the entropy relation

$$\eta_{\text{R}} = \sum_{\alpha=1}^{M} \eta^{(\alpha)}, \qquad \eta^{(\alpha)} = -\left[\frac{\partial \bar{\psi}^{e\,(\alpha)}(\mathcal{I}_{\mathbf{C}^{e\,(\alpha)}}, \vartheta)}{\partial \vartheta} + \frac{\partial \bar{\psi}^{p\,(\alpha)}(\mathcal{I}_{\mathbf{A}^{(\alpha)}}, \vartheta)}{\partial \vartheta}\right], \tag{2.142}$$

together with Fourier's law

$$\mathbf{q}_{\mathrm{R}} = -\kappa\, \nabla\vartheta, \tag{2.143}$$

with $\kappa(\vartheta) > 0$ the thermal conductivity.

2.8.2 Partial differential equations for the deformation and temperature fields

The partial differential equation for the deformation is obtained from the local force balance

$$\mathrm{Div}\,\mathbf{T}_{\mathrm{R}} + \mathbf{b}_{0\mathrm{R}} = \rho_{\mathrm{R}}\,\ddot{\boldsymbol{\chi}}, \tag{2.144}$$

where $\mathbf{b}_{0\mathrm{R}}$ is the non-inertial body force per unit volume of the reference body, $\rho_{\mathrm{R}} > 0$ is the mass density, and

$$\mathbf{T}_{\mathrm{R}} = J\mathbf{T}\mathbf{F}^{-\top} \tag{2.145}$$

is the standard first Piola stress, with $\mathbf{T}$ given by (2.129) through (2.131).

The specific heat in the theory is given by

$$c \stackrel{\mathrm{def}}{=} -\vartheta \left[\sum_{\alpha=1}^{M} \frac{\partial^2 \bar{\psi}^{e\,(\alpha)}(\mathcal{I}_{\mathbf{C}^{e\,(\alpha)}}, \vartheta)}{\partial \vartheta^2} + \sum_{\alpha=1}^{M} \frac{\partial^2 \bar{\psi}^{p\,(\alpha)}(\mathcal{I}_{\mathbf{A}^{(\alpha)}}, \vartheta)}{\partial \vartheta^2} \right], \tag{2.146}$$

and balance of energy gives the following partial differential equation for the temperature

$$\begin{aligned} c\dot{\vartheta} = -\mathrm{Div}\,\mathbf{q}_{\mathrm{R}} + q_{\mathrm{R}} + \sum_{\alpha=1}^{M} \left(|(\mathbf{M}_{\mathrm{eff}}^{e\,(\alpha)})_0| + \frac{\partial \bar{\psi}^{p\,(\alpha)}}{\partial \mathbf{A}^{(\alpha)}} : \mathbf{G}^{(\alpha)} \right) d^{p\,(\alpha)} + \sum_{\alpha=1}^{M} \frac{\partial \bar{\psi}^{p\,(\alpha)}}{\partial \mathbf{A}^{(\alpha)}} : \mathbf{G}^{(\alpha)}_{\mathrm{static}} \\ \underbrace{+ \vartheta \sum_{\alpha=1}^{M} \frac{\partial^2 \bar{\psi}^{e(\alpha)}}{\partial \vartheta\, \partial \mathbf{C}^{e\,(\alpha)}} : \dot{\mathbf{C}}^{e\,(\alpha)} + \vartheta \sum_{\alpha=1}^{M} \frac{\partial^2 \bar{\psi}^{p(\alpha)}}{\partial \vartheta\, \partial \mathbf{A}^{(\alpha)}} : \dot{\mathbf{A}}^{(\alpha)}}_{\text{“thermoelastic” coupling terms}}, \end{aligned} \tag{2.147}$$

with $\mathbf{q}_{\mathrm{R}}$ given by (5.59).[8]

[8] Classically, only the term $\vartheta \sum_{\alpha=1}^{M} \frac{\partial^2 \bar{\psi}^{e(\alpha)}}{\partial \vartheta\, \partial \mathbf{C}^{e\,(\alpha)}} : \dot{\mathbf{C}}^{e\,(\alpha)}$ in (2.147) is called the “thermoelastic coupling” term. Here, for lack of better terminology, we use this terminology to also include the term $\vartheta \sum_{\alpha=1}^{M} \frac{\partial^2 \bar{\psi}^{p(\alpha)}}{\partial \vartheta\, \partial \mathbf{A}^{(\alpha)}} : \dot{\mathbf{A}}^{(\alpha)}$.

Chapter 3

A constitutive theory for amorphous polymers below their glass transition temperature

3.1 Introduction

Over the past twenty-five years considerable effort has been devoted to develop constitutive models to represent the large deformation elastic-viscoplastic behavior of glassy amorphous polymers (e.g., Parks et al., 1985; Boyce et al., 1988; Govaert et al., 2000; Anand and Gurtin, 2003a; Anand and Ames, 2006). Although differing in detail, these models combine three-dimensional representations of linear elasticity, of non-Newtonian viscoplastic flow arising from the motion of polymer segments, and of stiffening arising due to the alignment and locking of the long-chain polymer molecules at large strains, in a manner similar to that which was originally proposed in a one-dimensional setting by Haward and Thackray (1968). These models have been primarily used to describe the isothermal deformation of polymeric components below their glass transition temperatures. However, thermo-mechanical coupling effects have also been studied; for example, Arruda et al. (1995) and Ames (2007) have studied the effects of adiabatic heating under nominally homogeneous deformations, while Van der Giessen and co-workers (e.g., Basu and Van der Giessen, 2002; Estevez et al., 2005; Estevez and Basu, 2008) have studied the effects of adiabatic heating in the context of effects of temperature changes on the fracture response at cracks and notches under high-rate mode-I loading.

It is the purpose of this chapter to specialize the general thermo-mechanically coupled theory presented in Chapter 2 to model the strain-rate and temperature dependent large deformation mechanical response of amorphous polymers below their glass transition temperature. The plan of this chapter is as follows. In §3.2 we describe experiments on cyclo-

olefin amorphous polymer Zeonex-690R[1] in a temperature range spanning room temperature to slightly below its glass transition temperature, in a strain rate range of $3 \times 10^{-4}\,s^{-1}$ to $3 \times 10^{-1}\,s^{-1}$, and compressive true strains exceeding 130%. In §3.3 we present our specialized constitutive theory to capture the salient features of the experimentally-measured mechanical response of Zeonex-690R, PC and PMMA. The compression experiments on PC were conducted by our colleague Shawn A. Chester and the experimental data for PMMA was obtained from Ames (2007). In Appendix A, we describe in reasonable detail our procedure to calibrate the material parameters/functions appearing in our constitutive theory. The quality of the fit of the specialized model to the experimentally-measured stress-strain curves for Zeonex-690R, PC and PMMA is discussed in §3.5. For the three amorphous polymers, the specialized constitutive model presented in this chapter is shown to perform well in reproducing the following major intrinsic features of the macroscopic stress-strain response of these materials: (a) the strain rate and temperature dependent yield strength; (b) the transient yield-peak and strain-softening which occurs due to deformation-induced disordering; (c) the subsequent rapid strain-hardening due to alignment of the polymer chains at large strains; (d) the unloading response at large strains; and (e) the temperature rise due to plastic-dissipation and the limited time for heat-conduction for the compression experiments performed at strain rates $\gtrapprox 0.01\,s^{-1}$.

We have implemented our thermo-mechanically-coupled constitutive model by writing a user material subroutine for the finite element program ABAQUS/Explicit (2009). In §3.6, we present results of a suite of experiments that we have conducted in collaboration with Shawn A. Chester to validate the predictive capabilities of our constitutive theory and its numerical implementation. We have performed the following validation experiments: (i) isothermal fixed-end large-strain reversed-torsion tests on PC; (ii) macroscale isothermal plane-strain cold- and hot-forming operations on PC; (iii) macroscale isothermal, axisymmetric hot-forming operations on Zeonex; (iv) microscale hot-embossing of Zeonex-690R; and (v) high-speed normal-impact of a circular plate of PC with a spherical-tipped cylindrical projectile. By comparing the results from this suite of validation experiments of some key macroscopic features, such as the experimentally measured deformed shapes and the load-displacement curves, against corresponding results from numerical simulations, we show that our theory is capable of reasonably accurately reproducing the experimental results obtained in the validation experiments.

3.2 Simple compression experiments on Zeonex-690R

Relative to conventional amorphous polymers such as PC and PMMA, Zeonex-690R, a cyclo-olefin polymer is biocompatible, has lower moisture uptake, has better light transmittance characteristics, and it is also chemical resistant to a wide variety of solvents. These characteristics make Zeonex-690R an attractive material for several applications such as microfluidic devices and therefore a focus of our study. To the best of our knowledge, comprehensive

[1]From Zeon Chemicals.

stress-strain data for Zeonex-690R does not exist in the current literature. Therefore, we have conducted simple compression experiments on Zeonex-690R: (i) to large strains exceeding 130%, including *loading and unloading*; (ii) at a variety of strain rates in the range 3×10^{-4} to $3 \times 10^{-1}\,s^{-1}$, achievable in modern servo-hydraulic testing machines; and (iii) in a temperature range from room temperature to 130 °C. The nominal glass transition temperatures of Zeonex-690R is 135 °C.

Cylindrical compression test specimens were 10.2 mm diameter and 10.2 mm tall, and were annealed before and after machining to final shape by heating in a furnace at a temperature about 10 °C above the glass transition temperature, and holding at that temperature for two hours, before quenching the specimens in ice-water. The experiments were conducted using a servo-hydraulic Instron testing machine, fitted with a high-temperature furnace. Amorphous polymers are poor thermal conductors; accordingly, in order to heat the compression specimens uniformly, we also used heated steel compression platens in addition to the furnace. The platens were heated with cartridge heaters, and thermocouples inserted into each platen were used to control the temperature. The top compression platen also had an integrated spherical seat to help minimize any effects of misalignment during compression testing. To reduce friction at the platen/specimen interface, the platens were polished, and thin Teflon (PTFE) films were used as lubricating layers between the specimen and the platens.[2] Before a given experiment, each specimen was allowed to anneal at the testing temperature for one hour prior to testing. The compression tests were carried out at constant *true strain-rates* to compressive true strains exceeding $\gtrapprox$ 130%; all strain measurements were made using an extensometer.

Fig. 3-1 shows true stress-strain curves[3] for Zeonex-690R at strain-rates of 3×10^{-4}, 3×10^{-3}, 3×10^{-2} and $3 \times 10^{-3}\,s^{-1}$ at temperatures ranging from 25 °C through 130 °C. Fig. 3-2 shows a more extensive set of stress-strain curves for Zeonex-690R at strain rates of 3×10^{-4}, 3×10^{-3}, 3×10^{-2}, and $3 \times 10^{-1}\,s^{-1}$ and temperatures of 25 °C through 130 °C. In Fig. 3-1, we see that in the glassy region:

(i) The stress-strain curves exhibit a well-defined yield-peak, followed by strain-softening, and eventual strain-hardening at large strains due to the limited extensibility of the polymer chains.

(ii) As the temperature increases in the glassy region from 25 °C to 130 °C, the magnitude of the yield-peak diminishes, the yield strength decreases with temperature from $\approx$ 65 MPa to $\approx$ 15 MPa, and the amount of strain-hardening observed at large strains diminishes.

(iii) Upon unloading after compression to strains exceeding 125%, approximately 5% of the strain is recovered, and there is permanent-set.

[2]For true strains up to 100% our compression specimens showed very little or no bulging; however, for larger strain levels, in spite of our precautions to minimize friction, small bulging did occur.

[3]As is customary, in order to calculate the deformed cross-sectional area (and thence the true stress), we have assumed plastic incompressibility to estimate the stretch in the lateral direction of the compression specimens.

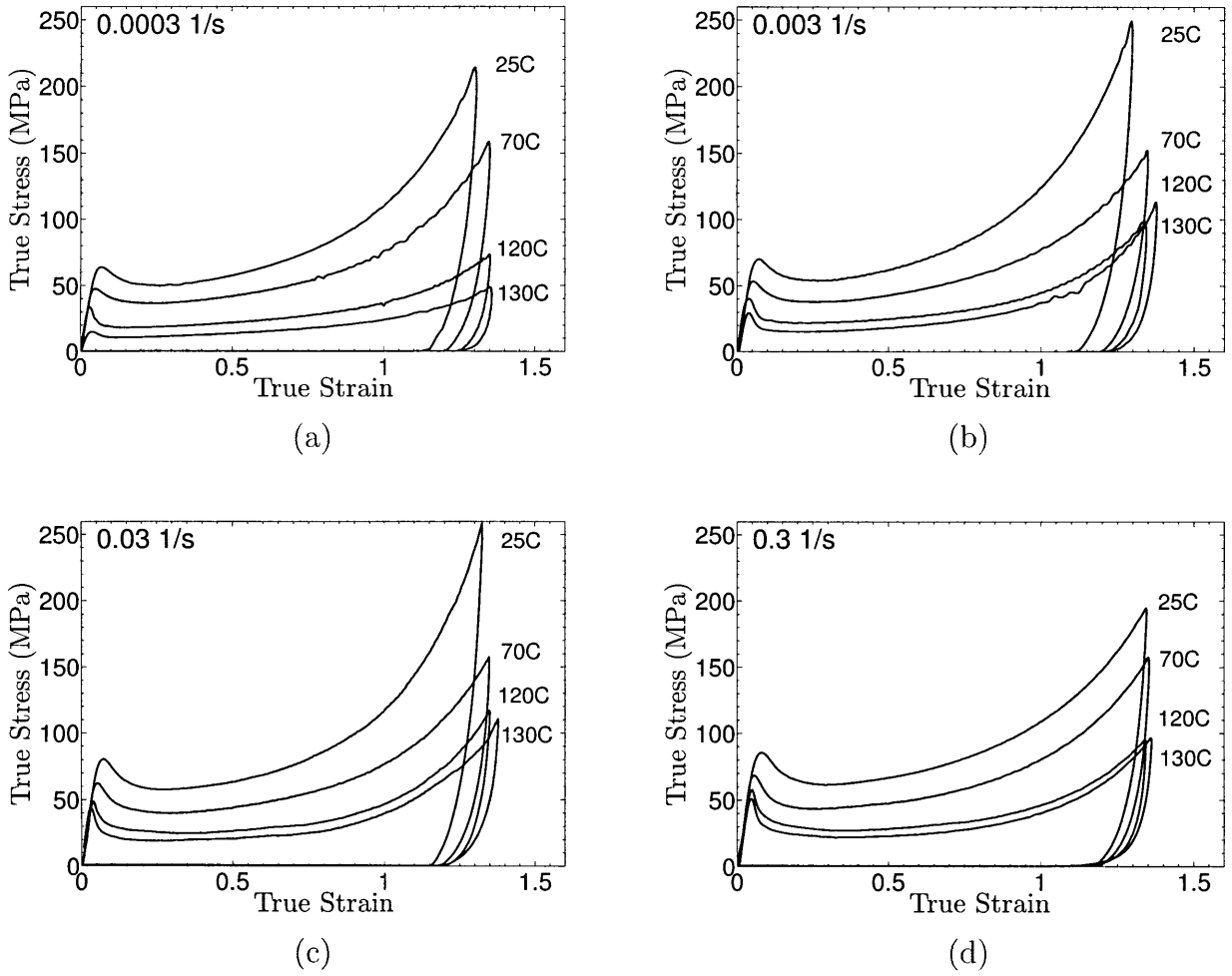

Figure 3-1: Stress-strain curves in simple compression for Zeonex-690R at various temperatures ranging from 25 °C, to 130 °C; at strain rates of (a) $3\times10^{-4}\,s^{-1}$, (b) $3\times10^{-3}\,s^{-1}$, (c) $3\times10^{-2}\,s^{-1}$, and (d) $3\times10^{-1}\,s^{-1}$.

Referring to Fig. 3-2 which shows stress-strain curves for Zeonex-690R at various fixed temperatures below ϑ_g and four different strain rates, we see obvious strain-rate dependent features of the material response. The yield strength of the material increases by about 10% for a one-decade increase in strain-rate at any given temperature. Another important strain-rate dependent feature is the softening observed at large strains at the highest strain rate of $3 \times 10^{-1}\,s^{-1}$ at temperatures of 25 °C, 70 °C, 120 °C and 130 °C. This softening is attributable to (near) "adiabatic" heating at the high strain rates.[4]

[4]While we did not measure the actual temperature rise in our specimens, Arruda et al. (1995) have shown that the surface temperature of a compression specimen of an amorphous polymer, for a test carried out at 20 °C, could increase by as much $\approx$ 20 °C after a 100% compressive strain at a strain rate of $10^{-1}\,s^{-1}$.

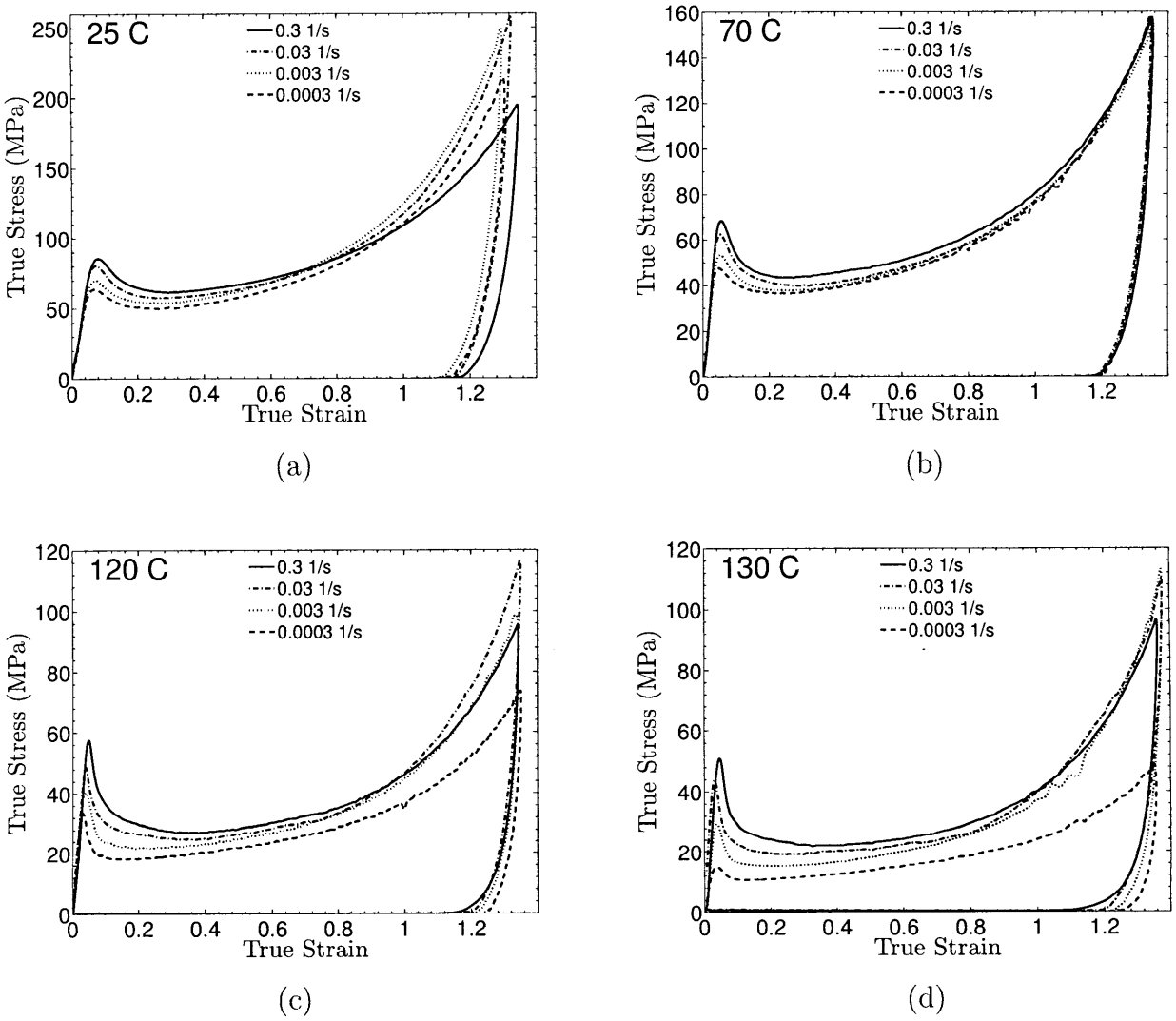

Figure 3-2: Stress-strain curves in simple compression for Zeonex-690R at strain rates of 3×10^{-4}, 3×10^{-4}, 3×10^{-4}, and $3\times10^{-4}\,s^{-1}$, and at temperatures of (a) 25 °C, (b) 70 °C, (c) 120 °C, and (d) 130 °C. Note change in scale for the stress axis between various figures.

3.3 Constitutive Theory

The fewer the "number of micromechanisms," M, which are needed to phenomenologically describe the response of a material, then the fewer the number of "material parameters" that are needed to flesh-out the constitutive theory delineated in Chapter 2. In order to model the response of amorphous polymers below ϑ_g, we find that a theory with $M = 2$ is quite adequate. Although no real material is composed of springs and dashpots, as a visual aid, Fig. 3-3 shows a schematic "spring-dashpot"- representation of these two micromechanisms:

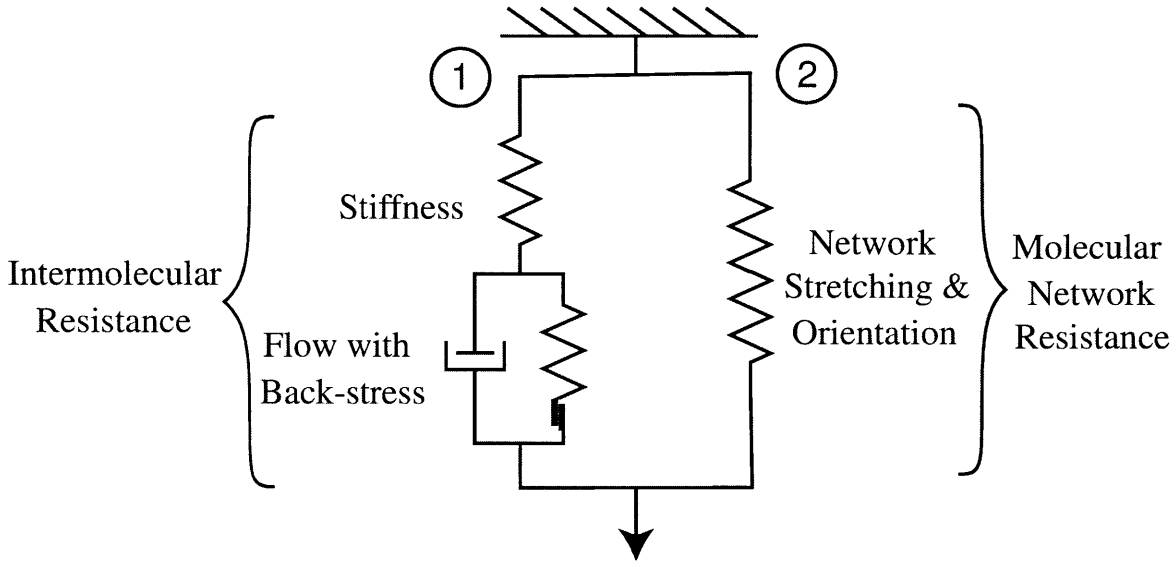

Figure 3-3: A schematic "spring-dashpot"-representation of the constitutive model for temperatures below ϑ_g.

- **The first micromechanism** ($\alpha = 1$): (a) The nonlinear spring represents an "elastic" resistance to intermolecular (and perhaps intramolecular) energetic bond-stretching. (b) The dashpot represents thermally-activated plastic flow due to "inelastic mechanisms," such as chain-segment rotation and relative slippage of the polymer chains between neighboring mechanical cross-linkage points. (c) The nonlinear spring in parallel with the dashpot represents an "energy storage" mechanism due to the local elastic incompatibilities caused by the viscoplastic flow mechanisms. We introduce a defect energy only for micromechanism $\alpha = 1$, via an internal variable $\mathbf{A}$; even for this micromechanism, the role of such a stored energy decreases as the molecular mobility increases when the temperatures approach ϑ_g.

- **The second micromechanism** ($\alpha = 2$): The nonlinear spring represent resistance due to changes in the free energy upon stretching of the molecular chains between the mechanical cross-links. We neglect any slippage in the molecular networks formed by

the "mechanical" cross-links for temperatures below ϑ_g; therefore there is no dashpot in micromechanism $\alpha = 2$. There is also no defect energy associated with $\alpha = 2$.

Polymeric materials exhibit a pronounced *Bauschinger-like* effect[5] upon unloading, even at moderate strain levels which are much smaller than those associated with the locking of polymeric chains at large strains (cf., e.g., Hasan and Boyce, 1995; Anand and Ames, 2006; Ames, 2007). In order to allow for important *energy storage mechanisms* due to plastic deformation, the development of an *internal back-stress*, and to account for Bauschinger-like phenomena on unloading and reverse loading, we have introduced a *symmetric and unimodular* tensor field

$$\mathbf{A}(\mathbf{X}, t), \quad \mathbf{A} = \mathbf{A}^\top, \quad \det \mathbf{A} = 1,$$

which represents a dimensionless *squared stretch-like* quantity.

Note that for the special case of temperatures below ϑ_g, from our constitutive assumption, the plastic deformation for micromechanism $\alpha = 2$ is neglected so that

$$\mathbf{F}^{p(2)} = \mathbf{1} \tag{3.1}$$

for all motions and all times. Therefore, for ease of notation, we introduce

$$\mathbf{F}^{p(1)} = \mathbf{F}^p, \quad \mathbf{F}^{e(1)} = \mathbf{F}^e, \quad \mathbf{F}^{e(2)} = \mathbf{F}, \tag{3.2}$$

and suppress the super-script α denoting micromechanisms wherever it is convenient to do so.

The underlying constitutive relations relate the following basic fields:

$\mathbf{x} = \boldsymbol{\chi}(\mathbf{X}, t)$,	motion;
$\mathbf{F} = \nabla\boldsymbol{\chi}, \quad J = \det \mathbf{F} > 0$,	deformation gradient;
$\mathbf{F} = \mathbf{F}^e\mathbf{F}^p$,	elastic-plastic decomposition of $\mathbf{F}$;
$\mathbf{F}^e, \quad J^e = \det \mathbf{F}^e = J > 0$,	elastic distortion;
$\mathbf{F}^p, \quad J^p = \det \mathbf{F}^p = 1$,	inelastic distortion;
$\mathbf{F} = \mathbf{RU} = \mathbf{VR}$,	polar decomposition of $\mathbf{F}$;
$\mathbf{F}^e = \mathbf{R}^e\mathbf{U}^e = \mathbf{V}^e\mathbf{R}^e$,	polar decomposition of $\mathbf{F}^e$;
$\mathbf{F}^p = \mathbf{R}^p\mathbf{U}^p = \mathbf{V}^p\mathbf{R}^p$,	polar decomposition of $\mathbf{F}^p$;
$\mathbf{C} = \mathbf{F}^\top\mathbf{F}, \quad \mathbf{B} = \mathbf{F}\mathbf{F}^\top$,	right and left Cauchy-Green tensors;
$\mathbf{C}^e = \mathbf{F}^{e\top}\mathbf{F}^e, \quad \mathbf{B}^e = \mathbf{F}^e\mathbf{F}^{e\top}$,	elastic right and left Cauchy-Green tensors;
$\mathbf{C}^p = \mathbf{F}^{p\top}\mathbf{F}^p, \quad \mathbf{B}^p = \mathbf{F}^p\mathbf{F}^{p\top}$,	plastic right and left Cauchy-Green tensors;

[5]The term "Bauschinger-effect" is used to describe a phenomenon first observed in metals by Bauschinger (1886). He reported that a metal specimen after receiving a certain amount of axial extension into the plastic range, showed a decrease in the magnitude of the yield strength upon subsequent compression. The origins of a Bauschinger-like effect are typically attributed to the generation of internal strains and corresponding stresses during deformation; the causes for such internal stresses are clearly different in polymers from those in metals (for which the term Bauschinger-effect was first coined).

$\mathbf{T} = \mathbf{T}^\top$,	Cauchy stress;
$\mathbf{T}_{\mathrm{R}} = J\mathbf{T}\mathbf{F}^{-\top}$,	Piola stress;
ψ_{R},	free energy density per unit reference volume;
$\boldsymbol{\xi} = (\xi_1, \xi_2, \ldots, \xi_m)$	m scalar internal variables;
$\mathbf{A}$, $\mathbf{A} = \mathbf{A}^\top$, $\det \mathbf{A} = 1$	tensorial internal variable;
$\vartheta > 0$,	absolute temperature;
$\nabla\vartheta$,	referential temperature gradient;
$\mathbf{q}_{\mathrm{R}}$,	referential heat flux vector.

3.3.1 Free energy

The free energy is given by

$$\psi_{\mathrm{R}} = \tilde{\psi}^{e\,(1)}(\mathcal{I}_{\mathbf{C}^e}, \vartheta) + \tilde{\psi}^{p\,(1)}(\mathcal{I}_{\mathbf{A}}, \vartheta) + \tilde{\psi}^{(2)}(\mathcal{I}_{\mathbf{C}}, \vartheta), \tag{3.3}$$

where $\mathcal{I}_{\mathbf{C}^e}$, $\mathcal{I}_{\mathbf{C}}$, and $\mathcal{I}_{\mathbf{A}}$ are the lists of the principal invariants of $\mathbf{C}^e$, $\mathbf{C}$, and $\mathbf{A}$, respectively. In (3.3), $\bar{\psi}^{e\,(1)}$ is an energy associated with intermolecular interactions and modeled using the elastic Cauchy-Green tensor $\mathbf{C}^e$; $\bar{\psi}^{p\,(1)}$ is an energy associated with plastic deformation, and assumed to depend on the internal variable $\mathbf{A}$; and $\bar{\psi}^{(2)}$ is an energy associated with the stretching of the polymer chains and modeled using the total Cauchy-Green tensor $\mathbf{C}$. The energy $\bar{\psi}^{(p)}$, also referred as "defect energy" leads to the development of a *back-stress*, and allows one to phenomenologically account for Bauschinger-like phenomena; in addition, it contributes in an important manner to the plastic source term in the balance of energy.

Free energy $\psi^{e\,(1)}$

The spectral representation of $\mathbf{C}^e$ is

$$\mathbf{C}^e = \sum_{i=1}^{3} \omega_i^e \mathbf{r}_i^e \otimes \mathbf{r}_i^e, \qquad \text{with} \qquad \omega_i^e = \lambda_i^{e\,2}, \tag{3.4}$$

where $(\mathbf{r}_1^e, \mathbf{r}_2^e, \mathbf{r}_2^e)$ are the orthonormal eigenvectors of $\mathbf{C}^e$ and $\mathbf{U}^e$, and $(\lambda_1^e, \lambda_2^e, \lambda_3^e)$ are the positive eigenvalues of $\mathbf{U}^e$. Instead of using the invariants $\mathcal{I}_{\mathbf{C}^e}$, the free energy $\psi^{(1)}$ for isotropic materials may be alternatively expressed in terms of the principal stretches and temperature as

$$\psi^{e\,(1)} = \breve{\psi}^{e\,(1)}(\lambda_1^e, \lambda_2^e, \lambda_3^e, \vartheta). \tag{3.5}$$

Let

$$\mathbf{E}^e \stackrel{\text{def}}{=} \ln \mathbf{U}^e = \sum_{i=1}^{3} E_i^e \, \mathbf{r}_i^e \otimes \mathbf{r}_i^e, \tag{3.6}$$

denote the logarithmic elastic strain with principal values

$$E_i^e \stackrel{\text{def}}{=} \ln \lambda_i^e \,, \tag{3.7}$$

and consider an elastic free energy function of the form

$$\breve{\psi}^{e\,(1)}(\lambda_1^e, \lambda_2^e, \lambda_3^e, \vartheta) = \breve{\psi}^{e\,(1)}(E_1^e, E_2^e, E_3^e, \vartheta). \tag{3.8}$$

We consider the following simple generalization of the classical strain energy function of infinitesimal isotropic elasticity which uses a logarithmic measure of finite strain[6]

$$\breve{\psi}^{(1)}(\mathbf{E}^e, \vartheta) = G|\mathbf{E}^e|^2 + \tfrac{1}{2}(K - \frac{2}{3}G)(\mathrm{tr}\,\mathbf{E}^e)^2 - (\vartheta - \vartheta_0)(3\,K\,\alpha)(\mathrm{tr}\,\mathbf{E}^e) + \tilde{f}(\vartheta), \tag{3.9}$$

where $\tilde{f}(\vartheta)$ is an entropic contribution to the free energy related to the temperature-dependent specific heat of the material. The temperature-dependent parameters

$$G(\vartheta) > 0, \quad K(\vartheta) > 0, \quad \alpha(\vartheta) > 0, \tag{3.10}$$

are the shear modulus, bulk modulus, and coefficient of thermal expansion, respectively, and ϑ_0 is a reference temperature.

Free energy $\psi^{p\,(1)}$

The spectral representation of $\mathbf{A}$ is

$$\mathbf{A} = \sum_{i=1}^{3} a_i \mathbf{l}_i \otimes \mathbf{l}_i, \tag{3.11}$$

where (a_1, a_2, a_3) are the positive eigenvalues, and $(\mathbf{l}_1, \mathbf{l}_2, \mathbf{l}_3)$ are the orthonormal eigenvectors of $\mathbf{A}$. The principal invariants of $\mathbf{A}$ are:

$$\left.\begin{aligned} I_1(\mathbf{A}) &= a_1 + a_2 + a_3, \\ I_2(\mathbf{A}) &= a_1 a_2 + a_2 a_3 + a_3 a_1, \\ I_3(\mathbf{A}) &= a_1 a_2 a_3 = 1 \quad (\text{since } \det \mathbf{A} = 1). \end{aligned}\right\} \tag{3.12}$$

Using (3.12), we express the defect energy as

$$\psi^{p\,(1)} = \tilde{\psi}^{p\,(1)}(\mathcal{I}_{\mathbf{A}}, \vartheta) = \breve{\psi}^{p\,(1)}(a_1, a_2, a_3, \vartheta). \tag{3.13}$$

[6]This is a useful free energy function for *moderately large elastic stretches*, Anand (1979, 1986).

Next, we consider the following simple defect energy:

$$\breve{\psi}^{p\,(1)}(a_1, a_2, a_3, \vartheta) = \frac{1}{4} B \left[(\ln a_1)^2 + (\ln a_2)^2 + (\ln a_3)^2\right], \tag{3.14}$$

where $B(\vartheta) \geq 0$ is a positive-valued temperature dependent parameter called back-stress modulus.

Free energy $\psi^{(2)}$

Since $J^e = J$, and we have already accounted for a volumetric elastic energy for $\psi^{e\,(1)}$, we do not allow for a volumetric elastic energy for $\psi^{(2)}$. We denote the distortional part of $\mathbf{F}$ by

$$\mathbf{F}_{\text{dis}} \stackrel{\text{def}}{=} J^{-1/3}\mathbf{F}, \quad \det \mathbf{F}_{\text{dis}} = 1. \tag{3.15}$$

Correspondingly, let

$$\mathbf{C}_{\text{dis}} \stackrel{\text{def}}{=} (\mathbf{F}_{\text{dis}})^{\top}\mathbf{F}_{\text{dis}} = J^{-2/3}\mathbf{C}, \tag{3.16}$$

denote the distortional (or volume preserving) right Cauchy-Green tensor, and consider a free energy function in the special form

$$\psi^{(2)} = \bar{\psi}^{(2)}(\mathcal{I}_{\mathbf{C}_{\text{dis}}}, \vartheta), \tag{3.17}$$

where $\mathcal{I}_{\mathbf{C}_{\text{dis}}}$ are the principal invariants of $\mathbf{C}_{\text{dis}}$.

In order to model the stress increase due to the stretching and locking of polymer chains at large strains, most previous theories for amorphous polymers (e.g., Parks et al., 1985; Boyce et al., 1988; Arruda and Boyce, 1993b; Wu and Van der Giessen, 1993a; Anand and Gurtin, 2003a) presume that polymer glasses behave like crosslinked rubber and use a free energy based on *entropic-network* models. There is a conceptual difficulty with using statistical-mechanical ideas of the theory of entropic rubber elasticity to describe the strain hardening due to chain-alignment at temperatures below the glass transition temperature, because at these temperatures the chains do not have sufficient mobility in the amorphous state to sample all possible molecular conformations, as visualized in the statistical-mechanical models of rubber elasticity. Here, we employ a simple *phenomenological* form for the free energy function $\psi^{(2)}$ due to Gent (1996). This model has been shown by Boyce (1996) to yield predictions for the stress-strain response similar to the entropic-network model of Arruda and Boyce (1993a). With

$$I_1 \stackrel{\text{def}}{=} \operatorname{tr} \mathbf{C}_{\text{dis}} \tag{3.18}$$

denoting the first principal invariant of $\mathbf{C}_{\text{dis}}$, the Gent free energy has the form

$$\psi^{(2)} = -\tfrac{1}{2}\mu\, I_m \ln\left(1 - \frac{I_1 - 3}{I_m}\right), \tag{3.19}$$

which involves two temperature-dependent material parameters

$$\mu(\vartheta) > 0, \qquad I_m(\vartheta) > 3. \tag{3.20}$$

In particular, μ represents the ground state rubbery shear modulus of the material, and I_m represents the upper limit of $(I_1 - 3)$, associated with limited chain extensibility of polymeric molecules.

3.3.2 Stress

Cauchy stress

The Cauchy stress is given by

$$\mathbf{T} = \mathbf{T}^{(1)} + \mathbf{T}^{(2)}, \tag{3.21}$$

where

$$\mathbf{T}^{(1)} \stackrel{\text{def}}{=} J^{-1}\left(\mathbf{F}^e\mathbf{S}^e\mathbf{F}^{e\top}\right), \qquad \text{with} \qquad \mathbf{S}^e = 2\frac{\partial\tilde{\psi}^{e\,(1)}(\mathcal{I}_{\mathbf{C}^e}, \vartheta)}{\partial\mathbf{C}^e}, \tag{3.22}$$

and

$$\mathbf{T}^{(2)} \stackrel{\text{def}}{=} J^{-1}\left(\mathbf{F}\mathbf{S}\mathbf{F}^{\top}\right), \qquad \text{with} \qquad \mathbf{S} = 2\frac{\partial\tilde{\psi}^{(2)}(\mathcal{I}_{\mathbf{C}}, \vartheta)}{\partial\mathbf{C}}. \tag{3.23}$$

In (3.22) and (3.23), $\mathbf{S}^e$ and $\mathbf{S}$ are symmetric; $\mathbf{S}^e$ represents a second Piola stress with respect to the intermediate structural space, while $\mathbf{S}$ represents a second Piola stress with respect to the reference space.

Mandel stress. Contribution $\mathbf{T}^{(1)}$ to Cauchy stress

By the chain-rule and $(3.22)_2$, the stress $\mathbf{S}^e$ is given by

$$\mathbf{S}^e = 2\frac{\partial\breve{\psi}^{e\,(1)}(\lambda_1^e, \lambda_2^e, \lambda_3^e, \vartheta)}{\partial\mathbf{C}^e} = 2\sum_{i=1}^{3}\frac{\partial\breve{\psi}^{e\,(1)}(\lambda_1^e, \lambda_2^e, \lambda_3^e, \vartheta)}{\partial\lambda_i^e}\frac{\partial\lambda_i^e}{\partial\mathbf{C}^e} = \sum_{i=1}^{3}\frac{1}{\lambda_i^e}\frac{\partial\breve{\psi}^{e\,(1)}(\lambda_1^e, \lambda_2^e, \lambda_3^e, \vartheta)}{\partial\lambda_i^e}\frac{\partial\omega_i}{\partial\mathbf{C}^e}. \tag{3.24}$$

Assume that the squared principal stretches ω_i^e are distinct, so that the ω_i^e and the principal directions $\mathbf{r}_i^e$ may be considered as functions of $\mathbf{C}^e$; then

$$\frac{\partial\omega_i^e}{\partial\mathbf{C}^e} = \mathbf{r}_i^e \otimes \mathbf{r}_i^e, \tag{3.25}$$

and, granted this, (3.25) and (3.24) imply that

$$\mathbf{S}^e = \sum_{i=1}^{3}\frac{1}{\lambda_i^e}\frac{\partial\breve{\psi}^{e\,(1)}(\lambda_1^e, \lambda_2^e, \lambda_3^e, \vartheta)}{\partial\lambda_i^e}\mathbf{r}_i^e \otimes \mathbf{r}_i^e. \tag{3.26}$$

Further, from $(3.22)_1$,

$$\mathbf{T}^{(1)} = J^{-1}\mathbf{F}^e\mathbf{S}^e\mathbf{F}^{e\top} = J^{-1}\mathbf{R}^e\mathbf{U}^e\mathbf{S}^e\mathbf{U}^e\mathbf{R}^{e\top} = J^{-1}\mathbf{R}^e\Big(\sum_{i=1}^{3}\lambda_i^e\frac{\partial\breve{\psi}^{e\,(1)}(\lambda_1^e,\lambda_2^e,\lambda_3^e,\vartheta)}{\partial\lambda_i^e}\mathbf{r}_i^e\otimes\mathbf{r}_i^e\Big)\mathbf{R}^{e\top}. \tag{3.27}$$

Next, since $\mathbf{M}^e = \mathbf{C}^e\mathbf{S}^e$ (cf. (2.132) in Chapter 2), use of (3.4) and (3.26) gives the Mandel stress as

$$\mathbf{M}^e = \sum_{i=1}^{3}\lambda_i^e\frac{\partial\breve{\psi}^{e\,(1)}(\lambda_1^e,\lambda_2^e,\lambda_3^e,\vartheta)}{\partial\lambda_i^e}\mathbf{r}_i^e\otimes\mathbf{r}_i^e, \tag{3.28}$$

which with (3.8) gives

$$\mathbf{M}^e = \sum_{i=1}^{3}\frac{\partial\breve{\psi}^{e\,(1)}(E_1^e,E_2^e,E_3^e,\vartheta)}{\partial E_i^e}\mathbf{r}_i^e\otimes\mathbf{r}_i^e. \tag{3.29}$$

Then, for the free energy considered in (3.9), we have

$$\mathbf{M}^e = 2G\mathbf{E}_0^e + K\,(\mathrm{tr}\,\mathbf{E}^e)\mathbf{1} - 3K\alpha(\vartheta-\vartheta_0)\mathbf{1}, \tag{3.30}$$

and on account of (3.27), (3.29), and (3.30),

$$\mathbf{T}^{(1)} = J^{-1}\mathbf{R}^e\mathbf{M}^e\mathbf{R}^{e\top}. \tag{3.31}$$

Back-stress. Effective stress

For the defect energy as (3.13), by chain rule we have

$$\frac{\partial\breve{\psi}^{p\,(1)}(a_1,a_2,a_3,\vartheta)}{\partial\mathbf{A}} = \sum_{i=1}^{3}\frac{\partial\breve{\psi}^{p\,(1)}(a_1,a_2,a_3,\vartheta)}{\partial a_i}\frac{\partial a_i}{\partial\mathbf{A}}. \tag{3.32}$$

Assume that a_i are distinct, so that the a_i and the principal directions $\mathbf{l}_i$ may be considered as functions of $\mathbf{A}$. Then,

$$\frac{\partial a_i}{\partial\mathbf{A}} = \mathbf{l}_i\otimes\mathbf{l}_i, \tag{3.33}$$

and, granted this, (3.32) implies that

$$\frac{\partial\breve{\psi}^{p\,(1)}(a_1,a_2,a_3,\vartheta)}{\partial\mathbf{A}} = \sum_{i=1}^{3}\frac{\partial\breve{\psi}^{p\,(1)}(a_1,a_2,a_3,\vartheta)}{\partial a_i}\mathbf{l}_i\otimes\mathbf{l}_i. \tag{3.34}$$

Also, use of (3.11) and (3.34) in (2.133) gives the deviatoric back-stress as

$$\mathbf{M}_{\text{back}} = 2\Big(\sum_{i=1}^{3} a_i \frac{\partial \breve{\psi}^{p\,(1)}(a_1, a_2, a_3, \vartheta)}{\partial a_i} \mathbf{l}_i \otimes \mathbf{l}_i\Big)_0. \tag{3.35}$$

For the simple defect energy assumed in (3.14)

$$\frac{\partial \breve{\psi}^{p\,(1)}(a_1, a_2, a_3, \vartheta)}{\partial \mathbf{A}} = \frac{1}{2} B \sum_{i=1}^{3} \frac{\ln a_i}{a_i} \mathbf{l}_i \otimes \mathbf{l}_i = \frac{1}{2} B (\ln \mathbf{A}) \mathbf{A}^{-1}, \tag{3.36}$$

where

$$\ln \mathbf{A} \overset{\text{def}}{=} \sum_{i=1}^{3} \ln a_i \, \mathbf{l}_i \otimes \mathbf{l}_i, \tag{3.37}$$

and

$$\mathbf{A}^{-1} = \sum_{i=1}^{3} a_i^{-1} \, \mathbf{l}_i \otimes \mathbf{l}_i. \tag{3.38}$$

Then, using (3.36) in (3.35) gives

$$\mathbf{M}_{\text{back}} = B(\ln \mathbf{A})_0. \tag{3.39}$$

Note that since $a_1 a_2 a_3 = 1$ (cf. $(3.12)_3$),

$$\operatorname{tr}(\ln \mathbf{A}) = \ln a_1 + \ln a_2 + \ln a_3 = \ln(a_1 a_2 a_3) = 0.$$

Hence the defect strain tensor $(\ln \mathbf{A})$ is *traceless*, and therefore a *symmetric and deviatoric* back-stress is

$$\mathbf{M}_{\text{back}} = B \ln \mathbf{A}. \tag{3.40}$$

With an *effective stress* defines as

$$\mathbf{M}^e_{\text{eff}} \overset{\text{def}}{=} \mathbf{M}^e - \mathbf{M}_{\text{back}}, \tag{3.41}$$

the driving stress for the plastic flow is taken as the stress difference

$$(\mathbf{M}^e_{\text{eff}})_0 = \mathbf{M}^e_0 - \mathbf{M}_{\text{back}}. \tag{3.42}$$

Contribution $\mathbf{T}^{(2)}$ to Cauchy stress

Using $(3.23)_2$, the stress $\mathbf{S}$ for a free energy of the form in (3.17) is

$$\mathbf{S} = 2\frac{\partial \bar{\psi}^{(2)}(\mathcal{I}_{\mathbf{C}_{\text{dis}}}, \vartheta)}{\partial \mathbf{C}} = 2\left\{\frac{\partial \mathbf{C}_{\text{dis}}}{\partial \mathbf{C}}\right\}^{\top} \frac{\partial \bar{\psi}^{(2)}(\mathcal{I}_{\mathbf{C}_{\text{dis}}}, \vartheta)}{\partial \mathbf{C}_{\text{dis}}}. \tag{3.43}$$

Next, since $J = \sqrt{\det \mathbf{C}}$, and since

$$\frac{\partial \det \mathbf{C}}{\partial \mathbf{C}} = (\det \mathbf{C})\, \mathbf{C}^{-1} = J^2\, \mathbf{C}^{-1},$$

we have

$$\frac{\partial J}{\partial \mathbf{C}} = \frac{1}{2}\, J\, \mathbf{C}^{-1}, \quad \text{and} \quad \frac{\partial J^{-2/3}}{\partial \mathbf{C}} = -\frac{1}{3} J^{-2/3} \mathbf{C}^{-1}\,. \tag{3.44}$$

Also,

$$\frac{\partial \mathbf{C}_{\text{dis}}}{\partial \mathbf{C}} = \frac{\partial (J^{-2/3}\mathbf{C})}{\partial \mathbf{C}} = J^{-2/3}\big(\mathbb{I} + J^{-2/3}\mathbf{C} \otimes \frac{\partial J^{-2/3}}{\partial \mathbf{C}}\big),$$

or using $(3.44)_2$,

$$\frac{\partial \mathbf{C}_{\text{dis}}}{\partial \mathbf{C}} = J^{-2/3}\Big(\mathbb{I} - \frac{1}{3}\mathbf{C} \otimes \mathbf{C}^{-1}\Big) = J^{-2/3}\Big(\mathbb{I} - \frac{1}{3}\mathbf{C}_{\text{dis}} \otimes \mathbf{C}_{\text{dis}}^{-1}\Big), \tag{3.45}$$

where $\mathbb{I}$ is the fourth-order identity tensor. Thus, using $(3.44)_1$ and (3.45) in (3.43), the stress $\mathbf{S}$ has the form

$$\begin{aligned}
\mathbf{S} &= 2J^{-2/3}(\mathbb{I} - \tfrac{1}{3}\mathbf{C}_{\text{dis}}^{-1} \otimes \mathbf{C}_{\text{dis}}) \frac{\partial \bar{\psi}^{(2)}(\mathcal{I}_{\mathbf{C}_{\text{dis}}}, \vartheta)}{\partial \mathbf{C}_{\text{dis}}} \\
&= 2J^{-2/3}\left[\frac{\partial \bar{\psi}^{(2)}(\mathcal{I}_{\mathbf{C}_{\text{dis}}}, \vartheta)}{\partial \mathbf{C}_{\text{dis}}} - \frac{1}{3}\left(\mathbf{C}_{\text{dis}} : \frac{\partial \bar{\psi}^{(2)}(\mathcal{I}_{\mathbf{C}_{\text{dis}}}, \vartheta)}{\partial \mathbf{C}_{\text{dis}}}\right)\mathbf{C}_{\text{dis}}^{-1}\right].
\end{aligned} \tag{3.46}$$

For the Gent free energy in (3.19), we note

$$\frac{\partial \bar{\psi}^{(2)}(\mathcal{I}_{\mathbf{C}_{\text{dis}}}, \vartheta)}{\partial \mathbf{C}_{\text{dis}}} = \tfrac{1}{2}\,\mu_{\text{R}}\left(1 - \frac{I_1 - 3}{I_m}\right)^{-1} \frac{\partial I_1}{\partial \mathbf{C}_{\text{dis}}} = \tfrac{1}{2}\,\mu_{\text{R}}\left(1 - \frac{I_1 - 3}{I_m}\right)^{-1} \mathbf{1}. \tag{3.47}$$

Using (3.47) in (3.46) gives

$$\mathbf{S} = J^{-2/3}\mu_{\text{R}}\left(1 - \frac{I_1 - 3}{I_m}\right)^{-1}\left[\mathbf{1} - \frac{1}{3}\left(\operatorname{tr}\mathbf{C}_{\text{dis}}\right)\mathbf{C}_{\text{dis}}^{-1}\right]. \tag{3.48}$$

Next, from $(3.23)_1$, the contribution $\mathbf{T}^{(2)}$ to the Cauchy stress is

$$\mathbf{T}^{(2)} = J^{-1}\mathbf{F}\mathbf{S}\mathbf{F}^{\top} = J^{-1/3}\mathbf{F}_{\text{dis}}\mathbf{S}\mathbf{F}_{\text{dis}}{}^{\top}, \tag{3.49}$$

and hence, using (3.48),

$$\mathbf{T}^{(2)} = J^{-1}\mu_{\text{R}}\left(1 - \frac{I_1 - 3}{I_m}\right)^{-1}\left[\mathbf{F}_{\text{dis}}\mathbf{F}_{\text{dis}}{}^{\top} - \frac{1}{3}\left(\operatorname{tr}\mathbf{C}_{\text{dis}}\right)\mathbf{F}_{\text{dis}}\mathbf{C}_{\text{dis}}^{-1}\mathbf{F}_{\text{dis}}{}^{\top}\right].$$

Then with

$$\mathbf{B}_{\text{dis}} \stackrel{\text{def}}{=} \mathbf{F}_{\text{dis}}\mathbf{F}_{\text{dis}}^{\top}, \tag{3.50}$$

$$\mathbf{T}^{(2)} = J^{-1}\mu_{\text{R}}\left(1-\frac{I_1-3}{I_m}\right)^{-1}\left[\mathbf{B}_{\text{dis}}-\frac{1}{3}\Big(\operatorname{tr}\mathbf{B}_{\text{dis}}\Big)\mathbf{1}\right],$$

or

$$\mathbf{T}^{(2)} = J^{-1}\,\mu_{\text{R}}\left(1-\frac{I_1-3}{I_m}\right)^{-1}(\mathbf{B}_{\text{dis}})_0. \tag{3.51}$$

3.3.3 Flow Rule. Internal variables

The evolution equation for $\mathbf{F}^p$ is

$$\dot{\mathbf{F}}^p = \mathbf{D}^p\,\mathbf{F}^p, \quad \text{with initial condition} \quad \mathbf{F}^p(\mathbf{X},0)=\mathbf{1}, \tag{3.52}$$

and with $\mathbf{D}^p$ given by

$$\mathbf{D}^p = d^p\,\mathbf{N}^p, \qquad \mathbf{N}^p = \frac{(\mathbf{M}^e_{\text{eff}})_0}{|(\mathbf{M}^e_{\text{eff}})_0|}, \tag{3.53}$$

where with

$$\mathbf{\Lambda} \stackrel{\text{def}}{=} \{\mathbf{C}^e, \mathbf{B}^p, \mathbf{A}, \boldsymbol{\xi}, \vartheta\} \tag{3.54}$$

denoting a list of constitutive variables, the scalar flow rate d^p is obtained by solving the scalar strength relation

$$|(\mathbf{M}^e_{\text{eff}})_0| = Y(d^p, \mathbf{\Lambda}), \tag{3.55}$$

for given $(\mathbf{M}^e_{\text{eff}})_0$ and $\mathbf{\Lambda}$, where $Y(d^p, \mathbf{\Lambda})$ is the strength function, which is an isotropic function of its arguments.

First, we define an *equivalent shear stress* by

$$\bar{\tau} \stackrel{\text{def}}{=} \frac{1}{\sqrt{2}}\,|(\mathbf{M}^e_{\text{eff}})_0|, \tag{3.56}$$

and an *equivalent shear strain rate* by

$$\nu^p \stackrel{\text{def}}{=} \sqrt{2}\,d^p = \sqrt{2}\,|\mathbf{D}^p|\,, \tag{3.57}$$

respectively.

Next, recalling (3.30) for the Mandel stress $\mathbf{M}^e$, we define the *mean normal pressure* by

$$\bar{p} \stackrel{\text{def}}{=} -\frac{1}{3}\operatorname{tr}\mathbf{M}^e = -K\,\{\operatorname{tr}\mathbf{E}^e - 3\,\alpha\,(\vartheta-\vartheta_0)\} = -K\left\{\frac{1}{2}\operatorname{tr}(\ln\mathbf{C}^e) - 3\,\alpha\,(\vartheta-\vartheta_0)\right\}. \tag{3.58}$$

Also let

$$\bar{\lambda} \stackrel{\text{def}}{=} \sqrt{\operatorname{tr}\mathbf{C}/3} \equiv \sqrt{\mathbf{C}^e:\mathbf{B}^p/3}, \tag{3.59}$$

define an *effective plastic stretch.* Then, as an (enormous) simplification of the theory, we assume that the strength function Y is independent of $\mathbf{A}$, and depends on $\mathbf{C}^e$ and $\mathbf{B}^p$ only through $\bar{p}$ and $\bar{\lambda}$.

Further, we restrict the list $\boldsymbol{\xi}$ of internal variables to three scalars

$$\varphi, \quad S_a, \quad \text{and} \quad S_b.$$

The two parameters φ and S_a are introduced to model the "yield-peak" of glassy polymers. A key microstructural feature controlling the strain-softening associated with the "yield-peak" is the deformation-induced disordering of glassy polymers.[7] The variable φ, a positive-valued dimensionless "order"-parameter, is introduced to represent such *deformation-induced disordering*; and S_a, a stress-dimensioned internal variable, represents the corresponding *transient resistance* to plastic flow accompanying the microstructural disordering. The parameter S_b, another positive-valued stress-dimensioned internal variable, is introduced to model additional "isotropic"-hardening aspects of the stress-strain response of these material as the chains are pulled taut between entanglements at large strains.

With these simplifications and internal variables, and using the definitions (3.56) – (3.59), we rewrite the strength relation (3.55) as

$$\bar{\tau} = g(\nu^p, \vartheta, \bar{p}, \bar{\lambda}, \varphi, S_a, S_b), \tag{3.60}$$

and assume further that at a fixed state $(\vartheta, \bar{p}, \bar{\lambda}, \varphi, S_a, S_b)$ the strength relation (4.72) is *invertible*, with inverse

$$\nu^p = f(\bar{\tau}, \vartheta, \bar{p}, \bar{\lambda}, \varphi, S_a, S_b) \geq 0. \tag{3.61}$$

Finally, guided by the literature (cf., e.g., Fotheringham et al., 1976; Fotheringham and Cherry, 1978; Povolo and Hermida, 1995; Povolo et al., 1996; Richeton et al., 2005a, 2006, 2007), for the flow function f in (4.83) we choose a thermally-activated relation in the specific form

$$\nu^p = \begin{cases} 0 & \text{if} \quad \tau_{\mathrm{e}} \leq 0, \\ \nu_0 \exp\left\{-\dfrac{Q}{k_B \vartheta}\right\} \left[\sinh\left(\dfrac{\tau_{\mathrm{e}} V}{2 k_B \vartheta}\right)\right]^{1/m} & \text{if} \quad \tau_{\mathrm{e}} > 0, \end{cases} \tag{3.62}$$

where

$$\tau_{\mathrm{e}} \stackrel{\text{def}}{=} \bar{\tau} - (S_a + S_b + \alpha_p \bar{p}) \tag{3.63}$$

denotes a *net shear stress for thermally activated flow*, and where $\alpha_p \geq 0$ is parameter introduced to account for the *pressure sensitivity* of plastic flow. Additionally, ν_0 is a pre-

[7]The deformation-induced disordering is often associated with the change in "free-volume" of glassy polymers. The "free-volume" terminology was introduced by Cohen and Grest (1979) for simple atomic glasses (amorphous metals), and there is a corresponding way to define it in glassy polymers (Shah et al., 1989). The deformation-induced disordering and its role in the yield drop in amorphous materials has also been discussed recently by Argon and Demkowicz (2008) (in the context of amorphous silicon).

exponental factor with dimensions of s^{-1}, Q is an *activation energy*, k_B is Boltzmann's constant, V is an *activation volume*, and m is a *strain rate sensitivity parameter*.

Some remarks: There are many models for the rate and temperature-dependent yield strength of polymers in the literature which consider plastic flow as a thermally-activated process (cf., e.g., Eyring, 1936; Robertson, 1966; Argon, 1973). Most of these models give a reasonably acceptable representation of the variation of the yield strength with temperature and strain rate, but over limited ranges of these variables. The flow function (3.62) used here is motivated by the recent work of Richeton et al. (2005a, 2006, 2007), who in turn base their model on the so-called "cooperative"-model of Fotheringham et al. (1976), Fotheringham and Cherry (1978), Povolo and Hermida (1995) and Povolo et al. (1996). Richeton et al. have shown that a flow function of the form (3.62) may be used to satisfactorily represent the variation of the yield strength of amorphous polymers over a wide range of strain rates and temperatures.[8] The major difference between the flow function proposed by Richeton et al. and the one considered here, is that instead of a tensorial back-stress $\mathbf{M}_{\text{back}}$ (cf., (3.40)) to define an effective stress which drives plastic flow (cf. (3.42)), they consider a temperature dependent scalar internal stress in their theory. This results in a profound difference between their model and the one considered here, specially in the ability of the two models to capture unloading and cyclic loading phenomena, as well as in a proper accounting of the energy dissipated during plastic flow. Also, the three-dimensional theory that they present in § 3 of their 2007 paper is substantially different in its mathematical structure from that considered here.

Mulliken and Boyce (2006), have recently proposed an alternate model to describe the variation of the yield strength of amorphous polymers over a wide range of strain rates and temperatures, albeit still for temperatures below the glass transition. Their model is a generalization of the model(s) proposed by Bauwens, Bauwens-Crowet and co-workers (cf., e.g., Bauwens et al., 1969; Bauwens-Crowet et al., 1969; Bauwens, 1972; Bauwens-Crowet, 1973), in which they introduce two rheological micro-mechanisms — designated as primary or α and secondary or β — which contribute to the yield strength of the material. The primary α-mechanism represents the rotations of the main-chain segments of the polymer, and the secondary β-mechanism represents the rotations of the ester side groups in PMMA, and the rotations of the phenyl groups in the main chains of PC. These two mechanisms are rate-limiting in different regimes of strain rates and/or temperatures; the α-mechanism is the dominant rate-limiting mechanism at low rates (or high temperatures), and the β-mechanism is the dominant rate-limiting mechanism at high strain rates (or low temperatures). Mulliken and Boyce assume that the α and β molecular processes are sufficiently decoupled, so that the overall material response may be described by a simple superposition of the two mechanisms. They develop a theory which employs a decomposition of the form $\mathbf{F} = \mathbf{F}^e_\alpha \mathbf{F}^p_\alpha = \mathbf{F}^e_\beta \mathbf{F}^p_\beta$ to account for the α and β mechanisms for the yield strength (instead, we have employed only one micromechanism $\alpha = 1$ for the yield). This results in a substantially different and

[8] Richeton et al. extend the flow rule (3.62) through the glass transition temperature, but in this paper we fix our attention in the regime of temperatures below ϑ_g.

more complex constitutive theory than that considered in this chapter, and also results in a doubling of the material parameters concerning pre-exponential factors, activation energies, deformation resistances, press-sensitivity parameters, and so on.

There maybe some physical merits of the multi-mechanism (α, β)-based model of Mulliken and Boyce, for operational economy our preference here is not to follow their approach, but instead to adopt a variant of the "cooperative"-model of Richeton et al. (2007), which from a macroscopic point of view appears to achieve the same goal of being able to represent the variation of the yield strength of amorphous polymers over a wide range of strain rates and temperatures.

3.3.4 Evolution equations for the internal variables

Evolution of φ and S_a

We assume that the material disorders, and is accompanied by a microscale dilatation as plastic deformation occurs, resulting in an increase of the order-parameter φ,[9] and this increase in disorder leads to a change in the resistance S_a, causing a transient change in the flow stress of the material as plastic deformation proceeds. Accordingly, the evolution of the resistance S_a is coupled to the evolution of the order-parameter φ. Specifically, we take the evolution of S_a to be governed by[10]

$$\left.\begin{aligned} \dot{S}_a &= H_a\,\nu^p, \qquad \text{with initial value} \qquad S_a(\mathbf{X},0) = S_{a0}\,, \\ H_a &= h_a\,(S_a^* - S_a)\,, \qquad \text{and} \qquad S_a^* = \hat{S}_a^*(\nu^p, \vartheta, \varphi), \end{aligned}\right\} \tag{3.64}$$

and we assume that

$$\left.\begin{aligned} \dot{\varphi} &= \beta\nu^p \qquad \text{with initial value} \qquad \varphi(\mathbf{X},0) = \varphi_0, \\ \beta &= g\,(\varphi^* - \varphi)\,, \qquad \text{with} \qquad \varphi^* = \hat{\varphi}^*(\nu^p, \vartheta) \geq 0; \end{aligned}\right\} \tag{3.65}$$

here β is a *shear-induced disordering function.*[11] In these coupled evolution equations for S_a and φ, the parameters h_a, g, S_{a0} and φ_0 are constants (possibly temperature-dependent). The function H_a represents the strain-hardening/softening function for the resistance S_a during plastic flow: the material hardens ($H_a > 0$) if $S_a < S_a^*$, and softens ($H_a < 0$) if $S_a > S_a^*$. The critical value S_a^* of S_a controlling such hardening/softening transitions is assumed to depend on the current values of the plastic strain rate, temperature, and the order-parameter φ. In the disordering function β, the parameter φ^* represents a strain rate and temperature dependent critical value for the order-parameter: the material disorders

[9]The microscale dilatation is extremely small, and at the macroscopic level we presume the plastic flow to be incompressible.

[10]Coupled differential evolution equations of this type have previously been used to model yield peaks in granular materials (Anand and Gu, 2000), as well as amorphous polymeric materials (Anand and Gurtin, 2003a; Ames, 2007) and amorphous metallic glasses (Henann and Anand, 2008).

[11]We concentrate only on deformation-induced disordering, and neglect any decrease in the degree of disorder due to temperature-dependent recovery effects in the absence of macroscopic plastic deformation.

($\beta > 0$) when $\varphi < \varphi^*$, and becomes less disordered ($\beta < 0$) when $\varphi > \varphi^*$. In a monotonic experiment at a given strain rate and temperature, the shear-induced disordering vanishes ($\beta = 0$) when $\varphi = \varphi^*$. However, in an experiment in which the strain rate and temperature are varying (e.g. strain rate or temperature jump experiments), the material will in general increase or decrease in disorder, depending on the strain rate and temperature history, and because of the coupling between the evolution equations for S_a and φ, the resistance S_a will also vary.

Particular forms for the function $\hat{\varphi}^*(\nu^p, \vartheta)$ and $\hat{S}^*(\nu^p, \vartheta, \varphi)$ need to be specified. The function φ^* controls the amount of disordering the material undergoes during deformation and is both strain rate and temperature dependent. The strain rate and temperature dependence of φ^* is quite nonlinear; φ^* is expected to decrease with increasing temperature at a fixed strain rate, and increase with strain rate at a fixed temperature. We model this temperature and strain rate dependence of φ^* using the following phenomenological form

$$\hat{\varphi}^*(\nu^p, \vartheta) = \begin{cases} z\left(1 - \dfrac{\vartheta^{\,r}}{\vartheta_c}\right)\left(\dfrac{\nu^p}{\nu_r}\right)^s & \text{if } (\vartheta < \vartheta_c) \text{ and } (\nu^p > 0), \\ 0 & \text{if } (\vartheta \geq \vartheta_c) \text{ or } (\nu^p = 0), \end{cases} \tag{3.66}$$

where ϑ_c is as strain rate dependent function given by[12]

$$\vartheta_c = \begin{cases} \vartheta_g + n \ln\left(\dfrac{\nu^p}{\nu_r}\right) & \text{for } \nu^p > \nu_r, \\ \vartheta_g & \text{for } \nu^p \leq \nu_r, \end{cases} \tag{3.67}$$

with $\{z, r, s, \nu_r, n\}$ as constants.

Further, the function S_a^*, which controls the magnitude of the stress-overshoot, is taken as

$$S_a^* = b\,(\varphi^* - \varphi)\,, \tag{3.68}$$

so that the value of S_a^* depends linearly on the difference between the current value of φ and the parameter φ^*.

Thus, gathering the number of material parameters introduced to phenomenologically model the yield-peak, we have the following rather large list

$$\{h_a, b, S_{a0}, g, \varphi_0, z, r, s, \nu_r, n\}\,,$$

with some of these parameters possessing additional temperature-dependence. *We note that modeling the temperature and rate-sensitivity of the yield-peak over a wide-range of temperatures and strain rates is known to be very complex.* If a simpler theory with fewer material parameters is desired, and if it is deemed that modeling the yield-peak is not of interest, then there is no need to introduce the internal variables φ and S_a, and thereby also the attendant constants in their evolution equations.

[12]This approximately models the rate-dependence of the glass transition temperature of the material.

Evolution of S_b

The evolution of S_b is taken to be governed by

$$\dot{S}_b = h_b \left(\bar{\lambda} - 1\right) \left(S_b^* - S_b\right) \nu^p \quad \text{with initial value} \quad S_b(\mathbf{X}, 0) = S_{b0} \geq 0, \tag{3.69}$$

where h_b is assumed to be constant and $S_b^*(\vartheta)$ is a temperature dependent material parameter. The resistance S_b increases and the material hardens as long as $S_b < S_b^*$.

Evolution of A

Finally, the evolution equation for $\mathbf{A}$ is taken as

$$\dot{\mathbf{A}} = \mathbf{D}^p \mathbf{A} + \mathbf{A}\mathbf{D}^p - \gamma\, \mathbf{A} \ln \mathbf{A}\, \nu^p, \qquad \mathbf{A}(\mathbf{X}, 0) = \mathbf{1}, \tag{3.70}$$

where $\gamma \geq 0$ is a constitutive parameter which governs the dynamic recovery of $\mathbf{A}$. This evolution equation is a generalization of the non-linear kinematic-hardening rule (Armstrong and Frederick, 1966) of the small deformation theory of classical metal viscoplasticity,[13] but here applied to polymer-viscoplasticity.

3.3.5 Fourier's law

The heat flux is taken to be governed by Fourier's law

$$\mathbf{q}_{\mathrm{R}} = -\kappa\, \nabla\vartheta, \tag{3.71}$$

where $\kappa(\vartheta) > 0$ is the thermal conductivity.

3.3.6 Partial differential equations for the deformation and temperature fields

The partial differential equation for the deformation is obtained from the local force balance

$$\mathrm{Div}\, \mathbf{T}_{\mathrm{R}} + \mathbf{b}_{0\mathrm{R}} = \rho_{\mathrm{R}} \ddot{\boldsymbol{\chi}}. \tag{3.72}$$

[13] Cf., e.g., Chaboche (2008) for a recent review of the large variety of kinematic-hardening rules in classical small deformation metal-viscoplasticity.

Also, balance of energy (cf. (2.147) in Chapter 2), when specialized, gives the following partial differential equation for the temperature,

$$c\dot{\vartheta} = -\mathrm{Div}\,\mathbf{q}_{\mathrm{R}} + q_{\mathrm{R}} + \underbrace{\left[\bar{\tau} + \tfrac{1}{2}B\gamma\,|\ln\mathbf{A}|^2\right]\nu^p}_{\text{rate of plastic dissipation}}$$
$$\underbrace{+\,\tfrac{1}{2}\vartheta\left(\mathbf{C}^{e-1}\frac{\partial\mathbf{M}^e}{\partial\vartheta}\right):\dot{\mathbf{C}}^e + \tfrac{1}{2}\vartheta\left(\frac{\partial\mathbf{S}}{\partial\vartheta}\right):\dot{\mathbf{C}} + \tfrac{1}{2}\frac{\partial B(\vartheta)}{\partial\vartheta}\Big((\ln\mathbf{A})\mathbf{A}^{-1}\Big):\dot{\mathbf{A}}}_{\text{"thermoelastic-coupling" terms}}, \tag{3.73}$$

where

$$\left.\begin{aligned}\frac{\partial\mathbf{M}^e}{\partial\vartheta} &= 2\frac{\partial G(\vartheta)}{\partial\vartheta}\mathbf{E}^e_0 + \frac{\partial K(\vartheta)}{\partial\vartheta}(\mathrm{tr}\,\mathbf{E}^e)\mathbf{1} - 3\frac{\partial}{\partial\vartheta}\Big(K(\vartheta)\alpha(\vartheta)(\vartheta-\vartheta_0)\Big)\mathbf{1},\\ \frac{\partial\mathbf{S}}{\partial\vartheta} &= \frac{\partial}{\partial\vartheta}\Big(\mu_{\mathrm{R}}(\vartheta)\left(1-\frac{I_1-3}{I_m(\vartheta)}\right)^{-1}\Big)\mathbf{F}^{-1}(\mathbf{B}_{\mathrm{dis}})_0\mathbf{F}^{-\top},\end{aligned}\right\} \tag{3.74}$$

and the specific heat in the theory is given by

$$c = \hat{c}(\mathcal{I}_{\mathbf{C}^e},\mathcal{I}_{\mathbf{C}},\mathcal{I}_{\mathbf{A}},\vartheta) = -\vartheta\left[\frac{\partial^2\bar{\psi}^{(1)}(\mathcal{I}_{\mathbf{C}^e},\vartheta)}{\partial\vartheta^2} + \frac{\partial^2\bar{\psi}^{(2)}(\mathcal{I}_{\mathbf{C}},\vartheta)}{\partial\vartheta^2} + \frac{\partial^2\bar{\psi}^{p)}(\mathcal{I}_{\mathbf{A}},\vartheta)}{\partial\vartheta^2}\right]. \tag{3.75}$$

At this stage of the development of the theory and the concomitant experimental database, the "thermoelastic-coupling" terms in (3.73) which give rise to a temperature change due to variations of $\mathbf{C}^e$, $\mathbf{C}$ and $\mathbf{A}$ are not well-characterized, nor is the dependence of the specific heat c on these quantities. *Much work needs to be done to characterize these dependencies.* Here, as *approximations*, (i) we assume that $c \approx \hat{c}(\vartheta)$ (independent of $\mathbf{C}^e$, $\mathbf{C}$ and $\mathbf{A}$), and may be obtained from experimental measurements; and (ii) we neglect the thermoelastic coupling terms, and assume instead that only a fraction $0 \lessapprox \omega \lessapprox 1$ of the rate of plastic dissipation contributes to the temperature changes. Under these approximative assumptions (3.73) reduces to

$$c\dot{\vartheta} = -\mathrm{Div}\,\mathbf{q}_{\mathrm{R}} + q_{\mathrm{R}} + \omega\left(\bar{\tau} + \frac{1}{2}B\gamma\,|\ln\mathbf{A}|^2\right)\nu^p, \qquad \text{with} \qquad c = \hat{c}(\vartheta). \tag{3.76}$$

3.3.7 Temperature dependence of material parameters

Temperature dependence of the thermo-elastic moduli G, K, and α:

For polymeric materials the magnitude of the elastic shear modulus G decreases as the temperature increases, and then decreases drastically as the temperature increases through the glass transition temperature ϑ_g of the material. For temperatures below ϑ_g we approximate the change of G with temperature by

$$G(\vartheta) = G_0 - M(\vartheta - \vartheta_g) \quad \text{for} \quad \vartheta < \vartheta_g, \tag{3.77}$$

where G_0 and M are constants, and ϑ_g is the glass transition temperature.

Below the glass transition temperature, the Poisson's ratio of the material is approximated as a constant

$$\nu_{\text{poi}} \approx \text{constant},$$

and the temperature dependence of the bulk modulus K is then obtained by using the standard relation

$$K(\vartheta) = G(\vartheta) \times \frac{2(1+\nu_{\text{poi}})}{3(1-2\nu_{\text{poi}})}. \tag{3.78}$$

In the temperature range of interest, the coefficient of thermal expansion is also approximated to be constant

$$\alpha \approx \text{constant}.$$

Temperature dependence of the back-stress modulus B:

The back-stress modulus B is assumed to decrease linearly with temperature,

$$B(\vartheta) = X(\vartheta_g - \vartheta) \quad \text{for} \quad \vartheta < \vartheta_g, \tag{3.79}$$

where $X > 0$ is a constant.

Temperature dependence of the plastic flow parameters Q, V and m:

For temperatures below ϑ_g, the activation energy Q, the activation volume V, and the strain rate sensitivity parameter m appearing in the thermally activated model (3.62) are assumed to be constants.

Temperature dependence of the material parameters in the evolution equations for φ, S_a, S_b, and A:

In the coupled evolution equations (3.64) and (3.65) for S_a and φ, the material parameters are

$$\{h_1, b, S_{a0}, g, \varphi_0, z, r, s, \nu_r, n\}.$$

We assume that all but g are independent of temperature. The parameter g in (3.65) controls the width of the yield-peak where a higher values of g results in a narrower peak; this parameter is assumed to increase linearly with temperature

$$g(\vartheta) = g_1 + g_2\,\vartheta \quad \text{for} \quad \vartheta < \vartheta_g. \tag{3.80}$$

In the evolution equation (3.69) the material parameters are h_b and S_b^*. We take h_b to be a temperature indepedent constant, while the saturation value S_b^* is taken to decrease linearly with temperature, with S_b^* vanishing above ϑ_g:

$$S_b^*(\vartheta) = l_1 - l_2\vartheta \quad \text{for} \quad \vartheta < \vartheta_g, \tag{3.81}$$

with l_1 and l_2 constant.

In the evolution equation (3.106), the only material parameter is γ; we take this to be temperature independent.

Temperature dependence of μ and I_m:

For the two material parameters μ and I_m in (3.20), experimental results indicate that the rubbery shear modulus μ decreases with increasing temperature, and the parameter I_m, which is related to limited chain extensibility, is approximately constant. The empirical function chosen to fit the experimentally-observed temperature dependence of μ is

$$\mu(\vartheta) = \mu_0 - N(\vartheta - \vartheta_g) \quad \text{for} \quad \vartheta < \vartheta_g, \tag{3.82}$$

where μ_0 and N are constants.

Temperature dependence of specific heat c and thermal conductivity κ:

For temperatures below ϑ_g, the specific heat c and the thermal conductivity κ are assumed to have the following empirical temperature dependencies (cf., e.g. Van Krevelen, 1990; Bicerano, 1993):

$$c(\vartheta) = c_0 - c_1(\vartheta - \vartheta_g) \quad \text{for} \quad \vartheta < \vartheta_g, \tag{3.83}$$

$$\kappa(\vartheta) = \kappa_0 \left(\frac{\vartheta}{\vartheta_g}\right)^{\kappa_1} \quad \text{for} \quad \vartheta < \vartheta_g. \tag{3.84}$$

3.4 Summary of the constitutive model

In this section, we summarize the specialized form of our thermo-mechanically coupled large-deformation theory for temperatures below ϑ_g.

3.4.1 Free energy

We consider the free energy to have a separable form as

$$\psi_{\mathrm{R}} = \psi^{e\,(1)} + \psi^{p\,(1)} + \psi^{(2)}. \tag{3.85}$$

With

$$\mathbf{U}^e = \sum_{i=1}^{3} \lambda_i^e \, \mathbf{r}_i^e \otimes \mathbf{r}_i^e, \tag{3.86}$$

denoting the spectral representation of $\mathbf{U}^e$, and with

$$\mathbf{E}^e = \sum_{i=1}^{3} E_i^e \, \mathbf{r}_i^e \otimes \mathbf{r}_i^e, \qquad E_i^e = \ln \lambda_i^e, \tag{3.87}$$

denoting an elastic logarithmic strain measure, we adopt the following special form for the free energy $\psi^{e\,(1)}$:

$$\psi^{e\,(1)} = G|\mathbf{E}^e|^2 + \tfrac{1}{2}(K - \frac{2}{3}G)(\mathrm{tr}\,\mathbf{E}^e)^2 - (\vartheta - \vartheta_0)(3\,K\,\alpha)(\mathrm{tr}\,\mathbf{E}^e) + \tilde{f}(\vartheta), \tag{3.88}$$

where $\tilde{f}(\vartheta)$ is an entropic contribution to the free energy related to the temperature-dependent specific heat of the material. The temperature-dependent parameters

$$G(\vartheta) > 0, \quad K(\vartheta) > 0, \quad \alpha(\vartheta) > 0, \tag{3.89}$$

are the shear modulus, bulk modulus, and coefficient of thermal expansion, respectively, and ϑ_0 is a reference temperature.

Further, with

$$\mathbf{A} = \sum_{i=1}^{3} a_i\,\mathbf{l}_i \otimes \mathbf{l}_i, \tag{3.90}$$

denoting the spectral representation of $\mathbf{A}$, we adopt a free energy $\psi^{p\,(1)}$ of the form

$$\psi^{(p)} = \frac{1}{4}B\,\left[(\ln a_1)^2 + (\ln a_2)^2 + (\ln a_3)^2\right], \tag{3.91}$$

where the positive-valued temperature-dependent parameter

$$B(\vartheta) \geq 0, \tag{3.92}$$

is a back-stress modulus.

Next, with

$$I_1 \stackrel{\text{def}}{=} \mathrm{tr}\,\mathbf{C}_{\text{dis}} \tag{3.93}$$

denoting the first principal invariant of $\mathbf{C}_{\text{dis}}$. We adopt the following special form for free energy $\psi^{(2)}$

$$\psi^{(2)} = -\tfrac{1}{2}\mu\,I_m\,\ln\Big(1 - \frac{I_1 - 3}{I_m}\Big), \tag{3.94}$$

where

$$\mu(\vartheta) > 0, \qquad I_m(\vartheta) > 3 \tag{3.95}$$

are two temperature-dependent material constants. In particular, μ represents the ground state rubbery shear modulus of the material, and I_m represents the upper limit of $(I_1 - 3)$, associated with limited chain extensibility.

3.4.2 Stress

Corresponding to the special free energy functions considered above, the Cauchy stress is given by

$$\mathbf{T} = \mathbf{T}^{(1)} + \mathbf{T}^{(2)}, \tag{3.96}$$

with

$$\mathbf{T}^{(1)} = J^{-1}\mathbf{R}^e\mathbf{M}^e\mathbf{R}^{e\top}, \tag{3.97}$$

where

$$\mathbf{M}^e = 2G\mathbf{E}^e_0 + K\,(\mathrm{tr}\,\mathbf{E}^e)\mathbf{1} - 3K\alpha(\vartheta - \vartheta_0)\mathbf{1}, \tag{3.98}$$

is the Mandel stress. The symmetric and deviatoric back-stress is defined by

$$\mathbf{M}_{\text{back}} = B\ln\mathbf{A}, \tag{3.99}$$

and the driving stress for plastic flow is the effective stress given by

$$(\mathbf{M}^e_{\text{eff}})_0 = \mathbf{M}^e_0 - \mathbf{M}_{\text{back}}. \tag{3.100}$$

The corresponding *equivalent shear stress* and *mean normal pressure* are given by

$$\bar{\tau} \stackrel{\text{def}}{=} \frac{1}{\sqrt{2}}\,|(\mathbf{M}^e_{\text{eff}})_0|, \quad \text{and} \quad \bar{p} \stackrel{\text{def}}{=} -\frac{1}{3}\mathrm{tr}\,\mathbf{M}^e, \tag{3.101}$$

respectively.

Also,

$$\mathbf{T}^{(2)} = J^{-1}\,\mu\left(1 - \frac{I_1 - 3}{I_m}\right)^{-1}(\mathbf{B}_{\text{dis}})_0. \tag{3.102}$$

3.4.3 Internal variables

The internal variables of the theory

$$\varphi \geq 0, \qquad S_a \geq 0, \qquad S_b \geq 0,$$

represent aspects of the intermolecular shear resistance to plastic flow. The parameter φ is a dimensionless order-parameter representing a local measure of disorder of the polymeric glass; S_a and S_b have dimensions of stress and, respectively, represent aspects of a transient shear resistance accompanying microstructural disordering, and aspects of increased shear resistance to plastic flow as the chains are pulled taut between entanglements at large strains.

3.4.4 Flow rule

The evolution equation for $\mathbf{F}^p$ is

$$\left.\begin{aligned}
&\dot{\mathbf{F}}^p = \mathbf{D}^p\,\mathbf{F}^p, \qquad \mathbf{F}^p(\mathbf{X},0) = \mathbf{1},\\
&\mathbf{D}^p = \nu^p\left(\frac{(\mathbf{M}^e_{\text{eff}})_0}{2\,\bar{\tau}}\right),\\
&\tau_{\text{e}} = \bar{\tau} - (S_a + S_b + \alpha_p \bar{p}),\\
&\nu^p = \begin{cases} 0 & \text{if} \quad \tau_{\text{e}} \le 0,\\ \nu_0\,\exp\left\{-\dfrac{Q}{k_B\,\vartheta}\right\}\left[\sinh\left(\dfrac{\tau_{\text{e}} V}{2k_B\vartheta}\right)\right]^{1/m} & \text{if} \quad \tau_{\text{e}} > 0, \end{cases}
\end{aligned}\right\} \tag{3.103}$$

where τ_{e} denotes a *net shear stress for thermally-activated flow*; α_p is a pressure-sensitivity parameter; ν_0 is a *pre-exponential factor* with units of 1/time; Q is an *activation energy*; k_B is Boltzmann's constant; V is an *activation volume*; and m is a *strain rate sensitivity parameter.*

3.4.5 Evolution equations for the internal variables

The internal variables S_a and φ are taken to obey the coupled evolution equations:

$$\left.\begin{aligned}
&\dot{S}_a = h_a\,(S_a^* - S_a)\,\nu^p, \quad \text{with} \quad S_a^* = b\,(\varphi^* - \varphi)\,, \quad \text{and} \quad S_a(\mathbf{X},0) = S_{a0};\\
&\text{and} \quad \dot{\varphi} = g\,(\varphi^* - \varphi)\,\nu^p, \quad \text{with} \quad \varphi(\mathbf{X},0) = \varphi_0,\\
&\text{where} \quad \varphi^* = \hat{\varphi}^*(\nu^p,\vartheta).
\end{aligned}\right\} \tag{3.104}$$

The evolution of S_b is taken to be governed by

$$\dot{S}_b = h_b\,(\bar{\lambda} - 1)\,(S_b^* - S_b)\,\nu^p, \quad \text{with} \quad S_b(\mathbf{X},0) = S_{b0} \ge 0, \tag{3.105}$$

where h_b is a constant and and $S_b^*(\vartheta)$ is taken to be temperature dependent.

Also, the evolution equation for $\mathbf{A}$ is taken as

$$\dot{\mathbf{A}} = \mathbf{D}^p\mathbf{A} + \mathbf{A}\mathbf{D}^p - \gamma\,\mathbf{A}\,\ln\mathbf{A}\,\nu^p, \quad \text{with} \quad \mathbf{A}(\mathbf{X},0) = \mathbf{1}, \tag{3.106}$$

where $\gamma \ge 0$ is a constitutive parameter which governs the dynamic recovery of $\mathbf{A}$.

3.4.6 Partial differential equation for temperature

$$c\dot{\vartheta} = -\text{Div}\,\mathbf{q}_{\text{R}} + q_{\text{R}} + \omega\left(\bar{\tau} + \frac{1}{2}\,B\,\gamma\,|\ln\mathbf{A}|^2\right)\nu^p, \qquad \text{with} \qquad c = \hat{c}(\vartheta). \tag{3.107}$$

3.5 Fit of the stress-strain curves and material parameters for Zeonex-690R, PC, and PMMA

We have implemented our thermo-mechanically-coupled constitutive model by writing a user material subroutine for the finite element program ABAQUS/Explicit (2009). The material parameters appearing in the model were calibrated by fitting the experimental stress-strain data for Zeonex-690R, PC and PMMA. The data for PMMA was obtained from Ames (2007) while the compression experiments on PC were performed by our colleague Shawn A. Chester. A one-dimensional version of the model is detailed in the Appendix A. The material parameters were calibrated with the help of a MATLAB implementation of the one-dimensional model, as well as three-dimensional finite element simulations using a single element. Under certain circumstances, when it became necessary to account for heat generation and thermal conduction in the simple compression experiments,[14] fully thermo-mechanically-coupled multi-element simulations were required (cf. Ames, 2007). A heuristic material parameter calibration procedure for our model is described in the Appendix A. The material parameters for Zeonex-690R, PC and PMMA determined by using this procedure are listed in Table 3.1.

The graphical fit of the constitutive model to the experimental stress-strain curves for Zeonex-690R at various temperatures ranging from 25 °C to 130 °C and strain rates ranging from 3×10^{-4} to $3 \times 10^{-1}\,\mathrm{s}^{-1}$ is shown in Fig. 3-4.

The fit of the constitutive model to experimental stress-strain curves for PC at various temperatures ranging from 25 °C to 130 °C and strain rates ranging from 10^{-3} to $10^{-1}\,\mathrm{s}^{-1}$ is shown in Fig. 3-5.

The fit of the model to the high strain rate experimental stress-strain data from Garg et al. (2008) for PC at rates of $0.5\,\mathrm{s}^{-1}$ and $3400\,\mathrm{s}^{-1}$, at an initial temperature of 25 °C, is shown in Fig. 3-6a.[15] The corresponding rise in the surface temperature of the compression specimens, as measured by Garg et al., and that predicted by the model are shown in Fig. 3-6b.

Finally, Fig. 3-7 shows the fit of the constitutive model to the experimental stress-strain curves for PMMA at various temperatures ranging from 25 °C to 100 °C and strain rates ranging from 3×10^{-4} to $10^{-1}\,\mathrm{s}^{-1}$.

For all three amorphous polymers (Zeonex-690R, PC and PMMA), our continuum-mechanical, thermodynamically-consistent, large deformation constitutive model performs acceptably in reproducing the following major features of the macroscopic stress-strain response of these materials: (a) the strain rate and temperature dependent yield strength; (b) the transient yield-peak and strain-softening which occurs due to deformation-induced disordering; (c) the subsequent rapid strain-hardening due to alignment of the polymer chains at large strains; (d) the unloading response at large strains; and (e) the temperature rise due to plastic-dissipation and the limited time for heat-conduction for the compression experiments performed at strain rates $\gtrapprox 0.01\,\mathrm{s}^{-1}$. Of particular note is the feature of the constitutive

[14] Typically to fit the experimental data at a strain rate of $0.01\ \mathrm{s}^{-1}$.

[15] Also see Bjerke et al. (2002) who report on temperature rise measurements in high rate experiments on PC.

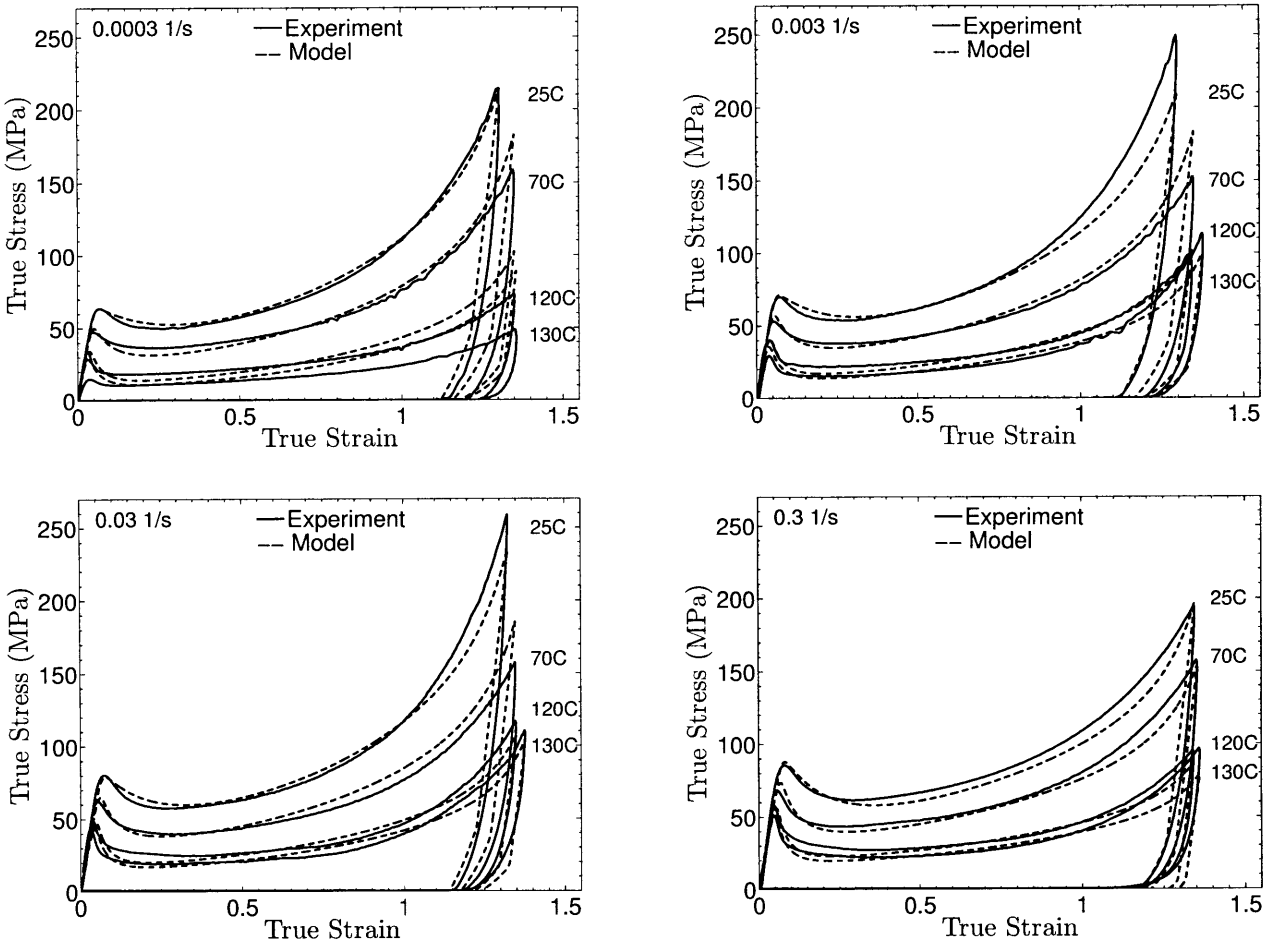

Figure 3-4: Fit of the constitutive model to the experimental stress-strain curves for Zeonex-690R at various temperatures ranging from 25 °C to 130 °C, and strain rates ranging from 3×10^{-4} to 3×10^{-1} s^{-1}. The experimental data is plotted as solid lines, while the fit is shown as dashed lines.

model to acceptably capture the deformation response of PC over a large range of strain rates:[16] from 10^{-3} to $3.4 \times 10^{3}\,s^{-1}$.

[16]High rate data for Zeonex-690R is not currently available. Split-Hopkinson-pressure-bar high rate compression experiments for PMMA have been conducted by Mulliken and Boyce (2006), but the data is unreliable because the material crazes after relatively small strains.

Table 3.1: Material parameters for Zeonex-690R, PC and PMMA

Parameter	Zeonex-690R	PC	PMMA
ϑ_g (K)	408	418	388
ρ (kg m^{-3})	1010	1200	1200
α (K^{-1})	7×10^{-5}	6.5×10^{-5}	7×10^{-5}
G_0 (MPa)	482	638	296
M (MPa K^{-1})	0.16	0.74	10
ν_{poi}	0.40	0.37	0.35
X (MPa K^{-1})	0.7	1.5	9.4
γ	6.92	26.0	34.6
α_p	0.116	0.116	0.2
ν_0 (s^{-1})	3.2×10^{11}	2.1×10^{16}	2×10^{16}
m	0.16	0.08	0.218
Q (J)	1.81×10^{-19}	1.46×10^{-19}	1.81×10^{-19}
V (m^3)	1.97×10^{-27}	2.95×10^{-28}	3.655×10^{-28}
S_{a0} (MPa)	0	0	0
h_a	173	58	70
b (MPa)	5850	5850	5850
g_1	-16.17	-5.66	-4.92
g_2 (K^{-1})	0.0693	0.0381	0.0318
φ_0	0	0	0
z	0.0055	0.0058	0.01
r	0.24	0.2	0.62
s	0.042	0.0	0.052
ν_r (s^{-1})	5.2×10^{-4}	5.2×10^{-4}	5.2×10^{-4}
n (K)	1.6	0.5	1.0
S_{b0} (MPa)	0	0	0
h_b	3.6	0.12	0
l_1 (MPa)	75	300	0
l_2 (MPa K^{-1})	0.16	0.35	0
μ_0 (MPa)	3.0	4.0	0.2
N (MPa K^{-1})	6.2×10^{-2}	11.4×10^{-2}	20.0×10^{-2}
I_m	6.2	7.8	5.5
c_0 (J kg^{-1} K^{-1})	2120	1630	1710
c_1 (J kg^{-1} K^{-2})	8	3.6	4.1
κ_0 (Watt m^{-1} K^{-1})	0.467	0.187	0.190
κ_1	0.46	0.22	0.22
ω	0.8	0.8	0.65

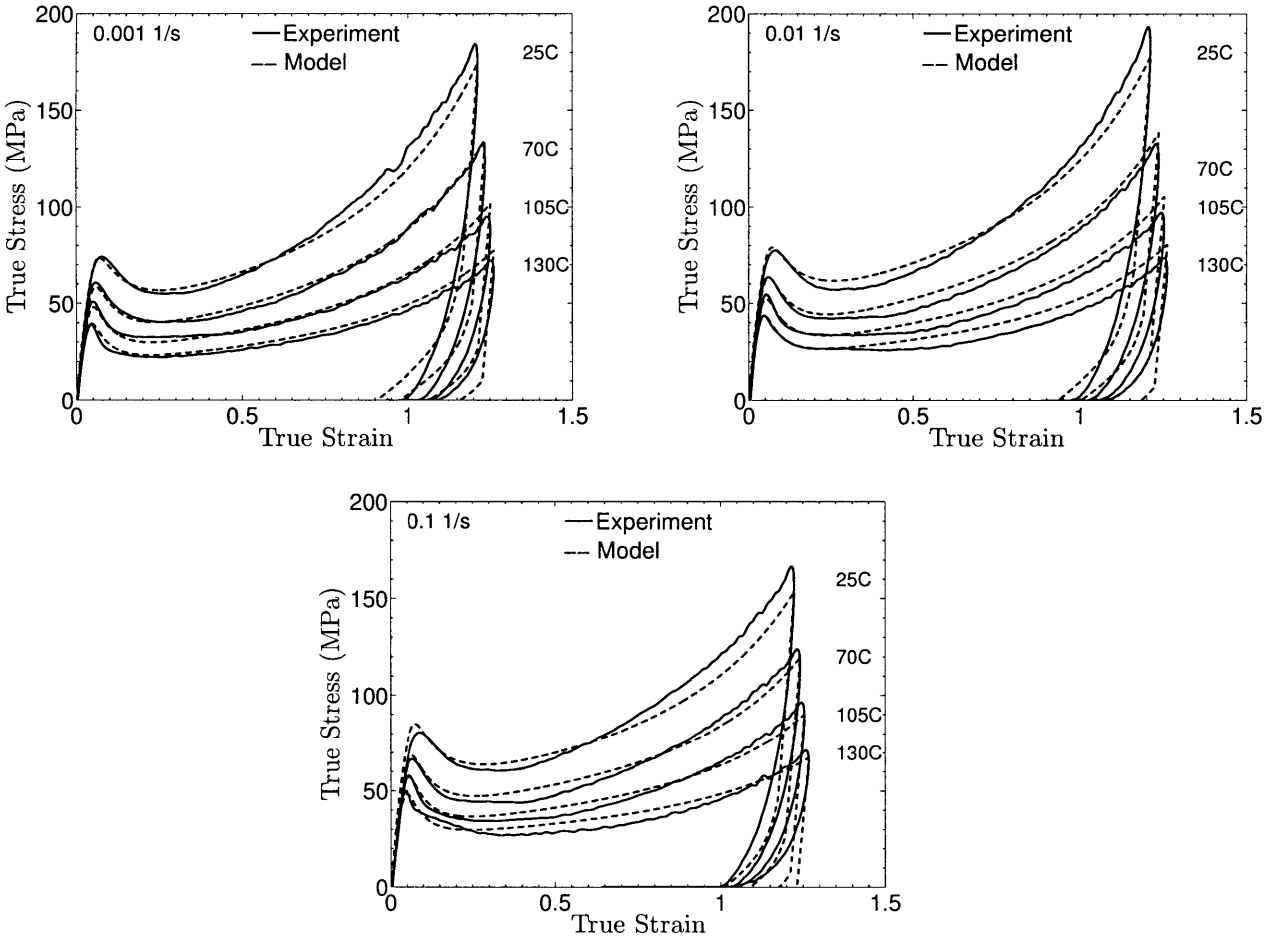

Figure 3-5: Fit of the constitutive model to the experimental stress-strain curves for PC at various temperatures ranging from 25 °C to 130 °C, and strain rates ranging from 10^{-3} to 10^{-1} s^{-1}. The experimental data (courtesy Shawn A. Chester) is plotted as solid lines, while the fit is shown as dashed lines.

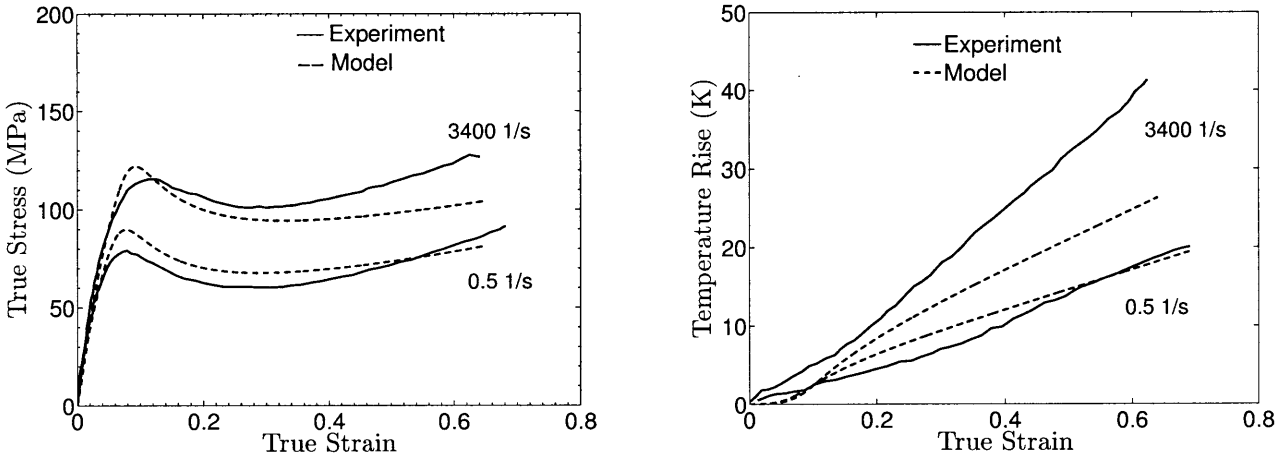

Figure 3-6: (a) Fit of the constitutive model to the high strain rate experimental stress-strain curves for PC at rates of 0.5 s^{-1} and 3400 s^{-1}, at an initial temperature of 25 °C. (b) The corresponding rise in the surface temperature of the compression specimens. The experimental data (from Garg et al., 2008) is plotted as solid lines, while the fit is shown as dashed lines.

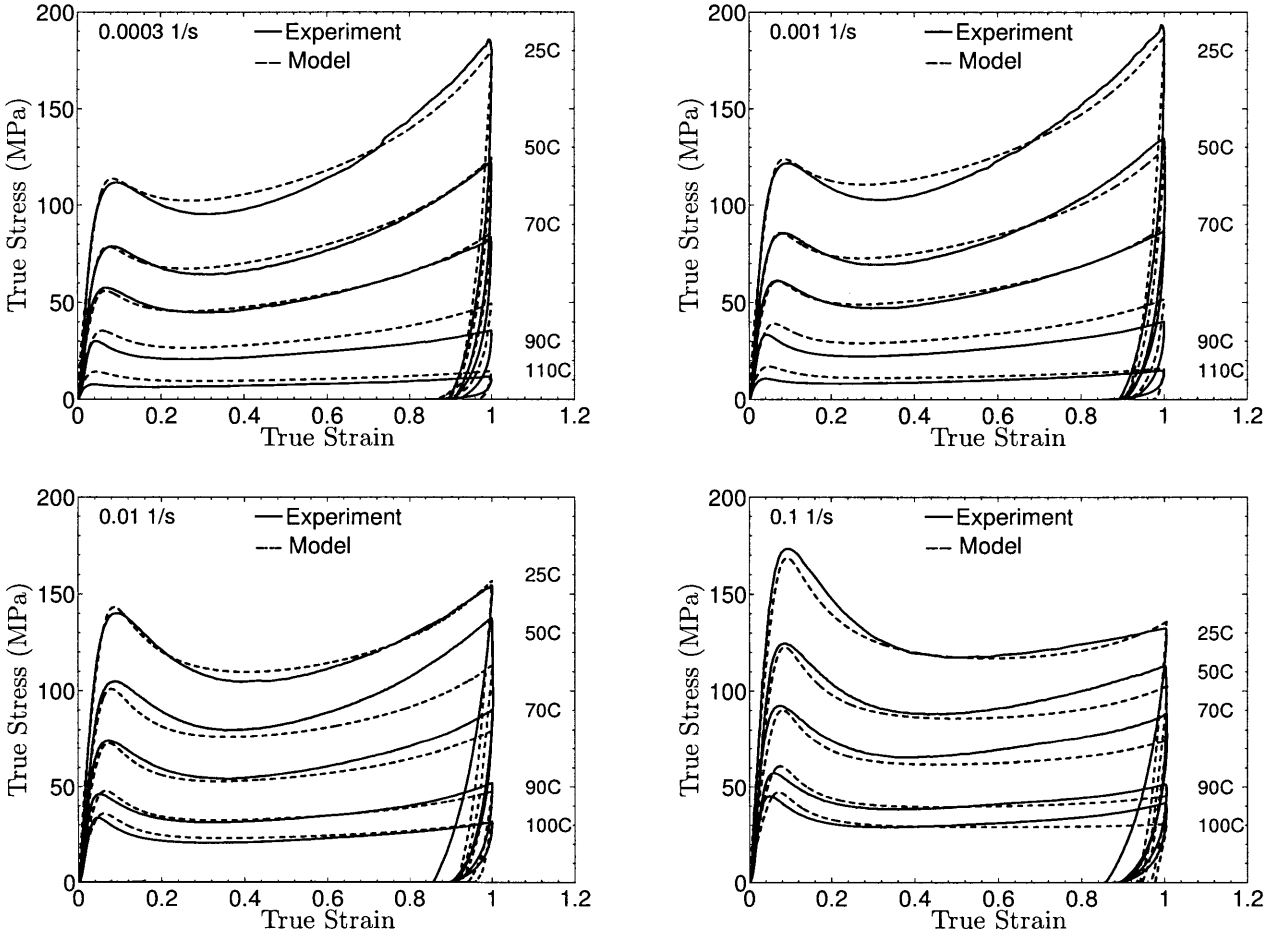

Figure 3-7: Fit of the constitutive model to the experimental stress-strain curves for PMMA at various temperatures ranging from 25 °C to 110 °C, and strain rates ranging from 3×10^{-4} to 10^{-1} s^{-1}. The experimental data (from Ames (2007)) is plotted as solid lines, while the fit is shown as dashed lines.

3.6 Validation experiments and simulations

In order to validate the predictive capabilities of our constitutive theory and its numerical implementation, in this section we show results of some non-homogeneous experiments (which were not used to determine the material parameters in our theory), and compare the results of some key macroscopic features of the experimental results against those from the corresponding numerical simulations. Our validation experiments have been performed on either Zeonex-690R or PC. The particular validation experiments considered below are: (i) isothermal fixed-end large-strain reversed-torsion on PC; (ii) macro-scale isothermal plane-strain cold- and hot-forming operations on PC; (iii) macro-scale isothermal, axisymmetric hot-forming operations on Zeonex-690R; (iv) a micro-scale hot-embossing of Zeonex-690R; and (v) high-speed normal-impact of a circular plate of PC with a spherical-tipped cylindrical projectile.

3.6.1 Fixed-end large-strain reversed-torsion on PC

The torsion of a solid circular bar is a seemingly simple deformation mode. However, when the large-strain torsion is conducted with axially traction-free ends, a measurable axial extension also develops; this fascinating and complex nonlinear phenomenon is known as the *Swift-effect.*[17] A complementary phenomenon is the development of an axial force when the ends of the bar are axially fixed during the large-strain torsion.

Free- or fixed-end large-strain torsion experiments provided simple yet effective means for assessing the validity of large-strain constitutive models for elastic-plastic materials.[18] Large-strain inelastic torsion of amorphous polymeric materials has been previously numerically studied by Wu and Van der Giessen (1993b). Here, for purposes of validating our constitutive theory, we study *fixed-end large-strain reversed torsion of a solid cylindrical specimen.* The torsion experiment was conducted at room temperature on a PC specimen with geometry shown in Fig. 5-10a. In the gage section, a torsion specimen has a diameter $D_0 = 31.75\,\text{mm}$, and a gage length of $L_0 = 8.89\,\text{mm}$. With ϕ denoting the angle of twist in radians, the shear-strain at the outer surface of the gage section of such a specimen is

$$\Gamma = \frac{\phi\, D_0}{2\, L_0}. \tag{3.108}$$

The reversed-cycle torsion experiment was performed on an Instron tension-torsion servo-hydraulic machine, equipped with precision-aligned hydraulic grips. The machine was programmed to fix the axial displacement, and twist the specimen by rotating the grips relative to each other at an angular velocity of ± 0.25 deg/sec, which corresponds to surface shear

[17] First studied by Swift (1947) for metals.

[18] For metallic materials it has been firmly established in recent years that these axial effects in large-strain torsion arise due to the development of crystallographic texture, and that the predictions of the axial effects during torsion are strongly dependent on the constitutive model used to predict such effects (cf., e.g., Bronkhorst et al., 1992).

strain rate of $\dot{\Gamma} = \pm 7.8 \times 10^{-3}\,\mathrm{s}^{-1}$ during the reversed-torsion experiment. The maximum surface shear strains achieved during the experiment, without initiating fracture, is $\Gamma \lessapprox \pm 1.4$.

For the corresponding finite element simulation, we have modeled only the gage section and the chamfered-section of the specimen leading into the gage section. The finite element mesh, consisting of 4,801 ABAQUS-C3D8R elements, is shown in Fig 5-10b. The deformed geometry at a surface shear strain of $\Gamma = 1.4$ is shown in Fig 5-10c. Note that for the specific geometry of the torsion specimen used here, the deformation is essentially confined to the gage-section of the specimen.

Fig. 5-10d shows an excellent agreement between the numerically-predicted and the experimentally-measured torque versus surface shear-strain response for both forward and reversed straining. Further, Fig. 5-10e shows the ability of our constitutive theory to capture the major trends of the induced axial-force versus the surface shear-strain response for both forward and reversed torsional straining. Although the precise magnitudes of the axial forces are not as well-predicted as the torque response, the prediction of the actual trends for the variation of the axial forces as the shear strain is cycled, is quite remarkable.

3.6.2 Plane-strain, cold- and hot-forging of PC

Channel-die, plane-strain, cold- and hot-forging experiments were performed on PC specimens. The plane-strain forming operation under consideration converts a cylindrical specimen with a circular cross-section into a specimen with a cross-section which is in the shape of a "cruciform". A schematic of a forging experiment is shown in Fig. 5-11. The PC specimens had an original diameter of 12.7 mm, and were 12.7 mm deep in the plane-strain direction, which is into the plane of the paper. The split-dies which impart the cruciform shape to the workpiece were made from hardened tool steel, and the interfaces between the workpiece and the dies were lubricated to minimize frictional effects. The forging experiments were carried out at 25 °C and 120 °C, at a constant die-closing velocity of 0.02 mm/s. The forging experiments at 25 °C were carried to three different die-displacement levels of 2.8 mm, 4.6 mm and 5.4 mm, while the experiment at 120 °C was only carried out to a final die-displacement of 5.4 mm.

For the finite element simulation of such a process, we make use of the symmetry of the geometry and only mesh one-quarter of the geometry, as shown in Fig. 5-12a. The quarter-circle of the workpiece cross-section is meshed with 976 ABAQUS-CPE4R elements, and the cruciform-die is modeled as a rigid surface. Since the physical experiment was well-lubricated, the contact between the die and the workpiece was modeled as frictionless.

Fig. 5-12b compares the numerically-predicted and the experimentally-measured, load-unload force versus displacement curves for the cruciform-forging processes at 25 °C and 120 °C. The agreement between the predicted and the measured force-displacement responses at 25 °C for die displacements of 2.8 mm, 4.6 mm, and 5.4 mm is very good, as is the agreement between the prediction and the experimental result for the experiment at 120 °C for a die displacement of 5.4 mm.

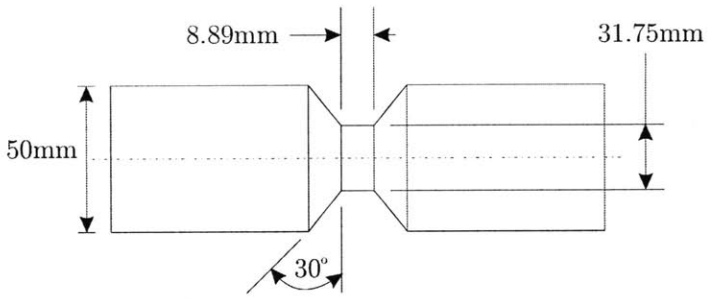

(a)

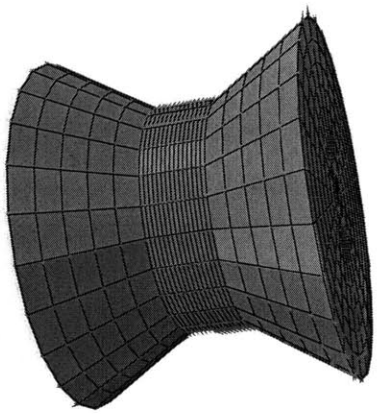

(b)

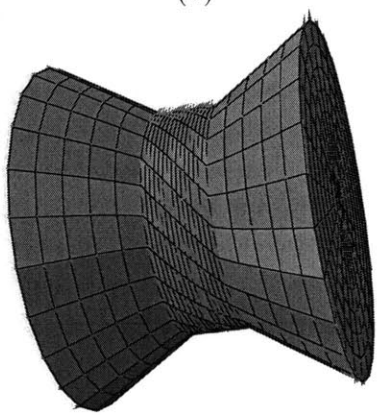

(c)

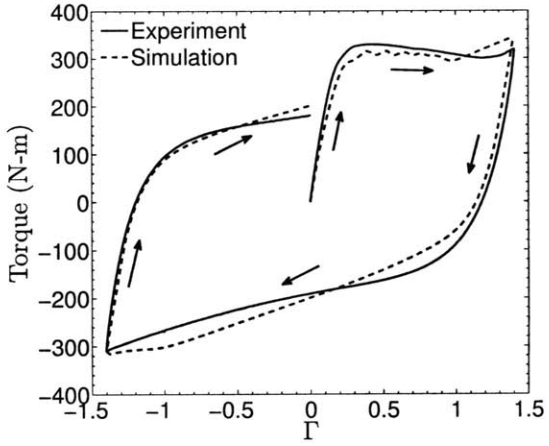

(d)

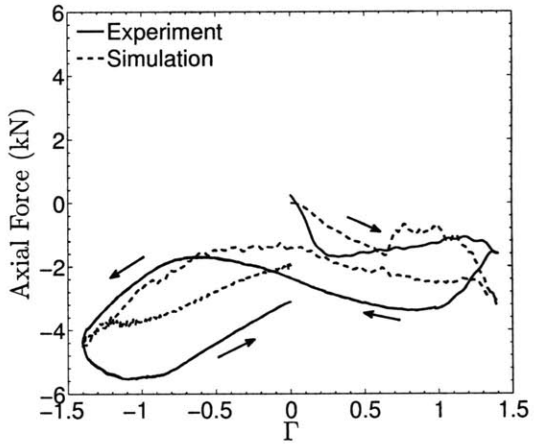

(e)

Figure 3-8: (a) Geometry of torsion specimen. (b) Undeformed finite element mesh for the torsion simulation. (c) Deformed finite element mesh at a surface shear strain of $\Gamma = 1.4$. (d) Torque versus surface shear-strain response for PC under reversed fixed-end torsion. (e) Axial-force versus surface shear-strain.

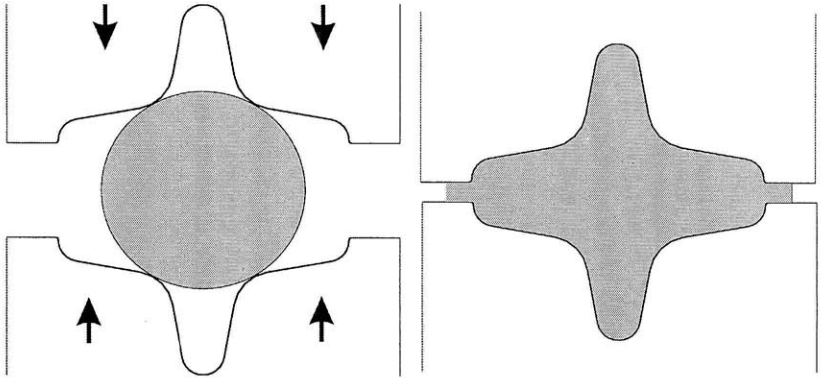

Figure 3-9: Schematic of the plane-strain cruciform-forging experiment.

After unloading, each forged specimen was sectioned, polished, and then photographed. Fig. 5-13a and Fig. 5-13b compare the numerically-predicted and the experimentally-measured deformed shapes after unloading the test specimens at 5.4 mm of die displacement for the forgings at 25 °C and 120 °C. The agreement between numerically-predicted and experimentally-measured deformed geometries is also quite good.

3.6.3 Axisymmetric, hot-forging of Zeonex-690R

Axisymmetric, hot-forging experiments were performed on Zeonex specimens. The axi-symmetric forming operation under consideration converts a cylindrical specimen with a circular cross-section into a specimen with a circular base, a bulged-middle, and a tapered neck. A schematic of a forging experiment is shown in Fig. 5-14. The Zeonex specimens had an original diameter of 10.16 mm, and were 10.16 mm tall. The split-dies which impart the particular shape to the workpiece were made from hardened tool steel, and (in contrast to the lubricated plane-strain forging experiments for PC) the interfaces between the Zeonex workpiece and the dies were *not lubricated*. The axi-symmetric forging experiments were carried out at 90 °C and 120 °C, at a constant die-closing velocity of 0.02 mm/s. The forging experiments at 90 °C were carried out to a final die-displacement of 4.5 mm, while the experiments at 120 °C were carried to two different die-displacement levels of 2 mm and 4.5 mm.

For the finite element simulation of such a process we make use of the axial-symmetry of the geometry, and mesh only a slice of the geometry, as shown in Fig. 5-15a. The workpiece was meshed with 802 ABAQUS-CAX4R elements, and the top and bottom forging dies were modeled as rigid surfaces; the axis of symmetry is labelled in Fig. 5-15a. Since no lubricant was used in the physical experiment, the contact between the die and the workpiece was modeled as "rough" with full-sticking.

Fig. 5-15b compares the numerically-predicted and the experimentally-measured, load-unload force versus displacement curves for the axisymmetric-forging processes at 90 °C and 120 °C. The fact that numerically-predicted loads are slightly higher than the experimentally-

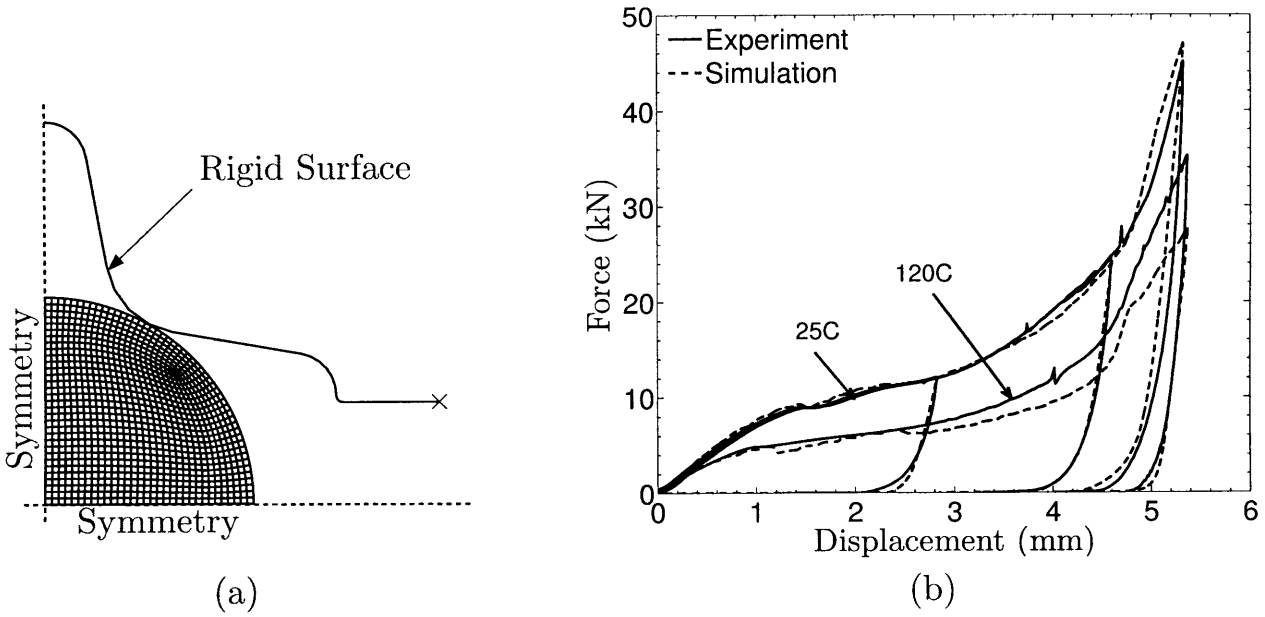

Figure 3-10: (a) Quarter-symmetry finite element mesh for the workpiece and the rigid surface used in the plane-strain cruciform-forging simulations for PC. (b) Comparison of numerically-predicted and experimentally-measured force-displacement curves for forgings at 25 °C and 120 °C.

measured loads is to be expected because the numerical simulation assumed perfect-sticking, while in the physical experiment the frictional conditions are less severe. Given the uncertainty in the precise frictional conditions at the interface between the dies and the workpiece in the physical experiment, the agreement between the predicted and the measured load-displacement responses at both temperatures is quite reasonable.

After unloading, the specimens that were forged at 120 °C to die-displacement levels of 2 mm and 4.5 mm. were photographed. Fig. 5-16 compares the numerically-predicted and the experimentally-measured deformed shapes after die-displacements of 2 mm and 4.5 mm. The numerically-predicted shapes are quite similar to those which were experimentally-measured.

3.6.4 Micro-scale hot-embossing of Zeonex-690R

As a simple example of a micro-hot-embossing process, we consider the embossing of a series of long channels into a Zeonex-690R substrate. The pattern consists of channels which are 55 μm wide, 43.5 μm deep, and are spaced 92 μm apart. To carry out the micro-hot-embossing in the polymer, a Zr-based metallic-glass tool with a negative of the desired channel pattern was manufactured by micro-scale thermoplastic forming (Henann and Anand, 2008). Fig. A-1a shows a schematic of the pattern of the tool, and Fig. A-1b shows a SEM photomicrograph of a portion of the metallic glass tool.

The hot-embossing experiment was carried out on a servo-hydraulic Instron testing machine equipped with heated compression platens. The details of our micro-hot-embossing set-up are provided in Appendix D. A 25.4 mm square and 2 mm thick sheet of Zeonex,

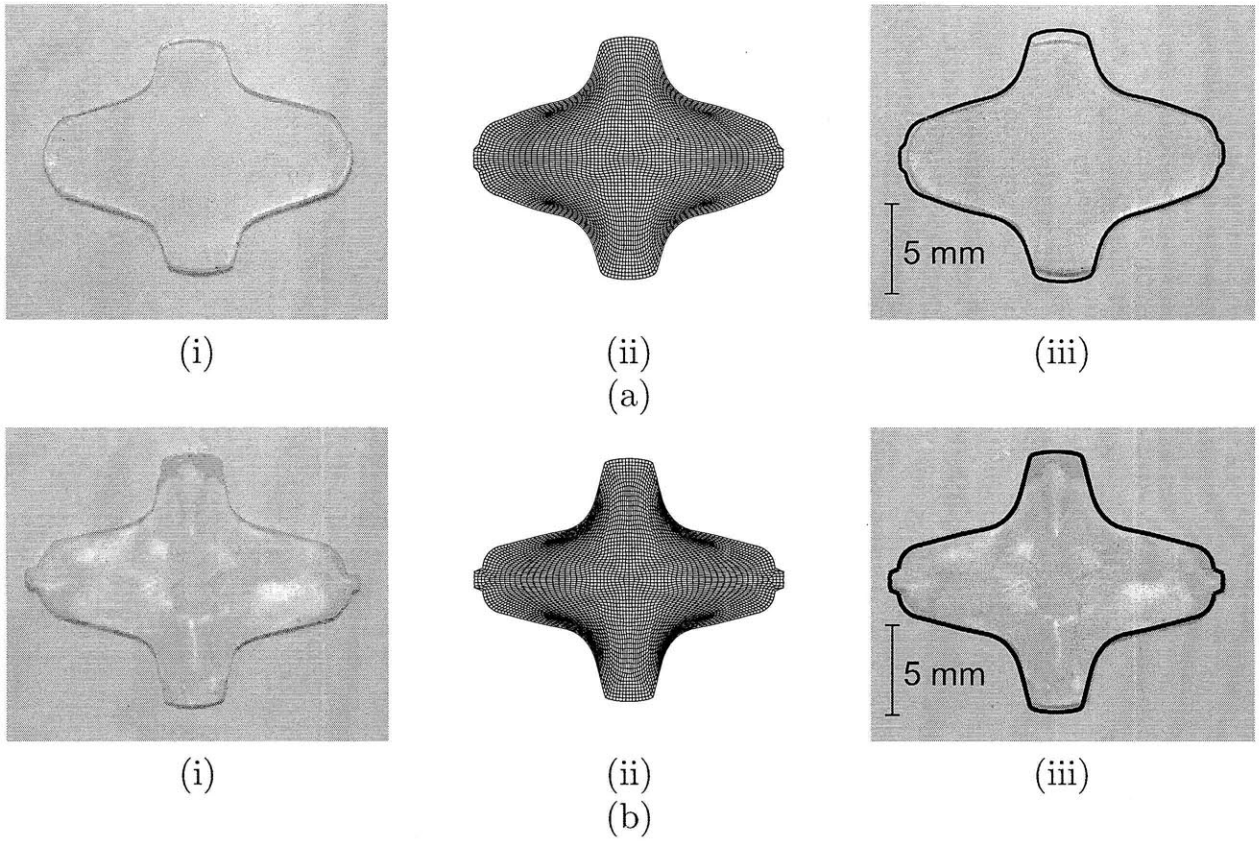

Figure 3-11: Comparison of numerically-predicted and experimentally-measured unloaded deformed shapes for the cruciform-forging. (a) For a forging at 25 °C at a die-displacement of 5.4 mm. (b) For a forging at 120 °C at a die-displacement of 5.4 mm. (i) experimental macrographs; (ii) deformed meshes; and (iii) outlines of simulated shapes (thick black lines) superimposed over the experimentally-measured shapes.

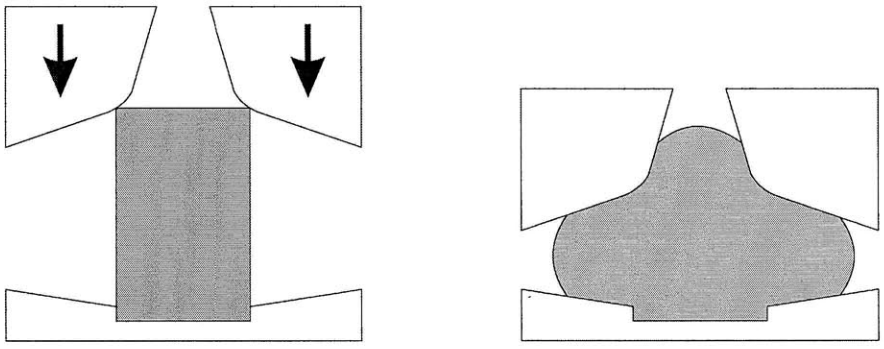

Figure 3-12: Schematic of the axi-symmetric forging experiment.

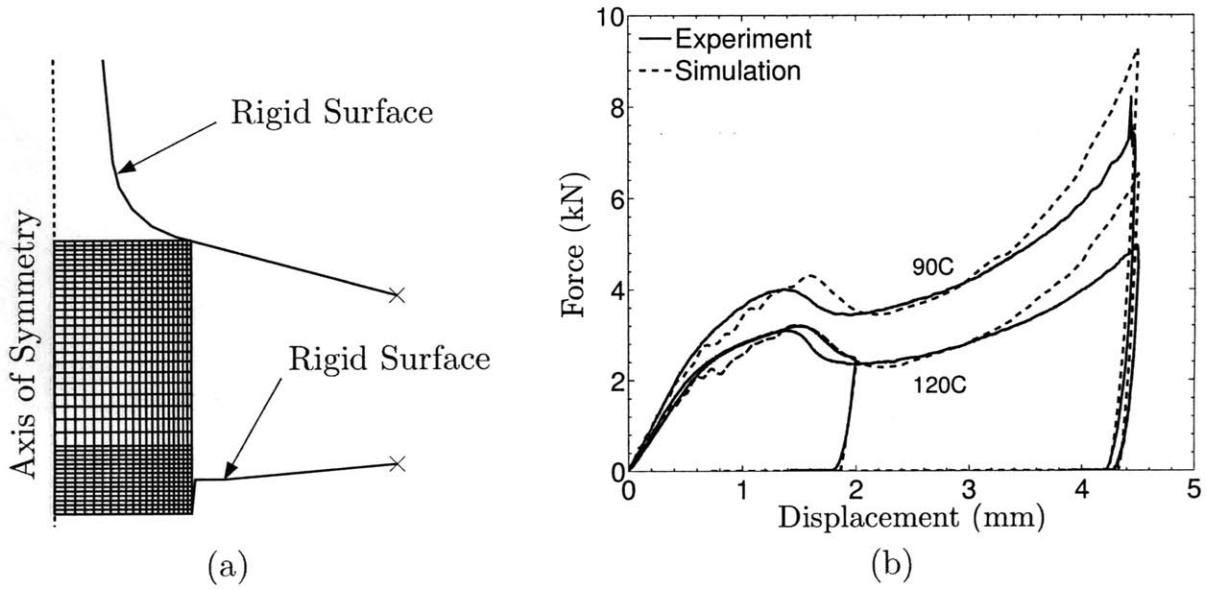

Figure 3-13: (a) Half-symmetry finite element mesh for the workpiece and the rigid surfaces used in the axi-symmetric cruciform-forging simulations for Zeonex. (b) Comparison of numerically-predicted and experimentally-measured force-displacement curves for forgings at 90 °C and 120 °C.

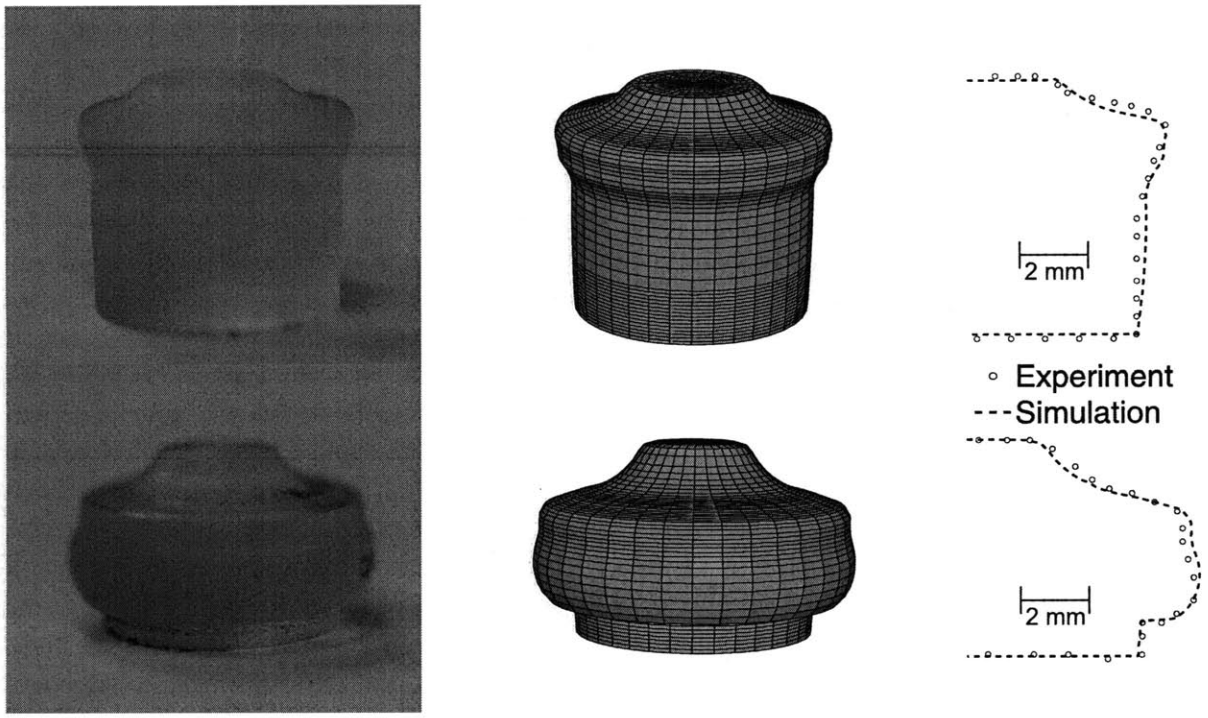

Figure 3-14: Comparison of numerically-predicted and experimentally-measured unloaded deformed shapes for the axi-symmetric forgings at 120 °C after die displacements of 2 mm (top) and 4.5 mm (bottom).

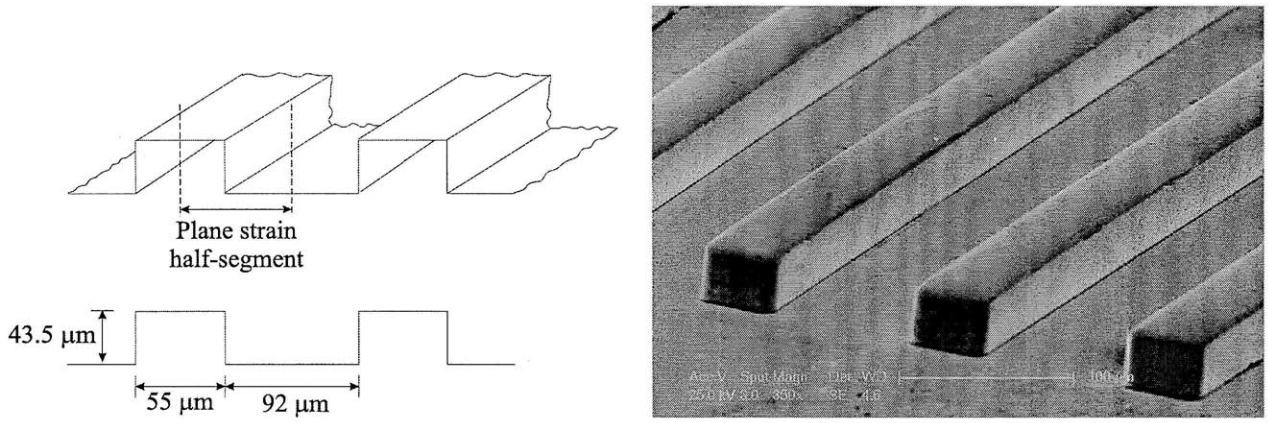

Figure 3-15: (a) Schematic of the plane-strain tool (not to scale), and (b) SEM micrograph of a portion of the metallic glass tool.

and a 11.7 mm square patterned metallic glass tool were aligned and placed between the heated compression platens. The embossing experiment was conducted under nominally isothermal conditions at a temperature of 130 °C in air. The load was ramped up to 13 kN to produce a nominal pressure of 95 MPa in 10 seconds, and held for 2 minutes before unloading, after which the tool was quickly removed from the substrate. The force-cycle for the micro-hot-embossing process is schematically shown in Fig. 4-17a.

Since the channels are long relative to their width, and there are a large number of them aligned in parallel, we employ a plane-strain idealization in our numerical simulation, and consider only a single half-segment, with suitable boundary conditions. Fig. 4-17b shows the finite element mesh. The Zeonex substrate is modeled using a mesh consisting of 849 ABAQUS-CPE4R plane strain elements, and the metallic glass tool is modeled using an appropriately shaped rigid surface. Contact between the substrate and tool was approximated as frictionless. The displacement boundary conditions on the portions AD and BC of the mesh boundary are $u_1 = 0$, while on the portion CD of the mesh, $u_1 = u_2 = 0$ are prescribed. The predicted embossed pattern in the Zeonex after hot-embossing is shown in Fig. 4-17c. The numerically-predicted pattern shown in Fig. 4-17c has been mirrored and repeated during post-processing to ease comparison with the corresponding experimental result, which is shown Fig. 4-17d. The final geometry of the embossed channels predicted by the simulations agrees well with the result from the micro-hot-embossing experiment. The simulation, Fig. 4-17c, predicts that at the embossing temperature of 130 °C and nominal pressure of 95 MPa, the micro-hot-embossing should result in channel heights which are the same as the depths in the embossing tool, but there is incomplete die-filling and the edges of the channels are rounded; this is also the result seen in the physical experiment, Fig. 4-17d.[19]

[19]In order to get complete die-filling, it would be ideal to conduct the hot-embossing at temperatures above the glass transition temperature of the polymer, a regime that is of considerable practical interest for the manufacture of microfluidic devices by micro-hot-embossing.

We further investigated the quality of the embossed features by using optical profilometry methods. Figure 4-17e compares representative cross-sections of the embossed features in the Zeonex (circles), against the numerically-predicted channel profile (dashed line). The depth of the embossed features closely match with the numerical prediction; note that the optical profilometry method that we used to measure the channel profile is not capable of providing data for the sharp vertical features.

3.6.5 Normal impact of a clamped circular plate of PC by a spherical-tipped cylindrical projectile

As a final validation experiment — one which is not quasi-static, conducted at high strain rates, and is not isothermal — we consider the normal impact of a circular plate of PC with a spherical-tipped cylindrical projectile. Experiments of this type are of substantial practical interest in the design and testing of *transparent lightweight armor*.

The circular plate specimen of PC, 203.2 mm in diameter and 5.334 mm thick (with bolt-holes for clamping), was fabricated using a water-jet machine. The PC plate was clamped (using steel clamping plates and bolts) in an Instron Dynatup testing machine, and subjected to normal impact by a spherical-tipped cylindrical steel projectile with a mass of 80 kg at an impact velocity of 3.6 m/s. The impact conditions were specially chosen such that the plate only deforms plastically at the high rates, and does not fracture. The force versus time was recorded during the impact, and the impacted plate specimen was recovered.

For the finite element simulation we make use of the axial-symmetry of the geometry, and mesh only a slice of the geometry, as shown in Fig. 4-18. The PC plate is modeled using 304 ABAQUS-CAX4RT reduced-integration, thermo-mechanically-coupled, axisymmetric elements. The actual clamping boundary conditions are modeled by rigid surfaces representing the clamping plates, but instead of individual clamping bolts, the surface interaction between the rigid surfaces representing the clamping plates and the PC plate is modeled using a high Coulomb friction coefficient of 0.75; thus the polymer is not completely constrained to remain in contact with the clamping surfaces. The spherical-tipped cylindrical steel projectile is modeled as a rigid body with a mass of 80 kg, and given an initial velocity of 3.6 m/s towards the plate specimen. The projectile/polymer interface is modeled as frictionless.

Fig. 4-19a shows an image of a sectioned one-half the specimen after the experiment, while Fig. 4-19b shows the corresponding numerically-predicted result. The predicted deformed profile of the polycarbonate plate is qualitatively very similar to that in the experiment. More quantitatively, Fig. 4-19c shows a comparison of the traced surface profile of the specimen after impact with the numerically calculated profile — the two compare very favorably. Fig. 4-20a shows the excellent agreement between the experimentally measured, and the simulated force-time response on the projectile — up to the time for which the experimental data was available. Lastly, Fig. 4-20b shows the temperature distribution in the plate 25 ms after the impact, when the projectile has rebounded and lost contact with the plate. As

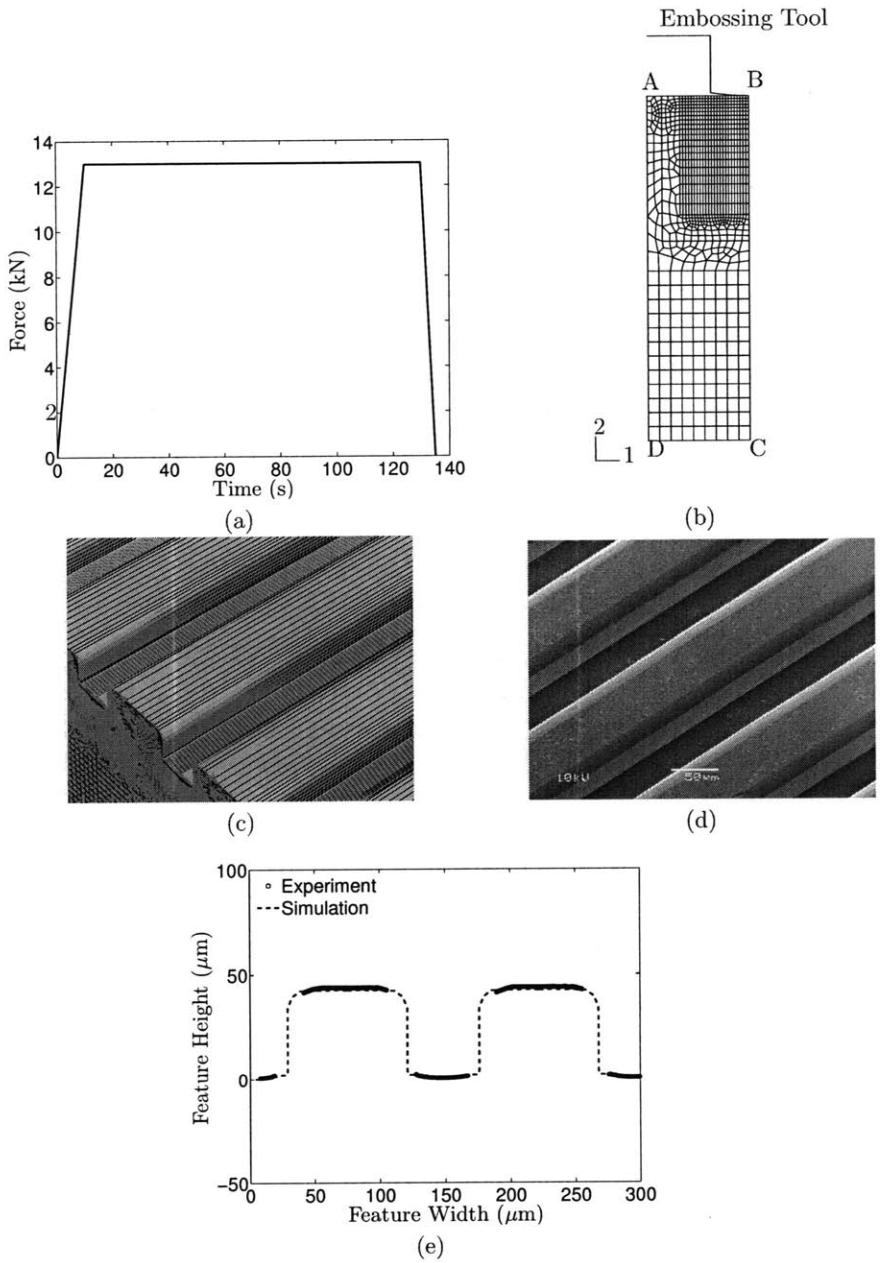

Figure 3-16: (a) The micro-hot-embossing was carried out at 130 °C under load control; the process force history is shown. (b) Finite element mesh for a plane strain simulation showing the meshed substrate and the tool modeled as a rigid surface. The displacement boundary conditions on the portions AD and BC of the mesh boundary are $u_1 = 0$, while on the portion CD of the mesh, $u_1 = u_2 = 0$ are prescribed. (c) Predicted deformed shape. (d) SEM image of the micro-channels embossed in Zeonex-690R. (e) Comparison of numerically-predicted channel profile (dashed line) with corresponding profilometer measurements.

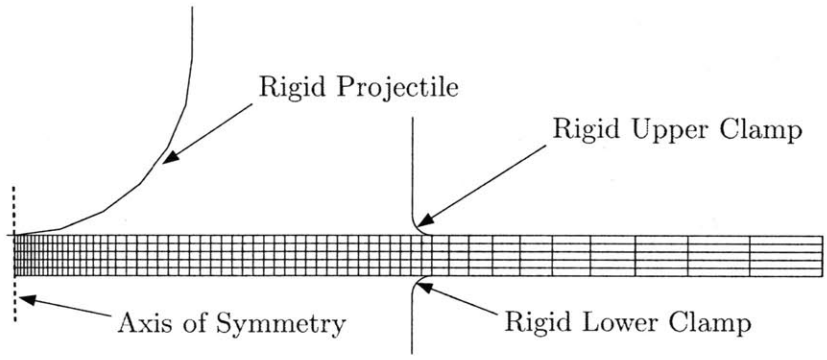

Figure 3-17: Finite element mesh used in the thermo-mechanically-coupled analysis of the plate impact experiment.

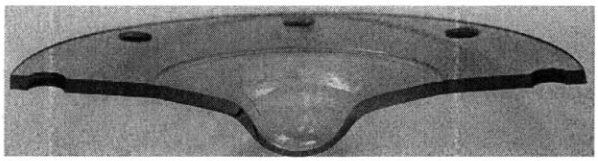

(a)

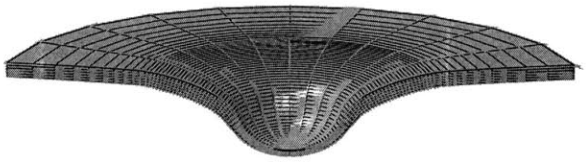

(b)

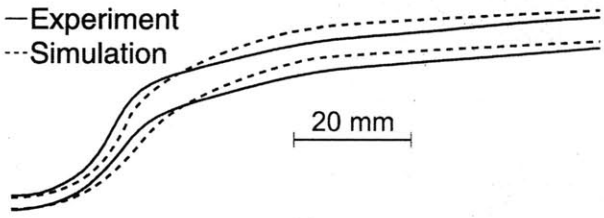

(c)

Figure 3-18: (a) Final shape of the impacted plate from the experiment. (b) Corresponding numerical prediction. (c) Comparison of traced surface profile of the specimen after impact with the numerically-calculated profile.

expected, the temperature rise is largest under the tip of the projectile, where it increases by approximately 45 K, from 298 K to 343 K.

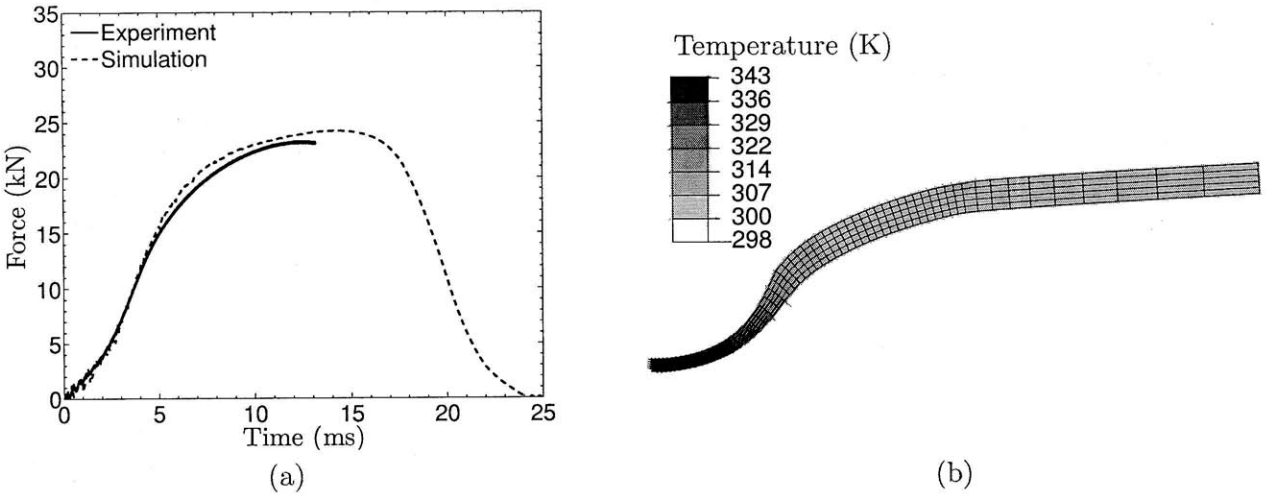

Figure 3-19: (a) Comparison of numerically-predicted and experimentally-measured reaction force versus time response for the projectile. (b) Contours of temperature in the deformed plate immediately after the impact.

Chapter 4

A constitutive theory for amorphous polymers in a temperature range which spans their glass transition

4.1 Introduction

Strongly temperature- and rate-dependent elastic-viscoplastic nonliear behavior of amorphous polymers is not very well understood, and is modeled by existing constitutive theories with varying degrees of success. There is no generally agreed upon theory to model the large-deformation, thermo-mechanically-coupled, elastic-viscoplastic response of these materials in a temperature range which *spans their glass transition temperature*. Such a theory is crucial for the development of a numerical capability for the simulation and design of important polymer processing operations, and also for predicting the relationship between processing methods and the subsequent mechanical properties of polymeric products. There exists a major need to develop a thermo-mechanically-coupled theory which can model the glassy response as well as extends to a temperature range which includes temperatures above the glass transition temperature of these materials — a range extending to $\lessapprox 50\,^{\circ}\mathrm{C}$ above the ϑ_g of the material, where the material response still has some "solid"-like characteristics, and is not quite yet a viscoelastic fluid. Such a theory would be useful, for example, for modeling certain important polymer processing operations, such as micro-hot-embossing for the manufacture of microfluidic devices, hot-drawing of fibers and films, and thermoforming and blow-molding for manufacture of various thin-walled containers and bottles.

Constitutive theories aimed at this class of applications have been proposed by Boyce and co-workers (e.g., Boyce et al., 2000; Dupaix and Boyce, 2007), as well as Buckley and co-workers (e.g., Buckley and Jones, 1995; Dooling et al., 2002). Guided by the work of Boyce, Buckley and their co-workers, and our own constitutive theory presented in Chapter 3 for the mechanical behavior of polymers below ϑ_g, it is the purpose of this chapter to:

- Specialize the general framework presented in Chapter 2 to model the response of three representative amorphous polymeric materials — Zeonex-690R (a cyclo-olefin polymer), polycarbonate (PC), and poly(methyl methacrylate) (PMMA) — in a temperature range from room temperature to approximately 50 °C above the glass transition temperature of each material, in a strain rate range of $\approx 10^{-4}$ to $10^{-1}\,\mathrm{s}^{-1}$, and compressive true strains exceeding 100%. The constitutive theory for the response of Zeonex-690R, PC, and PMMA reported in this chapter, represents an *important extension* of our work in Chapter 3 on the response of these materials for temperatures *below* ϑ_g.

- Demonstrate that apart from its intrinsic theoretical importance from the viewpoint of mechanics and physics of materials, our new theory is useful for modeling important polymer processing operations, such as micro-hot-embossing for the manufacture of microfluidic devices, hot-forging of complex shapes and blow-molding of thin-walled semi-spherical shapes.

The plan of this chapter is as follows. In §4.2 we briefly describe our simple compression experiments on Zeonex-690R. In §4.3 we present the major constitutive and field equations of our specialized theory so that it is capable of reproducing the salient features of the experimentally-measured mechanical response of Zeonex-690R, PC and PMMA. In Appendix B, we describe in reasonable detail our method to calibrate the (numerous) material parameters/functions appearing in our constitutive theory. The quality of the fit of the specialized model to the experimentally-measured stress-strain curves is discussed in §4.4, where we show that the model reproduces the major features of the macroscopic response of these materials in a reasonably acceptable fashion.

Our thermo-mechanically-coupled constitutive theory was implemented by our colleague Shawn A. Chester by writing a user material subroutine for the finite element program ABAQUS/Standard (2009). In order to validate the predictive capabilities of our theory and its numerical implementation, we have performed the following validation experiments: (i) a plane-strain forging of PC at a temperature below ϑ_g, and another at a temperature above ϑ_g; (ii) blow-forming of thin-walled semi-spherical shapes of PC above ϑ_g; and (iii) micro-scale, hot-embossing of channels in Zeonex-690R above ϑ_g. In §4.5, by comparing the results from this suite of validation experiments of some key features, such as the experimentally-measured deformed shapes and the load-displacement curves, against corresponding results from numerical simulations, we show that our theory is capable of reasonably accurately reproducing the experimental results obtained in the validation experiments.

4.2 Simple compression experiments on Zeonex-690R

Following the procedure described in Chapter 3, we have conducted simple compression experiments on Zeonex-690R: (i) to large strains exceeding 130%, including *loading and unloading*; (ii) at a variety of strain rates in the range 3×10^{-4} to $3 \times 10^{-1}\,\mathrm{s}^{-1}$, achievable

in modern servo-hydraulic testing machines; and (iii) in a temperature range from room temperature to $\approx 40\,^{\circ}\mathrm{C}$ above the glass transition temperature of the material. The nominal glass transition temperatures of Zeonex-690R is $135\,^{\circ}\mathrm{C}$.

Fig. 4-1 shows true stress-strain curves[1] for Zeonex-690R at a strain-rate of $3 \times 10^{-4}\,\mathrm{s}^{-1}$ at temperatures ranging from $25\,^{\circ}\mathrm{C}$ through $160\,^{\circ}\mathrm{C}$. Fig. 4-2 shows true stress-strain curves at strain-rates of 3×10^{-2}, 3×10^{-2} and $3 \times 10^{-1}\,\mathrm{s}^{-1}$ at temperatures ranging from $25\,^{\circ}\mathrm{C}$ through $180\,^{\circ}\mathrm{C}$. For temperatures less than $\vartheta_g \approx 135\,^{\circ}\mathrm{C}$ in Fig. 4-1a, we see that in the glassy region:

(i) The stress-strain curves exhibit a well-defined yield-peak, followed by strain-softening, and eventual strain-hardening at large strains due to the limited extensibility of the polymer chains.

(ii) As the temperature increases in the glassy region from $25\,^{\circ}\mathrm{C}$ to $130\,^{\circ}\mathrm{C}$, the magnitude of the yield-peak diminishes, the yield strength decreases with temperature from $\approx$ $65\,\mathrm{MPa}$ to $\approx$ $15\,\mathrm{MPa}$, and the amount of strain-hardening observed at large strains diminishes.

(iii) Upon unloading after compression to strains exceeding 130%, approximately 5% of the strain is recovered, and there is permanent-set.

In contrast, referring to temperatures above $\vartheta_g \approx 135\,^{\circ}\mathrm{C}$ in Fig. 4-1b, we see that above the glass transition temperature:

(i) The initial stiffness of the material has dropped dramatically.

(ii) The yield-peak has disappeared.

(iii) The stress-strain response during the loading-phase is highly non-linear and exhibits strain-hardening. However, the stress levels at large strains are below $3\,\mathrm{MPa}$ at $140\,^{\circ}\mathrm{C}$, and no more than $0.5\,\mathrm{MPa}$ at $160\,^{\circ}\mathrm{C}$.

(iv) Upon unloading after compression to strains exceeding 130%, the material exhibits a highly non-linear unloading response and significant permanent-set. The amount of permanent-set increases dramatically as the temperature increases form $140\,^{\circ}\mathrm{C}$ to $160\,^{\circ}\mathrm{C}$.

Fig. 4-3 and Fig. 4-4 show a more extensive set of stress-strain curves for Zeonex-690R at strain rates of 3×10^{-4}, 3×10^{-3}, 3×10^{-2}, and $3 \times 10^{-1}\,\mathrm{s}^{-1}$ and temperatures of $25\,^{\circ}\mathrm{C}$ through $180\,^{\circ}\mathrm{C}$. Referring to Fig. 4-3 which shows stress-strain curves for Zeonex-690R at various fixed temperatures below ϑ_g and four different strain rates, we see obvious strain-rate dependent features of the material response. In the low-temperature glassy region,

[1] As is customary, in order to calculate the deformed cross-sectional area (and thence the true stress), we have assumed plastic incompressibility to estimate the stretch in the lateral direction of the compression specimens.

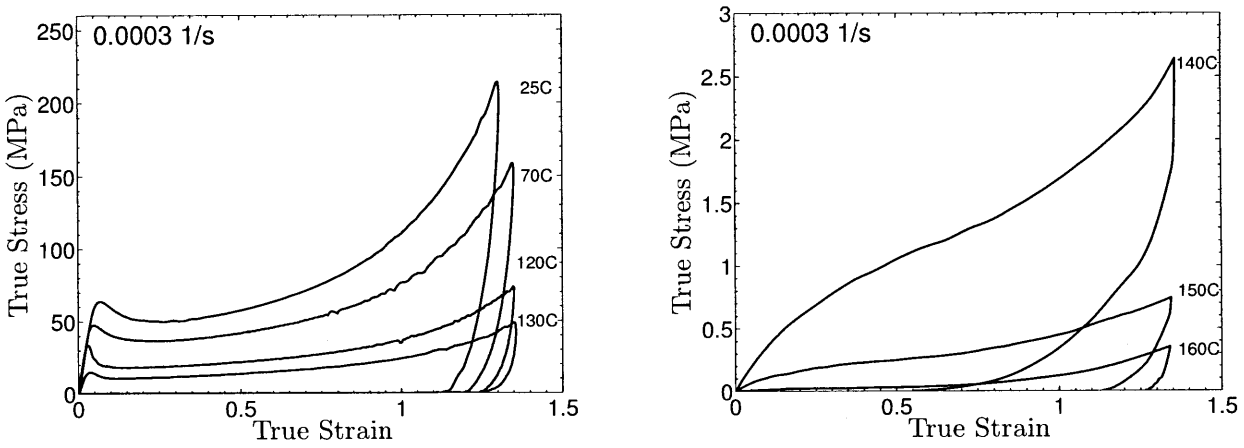

Figure 4-1: Stress-strain curves in simple compression for Zeonex-690R at various temperatures ranging from 25 °C, to 160 °C; at a strain rate of $3\times10^{-4}\,s^{-1}$: (a) for temperatures below $\vartheta_g \approx 135\,°C$, and (b) for temperatures above ϑ_g. Note change in scale for the stress axis between various figures.

$\vartheta < 135\,°C$, the yield strength of the material increases by about 10% for a one-decade increase in strain-rate at any given temperature. Another important strain-rate dependent feature is the softening observed at large strains at the highest strain rate of $3 \times 10^{-1}\,s^{-1}$ at temperatures of 25 °C, 70 °C, 120 °C and 130 °C. This softening is attributable to (near) "adiabatic" heating at the high strain rates.[2] Significant strain rate sensitivity can also be observed at temperatures above the glass transition temperature in Fig. 4-4; similar to the behavior below glass transition, the stress levels are higher for higher strain rates.

An important feature of the stress-strain behavior of amorphous polymers is their strain-rate sensitive response in a temperature range slightly above their "nominal glass transition temperature." Consider the stress-strain curves for Zeonex-690R in Fig. 4-4 at 140 °C: at the lowest strain rate of $3\times10^{-4}\,s^{-1}$ the material responds as if it were "above" its glass transition temperature. However, at the highest strain rate of $3 \times 10^{-1}\,s^{-1}$, the material exhibits a glassy-response with a significantly higher stress magnitude, a yield-peak, strain-softening and subsequent strain-hardening due to chain-locking. Thus, in accordance with well-known results from frequency-dependent dynamic-mechanical-tests on amorphous polymers, this result clearly shows that the "glass transition temperature" is *not a constant* for a material, and increases as the strain rate increases.

[2]While we did not measure the actual temperature rise in our specimens, Arruda et al. (1995) have shown that the surface temperature of a compression specimen of an amorphous polymer, for a test carried out at 20 °C, could increase by as much $\approx 20\,°C$ after a 100% compressive strain at a strain rate of $10^{-1}\,s^{-1}$.

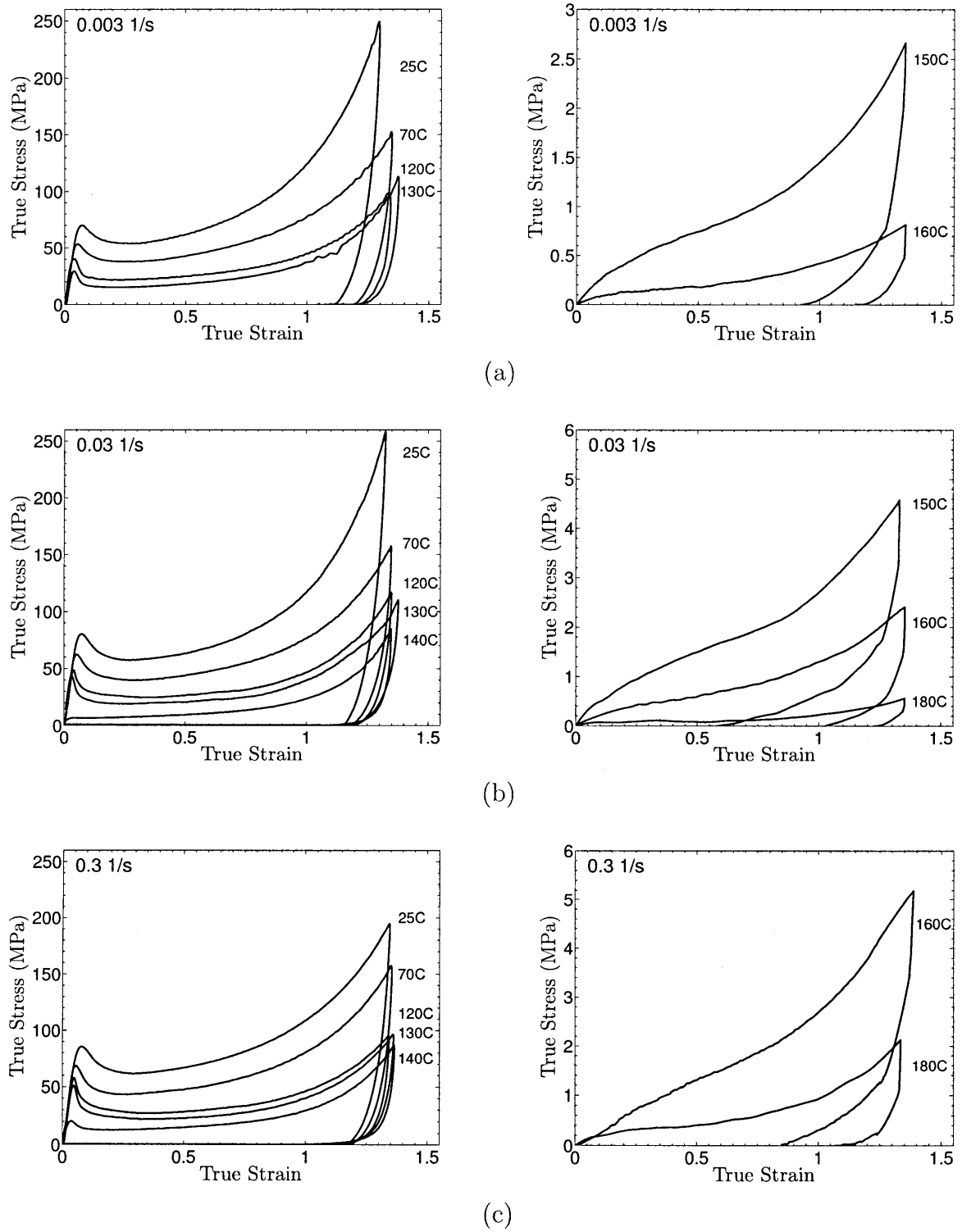

Figure 4-2: Stress-strain curves in simple compression for Zeonex-690R at various temperatures ranging from 25 °C, to 180 °C; at strain rates of (a) $3\times10^{-3}\,s^{-1}$, (b) $3\times10^{-2}\,s^{-1}$, and (c) $3\times10^{-1}\,s^{-1}$. Note change in scale for the stress axis between various figures.

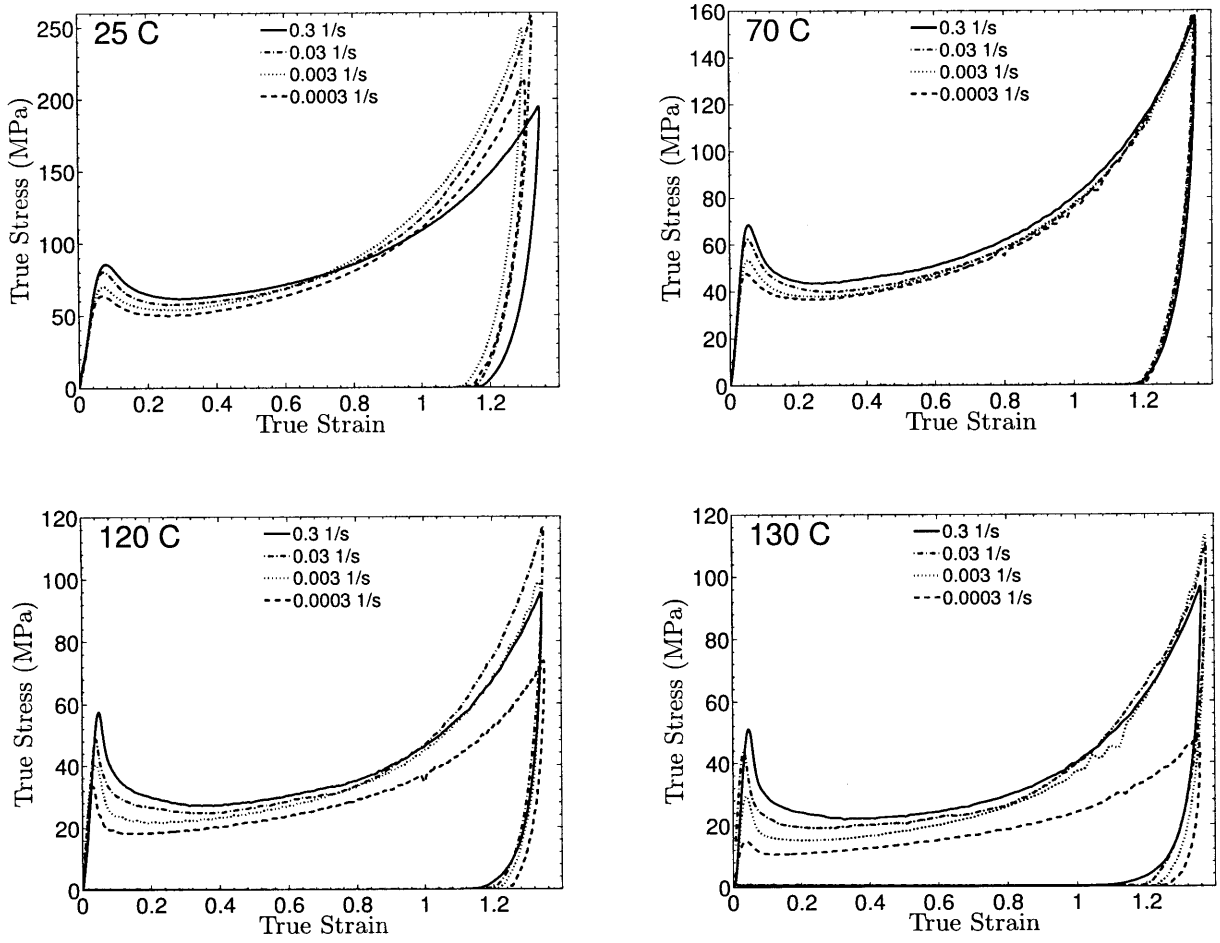

Figure 4-3: Stress-strain curves in simple compression for Zeonex at strain rates of 3×10^{-4}, 3×10^{-4}, 3×10^{-4}, and $3\times10^{-4}\,s^{-1}$, and at temperatures of 25 °C, 70 °C, 120 °C, and 130 °C. Note change in scale for the stress axis between various figures.

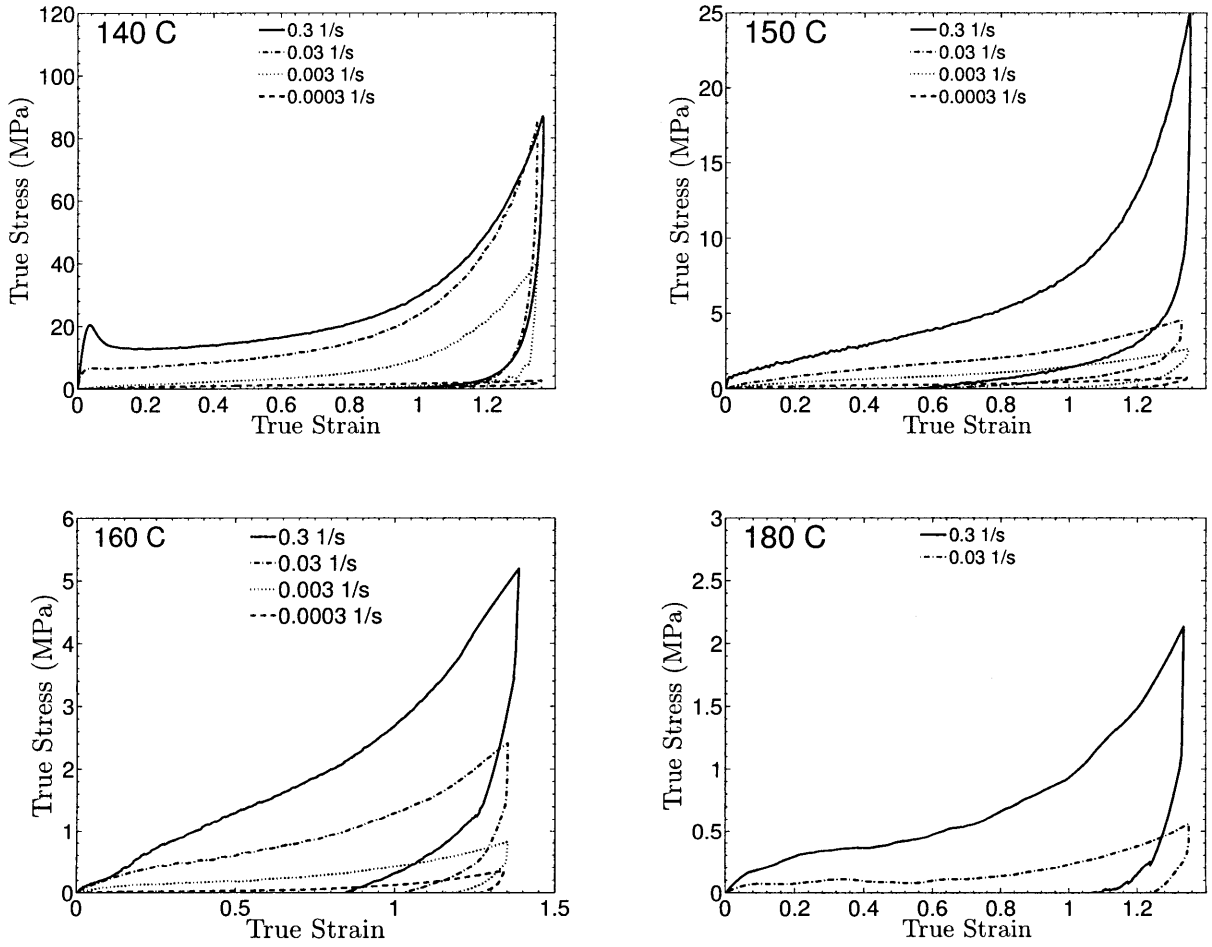

Figure 4-4: Stress-strain curves in simple compression for Zeonex at strain rates of 3×10^{-4}, 3×10^{-4}, 3×10^{-4}, and $3\times10^{-4}\,s^{-1}$, and at temperatures of 140 °C, 150 °C, 160 °C, and 180 °C. Note change in scale for the stress axis between various figures.

4.3 Constitutive theory

Since we wish to model the behavior of glassy polymers in the technologically important temperature range which *spans their glass transition temperatures*, and since the number of *microscopic relaxation mechanisms* in these polymers increases as the temperature is increased, we base our theory on a "multimechanism" generalization of the classical Kröner (1960) – Lee (1969) multiplicative decomposition,

$$\mathbf{F} = \mathbf{F}^{e\,(\alpha)}\mathbf{F}^{p\,(\alpha)}, \qquad \text{with} \qquad \det\mathbf{F}^{e\,(\alpha)} > 0 \quad \text{and} \quad \det\mathbf{F}^{p\,(\alpha)} > 0, \qquad \alpha = 1,\ldots,M, \quad (4.1)$$

where each α denotes a local micromechanism of deformation. Such a multi-mechanism generalization forms the basis of the earlier work by Buckley and Jones (1995), Boyce et al. (2000), Dooling et al. (2002), Dupaix and Boyce (2007) and Ames (2007). For each micromechanism indexed by α, we refer to $\mathbf{F}^{p\,(\alpha)}$ and $\mathbf{F}^{e\,(\alpha)}$ as the *plastic and elastic parts* of $\mathbf{F}$.[3]

It is important to note from the outset, that each $\mathbf{F}^{p\,(\alpha)}$ is to be regarded as an internal variable of the theory which is defined as a solution of the differential equation (the *flow rule* to be discussed shortly)

$$\dot{\mathbf{F}}^{p\,(\alpha)} = \mathbf{D}^{p\,(\alpha)}\mathbf{F}^{p\,(\alpha)} \quad \text{with} \quad \det\mathbf{F}^{p\,(\alpha)} = 1, \quad \text{and with initial condition} \quad \mathbf{F}^{p\,(\alpha)}(\mathbf{X},0) = \mathbf{1}. \quad (4.2)$$

The corresponding $\mathbf{F}^{e\,(\alpha)}$ is then defined by $\mathbf{F}^{e\,(\alpha)} \stackrel{\text{def}}{=} \mathbf{F}\mathbf{F}^{p\,(\alpha)-1}$. Hence the decompositions (4.1) are not purely kinematical in nature as they are not defined independently of constitutive equations; they are to be viewed as *kinematical constitutive equations.*

The fewer the "number of micromechanisms," M, which are needed to phenomenologically describe the response of a material, then the fewer the number of "material parameters" that are needed to flesh-out the constitutive theory. In Chapter 3 on modeling the response of amorphous polymers below ϑ_g, we found that a theory with $M = 2$ was quite adequate. In order to model the response of these materials, which extends to temperatures which are approximately 50 °C above ϑ_g, we find that we need to increase the number of micromechanisms to $M = 3$. As a visual aid, Fig. 5-6 shows a schematic "spring-dashpot"- representation of these three micromechanisms:

- **The first micromechanism ($\alpha = 1$)**: (a) The nonlinear spring represents an "elastic" resistance to intermolecular (and perhaps intramolecular) energetic bond-stretching. (b) The dashpot represents thermally-activated plastic flow due to "inelastic mechanisms," such as chain-segment rotation and relative slippage of the polymer chains between neighboring mechanical cross-linkage points. (c) The nonlinear spring in par-

[3] In a one-dimensional theory of linear viscoelasticity, which is based on a widely-used mechanical analog of M Maxwell-elements assembled in parallel, the one-dimensioinal strain ϵ is decomposed as

$$\epsilon = \epsilon^{e(\alpha)} + \epsilon^{p(\alpha)}, \qquad \alpha = 1,\ldots,M;$$

the decomposition (4.1) is a three-dimensional, large-deformation, generalization of such a decomposition.

allel with the dashpot represents an "energy storage" mechanism due to the local elastic incompatibilities caused by the viscoplastic flow mechanisms. We introduce a defect energy only for micromechanism $\alpha = 1$, via an internal variable $\mathbf{A}$; even for this micromechanism, the role of such a stored energy decreases as the molecular mobility increases when the temperatures approach and exceed ϑ_g.

- **The second and third micromechanisms** ($\alpha = 2, 3$): (a) The nonlinear springs represent resistances due to changes in the free energy upon stretching of the molecular chains between the mechanical cross-links. (b) The dashpots represent thermally-activated plastic flow due to slippage of the "mechanical" cross-links, which are relatively strong below ϑ_g, but are progressively destroyed at temperatures above ϑ_g. The fact that we employ two such mechanisms is necessitated by the experimentally-observed increased complexity of the response of amorphous polymers as the temperature transitions across the range of temperatures from below ϑ_g to sufficiently above ϑ_g. We neglect any defect energies associated with mechanisms $\alpha = 2, 3$.

Our strategy to phenomenologically model the response of the material as the temperature is increased to ϑ_g and beyond, is as follows:

(i) For temperatures $\vartheta < \vartheta_g$, *we do not allow any plastic flow in the dashpots associated with micromechanisms* $\alpha = 2$ and $\alpha = 3$. Thus, since the springs in $\alpha = 2$ and $\alpha = 3$ are in parallel, for all practical purposes the three-micromechanism model reduces to a simpler two-micromechanism model, which we have successfully used in Chapter 3 to model the response of amorphous polymers for temperatures $\vartheta < \vartheta_g$.

A schematic of the individual contributions from each micromechanism, to an overall stress-strain curve in compression at a temperature $\vartheta < \vartheta_g$ is shown in Fig. 5-7a.

(ii) For temperatures $\vartheta > \vartheta_g$, we allow for plastic flow in the dashpots associated with micromechanisms $\alpha = 2$ and $\alpha = 3$, but *quickly drop the plastic flow resistance in mechanism* $\alpha = 2$ *to a very small value*, so that for all practical purposes in this temperature range, only mechanisms $\alpha = 1$ and $\alpha = 3$ contribute to the macroscopic stress.

A schematic of the individual contributions from each micromechanism, to an overall stress-strain curve in compression at a temperature $\vartheta > \vartheta_g$ is shown in Fig. 5-7b.

Remark 1: At first blush it might appear possible to combine mechanisms $\alpha = 2$ and $\alpha = 3$ into a single micromechanism, say $\alpha = 2$, and simply make the modulus associated with the spring in this single branch to be strongly *temperature-dependent* — taking on high values below ϑ_g and low values above ϑ_g. However, this would lead to *incorrect* predictions concerning the amount of "elastic recovery" in circumstances where the polymer is first heated to a temperature above ϑ_g, subjected to a large deformation which includes large stretching of the spring, and then cooled to below ϑ_g under traction boundary conditions. Thus, since by assumption the modulus associated with spring in the single additional branch

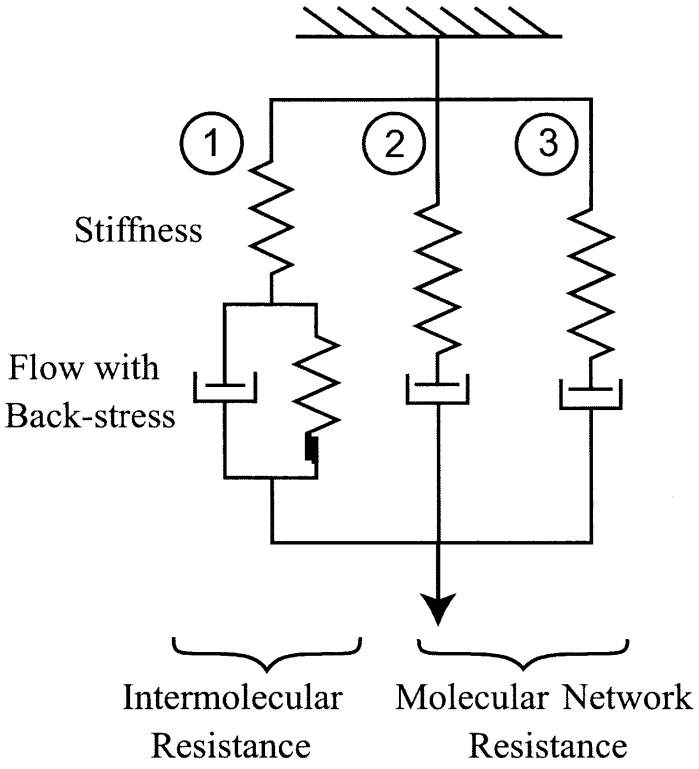

Figure 4-5: A schematic "spring-dashpot"-representation of the constitutive model.

$\alpha = 2$ increases with decreasing temperature, the amount of "elastic recovery" (spring-back) upon cooling under traction boundary conditions would be unphysically too large. Conversely, cooling under displacement boundary conditions, would result in large residual stresses.

In our discussion above, we have implicitly assumed that the glass transition temperature ϑ_g is a *constant* for each material. However, the "glass transition" actually occurs over a narrow range of temperatures, and whatever the means that are used to define *a glass transition temperature*,[4] such a glass transition temperature is not a constant, but depends strongly on the strain rate to which the material is subjected. With $\mathbf{D}_0 = \mathrm{sym}_0(\dot{\mathbf{F}}\mathbf{F}^{-1})$ denoting the total deviatoric stretching tensor, let

$$\nu \stackrel{\text{def}}{=} \sqrt{2}|\mathbf{D}_0| \tag{4.3}$$

[4]Such as the peak in the tan-δ curve in a DMA experiment.

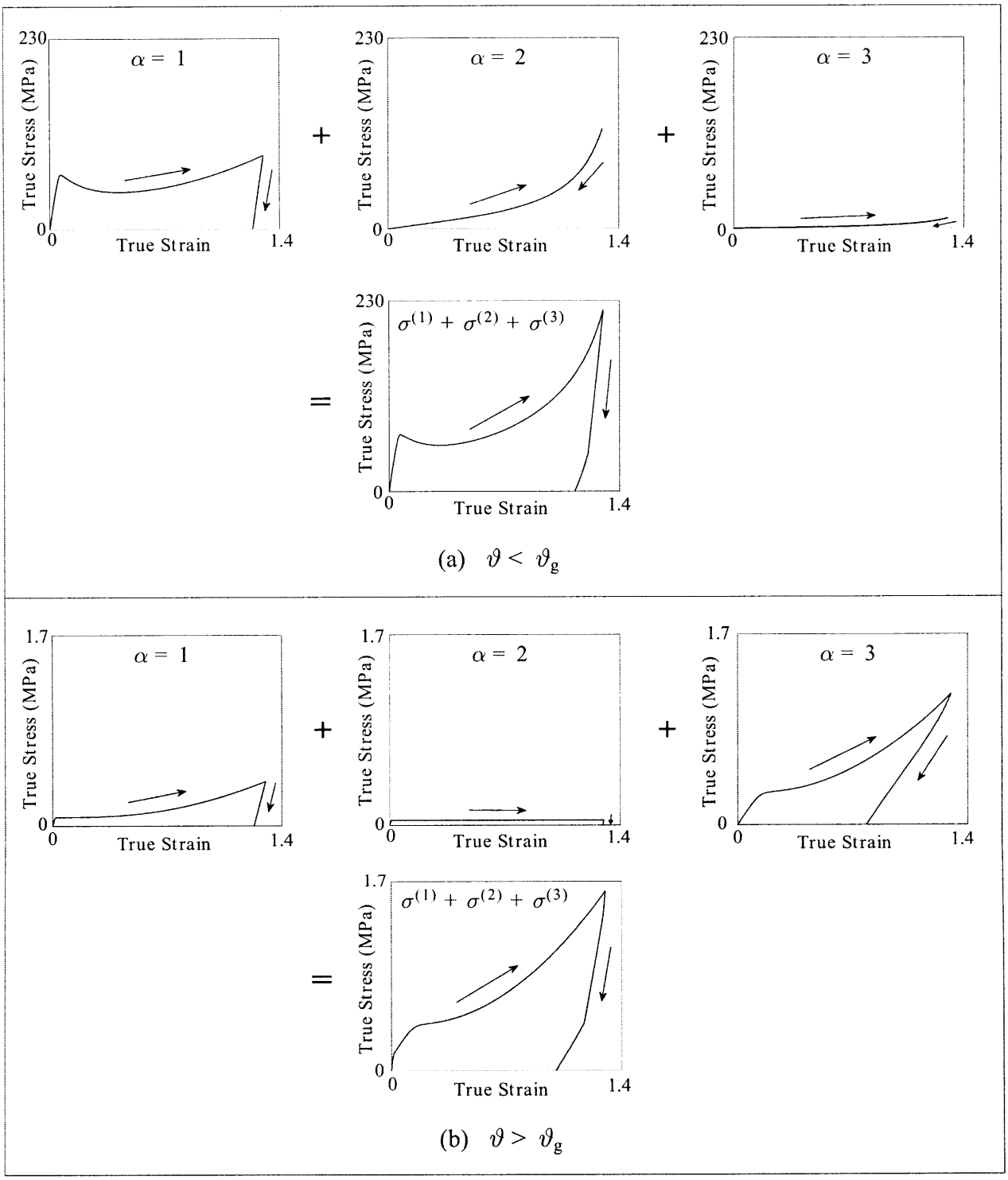

Figure 4-6: Schematic plots of stress-strain contributions from individual micromechanisms to an overall simple compression stress-strain response for: (a) a temperature below ϑ_g; and (b) a temperature above ϑ_g. Note change in scale for the stress axis between the figures in (a) and (b).

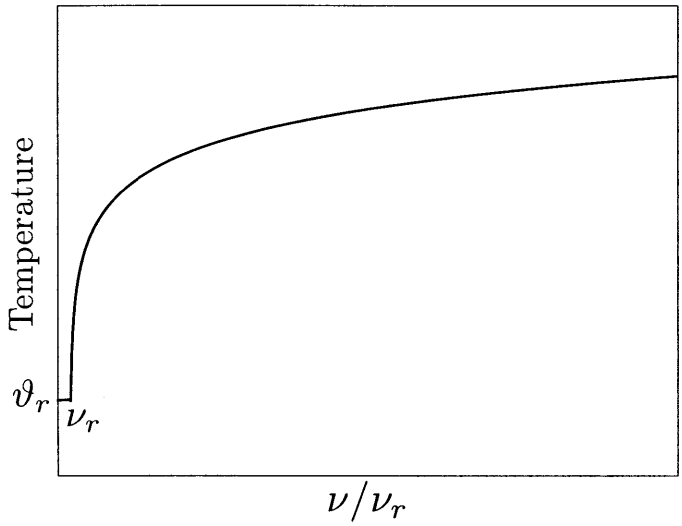

Figure 4-7: Schematic of dependence of glass transition temperature on the shear strain rate ν. Here ϑ_r is a reference glass transition temperature at a a low reference shear strain rate ν_r.

denote an *equivalent shear strain rate.*[5] As a simple model for the variation of the glass transition temperature with strain rate, we assume that

$$\vartheta_g = \begin{cases} \vartheta_r & \text{if } \nu \leq \nu_r, \\ \vartheta_r + n \log\left(\dfrac{\nu}{\nu_r}\right) & \text{if } \nu > \nu_r, \end{cases} \tag{4.4}$$

where ϑ_r a *reference glass transition temperature* at a *reference strain rate* ν_r, and n is a material parameter. The change in glass transition temperature with strain rate modeled by (4.4) is qualitatively shown in Fig. 5-8.

The specialized constitutive theory relates the following basic fields:

$\mathbf{x} = \boldsymbol{\chi}(\mathbf{X}, t)$,	motion;
$\mathbf{F} = \nabla\boldsymbol{\chi}, \quad J = \det \mathbf{F} > 0$,	deformation gradient;
$\mathbf{F} = \mathbf{F}^{e\,(\alpha)}\mathbf{F}^{p\,(\alpha)}, \quad \alpha = 1, 2, 3,$	elastic-plastic decomposition of $\mathbf{F}$;
$\mathbf{F}^{e\,(\alpha)}, \quad J^{e\,(\alpha)} = \det \mathbf{F}^{e\,(\alpha)} = J > 0,$	elastic distortions;
$\mathbf{F}^{p\,(\alpha)}, \quad J^{p\,(\alpha)} = \det \mathbf{F}^{p\,(\alpha)} = 1,$	inelastic distortions;
$\mathbf{F}^{e\,(\alpha)} = \mathbf{R}^{e\,(\alpha)}\mathbf{U}^{e\,(\alpha)}$,	polar decomposition of $\mathbf{F}^{e\,(\alpha)}$;
$\mathbf{C}^{e\,(\alpha)} = \mathbf{F}^{e\,(\alpha)\top}\mathbf{F}^{e\,(\alpha)}$,	elastic right Cauchy-Green tensors;
$\mathbf{B}^{p\,(\alpha)} = \mathbf{F}^{p\,(\alpha)}\mathbf{F}^{p\,(\alpha)\top}$,	plastic left Cauchy-Green tensors;

[5]We emphasize that throughout our paper ν, ν^p etc., *do not* denote Poisson's ratios, but denote *equivalent shear strain rates.* The Poisson's ratio is explicitly denoted by ν^{poi}.

$\mathbf{T} = \sum_\alpha \mathbf{T}^{(\alpha)}$,	$\mathbf{T}^{(\alpha)} = \mathbf{T}^{(\alpha)\top}$,	Cauchy stress;
$\mathbf{T}_{\mathrm{R}} = J\mathbf{T}\mathbf{F}^{-\top}$,		Piola stress;
$\psi_{\mathrm{R}} = \sum_{\alpha=1}^{3} \bar{\psi}^{(\alpha)}$,		free energy density per unit reference volume;
$\eta_{\mathrm{R}} = \sum_{\alpha=1}^{3} \bar{\eta}^{(\alpha)}$,		entropy density per unit reference volume;
$\vartheta > 0$,		absolute temperature;
$\nabla\vartheta$,		referential temperature gradient;
$\mathbf{q}_{\mathrm{R}}$,		referential heat flux vector;
q_{R},		scalar heat supply.

In the following subsections we present special constitutive equations for the three micromechanisms. For brevity, we only present the major results of our specialization; the reader is referred to Chapter 2 for a detailed development of the theory, and Chapter 3 for the intermediate steps of continuum-mechanical arguments and derivations.

4.3.1 Constitutive equations for micromechanism $\alpha = 1$

Free energy

The free energy is given by

$$\psi_{\mathrm{R}}^{(1)} = \underbrace{\bar{\psi}^{e\,(1)}(\mathcal{I}_{\mathbf{C}^{e(1)}}, \vartheta)}_{\text{elastic energy}} + \underbrace{\bar{\psi}^{p\,(1)}(\mathcal{I}_{\mathbf{A}}, \vartheta)}_{\text{defect energy}}, \tag{4.5}$$

with $\bar{\psi}^{e\,(1)}$ an elastic energy, and $\bar{\psi}^{p\,(1)}$ a defect energy associated with plastic flow, for $\alpha = 1$. Also, $\mathcal{I}_{\mathbf{C}^{e(1)}}$ and $\mathcal{I}_{\mathbf{A}}$ represent lists of the principal invariants of $\mathbf{C}^{e(1)}$ and $\mathbf{A}$, respectively.

The "defect energy" $\bar{\psi}^{p\,(1)}$ associated with local microscopic plastic strain incompatibilities, and introduced via the internal variables $\mathbf{A}$, leads to the development of important *back-stresses*, and allows one to phenomenologically account for Bauschinger-like phenomena on unloading and reverse loading. In addition, they contribute in an important manner to the plastic source term in the balance of energy.

The elastic energy $\bar{\psi}^{e\,(1)}$:

Let

$$\mathbf{C}^{e(1)} = \sum_{i=1}^{3} \omega_i^e \, \mathbf{r}_i^e \otimes \mathbf{r}_i^e, \quad \text{with} \quad \omega_i^e = \lambda_i^{e\,2}, \tag{4.6}$$

denote the spectral representation of $\mathbf{C}^{e(1)}$, where $(\lambda_1^e, \lambda_2^e, \lambda_3^e)$ are the positive eigenvalues of $\mathbf{U}^{e(1)}$, and $(\mathbf{r}_1^e, \mathbf{r}_2^e, \mathbf{r}_3^e)$ are the orthonormal eigenvectors of $\mathbf{C}^{e(1)}$ and $\mathbf{U}^{e(1)}$. Instead of using the invariants $\mathcal{I}_{\mathbf{C}^{e(1)}}$, the free energy $\bar{\psi}^{e\,(1)}$ for isotropic materials may be alternatively

expressed in terms of the principal stretches, or functions thereof. With

$$\mathbf{E}^{e(1)} = \sum_{i=1}^{3} E_i^e \, \mathbf{r}_i^e \otimes \mathbf{r}_i^e, \qquad E_i^e = \ln \lambda_i^e, \tag{4.7}$$

denoting an elastic logarithmic strain measure, we adopt the following special form for the free energy $\bar{\psi}^{e(1)}$:[6]

$$\bar{\psi}^{e\,(1)} = G|\mathbf{E}_0^{e\,(1)}|^2 + \tfrac{1}{2}K(\mathrm{tr}\,\mathbf{E}^{e(1)})^2 - 3\,K\,(\mathrm{tr}\,\mathbf{E}^{e(1)})\alpha^{\mathrm{th}}(\vartheta - \vartheta_0) + \tilde{f}(\vartheta), \tag{4.8}$$

where $\tilde{f}(\vartheta)$ is an entropic contribution to the free energy related to the temperature-dependent specific heat of the material. The temperature-dependent parameters

$$G(\vartheta) > 0, \quad K(\vartheta) > 0, \quad \alpha^{\mathrm{th}}(\vartheta) > 0, \tag{4.9}$$

are the shear modulus, bulk modulus, and coefficient of thermal expansion, respectively, and ϑ_0 is a reference temperature.

For polymeric materials the magnitude of the elastic shear modulus G decreases drastically as the temperature increases through the glass transition temperature ϑ_g of the material. Following Dupaix and Boyce (2007), we assume that the temperature dependence of the shear modulus may be adequately approximated by the following function:

$$G(\vartheta) = \tfrac{1}{2}(G_{gl} + G_r) - \tfrac{1}{2}(G_{gl} - G_r)\tanh\Big(\frac{1}{\Delta}(\vartheta - \vartheta_g)\Big) - M(\vartheta - \vartheta_g), \tag{4.10}$$

where ϑ_g is the glass transition temperature, G_{gl} and G_r ($< G_{gl}$) are values of the shear modulus in the glassy and rubbery regions, and Δ is a parameter related to the temperature range across which the glass transition occurs. The parameter M represents the slope of the temperature variation of G beyond the transition region, with

$$M = \begin{cases} M_{gl} & \vartheta \le \vartheta_g, \\ M_r & \vartheta > \vartheta_g. \end{cases} \tag{4.11}$$

Next, the temperature dependence of Poisson's ratio ν^{poi} of the material is assumed to be

$$\nu^{\mathrm{poi}}(\vartheta) = \frac{1}{2}(\nu_{gl}^{\mathrm{poi}} + \nu_r^{\mathrm{poi}}) - \frac{1}{2}(\nu_{gl}^{\mathrm{poi}} - \nu_r^{\mathrm{poi}})\tanh\Big(\frac{1}{\Delta}(\vartheta - \vartheta_g)\Big), \tag{4.12}$$

with ν_{gl}^{poi} and ν_r^{poi} representing values below and above ϑ_g, respectively. The temperature dependence of the bulk modulus K is then obtained by using the standard relation for

[6]This is a useful free energy function for *moderately large elastic stretches*, Anand (1979, 1986).

isotropic materials

$$K(\vartheta) = G(\vartheta) \times \frac{2(1+\nu^{\text{poi}}(\vartheta))}{3(1-2\,\nu^{\text{poi}}(\vartheta))}. \tag{4.13}$$

The temperature dependence of the shear modulus G, the Poisson's ratio ν_{poi}, and the bulk modulus K are schematically shown in Fig. 5-9.

The coefficient of thermal expansion is taken to have a bilinear temperature dependence, with the following contribution to the thermal expansion term $\alpha^{\text{th}}(\vartheta-\vartheta_0)$ in the free energy relation (4.8):

$$\alpha^{\text{th}}(\vartheta-\vartheta_0) = \begin{cases} \alpha_{gl}(\vartheta-\vartheta_0) & \text{if} \quad \vartheta \le \vartheta_g, \\ \alpha_{gl}(\vartheta-\vartheta_0) + (\alpha_r - \alpha_{gl})(\vartheta-\vartheta_g) & \text{if} \quad \vartheta > \vartheta_g. \end{cases} \tag{4.14}$$

The defect energy $\bar{\psi}^{p\,(1)}$:

With

$$\mathbf{A} = \sum_{i=1}^{3} a_i\, \mathbf{l}_i \otimes \mathbf{l}_i, \tag{4.15}$$

denoting the spectral representation of $\mathbf{A}$, and with

$$\ln \mathbf{A} = \sum_{i=1}^{3} \ln a_i\, \mathbf{l}_i \otimes \mathbf{l}_i, \tag{4.16}$$

denoting a defect logarithmic strain measure, we assume a free energy $\bar{\psi}^{p\,(1)}$ of the form

$$\bar{\psi}^{p\,(1)} = \frac{1}{4} B \left[(\ln a_1)^2 + (\ln a_2)^2 + (\ln a_3)^2 \right], \tag{4.17}$$

where the positive-valued temperature-dependent parameter

$$B(\vartheta) \ge 0, \tag{4.18}$$

is a back-stress modulus. The back-stress modulus B is assumed to be a linearly decreasing function of temperature, with B vanishing above ϑ_g:

$$B(\vartheta) = \begin{cases} -X(\vartheta-\vartheta_g) & \text{if} \quad \vartheta \le \vartheta_g, \\ 0 & \text{if} \quad \vartheta > \vartheta_g, \end{cases} \tag{4.19}$$

where $X > 0$ is a constant.

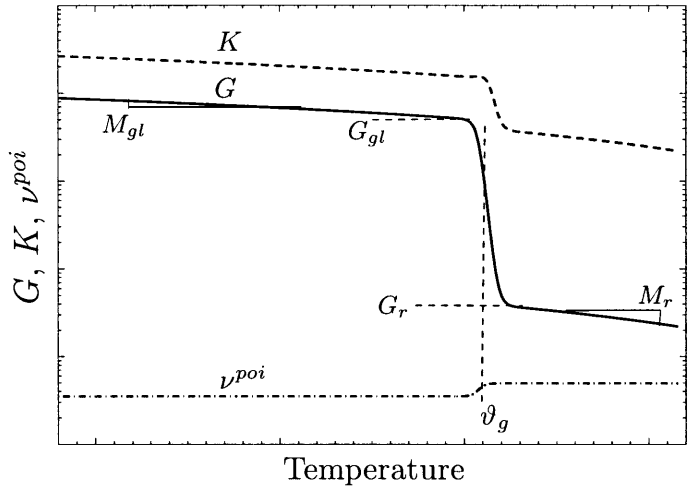

Figure 4-8: Schematic of temperature-dependence of shear modulus G, bulk modulus K and Poisson's ratio ν^{poi}. Note that the ordinate is plotted on a logarithmic scale.

Cauchy stress. Mandel stress. Back-stress. Effective stress

Corresponding to the special free energy functions considered above, the contribution $\mathbf{T}^{(1)}$ to the Cauchy stress is given by

$$\mathbf{T}^{(1)} \stackrel{\text{def}}{=} J^{-1}\,\mathbf{R}^{e\,(1)}\,\mathbf{M}^{e(1)}\,\mathbf{R}^{e\,(1)\top}, \tag{4.20}$$

where

$$\mathbf{M}^{e(1)} = \frac{\partial\tilde{\psi}^{e\,(1)}(\mathbf{E}^{e(1)},\vartheta)}{\partial\mathbf{E}^{e(1)}} = 2G\mathbf{E}_0^{e\,(1)} + K\,(\operatorname{tr}\mathbf{E}^{e(1)})\mathbf{1} - 3K\alpha^{\text{th}}(\vartheta-\vartheta_0)\mathbf{1}, \tag{4.21}$$

is the corresponding symmetric Mandel stress.

The symmetric and deviatoric back-stress is

$$\mathbf{M}_{\text{back}} = 2\Big(\frac{\partial\tilde{\psi}^{p\,(1)}}{\partial\mathbf{A}}\mathbf{A}\Big)_0 = B\ln\mathbf{A}. \tag{4.22}$$

Further, the driving stress for plastic flow is the effective stress given by

$$(\mathbf{M}_{\text{eff}}^{e\,(1)})_0 = \mathbf{M}_0^{e\,(1)} - \mathbf{M}_{\text{back}}. \tag{4.23}$$

The corresponding *equivalent shear stress* and *mean normal pressure* are given by

$$\bar{\tau}^{(1)} \stackrel{\text{def}}{=} \frac{1}{\sqrt{2}}\,|(\mathbf{M}_{\text{eff}}^{e\,(1)})_0|, \quad \text{and} \quad \bar{p} \stackrel{\text{def}}{=} -\frac{1}{3}\operatorname{tr}\mathbf{M}^{e(1)}, \tag{4.24}$$

respectively.

Flow rule

The evolution equation for $\mathbf{F}^{p(1)}$ is

$$\dot{\mathbf{F}}^{p(1)} = \mathbf{D}^{p(1)}\,\mathbf{F}^{p(1)}, \tag{4.25}$$

with $\mathbf{D}^{p(1)}$ given by

$$\mathbf{D}^{p(1)} = \nu^{p(1)}\left(\frac{(\mathbf{M}^{e\,(1)}_{\text{eff}})_0}{2\bar{\tau}^{(1)}}\right), \qquad \text{where} \qquad \nu^{p(1)} \stackrel{\text{def}}{=} \sqrt{2}|\mathbf{D}^{p(1)}|. \tag{4.26}$$

The equivalent plastic shear strain rate $\nu^{p(1)}$ is obtained by solving the scalar strength relation

$$\bar{\tau}^{(1)} = Y^{(1)}(\mathbf{\Lambda}^{(1)}, \nu^{p(1)}), \tag{4.27}$$

where

$$\mathbf{\Lambda}^{(1)} \stackrel{\text{def}}{=} \left(\mathbf{C}^{e(1)}, \mathbf{B}^{p(1)}, \mathbf{A}, \boldsymbol{\xi}^{(1)}, \vartheta\right) \tag{4.28}$$

denotes a list of constitutive variables. With the mean normal pressure defined by $(4.24)_2$ and a (total) *effective stretch* defined by

$$\bar{\lambda} \stackrel{\text{def}}{=} \sqrt{\text{tr}\,\mathbf{C}/3} \equiv \sqrt{\mathbf{C}^{e(1)} : \mathbf{B}^{p(1)}/3}, \tag{4.29}$$

as a simplification of the theory, we assume henceforth that the strength function $Y^{(1)}$ is independent of $\mathbf{A}$, and depends on $\mathbf{C}^{e(1)}$ and $\mathbf{B}^{p(1)}$ only through $\bar{p}$ and $\bar{\lambda}$, so that

$$\bar{\tau}^{(1)} = Y^{(1)}(\bar{p}, \bar{\lambda}, \boldsymbol{\xi}^{(1)}, \vartheta, \nu^{p(1)}). \tag{4.30}$$

We assume further that at a fixed state $(\bar{p},\bar{\lambda}, \boldsymbol{\xi}^{(1)}, \vartheta)$ the strength relation (4.30) is *invertible*, with inverse

$$\nu^{p(1)} = f(\vartheta, \bar{\tau}^{(1)}, \bar{p}, \bar{\lambda}, \boldsymbol{\xi}^{(1)}) \geq 0. \tag{4.31}$$

Next, we restrict the list of the internal variables $\boldsymbol{\xi}^{(1)}$ to three positive-valued scalars,

$$\boldsymbol{\xi}^{(1)} = \left(\varphi, S_a, S_b\right),$$

where

- $\varphi \geq 0$ is an "order-parameter" representing the local change in molecular-packing due to deformation-induced disordering.

- $S_a \geq 0$ represents a transient resistance to plastic flow coupled to the disordering of material. The internal variables φ and S_a are introduced to model the "yield-peak" which is widely-observed in the intrinsic stress-strain response of glassy polymers.

- $S_b \geq 0$ represents a dissipative resistance to plastic flow introduced to model "isotropic hardening" at large strains as the chains are pulled taut between entanglements at large strains, and there is increasing frictional interaction between the pendant side-groups; this is in addition to any entropic or energetic contribution from network chain-stretching.

Thus, the constitutive equation for the equivalent plastic strain rate (4.31) becomes

$$\nu^{p(1)} = f(\vartheta, \bar{\tau}^{(1)}, \bar{p}, \bar{\lambda}, \varphi, S_a, S_b) \geq 0. \tag{4.32}$$

Finally, guided by the literature (e.g., Eyring, 1936; Fotheringham et al., 1976; Fotheringham and Cherry, 1978; Povolo and Hermida, 1995; Povolo et al., 1996; Richeton et al., 2005a, 2006, 2007) and our flow rule in Chapter 3, for the flow function f in (4.32) we choose a thermally-activated relation in the specific form

$$\nu^{p(1)} = \begin{cases} 0 & \text{if} \quad \tau_{\mathrm{e}}^{(1)} \leq 0, \\ \nu_0^{(1)} \exp\Big(-\dfrac{1}{\zeta}\Big) \exp\Big(-\dfrac{Q}{k_B\,\vartheta}\Big) \left[\sinh\Big(\dfrac{\tau_{\mathrm{e}}^{(1)} V}{2k_B\vartheta}\Big)\right]^{1/m^{(1)}} & \text{if} \quad \tau_{\mathrm{e}}^{(1)} > 0, \end{cases} \tag{4.33}$$

where

$$\tau_{\mathrm{e}}^{(1)} \stackrel{\text{def}}{=} \bar{\tau}^{(1)} - (S_a + S_b + \alpha_p\,\bar{p}), \tag{4.34}$$

denotes a *net shear stress for thermally-activated flow*; here $\alpha_p \geq 0$ is a parameter introduced to account for the *pressure sensitivity* of plastic flow. The parameter $\nu_0^{(1)}$ is a *pre-exponential factor* with units of 1/time, the term $\exp(-1/\zeta)$ in (4.33) represents a *concentration of "flow defects,"* Q is an *activation energy*, k_B is Boltzmann's constant, V is an activation volume, and $m^{(1)}$ is a *strain rate sensitivity parameter.*

Remark 2: There are many models for the rate and temperature-dependent yield strength of polymers in the literature which consider plastic flow as a thermally-activated process (e.g., Eyring, 1936; Robertson, 1966; Argon, 1973). Most of these models give a reasonably acceptable representation of the variation of the yield strength with temperature and strain rate, but over limited ranges of these variables. The equation for the plastic shear strain rate (4.33) used here is motivated by the recent work of (Richeton et al., 2005a, 2006, 2007), who in turn base their model on the so-called "cooperative"-model of Fotheringham et al. (1976) , Fotheringham and Cherry (1978), Povolo and Hermida (1995) and Povolo et al. (1996). Richeton et al. have shown that a flow function of the form (4.33) may be used to satisfactorily represent the variation of the yield strength of amorphous polymers over a wide range of strain rates and temperatures. The major difference between the flow function proposed by Richeton et al. and the one considered here, is that instead of a tensorial back-

stress $\mathbf{M}_{\text{back}}$ (cf., (4.22)) to define an effective stress which drives plastic flow (cf. (4.23)), they consider a temperature-dependent scalar internal stress in their theory. This results in a profound difference between their model and the one considered here, specially in the ability of the two models to capture unloading and cyclic loading phenomena, as well as in a proper accounting of the energy dissipated during plastic flow (below ϑ_g). Also, the three-dimensional theory that they present in § 3 of their 2007 paper is substantially different in its *mathematical structure* from that considered here.

Remark 3: In the literature on amorphous materials, the dimensionless parameter ζ in the term $\exp(-1/\zeta)$ for the concentration of flow defects, is called the *normalized equilibrium free-volume*, and given by (e.g., Spaepen, 1977)

$$\zeta = \frac{v_f}{v_f^*}, \tag{4.35}$$

where v_f is a local "equilibrium free volume," *a measure of the local packing density of the amorphous material at a given temperature*, and v_f^* is a *normalizing constant*. Assume that the variation of v_f at temperatures $\vartheta < \vartheta_g$ is small, and that for $\vartheta > \vartheta_g$ the temperature dependence of v_f may be approximated by a linear relation

$$v_f = v_g + \alpha_f(\vartheta - \vartheta_g), \tag{4.36}$$

where v_g is the free-volume at ϑ_g, and α_f is the temperature coefficient of expansion of the free-volume. Thus, for temperatures $\vartheta > \vartheta_g$,

$$\exp\Big(-\frac{1}{\zeta}\Big) = \exp\Big(-\frac{v_f^*}{v_g + \alpha_f(\vartheta - \vartheta_g)}\Big) = \exp\Big(-\frac{(v_f^*/\alpha_f)}{\vartheta - (\vartheta_g - v_g/\alpha_f)}\Big), \tag{4.37}$$

and introducing two *constant* material parameters with dimensions of temperature,

$$C \stackrel{\text{def}}{=} (v_f^*/\alpha_f) \quad \text{and} \quad \vartheta_\infty \stackrel{\text{def}}{=} (\vartheta_g - v_g/\alpha_f), \tag{4.38}$$

we obtain

$$\exp\Big(-\frac{1}{\zeta}\Big) = \exp\Big(-\frac{C}{\vartheta - \vartheta_\infty}\Big), \tag{4.39}$$

which is the famous Vogel-Fulcher-Tamman (VFT) term, used widely to describe the temperature-dependence of the viscosity of polymeric liquids near their glass transition temperature (Vogel, 1921; Fulcher, 1925; Tammann and Hesse, 1926).[7] Here, instead of manipulating as

[7]Instead of the VFT form (4.39), Richeton et al. (2005a, 2006, 2007) extend their equation for the plastic shear strain rate to temperatures $\vartheta > \vartheta_g$, (cf. equation (17) in Richeton et al. (2005a)), by using a Williams-Landel-Ferry (WLF)-type temperature-dependent expression (Williams et al., 1955)

$$\exp\Big(-\frac{1}{\zeta}\Big) = \exp\Big(\frac{(\log_e 10) \times C_1\,(\vartheta - \vartheta_g)}{C_2 + \vartheta - \vartheta_g}\Big), \tag{4.40}$$

above to obtain the VFT-expression

$$\zeta = \frac{\vartheta - \vartheta_\infty}{C} \tag{4.41}$$

for the equilibrium normalized free volume ζ, we use (4.35) and (4.36) to directly write

$$\zeta = \zeta_{gl} + d\,(\vartheta - \vartheta_g), \tag{4.42}$$

where

$$\zeta_{gl} \stackrel{\text{def}}{=} \frac{v_g}{v_f^*} \qquad \text{and} \qquad d \stackrel{\text{def}}{=} \frac{\alpha_f}{v_f^*} \tag{4.43}$$

are constants, with ζ_{gl} dimensionless, and d with dimensions of inverse temperature. Indeed, since the variation in ζ is expected to be small for temperatures $\vartheta \leq \vartheta_g$, we assume that $\zeta = \zeta_{gl} \equiv$ constant for $\vartheta < \vartheta_g$, and rewrite (4.42) as

$$\zeta = \begin{cases} \zeta_{gl} & \text{for } \vartheta \leq \vartheta_g, \\ \zeta_{gl} + d\,(\vartheta - \vartheta_g) & \text{for } \vartheta > \vartheta_g. \end{cases} \tag{4.44}$$

The simple relation (5.22) is well-defined at temperatures lower than ϑ_g, and has a linear VFT-type form at higher temperatures; we use it in what follows. The variation of normalized free volume parameter ζ with temperature is schematically shown in Fig. 5-10a.

Further, we find that in addition to a temperature-dependent ζ above ϑ_g, in order to model the plastic flow response of polymers over a wide range of temperatures spanning the glass transition temperature, the activation energy Q also needs to be *taken to be temperature-dependent.* We assume that it varies as

$$Q(\vartheta) = \tfrac{1}{2}(Q_{gl} + Q_r) - \tfrac{1}{2}(Q_{gl} - Q_r) \tanh\left(\frac{1}{\Delta}(\vartheta - \vartheta_g)\right), \tag{4.45}$$

where, $Q = Q_{gl}$ in the glassy regime, and $Q = Q_r < Q_{gl}$ in the rubbery regime, and as in (5.8), Δ is a parameter related to the temperature range across which the glass transition occurs. The variation of activation energy Q with temperature is schematically shown in Fig. 5-10b.

where C_1 and C_2 are constants with dimensions of temperature. As is well-known, using suitable manipulations, the VFT and the WLF forms may be shown to be equivalent. Although the WLF and VFT equations are equivalent, the slightly simpler form of the VFT equation is often preferred.

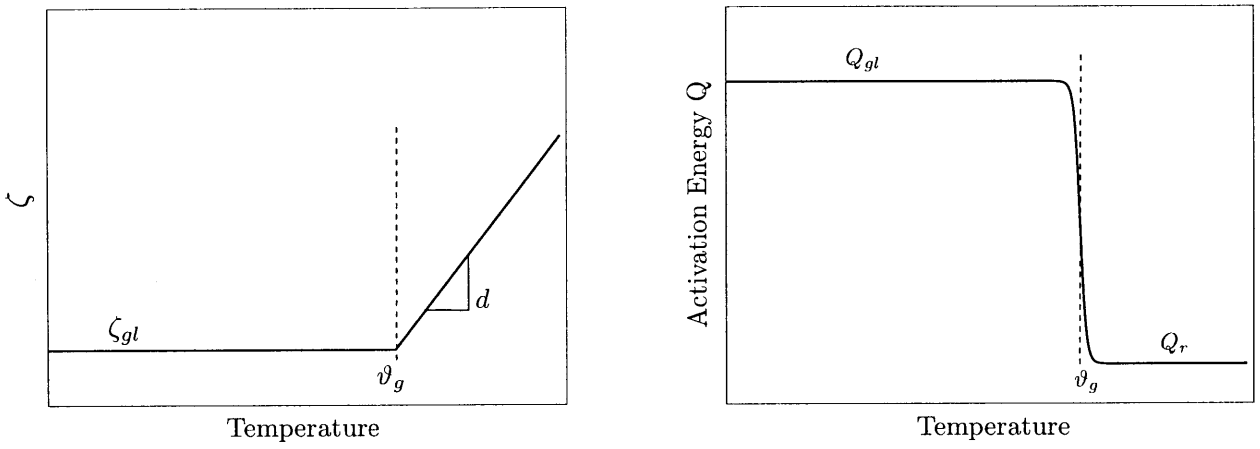

Figure 4-9: Schematic of temperature dependence of (a) normalized free volume ζ, and (b) activation energy Q.

Evolution equations for internal variables

In a general form, the internal variables $\boldsymbol{\xi}^{(1)}$ and $\mathbf{A}$ are presumed to evolve according to the differential equations (cf. (2.140) in Chapter 2)

$$\left.\begin{aligned} \dot{\xi}_i^{(1)} &= \underbrace{\mathbf{h}_i(\boldsymbol{\Lambda}^{(1)})\,\nu^{p(1)}}_{\text{dynamic evolution}} - \underbrace{\mathcal{R}_i(\boldsymbol{\Lambda}^{(1)})}_{\text{static recovery}}\,, \\ \dot{\overline{\mathbf{A}}} &= \underbrace{\mathbf{D}^{p(1)}\mathbf{A} + \mathbf{A}\mathbf{D}^{p(1)} - \mathbf{G}(\boldsymbol{\Lambda}^{(1)})\,\nu^{p(1)}}_{\text{dynamic evolution}} - \underbrace{\mathbf{G}_{\text{static}}(\boldsymbol{\Lambda}^{(1)})}_{\text{static recovery}}, \end{aligned}\right\} \tag{4.46}$$

with the functions h_i, $\mathcal{R}_i$, $\mathbf{G}$, and $\mathbf{G}_{\text{static}}$ isotropic functions of their arguments.

Remark 4: In (4.46), the functions $\mathcal{R}_i$ and $\mathbf{G}_{\text{static}}$ represent *static recovery* (or time recovery, or thermal recovery), since they do not depend on the plastic strain rate. The static recovery terms are important in *long time* situations such as creep experiments over a period of hours and days at high temperatures. Here, we focus our attention on thermal forming processes that occur in relatively shorter periods of time (typically less than 5 to 20 minutes), in which case the slow static recovery effects may be neglected. Accordingly, in what follows, as a simplification, *we neglect the effects of any static recovery in the evolution of the internal variables.*

(i) **Evolution of φ and S_a:**

We assume that the material disorders, and is accompanied by a microscale dilatation as plastic deformation occurs, resulting in an increase of the order-parameter φ,[8] and this increase in disorder leads to a change in the resistance S_a, causing a transient change in the flow stress of the material as plastic deformation proceeds. Accordingly, the evolution of the resistance S_a is coupled to the evolution of the order-parameter φ. Specifically, we take the evolution of S_a to be governed by[9]

$$\left.\begin{aligned} \dot{S}_a &= H_a\, \nu^{p(1)}, \qquad \text{with initial value} \qquad S_a(\mathbf{X},0) = S_{a0}, \\ H_a &= h_a\, (S_a^* - S_a)\,, \qquad \text{and} \qquad S_a^* = \hat{S}_a^*(\nu^{p(1)}, \vartheta, \varphi), \end{aligned}\right\} \tag{4.47}$$

and assume that

$$\left.\begin{aligned} \dot{\varphi} &= \beta \nu^{p(1)}, \qquad \text{with initial value} \qquad \varphi(\mathbf{X},0) = \varphi_0, \\ \beta &= g\, (\varphi^* - \varphi)\,, \qquad \text{with} \qquad \varphi^* = \hat{\varphi}^*(\nu^{p(1)}, \vartheta) \geq 0; \end{aligned}\right\} \tag{4.48}$$

here β is a *shear-induced disordering function.*

In the coupled evolution equations for S_a and φ, the parameters h_a, g, S_{a0} and φ_0 are constants (possibly temperature-dependent). The function H_a represents the strain-hardening/softening function for the resistance S_a during plastic flow: the material hardens if $S_a < S_a^*$, and softens if $S_a > S_a^*$. The critical value S_a^* of S_a controlling such hardening/softening transitions is assumed to depend on the current values of the plastic strain rate, temperature, and the order-parameter φ. The function S_a^*, which controls the magnitude of the stress-overshoot, is taken as

$$S_a^* = b\,(\varphi^* - \varphi)\,. \tag{4.49}$$

In the disordering function β, the parameter φ^* represents a strain-rate and temperature dependent critical value for the order-parameter: the material disorders when $\varphi < \varphi^*$, and becomes less disordered when $\varphi > \varphi^*$. Considering the temperature and strain-rate dependence of φ^*, it is expected to decrease with increasing temperature at a fixed strain-rate, and increase with strain-rate at a fixed temperature. We model this temperature and strain rate dependence of φ^* using the following phenomenological

[8]The microscale dilatation is extremely small, and at the macroscopic level we presume the plastic flow to be incompressible.

[9]Coupled differential evolution equations of this type have previously been used to model yield peaks in granular materials (Anand and Gu, 2000), as well as amorphous polymeric materials (Anand and Gurtin, 2003a; Ames, 2007), and amorphous metallic glasses (Henann and Anand, 2008).

equation

$$\varphi^*(\nu^{p(1)},\vartheta) = \begin{cases} z\left(1-\dfrac{\vartheta}{\vartheta_g}\right)^r \left(\dfrac{\nu^{p(1)}}{\nu_r}\right)^s & \text{if } (\vartheta \le \vartheta_g) \text{ and } (\nu^{p(1)} > 0), \\ 0 & \text{if } (\vartheta > \vartheta_g) \text{ or } (\nu^{p(1)} = 0), \end{cases} \tag{4.50}$$

with constants (z, r, s).

Thus, gathering the number of material parameters introduced to phenomenologically model the yield-peak, we have the following rather large list

$$\big(h_a, b, S_{a0}, g, \varphi_0, z, r, s\big),$$

with some of these parameters possessing additional temperature-dependence. We assume that all but g are independent of temperature. The parameter g in (5.29), which controls the width of the yield-peak (higher values of g results in a narrower peak), is assumed to increase linearly with temperature:

$$g(\vartheta) = g_1 + g_2\,\vartheta. \tag{4.51}$$

Using these equations, the evolution of the order parameter φ with strain, and corresponding evolution of internal resistance S_a is schematically shown in Fig. 5-11a. By suitable choice of material constants, the coupled evolution equations for the internal variables φ and S_a may be used to model the "yield-peak" in the stress-strain response of glassy polymers.

Remark 5: Modeling the temperature and rate-sensitivity of the yield-peak over a wide-range of temperatures and strain rates is known to be complex. If a simpler theory with fewer material parameters is desired, and if it is deemed that modeling the yield-peak is not of interest, then there is no need to introduce the internal variables φ and S_a, and thereby also the attendant constants in their evolution equations.

(ii) **Evolution of S_b**:

In most of the literature on amorphous polymers, the rapid increase in stress levels at large deformations has been attributed to entropic-elasticity and the limited-extensibility of the polymer chains. However, our experience with experiments that involve both loading to large strains and *subsequent unloading*, indicate that if in a corresponding theoretical model the rapid increase in stress levels during loading is attributed entirely to the limited chain-extensibility and entropic-elasticity effects, then the unloading response is incorrectly predicted — there is too much "elastic recovery" upon unloading. It is for this reason that we have introduced the internal variable S_b to model a *dissipative* resistance to plastic flow which arises at large strains as the

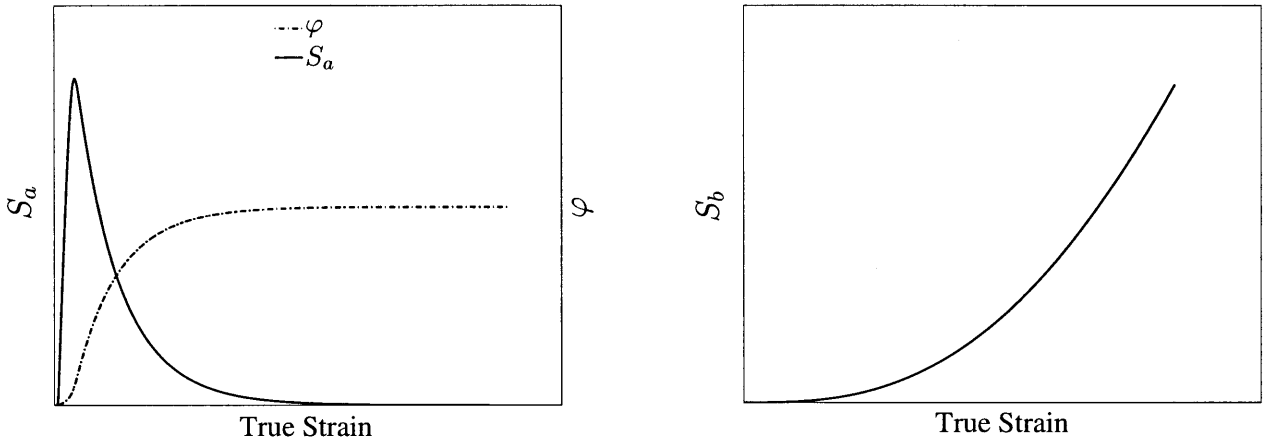

Figure 4-10: Schematic of the evolution of internal variables (φ, S_a, S_b) with strain: (a) evolution of φ and S_a; and (b) evolution of S_b.

chains are pulled taut between entanglements, and there is increasing frictional interaction between the pendant side-groups; this resistance is *in addition* to any entropic contribution from network chain-stretching.

The evolution of the internal variable S_b is taken to be governed by the differential equation

$$\dot{S}_b = h_b\,(\bar{\lambda} - 1)\,(S_b^* - S_b)\,\nu^{p(1)}, \quad \text{with initial value} \quad S_b(\mathbf{X}, 0) = S_{b0} \geq 0. \tag{4.52}$$

In (4.52) the material parameters are h_b and S_b^*. We take h_b to be a temperature independent constant, while the saturation value S_b^* is taken to have the following temperature dependence

$$S_b^*(\vartheta) = \frac{1}{2}\,(S_{gl} + S_r) - \frac{1}{2}\,(S_{gl} - S_r)\tanh\left(\frac{1}{\Delta}(\vartheta - \vartheta_g)\right) - L(\vartheta - \vartheta_g), \tag{4.53}$$

where S_{gl} and S_r $(< S_{gl})$ are values of S_b^* in the glassy and rubbery regions near the glass transition temperature ϑ_g, and L represents the slope of the temperature variation of S_b^* beyond the glass transition region, with

$$L = \begin{cases} L_{gl} & \vartheta \leq \vartheta_g, \\ L_r & \vartheta > \vartheta_g. \end{cases} \tag{4.54}$$

A schematic of the evolution of S_b with an equivalent strain in a monotonic isothermal experiment is shown in Fig. 5-11b.

(iii) **Evolution of A**:

Finally, the evolution equation for $\mathbf{A}$ is taken as

$$\dot{\mathbf{A}} = \mathbf{D}^{p(1)}\mathbf{A} + \mathbf{A}\mathbf{D}^{p(1)} - \gamma\,\mathbf{A}\,\ln\mathbf{A}\,\nu^{p(1)}, \qquad \mathbf{A}(\mathbf{X},0) = \mathbf{1}, \tag{4.55}$$

where $\gamma \geq 0$ is a constitutive parameter which governs the dynamic recovery of $\mathbf{A}$; we take it to be independent of temperature. This evolution equation is a generalization of the non-linear kinematic-hardening rule of the small deformation theory of classical metal viscoplasticity (e.g., Chaboche, 2008), but here, as in Chapter 3, applied to large deformation polymer-viscoplasticity. Note that on account of the assumed temperature dependence of the back stress modulus B in (4.19), the back-stress $\mathbf{M}_{\text{back}}$ decreases as ϑ approaches ϑ_g, and vanishes for all $\vartheta > \vartheta_g$.

4.3.2 Constitutive equations for micromechanism $\alpha = 2$

1. Free energy

Let

$$\mathbf{F}^{e\,(2)}_{\text{dis}} \stackrel{\text{def}}{=} J^{-1/3}\,\mathbf{F}^{e(2)}, \quad \det\mathbf{F}^{e\,(2)}_{\text{dis}} = 1, \tag{4.56}$$

denote the distortional part of $\mathbf{F}^{e(2)}$. Correspondingly, let

$$\mathbf{C}^{e\,(2)}_{\text{dis}} \stackrel{\text{def}}{=} (\mathbf{F}^{e\,(2)}_{\text{dis}})^{\top}\mathbf{F}^{e\,(2)}_{\text{dis}} = J^{-2/3}\mathbf{C}^{e(2)}, \tag{4.57}$$

denote the distortional right Cauchy-Green tensor and consider a free energy function in the special form [10]

$$\psi^{(2)} = \bar{\psi}^{e\,(2)}(\mathbf{C}^{e\,(2)}_{\text{dis}}, \vartheta). \tag{4.58}$$

As discussed in Chapter 3, there is a conceptual difficulty with using statistical-mechanical ideas of the theory of entropic rubber elasticity to describe the strain hardening due to chain-stretching at temperatures below the glass transition temperature, because at these temperatures the chains do not have sufficient mobility to sample all possible molecular conformations. For this reason, we employ a simple *phenomenological* form for the free energy function $\psi^{(2)}$ proposed by Gent (1996):

$$\psi^{(2)} = -\tfrac{1}{2}\mu^{(2)}\,I_m^{(2)}\,\ln\Big(1 - \frac{I_1^{(2)} - 3}{I_m^{(2)}}\Big), \qquad \text{with} \qquad I_1^{(2)} \stackrel{\text{def}}{=} \operatorname{tr}\mathbf{C}^{e\,(2)}_{\text{dis}}, \tag{4.59}$$

where

$$\mu^{(2)}(\vartheta) > 0, \qquad \text{and} \qquad I_m^{(2)}(\vartheta) > 3 \tag{4.60}$$

are two temperature-dependent material constants, with $\mu^{(2)}$ representing the ground state rubbery shear modulus of the material, and $I_m^{(2)}$ representing maximum value of $(I_1^{(2)} - 3)$, associated with the limited extensibility of the polymer chains.

[10] Since $J^{e\,(\alpha)} = J$, and we have already accounted for a volumetric elastic energy for $\psi^{(1)}$, we do not allow for a volumetric elastic energy for $\psi^{(2)}$ or $\psi^{(3)}$.

The Gent free energy function has been shown by Boyce (1996) to yield predictions for the stress-strain response similar to the entropic-network model of Arruda and Boyce (1993a). However, since the Gent free-energy function is phenomenological, we are free to specify a temperature variation of the moduli $\mu^{(2)}(\vartheta) > 0$ and $I_m^{(2)}(\vartheta)$ to fit experimentally-observed trends, rather than those dictated by statistical mechanics theories of entropic elasticity. The material parameter $\mu^{(2)}$ in (5.38) is strongly temperature dependent. Experimental results indicate that the rubbery shear modulus $\mu^{(2)}$ *decreases* with increasing temperature. The empirical function chosen to fit the experimentally-observed temperature dependence of $\mu^{(2)}$ is

$$\mu^{(2)}(\vartheta) = \mu_g^{(2)} \exp\Big(- N(\vartheta - \vartheta_g)\Big), \tag{4.61}$$

$\mu_g^{(2)}$ is the value of $\mu^{(2)}$ at the glass transition temperature (ϑ_g), and N is a parameter that represents the slope of temperature variation on a logarithmic scale. The parameter $I_m^{(2)}$ is taken to be temperature-independent constant

$$I_m^{(2)}(\vartheta) \approx \text{constant}. \tag{4.62}$$

2. Cauchy stress. Mandel stress

Using (2.131), the free energy (5.38) yields the corresponding second-Piola stress as

$$\mathbf{S}^{e(2)} = 2\frac{\partial \psi^{(2)}}{\partial \mathbf{C}^{e(2)}} \tag{4.63}$$

$$= J^{-2/3}\mu^{(2)}\left(1 - \frac{I_1^{(2)} - 3}{I_m^{(2)}}\right)^{-1}\left[1 - \frac{1}{3}\left(\operatorname{tr}\mathbf{C}_{\text{dis}}^{e\,(2)}\right)\mathbf{C}_{\text{dis}}^{e(2)\,-1}\right], \tag{4.64}$$

and use of (3.22) gives the contribution $\mathbf{T}^{(2)}$ to Cauchy stress as

$$\mathbf{T}^{(2)} = J^{-1}\mathbf{F}^{e(2)}\mathbf{S}^{e(2)}\mathbf{F}^{e(2)\top} \tag{4.65}$$

$$= J^{-1}\left[\mu^{(2)}\left(1 - \frac{I_1^{(2)} - 3}{I_m^{(2)}}\right)^{-1}(\mathbf{B}_{\text{dis}}^{e\,(2)})_0\right], \tag{4.66}$$

where

$$\mathbf{B}_{\text{dis}}^{e\,(2)} \overset{\text{def}}{=} \mathbf{F}_{\text{dis}}^{e\,(2)}(\mathbf{F}_{\text{dis}}^{e\,(2)})^{\top} = J^{-2/3}\mathbf{B}^{e\,(2)} \tag{4.67}$$

denotes the elastic distortional left Cauchy-Green tensor. Also, from (2.132) and (5.42) the corresponding Mandel stress is

$$\mathbf{M}^{e(2)} = \mathbf{C}^{e(2)}\mathbf{S}^{e(2)} = \mu^{(2)}\left(1 - \frac{I_1^{(2)} - 3}{I_m^{(2)}}\right)^{-1}(\mathbf{C}_{\text{dis}}^{e\,(2)})_0, \tag{4.68}$$

which gives the *equivalent shear stress* for plastic flow as

$$\bar{\tau}^{(2)} \stackrel{\text{def}}{=} \frac{1}{\sqrt{2}} |\mathbf{M}^{e(2)}|. \tag{4.69}$$

3. Flow rule. Internal variables

The evolution equation for $\mathbf{F}^{p(2)}$ is

$$\dot{\mathbf{F}}^{p(2)} = \mathbf{D}^{p(2)} \mathbf{F}^{p(2)}, \tag{4.70}$$

with the plastic stretching $\mathbf{D}^{p(2)}$ given by

$$\mathbf{D}^{p(2)} = \nu^{p(2)} \left(\frac{\mathbf{M}^{e(2)}}{2\bar{\tau}^{(2)}} \right), \qquad \text{where} \quad \nu^{p(2)} \stackrel{\text{def}}{=} \sqrt{2} |\mathbf{D}^{p(2)}| \tag{4.71}$$

is the corresponding equivalent plastic shear strain rate. With $S^{(2)}(\vartheta)$ a positive-valued stress-dimensioned shear resistance, we take the corresponding strength relation as a simple power law

$$\bar{\tau}^{(2)} = S^{(2)} \left(\frac{\nu^{p(2)}}{\nu_0^{(2)}} \right)^{m^{(2)}}, \tag{4.72}$$

where $\nu_0^{(2)}$ is a reference plastic shear strain rate with units of 1/time, and $m^{(2)}$ is a positive-valued strain-rate sensitivity parameter. This gives

$$\nu^{p(2)} = \nu_0^{(2)} \left(\frac{\bar{\tau}^{(2)}}{S^{(2)}} \right)^{1/m^{(2)}}. \tag{4.73}$$

We assume that $S^{(2)}$ varies with temperature,

$$S^{(2)}(\vartheta) = \tfrac{1}{2}(S_{gl}^{(2)} + S_r^{(2)}) - \tfrac{1}{2}(S_{gl}^{(2)} - S_r^{(2)}) \tanh\left(\frac{1}{\Delta}(\vartheta - \vartheta_g) \right), \tag{4.74}$$

where, $S^{(2)} = S_{gl}^{(2)}$ in the glassy regime, and $S^{(2)} = S_r^{(2)} (< S_{gl}^{(2)})$ in the rubbery regime, and as in (5.8), Δ is a parameter related to the temperature range across which the glass transition occurs. A high value of $S^{(2)} = S_{gl}^{(2)}$ leads to $\nu^{p(2)} \approx 0$ when $\vartheta < \vartheta_g$, and as the temperature increases through the glass transition, the value of $S^{(2)}$ smoothly transitions to a very low value, allowing for plastic flow above ϑ_g. This assumption is meant to reflect the major effect of the rapid destruction of a *large fraction* of the mechanical crosslinks as the temperature increases beyond ϑ_g. Thus, under a macroscopically-imposed deformation history at temperatures greater than a few degrees higher than ϑ_g, micromechanism $\alpha = 2$ freely deforms inelastically by

relative chain-slippage, and there is no further increase in the corresponding elastic stretch $\mathbf{U}^{e\,(2)}$, and thereby the corresponding stress; cf. Fig. 5-7b for $\alpha = 2$.

4.3.3 Constitutive equations for micromechanism $\alpha = 3$

1. Free energy

As for micromechanism $\alpha = 2$, we take the free energy in a Gent form:

$$\psi^{(3)} = -\tfrac{1}{2}\mu^{(3)} I_m^{(3)} \ln\left(1 - \frac{I_1^{(3)} - 3}{I_m^{(3)}}\right), \qquad \text{with} \qquad I_1^{(3)} \stackrel{\text{def}}{=} \operatorname{tr} \mathbf{C}_{\text{dis}}^{e\,(3)}, \tag{4.75}$$

where

$$\mu^{(3)} > 0, \qquad \text{and} \qquad I_m^{(3)} > 3 \tag{4.76}$$

are two material constants, with $\mu^{(3)}$ representing the ground-state rubbery shear modulus of the material, and $I_m^{(3)}$ representing maximum value of $(I_1^{(3)} - 3)$. For simplicity, these two material constants are assumed to be *temperature-independent.*

2. Mandel stress. Cauchy stress

Using (2.131), the free energy (5.54) yields the corresponding second Piola stress as

$$\mathbf{S}^{e(3)} = J^{-2/3}\mu^{(3)}\left(1 - \frac{I_1^{(3)} - 3}{I_m^{(3)}}\right)^{-1}\left[\mathbf{1} - \frac{1}{3}\left(\operatorname{tr} \mathbf{C}_{\text{dis}}^{e\,(3)}\right)\mathbf{C}_{\text{dis}}^{e(3)\,-1}\right], \tag{4.77}$$

and use of (3.22) gives the contribution $\mathbf{T}^{(3)}$ to Cauchy stress as

$$\mathbf{T}^{(3)} = J^{-1}\left[\mu^{(3)}\left(1 - \frac{I_1^{(3)} - 3}{I_m^{(3)}}\right)^{-1}(\mathbf{B}_{\text{dis}}^{e\,(3)})_0\right]. \tag{4.78}$$

Also, from (2.132) and (5.56) the corresponding Mandel stress is

$$\mathbf{M}^{e(3)} = \mu^{(3)}\left(1 - \frac{I_1^{(3)} - 3}{I_m^{(3)}}\right)^{-1}(\mathbf{C}_{\text{dis}}^{e\,(3)})_0, \tag{4.79}$$

which gives the *equivalent shear stress* for plastic flow for micromechanism $\alpha = 3$ as

$$\bar{\tau}^{(3)} \stackrel{\text{def}}{=} \frac{1}{\sqrt{2}}|\mathbf{M}^{e(3)}|. \tag{4.80}$$

3. Flow rule. Internal variables

The evolution equation for $\mathbf{F}^{p(3)}$ is

$$\dot{\mathbf{F}}^{p\,(3)} = \mathbf{D}^{p(3)}\,\mathbf{F}^{p(3)}, \tag{4.81}$$

with the plastic stretching $\mathbf{D}^{p(3)}$ given by

$$\mathbf{D}^{p(3)} = \nu^{p(3)} \left(\frac{\mathbf{M}^{e(3)}}{2\bar{\tau}^{(3)}} \right), \qquad \text{where} \quad \nu^{p(3)} \stackrel{\text{def}}{=} \sqrt{2} |\mathbf{D}^{p(3)}| \tag{4.82}$$

is the corresponding equivalent plastic shear strain rate. We assume that $\nu^{p(3)} = 0$ when $\vartheta < \vartheta_g$, and for $\vartheta > \vartheta_g$, with $S^{(3)}$ a positive-valued stress-dimensioned shear resistance, we take the corresponding strength relation as a simple power law

$$\bar{\tau}^{(3)} = S^{(3)} \left(\frac{\nu^{p(3)}}{\nu_0^{(3)}} \right)^{m^{(3)}}, \tag{4.83}$$

where $\nu_0^{(3)}$ is a reference plastic shear strain rate with units of 1/time, and $m^{(3)}$ is a positive-valued strain-rate sensitivity parameter. This gives

$$\nu^{p(3)} = \begin{cases} 0 & \text{if} \quad \vartheta < \vartheta_g, \\ \nu_0^{(3)} \left(\dfrac{\bar{\tau}^{(3)}}{S^{(3)}} \right)^{1/m^{(3)}} & \text{if} \quad \vartheta \geq \vartheta_g. \end{cases} \tag{4.84}$$

4. Evolution equations for internal variable $S^{(3)}$

The internal variable $S^{(3)}$ models the dissipative resistance caused by the sliding polymer chains during the tortuous process of molecular disengagement that has come to be know as "reptation" at temperatures above ϑ_g. The evolution of $S^{(3)}$ is taken to be governed by

$$\dot{S}^{(3)} = h_3 \left(\bar{\lambda}_{\text{dis}} - 1 \right) \nu^{p(3)}, \quad \text{with initial value} \quad S^{(3)}(\mathbf{X}, 0) = S_0^{(3)} \geq 0. \tag{4.85}$$

Here $h_3(\vartheta)$ and $S_0^{(3)}(\vartheta)$ are temperature dependent material parameters, and

$$\bar{\lambda}_{\text{dis}} \stackrel{\text{def}}{=} \sqrt{\text{tr}\, \mathbf{C}_{\text{dis}}/3} = \sqrt{\mathrm{B}^{p\,(3)} : \mathbf{C}_{\text{dis}}^{e\,(3)}/3} \tag{4.86}$$

is an effective *distortional stretch.* The temperature dependence of $S_0^{(3)}$ and h_3 is taken to obey the following simple forms

$$S_0^{(3)} = S_g^{(3)} \exp\Big(- Y(\vartheta - \vartheta_g) \Big), \tag{4.87}$$

$$h_3 = h_{3g} \exp\Big(- Z(\vartheta - \vartheta_g) \Big). \tag{4.88}$$

4.3.4 Fourier's Law

The heat flux is taken to be given by Fourier's law

$$\mathbf{q}_{\mathrm{R}} = -\kappa \nabla \vartheta, \tag{4.89}$$

with $\kappa(\vartheta) > 0$ the thermal conductivity. The temperature dependence of the thermal conductivity for the three polymers is shown in Fig. 5-12a.[11]

4.3.5 Partial differential equations for the deformation and temperature fields

The partial differential equation for the deformation is obtained from the local force balance

$$\mathrm{Div}\,\mathbf{T}_{\mathrm{R}} + \mathbf{b}_{0\mathrm{R}} = \rho_{\mathrm{R}} \ddot{\boldsymbol{\chi}}, \tag{4.90}$$

where $\mathbf{b}_{0\mathrm{R}}$ is the non-inertial body force per unit volume of the reference body, $\rho_{\mathrm{R}} > 0$ is the mass density, and

$$\mathbf{T}_{\mathrm{R}} = J\mathbf{T}\mathbf{F}^{-\top} \tag{4.91}$$

is the standard first Piola stress, with $\mathbf{T}$ given by the sum of (5.13), (5.43) and (5.57).

At this stage of the development of the theory and the concomitant experimental database, the "thermoelastic coupling" terms in (2.147) which give rise to a temperature change due to variations of $\mathbf{C}^{e\,(\alpha)}$ and $\mathbf{A}$ are not well-characterized, nor is the dependence of the specific heat c, defined in (2.146), on these quantities. *Much work needs to be done to characterize these dependencies.* Here, as *approximations*, (i) we assume that $c \approx \hat{c}(\vartheta)$ (independent of $\mathbf{C}^{e\,(\alpha)}$ and $\mathbf{A}$), and may be obtained from experimental measurements; and (ii) we neglect the thermoelastic coupling terms, and assume instead that only a fraction $0 \lessapprox \omega \lessapprox 1$ of the rate of plastic dissipation contributes to the temperature changes. Under these approximative assumptions, and since we have neglected static recovery of $\mathbf{A}$, (2.147) in Chapter 2 reduces to

$$c\dot{\vartheta} = -\mathrm{Div}\,\mathbf{q}_{\mathrm{R}} + q_{\mathrm{R}} + \omega \left(\bar{\tau}^{(1)} \nu^{p\,(1)} + \tfrac{1}{2} B \gamma \, |\ln \mathbf{A}|^2 \nu^{p\,(1)} + \bar{\tau}^{(2)} \nu^{p\,(2)} + \bar{\tau}^{(3)} \nu^{p\,(3)} \right). \tag{4.92}$$

The temperature dependence of specific heat for the three polymers is shown in Fig. 5-12b.[12]

[11] For Zeonex-690R, the data was obtained from Zeon chemicals. For PC and PMMA, the data was obtained from the material database of the commercial software program Moldflow.

[12] For Zeonex, data was obtained from Zeon chemicals. For PC and PMMA see (Bicerano, 1993; Van Krevelen, 1990).

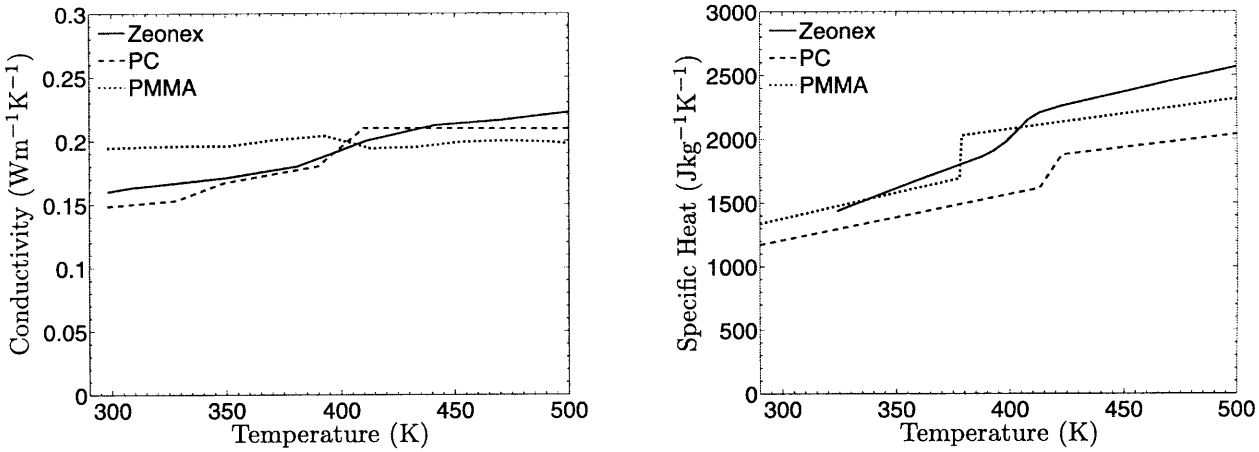

Figure 4-11: Temperature dependence of (a) thermal conductivity, and (b) specific heat.

4.4 Fit of the stress-strain curves and material parameters for Zeonex-690R, PC, and PMMA

The material parameters appearing in our model were calibrated by fitting the experimental stress-strain data for Zeonex-690R, PC, and PMMA with the help of a MATLAB implementation of a one-dimensional version of our model which is detailed in the Appendix B, as well as three-dimensional finite element simulations using a single element. Under certain circumstances, when it became necessary to account for heat generation due to plastic dissipation and thermal conduction in the simple compression experiments,[13] fully thermo-mechanically-coupled multi-element simulations were required (cf. Ames, 2007). Our heuristic material parameter calibration procedure for our model is described in the Appendix B. The material parameters for Zeonex-690R, PC, and PMMA determined by using this procedure are listed in Table 4.1.

The fit of the constitutive model to the experimental stress-strain curves for Zeonex-690R, at various temperatures ranging from 25 °C to 180 °C and strain rates ranging from 3×10^{-4} to $3 \times 10^{-1}\,\mathrm{s}^{-1}$, is shown in Fig. 5-13. The fit of the constitutive model to experimental stress-strain curves for PC (experiments on PC were conducted by Shawn A. Chester), at various temperatures ranging from 25 °C to 175 °C and strain rates ranging from 10^{-3} to $10^{-1}\,\mathrm{s}^{-1}$, is shown in Fig. 5-14. Finally, Fig. 5-15 shows the fit of the constitutive model to the experimental stress-strain curves for PMMA (from Ames, 2007) at various temperatures ranging from 25 °C to 170 °C and strain rates ranging from 3×10^{-4} to $10^{-1}\,\mathrm{s}^{-1}$.

For all three amorphous polymers (Zeonex-690R, PC, and PMMA), the specialized constitutive model performs *acceptably* (but not perfectly!) in reproducing the following major features of the macroscopic stress-strain response of these materials:

[13] Typically to fit the experimental data at strain rates of 0.01 s^{-1} and 0.03 s^{-1}.

- **For temperatures** $\vartheta < \vartheta_g$: (a) the strain rate and temperature dependent yield strength; (b) the transient yield-peak and strain-softening which occurs due to deformation-induced disordering; (c) the subsequent rapid strain-hardening due to alignment of the polymer chains at large strains; (d) the unloading response at large strains; and (e) the temperature rise due to plastic-dissipation and the limited time for heat-conduction for the compression experiments performed at strain rates $\gtrapprox 0.01\,\mathrm{s}^{-1}$.

- **For temperatures** $\vartheta > \vartheta_g$: (a) the extreme drop in initial stiffness at these temperatures, relative to those below ϑ_g; (b) the lack of a yield-peak; (c) the significant drop in maximum stress levels to $\lessapprox 5\,\mathrm{MPa}$, relative to $\approx 250\,\mathrm{MPa}$ at temperatures below ϑ_g; (c) the highly non-linear, strain-hardening stress-strain response during the loading-phase; (f) the non-linear unloading response and permanent-set — for Zeonex-690R and PC the amount of permanent-set increases dramatically as the temperature increases, while for PMMA the amount of permanent-set is substantially smaller.

Overall, the model better reproduces the experimentally-observed stress-strain response for the three materials at temperatures below ϑ_g, than it does for those for temperatures above ϑ_g. However, with "only three micromechanisms" (but, numerous material parameters) we feel that the model, as it stands, should be useful for modeling, simulation, and design of various polymer-processing operations, which we turn to next.

Table 4.1: Material parameters for Zeonex-690R, PC and PMMA

Parameter	Zeonex-690R	PC	PMMA
ρ (kg m^{-3})	1010	1200	1200
α_{gl} (K^{-1})	7×10^{-5}	6.5×10^{-5}	7×10^{-5}
α_r (K^{-1})	12×10^{-5}	12×10^{-5}	16×10^{-5}
ν_r (s^{-1})	5.2×10^{-4}	5.2×10^{-4}	5.2×10^{-4}
ϑ_r (K)	404	415	385
n (K)	2.5	2.2	2.2
Δ (K)	2.0	1.6	1.7
G_{gl} (MPa)	482	640	300
G_r (MPa)	3.4	4.0	1.4
M_{gl} (MPa K^{-1})	0.16	0.73	10
M_r (MPa K^{-1})	0.034	0.017	.003
ν_{gl}^{poi}	0.40	0.37	0.35
ν_r^{poi}	0.49	0.49	0.49
X (MPa K^{-1})	0.7	1.5	12.2
γ	6.93	26.0	34.6
α_p	0.116	0.116	0.2
$\nu_0^{(1)}$ (s^{-1})	1.73×10^{13}	1.73×10^{13}	1.73×10^{13}
$m^{(1)}$	0.16	0.14	0.22
V (m^3)	1.7×10^{-27}	1.62×10^{-27}	0.52×10^{-27}
Q_{gl} (J)	1.56×10^{-19}	1.72×10^{-19}	1.12×10^{-19}
Q_r (J)	1×10^{-20}	2×10^{-20}	2.5×10^{-20}
ζ_{gl}	0.135	0.13	0.18
d (K^{-1})	0.015	0.01	0.005
S_{a0} (MPa)	0	0	0
h_a	173	58	70
b (MPa)	5850	5850	5850
g_1	-16.17	-5.66	-5.77
g_2 (K^{-1})	0.0693	0.0381	0.0318
φ_0	0	0	0
z	0.0055	0.0058	0.012
r	0.24	0.2	0.62
s	0.042	0	0.052
S_{b0} (MPa)	0	0	0
h_b	0.577	0.173	0.577
S_{gl} (MPa)	42.7	27.7	6.9
L_{gl} (MPa K^{-1})	0.65	1.27	1.73
S_r (MPa)	1.15	0.69	0.0
L_r (MPa K^{-1})	0.029	0.023	0.0
$\mu_g^{(2)}$ (MPa)	2.8	3.5	1.3
N (K^{-1})	11.1×10^{-3}	13.5×10^{-3}	29.0×10^{-3}
$I_m^{(2)}$	6.2	6.6	5.0
$\nu_0^{(2)}$ (s^{-1})	5.2×10^{-4}	5.2×10^{-4}	5.2×10^{-4}
$m^{(2)}$	0.18	0.18	0.22
$S_{gl}^{(2)}$ (MPa)	87	87	87
$S_r^{(2)}$ (MPa)	0.01	0.01	0.01
$\mu^{(3)}$ (MPa)	0.75	0.85	0.75
$I_m^{(3)}$	6.5	12.0	9.0
$\nu_0^{(3)}$ (s^{-1})	5.2×10^{-4}	5.2×10^{-4}	5.2×10^{-4}
$m^{(3)}$	0.18	0.18	0.22
$S_g^{(3)}$ (MPa)	3.0	2.77	3.1
Y (K^{-1})	0.19	0.2	0.04
h_{3g} (MPa)	17.3	16.7	46.6
Z (K^{-1})	0.178	0.19	0.028
ω	0.8	0.8	0.65

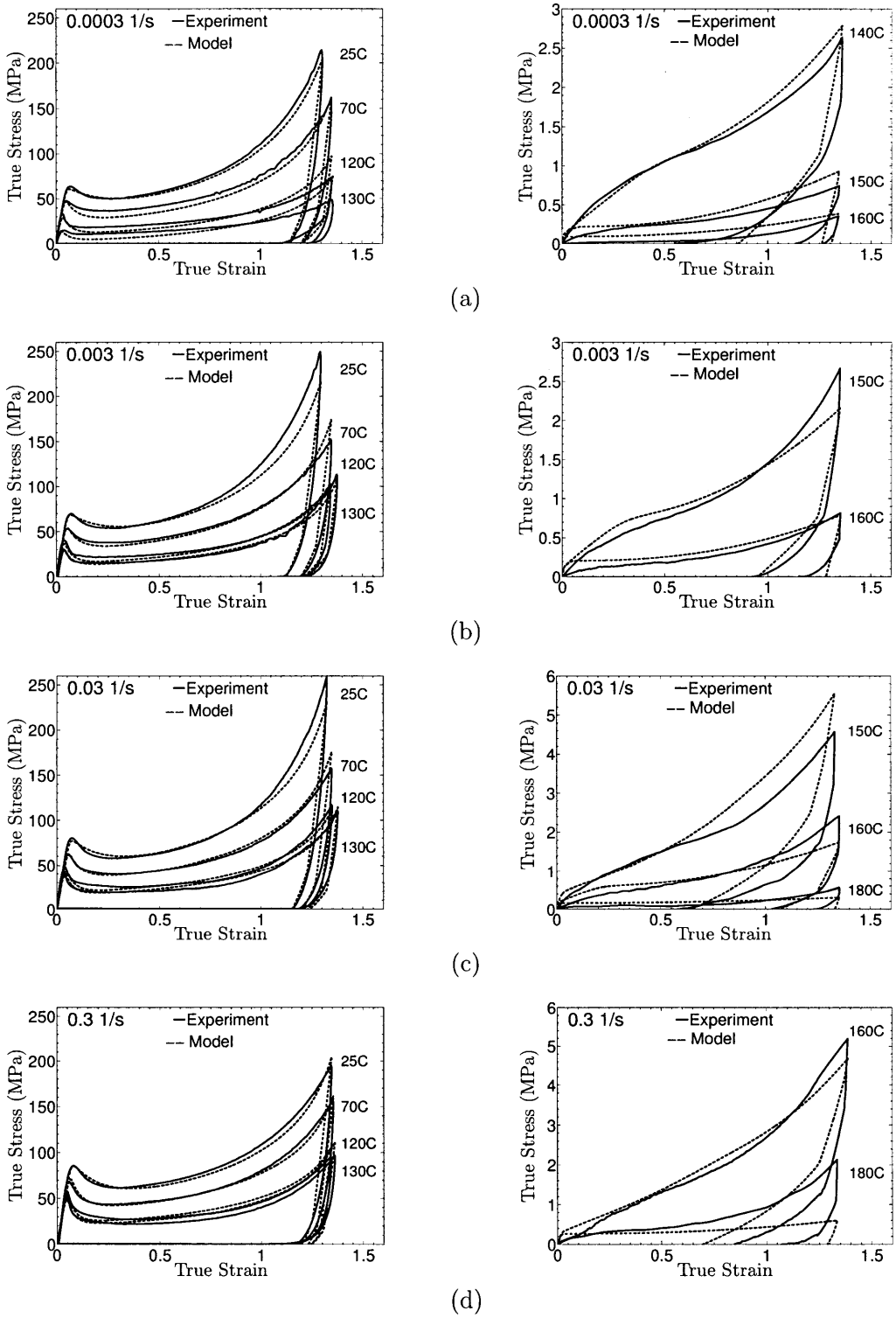

Figure 4-12: Fit of the model to experimental stress-strain curves for Zeonex-690R at various temperatures ranging from 25 °C to 180 °C at four strain rates (a) 3×10^{-4} s^{-1}, (b) 3×10^{-3} s^{-1}, (c) 3×10^{-2} s^{-1}, and (d) 3×10^{-1} s^{-1}. The experimental data is plotted as solid lines, while the fit is shown as dashed lines.

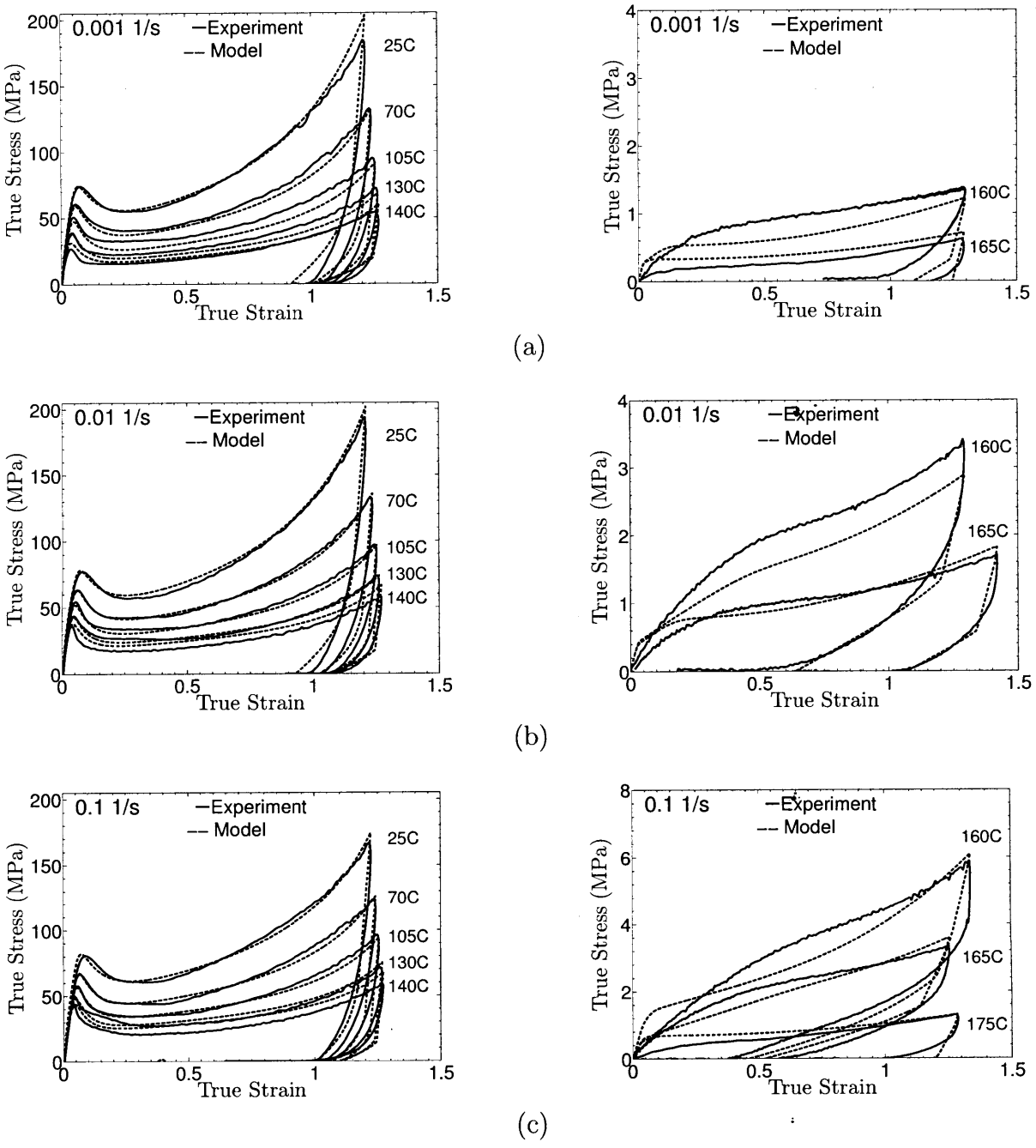

Figure 4-13: Fit of the model to experimental stress-strain curves for PC at various temperatures ranging from 25 °C to 175 °C at three strain rates (a)10^{-3} s^{-1}, (b) 10^{-2} s^{-1}, and (c) 10^{-1} s^{-1}. The experimental data (courtesy Shawn A. Chester) is plotted as solid lines, while the fit is shown as dashed lines.

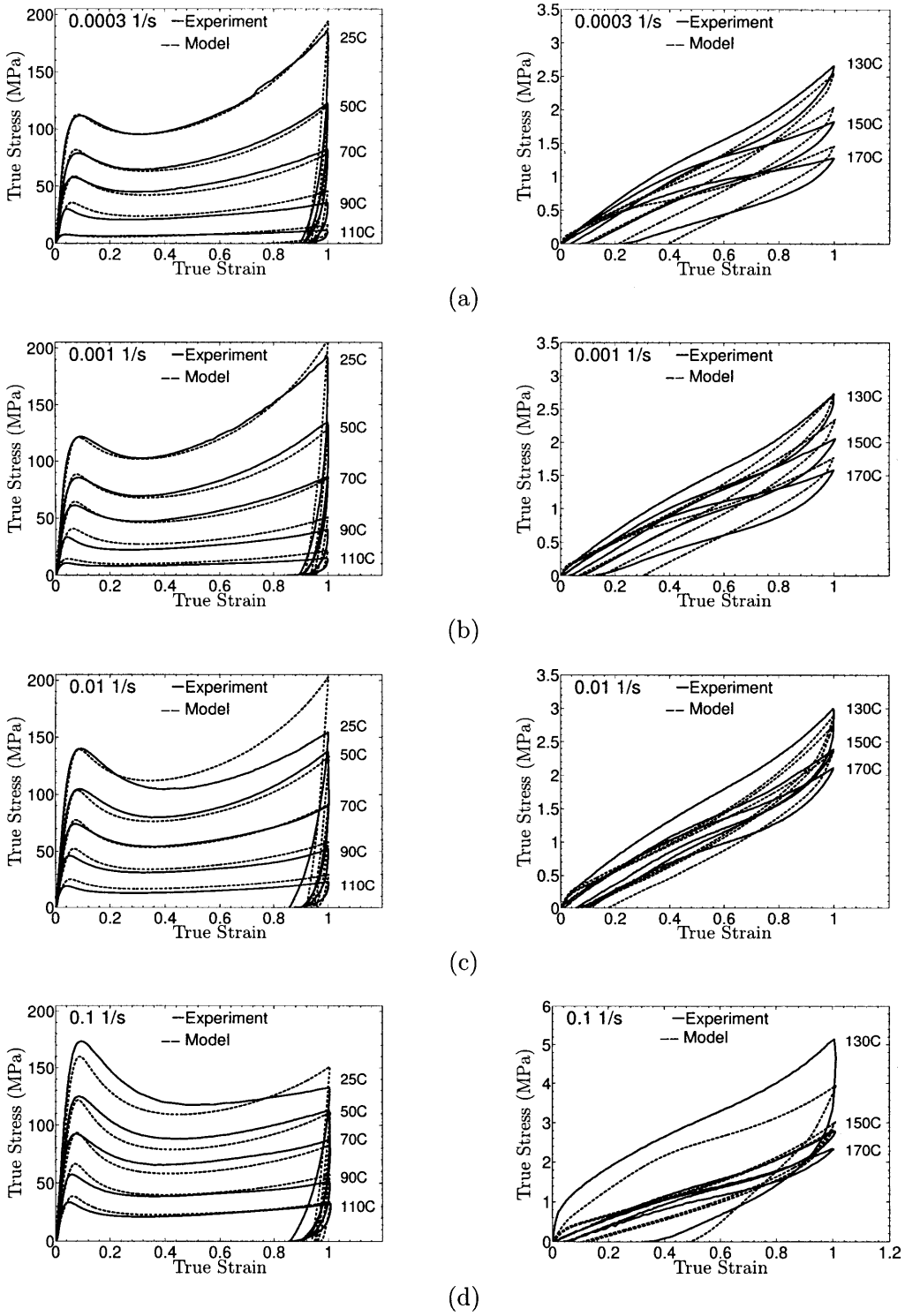

Figure 4-14: Fit of the model to experimental stress-strain curves for PMMA at various temperatures ranging from 25 °C to 170 °C at four strain rates (a) 3×10^{-4} s^{-1}, (b) 10^{-3} s^{-1}, (c) 10^{-2} s^{-1}, and (d) 10^{-1} s^{-1}. The experimental data (from Ames (2007)) is plotted as solid lines, while the fit is shown as dashed lines.

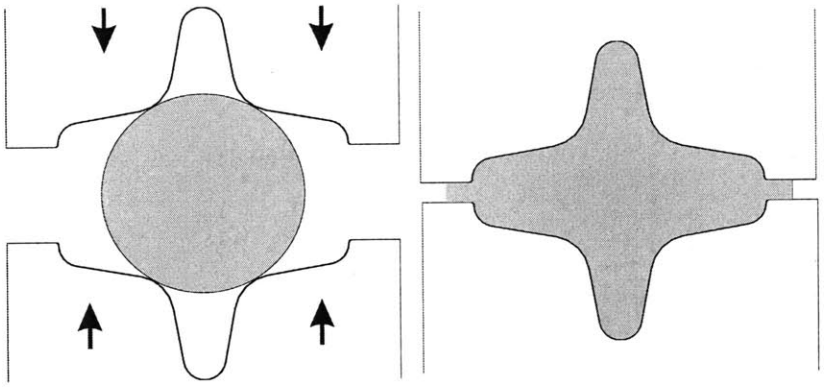

Figure 4-15: Schematic of the plane-strain cruciform forging experiment.

4.5 Validation experiments and simulations

In this section we show the results of some *validation experiments* (which were not used to determine the material parameters of our theory), and compare the results of some key macroscopic features of the experimental results against those from corresponding numerical simulations. The validation experiments include: (a) a plane-strain forging of PC at a temperature below ϑ_g, and another forging at a temperature above ϑ_g; (b) blow-forming of thin-walled semi-spherical shapes of PC above ϑ_g; and (b) micron-scale, hot-embossing of channels in Zeonex-690R above ϑ_g.

4.5.1 Plane-strain cold and hot forging of PC

Plane-strain forging experiments at 25 °C and 160 °C, under isothermal conditions, were performed on PC specimens ($\vartheta_g \approx 145\,°C$). The forging operation, cf. Fig. 5-16, converts a cylindrical specimen with a circular cross-section into a specimen with a cross-section which is in the shape of a "cruciform." The PC forging specimens had an original diameter of 12.7 mm, and were 12.7 mm deep in the plane-strain direction, which is into the plane of the paper. The split-dies which impart the cruciform shape to the workpiece, were made from hardened tool steel. For the experiment conducted at 25 °C the interfaces between the workpiece and the dies were lubricated to minimize frictional effects; however, no lubrication was used for the experiment conducted at 160 °C due to degradation of the lubricant at high temperatures. The forging experiments were carried out under displacement control to a relative die-displacement of 4.6 mm at a constant die-closing velocity of 0.02 mm/s, and then the die motion was reversed at the same absolute velocity to unload the specimen. After unloading, the specimen which was forged at 160 °C was immediately air-cooled to room temperature.

For the finite element simulation of the forging process we made use of the symmetry of the geometry, and only meshed one-quarter of the geometry, as shown in Fig. 5-17. The quarter-circle of the workpiece cross-section was meshed using 277 ABAQUS-CPE4HT thermo-mechanically coupled elements, and the cruciform-die was modeled as a rigid surface.

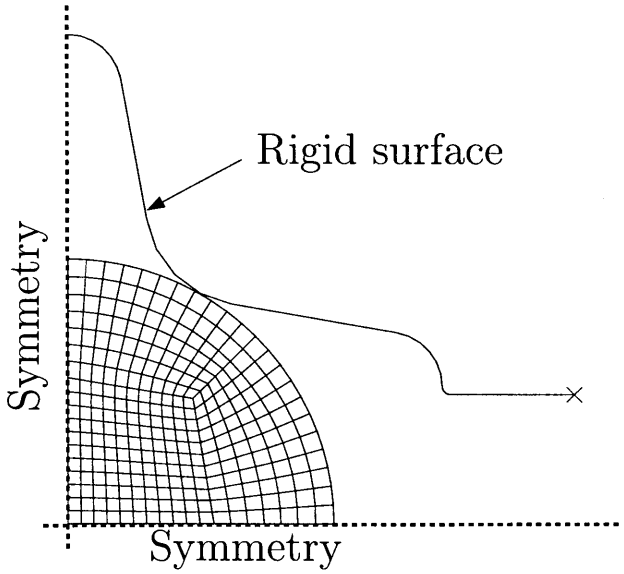

Figure 4-16: Quarter-symmetry finite element mesh for the workpiece and the rigid surface used in the plane-strain cruciform forging simulations.

For the experiment at 25 °C the workpiece was well-lubricated, and therefore the contact between the die and the workpiece was modeled as frictionless. However, since no lubrication was applied in the experiment at 160 °C, the contact between the die and the workpiece was modeled as frictional, with a high Coulomb friction coefficient of 0.75.

Fig. 4-17a and Fig. 4-17b compare the numerically-predicted and experimentally-measured, load-unload force versus displacement curves for the forging processes at 25 °C and 160 °C, respectively. The numerical simulations are able to reasonably accurately predict load-displacement behaviors at both 25 °C, which is well below ϑ_g, as well as at 160 °C, which is 15 °C higher than ϑ_g of PC. Note that the maximum force for forging at 25 °C is 25 kN, while the maximum force for forging at 160 °C is only 0.8 kN.

At the end of the loading process, with the dies still closed, the polycarbonate specimens conform with the shape of the cruciform forging dies. Upon die retraction and unloading, the polycarbonate specimens undergo some shape-recovery. For the forging experiment conducted at 25 °C there is only a little shape-recovery after unloading, while for the forging experiment conducted at 160 °C there is significant shape-recovery after unloading. After unloading, and cooling down to room temperature, each forged specimen was sectioned, polished, and photographed. Fig. 4-18a and Fig. 4-18b compare the experimentally-measured and numerically-predicted deformed shapes after unloading, die removal, and cooling for the forgings conducted at 25 °C and 160 °C, respectively. For both cases the numerically-predicted final geometry is in reasonably good agreement with that which is experimentally-measured.

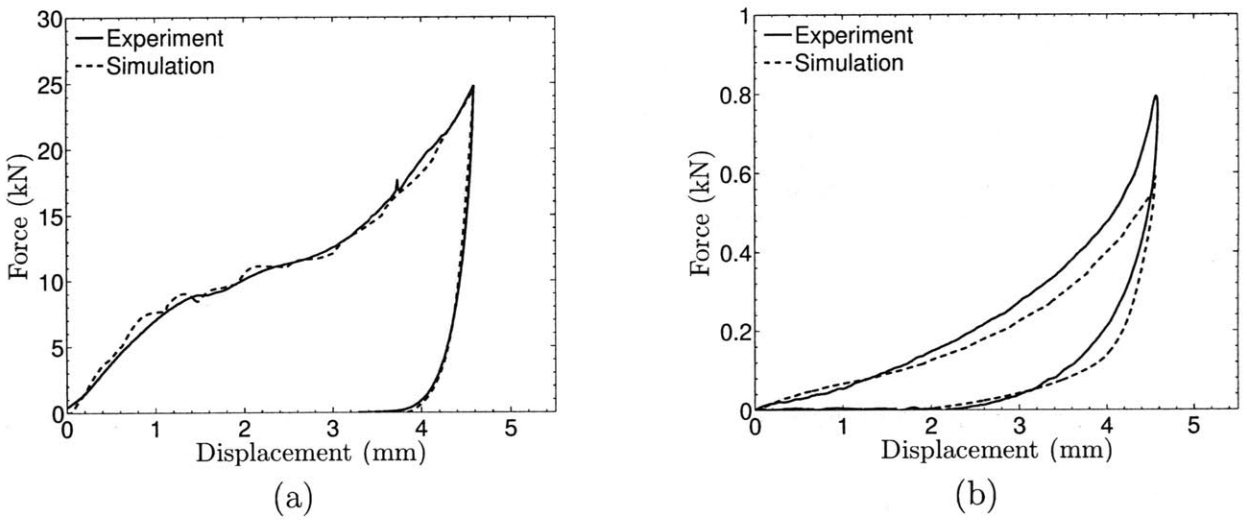

Figure 4-17: Comparison of the numerically-predicted and experimentally-measured force-displacement curves for forgings of PC at (a) 25 °C and (b) 160 °C. Note change in scale for the force axis between the two figures.

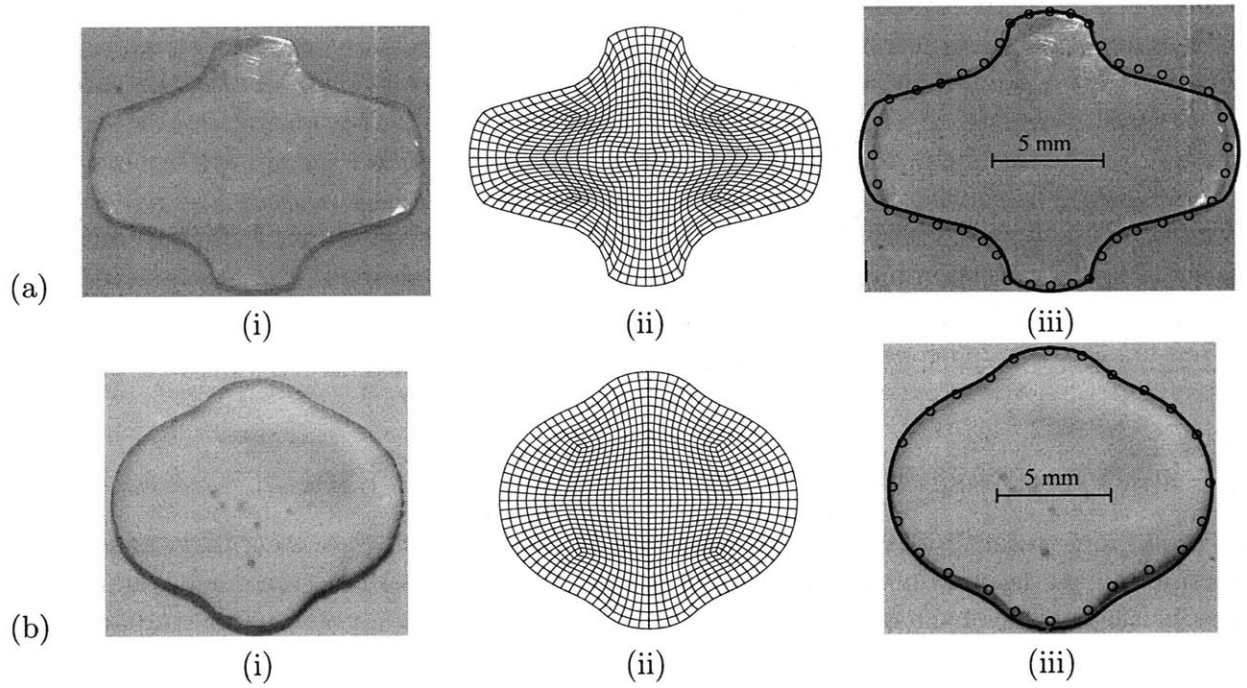

Figure 4-18: Comparison of the numerically-predicted and experimentally-measured deformed shapes from the cruciform forgings for (a) the forging at 25 °C, top row, and (b) the forging at 160 °C, bottom row: (i) Experimental macrographs; (ii) deformed meshes after unloading, die removal, and cooling to room temperature; and (iii) outlines of simulated shapes superimposed over the experimentally-measured shapes — the solid lines are the edge-geometries from the numerical simulations, and the circles outline the geometry of the specimens from the experiments.

4.5.2 Blow-forming of semi-spherical shapes of PC

Next, we consider blow-forming of flat PC sheets into thin-walled semi-spherical shapes above ϑ_g. The starting circular blanks, 102 mm in diameter, were machined from 3 mm thick PC sheets. The blanks were clamped in a blow-forming fixture; the bottom part of the fixture was essentially a 50 mm diameter thick-walled cylinder which was attached to a high-pressure regulated air-supply, and the top clamping plate contained a 50 mm diameter hole for the polymer to freely expand under pressure. The experiments were performed under two different processing conditions: (i) at 155 °C under a forming pressure of 20 psi (0.14 MPa), and (ii) at 160 °C under a pressure of 35 psi (0.24 MPa). A schematic of the temperature-pressure process cycle is shown in Fig. 4-19a. The forming process consists of three steps: (a) heating from room temperature to the processing-temperature over a period of 10 minutes; (b) ramping the pressure to the processing pressure in 2 minutes; (c) holding at the processing-pressure while simultaneously cooling back to room temperature in 15 minutes; and (d) finally relieving the pressure.

For the finite element simulation of such a process, we make use of the axial-symmetry of the geometry, and mesh only a slice of the geometry as shown in Fig. 4-19b. The polymer sheet is modeled using 252 ABAQUS-CAX4HT axi-symmetric, thermo-mechanically-coupled elements with 5 elements through the sheet thickness. The clamps are modeled as rigid surfaces, and surface-interaction between the workpiece and the clamps is modeled as frictional, with a high Coulomb friction coefficient of 0.9. The pressure was applied at the surface of the bottom elements, as indicated in Fig. 4-19b. Fig. 4-20a shows an image of a sectioned one-half of the specimen for the blow-forming experiment conducted at 155 °C and 20 psi, while Fig. 4-20b shows the corresponding numerically-predicted result. Fig. 4-20c shows a comparison of the experimentally-measured profiles of the specimen cross-sections (solid lines), against corresponding numerically-predicted profiles (dashed lines): the figure at the top is for blow-forming at 160 °C and 35 psi, and that at the bottom is for blow-forming at 155 °C and 20 psi. The predictions of the bulged-shapes from the simulations are in good agreement with the experiments.

4.5.3 Micron-scale hot-embossing of Zeonex-690R

Of major importance for creating micron-scale surface features (such as capillary channels for microfluidic chips) in polymeric substrates is the replication method of micro-hot-embossing. The basic process of micro-hot-embossing is as follows: the polymeric substrate is heated to 10–40 °C above its glass transition temperature and a rigid stamp containing micron-scale features is pressed into the heated polymer to allow the polymer to flow and fill the cavities, transferring the features in the tool to the polymeric substrate. Pressure is then held and the system is cooled to the demolding temperature (typically 20-60 °C below the glass transition temperature), and the tool is removed from the polymer part. Although there are numerous reports on successfully micro-hot-embossed microfluidic chips in the literature (cf., e.g., Chou, 2001; Bilenberg et al., 2005), the field of polymer hot-embossing process modeling is still not well developed because of the complex material modeling challenges, and there

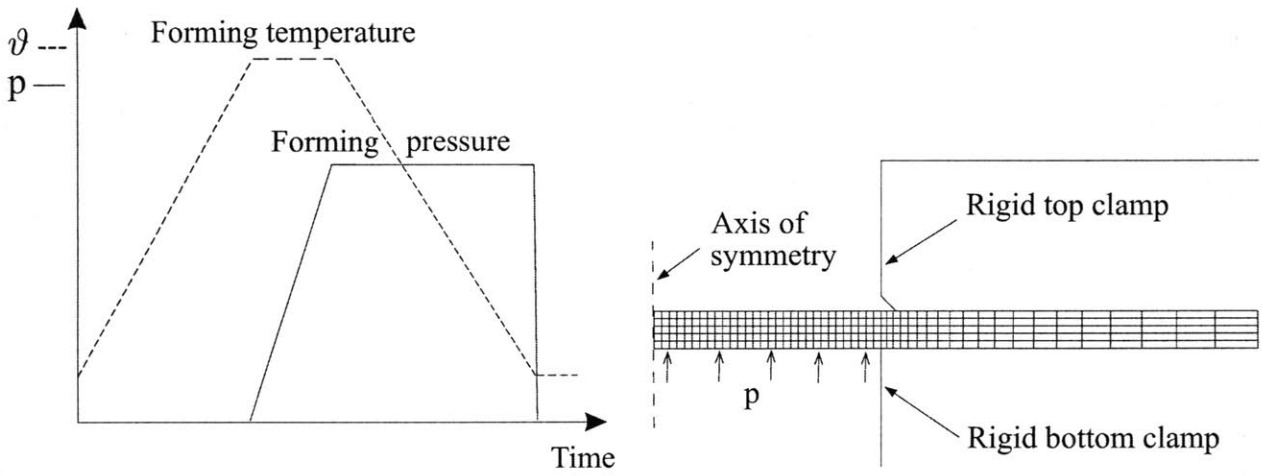

Figure 4-19: (a) Schematic of the temperature and pressure process history for the blow-forming operation. (b) Half-symmetry finite element mesh used for the axi-symmetric blow-forming simulations.

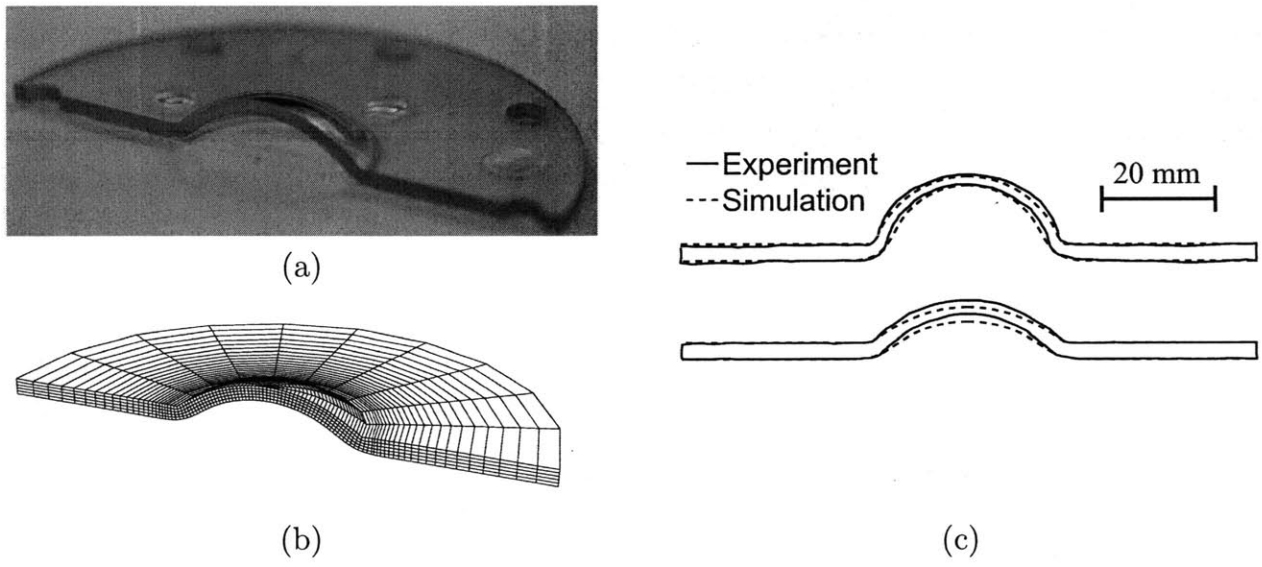

Figure 4-20: (a) One-half of final shape of the blow-formed PC plate at 155 °C and 20 psi. (b) A three-dimensional representation of corresponding numerical prediction. (c) Comparison of the numerically-predicted profiles (dashed lines), against corresponding experimentally-measured traced surface profiles of the specimens (solid lines): the figure at the top is for blow-forming at 160 °C and 35 psi (0.24 MPa), and that at the bottom is for blow-forming at 155 °C and 20 psi (0.14 MPa).

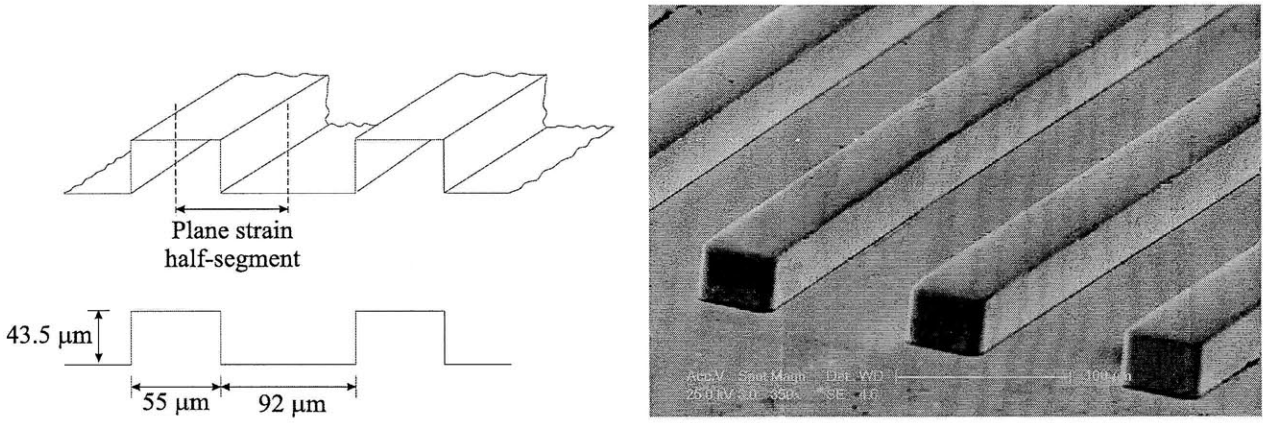

Figure 4-21: (a) Schematic of the plane-strain tool (not to scale), and (b) SEM micrograph of a portion of the metallic glass tool.

are only a few recent reports on numerical process-modeling studies for micro-hot-embossing (cf., e.g., Juang et al., 2002). Here we consider two micro-hot-embossing experiments and corresponding numerical simulations.

Embossing of a series of long micro-channels in a Zeonex-690R substrate

As a simple example of a micro-hot-embossing experiment and simulation, we first consider embossing of a series of long channels into a Zeonex-690R substrate ($\vartheta_g \approx 135\,°\text{C}$). The pattern consists of channels which are 55 μm wide, 43.5 μm deep, and are spaced 92 μm apart. Fig. A-1a shows a schematic of the tool-pattern, and Fig. A-1b shows a SEM micrograph of a portion of an actual embossing tool made from Zr-based metallic glass.

The hot-embossing experiment was carried out on a servo-hydraulic Instron testing machine equipped with heated compression platens. The details of our micro-hot-embossing set-up are provided in Appendix D. A 25 mm square, 1 mm thick sheet of Zeonex-690R, and a 11.7 mm square patterned metallic glass tool were aligned and placed between the heated compression platens. In the micro-hot-embossing experiment, the polymer and the embossing tool were brought into contact and heated to an embossing temperature 160 °C. Once at the embossing temperature, a compressive embossing force was slowly ramped to 0.41 kN to produce a nominal pressure of 3 MPa in 60 seconds, and held for 60 seconds before both the tool and the polymer were cooled down over 10 minutes to the demolding temperature of 85 °C, after which the pressure was removed and the tool was separated from the polymer substrate. The temperature-force-cycle for the micro-hot-embossing process is schematically shown in Fig. A-2a.

Since the channels are long relative to their width, and there are a large number of them aligned in parallel, we employ a plane-strain idealization in our numerical simulation, and consider only a single half-segment with suitable boundary conditions. Fig. A-2b shows the

finite element mesh. The Zeonex substrate is modeled using 742 ABAQUS-CPE4HT plane strain, thermo-mechanically-coupled elements, and the metallic glass tool is modeled using an appropriately shaped rigid surface. Contact between the substrate and tool was modeled as frictional, with a Coulomb friction coefficient of 0.75. The displacement boundary conditions on the portions AD and BC of the mesh boundary are $u_1 = 0$, while on the portion CD of the mesh, $u_1 = u_2 = 0$ are prescribed.

A scanning electron microscope (SEM) image of the embossed pattern is shown in Fig. A-3a, and the numerically-predicted pattern is shown in Fig. A-3b.[14] We further investigated the quality of the embossed features using an optical profilometer; Fig. A-4 compares representative cross-sections of the embossed features in the Zeonex-690R (circles), against the numerically-predicted channel profile (dashed line).[15] The final geometry of the embossed channels predicted by the numerical-simulation agrees well with the results from the micro-hot-embossing experiment.

Embossing of a micro-mixer pattern for a microfluidic device in a Zeonex-690R substrate

Next, we turn our attention to micro-hot-embossing of a pattern with relevance to microfluidic applications, and consider a simple micro-mixer design shown in Fig. A-5 (Hardt et al., 2008). The micro-mixer has two inlets which converge into a single long serpentine mixing channel with a single outlet. In addition to the serpentine micro-mixing channel, the device also has many micron-sized markers and other features for alignment and diagnostics (e.g. rectangular and triangular wells of the order of 100 μm). The mixing channel itself is 50 μm wide and 38.3 μm deep and the overall dimension of the device is 25 mm by 35 mm.

In order to determine suitable temperature and pressure process conditions for hot-embossing this micro-mixer geometry in the Zeonex substrate, we did not attempt to model the full geometry, but considered only the long parallel portions of the serpentine channels, and modeled these channels using a plane-strain idealization and periodic boundary conditions in our finite element simulations. The Zeonex substrate was modeled using a mesh consisting of 443 ABAQUS-CPE4HT plane strain, thermo-mechanically-coupled elements, and the metallic glass embossing-tool is modeled using an appropriately shaped rigid surface; the finite element mesh is shown in Fig. 4-26. The displacement boundary conditions on the portions AD and BC of the mesh boundary are $u_1 = 0$, while on the portion CD of the mesh, $u_1 = u_2 = 0$ are prescribed. Contact between the substrate and tool was modeled as frictional, with Coulomb friction coefficient of 0.75. We chose an embossing temperature of 160 °C, and sought to determine an appropriate embossing pressure, holding time, and demolding temperature which would result in good replication.

[14]The numerical pattern has been mirrored and repeated during post-processing to ease comparison with the corresponding experimental result.

[15]The optical profilometry method that we used to measure the channel profile is not capable of providing data for the sharp vertical features.

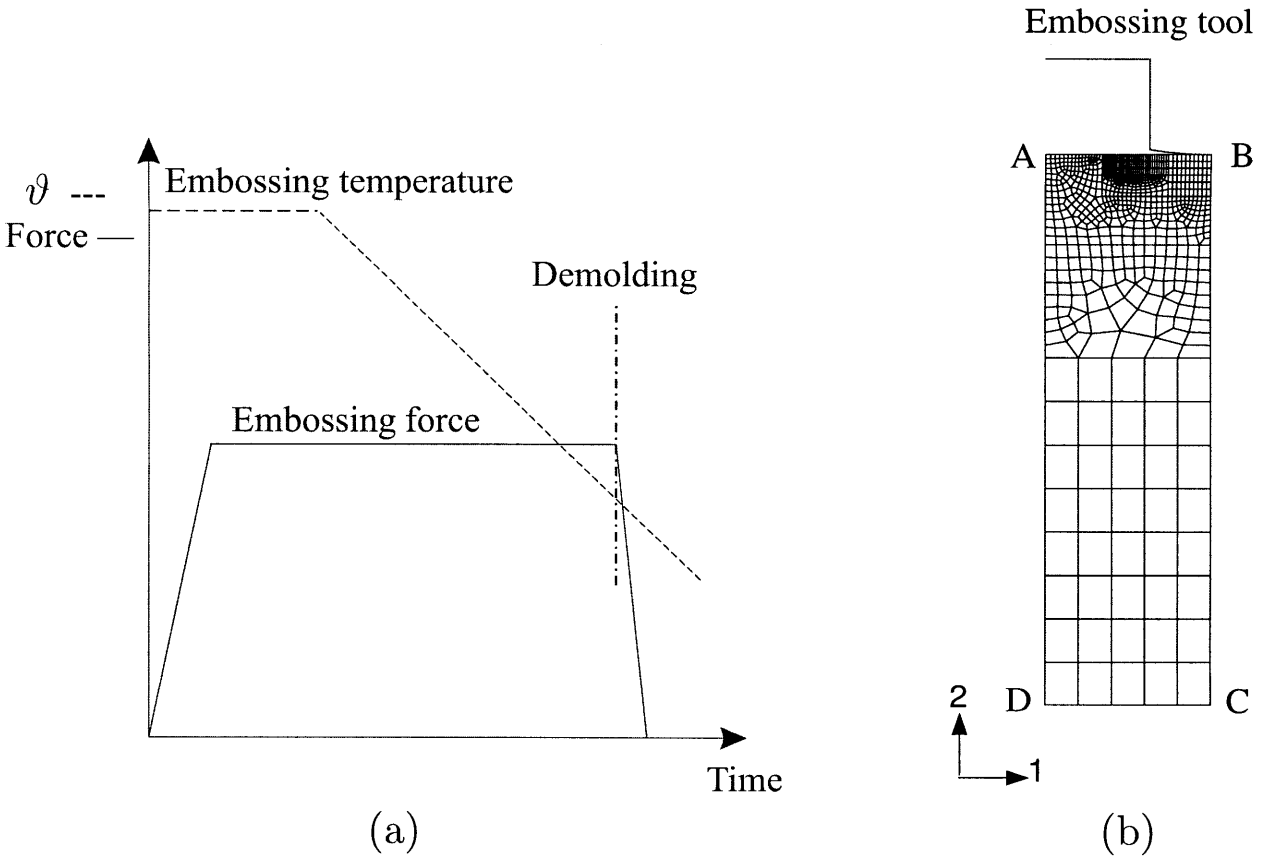

Figure 4-22: (a) Schematic of the processing conditions for the micro-hot-embossing, and (b) finite element mesh for the plane-strain simulation. The displacement boundary conditions on portions AD and BC of the mesh are u_1=0, while on portion CD, $u_1 = u_2 = 0$ are prescribed.

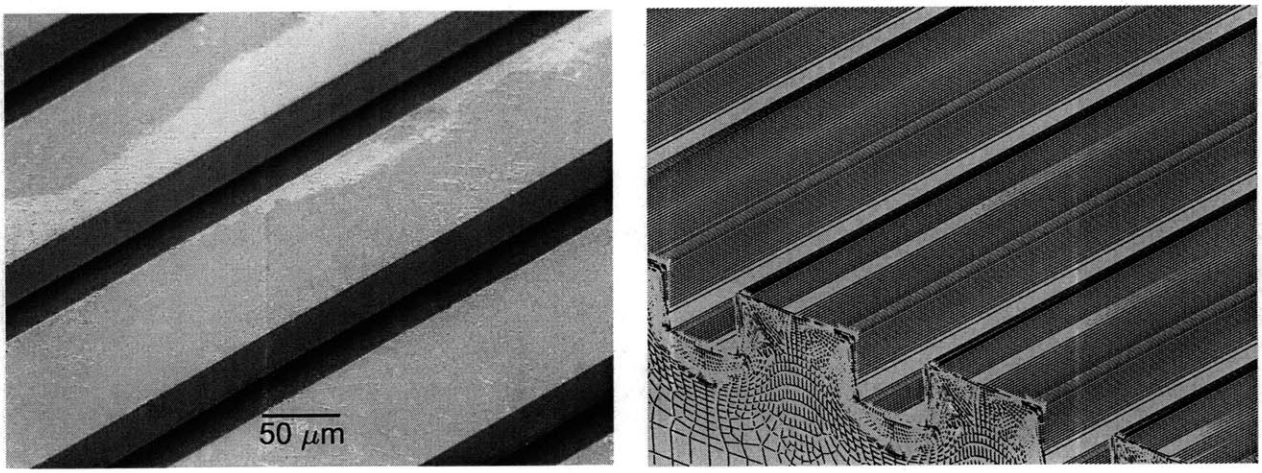

Figure 4-23: (a) SEM micrograph of the micro channels hot-embossed in Zeonex-690R, and (b) the corresponding numerical prediction. The plane-strain simulation has been extruded and mirrored to make the comparison more clear.

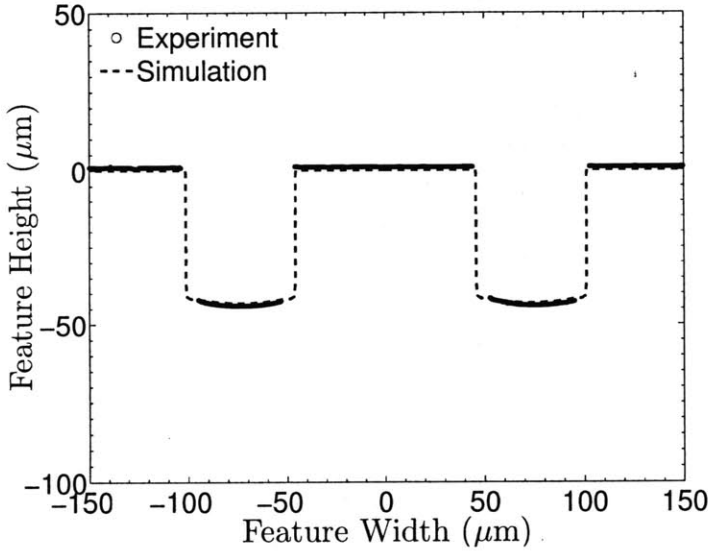

Figure 4-24: Comparison of the experimentally-measured (circles) and numerically-predicted channel profile (dashed line) in Zeonex-690R.

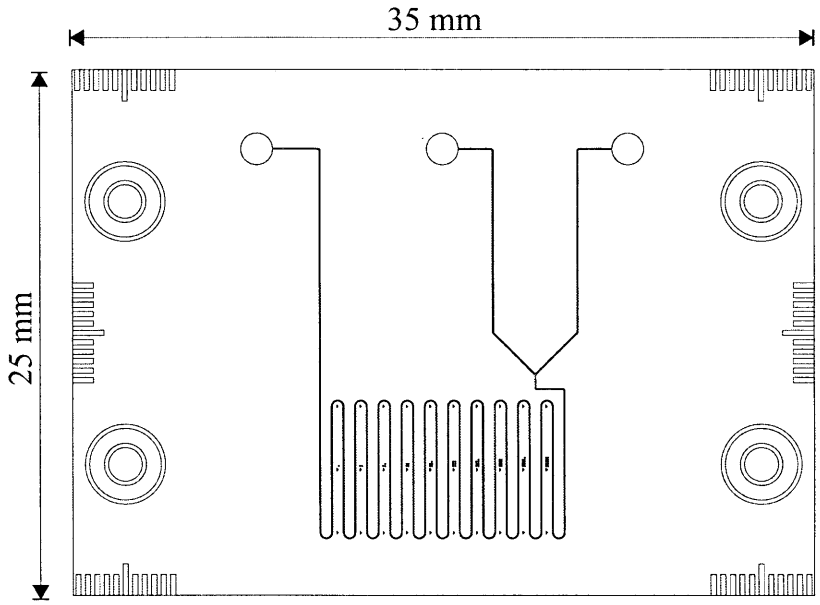

Figure 4-25: Geometry of the microfluidic mixer.

After a few trial simulations, we found that at 160 °C, ramping the pressure to 2 MPa in 30 seconds, and holding the pressure at temperature for 60 seconds would result in a completely filled die. Fig. 4-27 shows two snapshots of the die-filling process: Fig. 4-27a shows contours of the equivalent plastic strain[16] after 10 s when the nominal pressure is 0.67 MPa and the die is only partially filled, and Fig. 4-27b shows the contours of equivalent plastic strain at 90 s when the pressure has been held at 2 MPa for 60 seconds and the die has completely filled. Our numerical simulations also showed that further cooling down under pressure to 85 °C over a period of 10 minutes, and then demolding, would lock-in the embossed geometry.

After estimating the process conditions from our numerical simulations, we conducted an actual embossing experiment for the complete micro-mixer geometry (cf. Fig. A-5) in our servo-hydraulic testing machine equipped with heated compression platens. The temperature of polymer and metallic glass tool was increased to the embossing temperature of 160 °C, and a compressive force of 1.75 kN was applied to produce a *nominal* pressure of 2 MPa in 30 seconds. The pressure was then held for another 60 seconds at temperature, followed by cooling down under pressure to 85 °C over a period of 10 minutes, after which the pressure was removed and the tool was quickly removed from the substrate.

SEM images of several different features in the metallic glass tool, along with the corresponding images of the embossed features in the Zeonex-690R, are shown in Fig. 4-28. As seen in this figure, the micro-hot-embossing process determined from the numerical simulations, when actually executed, was able to successfully reproduce all the major micron-scale features of the metallic glass tool onto the polymeric substrate.

[16]Defined as $\int_0^t \nu^{p(1)}(\chi)d\chi$ in branch 1.

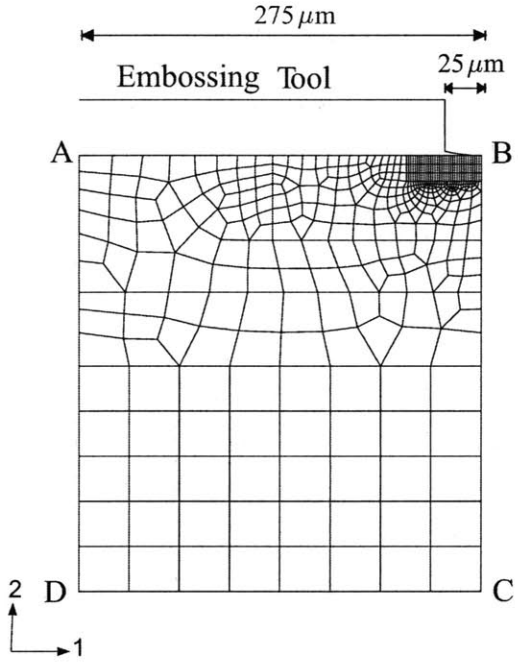

Figure 4-26: Finite element mesh for a plane-strain simulation showing the meshed substrate and the tool modeled as a rigid surface. The displacement boundary conditions on portions AD and BC of the mesh are $u_1 = 0$, while on portion CD $u_1 = u_2 = 0$ are prescribed.

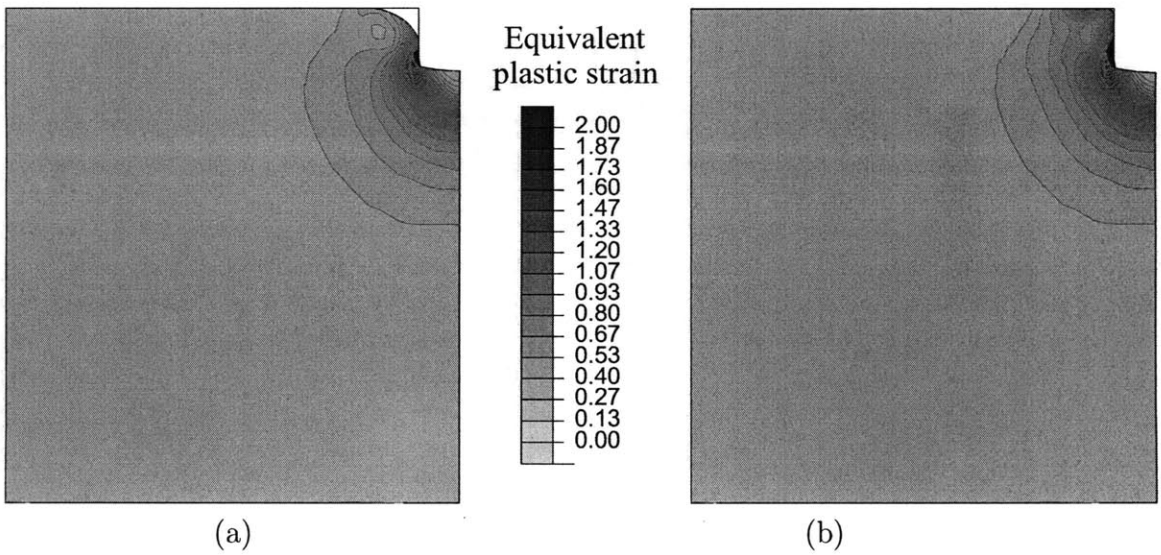

Figure 4-27: Numerically predicted Zeonex-690R deformation history during micro-hot-embossing. (a) Partially-filled die at 10 s, and (b) filled die at 90 s.

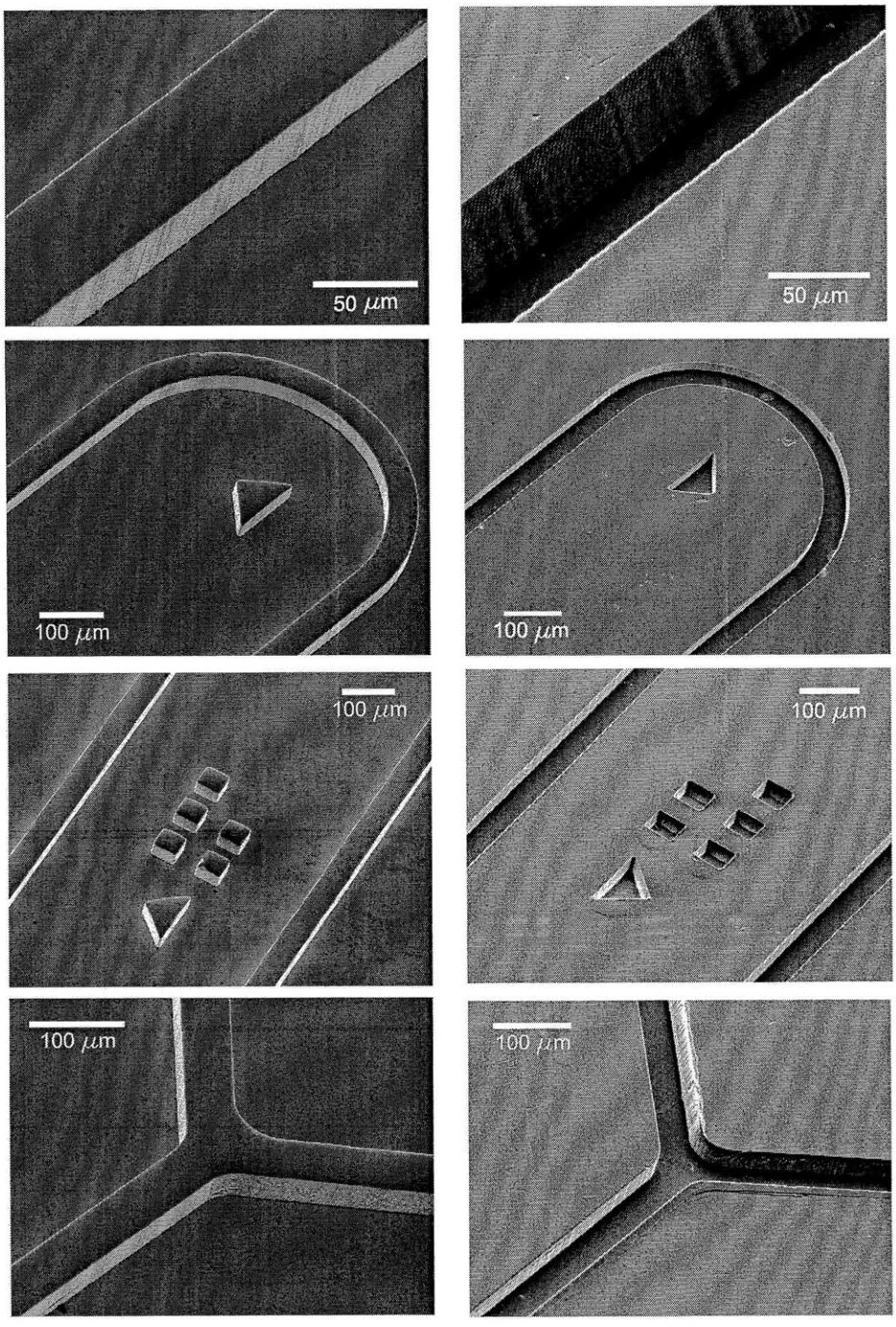

Figure 4-28: SEM micrographs of (a) features in bulk metallic glass tool, and (b) corresponding features in micro-hot-embossed Zeonex-690R part.

Chapter 5

Shape memory polymer

5.1 Introduction

An important class of polymers which has gained significant interest over the last decade is *thermally-activated*[1] amorphous shape memory polymers (e.g., Behl and Lendlein, 2007; Ratna and Kocsis, 2008). A body made from such a material may be subjected to large deformations at an elevated temperature above its glass transition temperature ϑ_g. Cooling the deformed body to a temperature below ϑ_g under active kinematical constraints fixes the deformed shape of the body. The original shape of the body may be recovered if the material is heated back to a temperature above ϑ_g without the kinematical constraints. This phenomenon is known as the *shape-memory effect*. If the shape recovery is partially constrained, the material exerts a recovery force and the phenomenon is known as *force- or constrained-recovery*.

One of the first wide spread applications of shape memory polymers was as heat-shrinkable tubes (Ota, 1981). Such rudimentary early applications did not necessitate a detailed understanding or modeling of the thermomechanical behavior of these materials. However, in recent years shape-memory polymers are beginning to be used for critical biomedical applications (e.g., Lendlein and Langer, 2002; Maitland et al., 2003; Baer et al., 2007b), microsystems (e.g., Maitland et al., 2002; Metzger et al., 2002; Gall et al., 2004), re-writable media for data storage (e.g., Vettiger et al., 2002; Wornyo et al., 2007), and self-deployable space structures (Campbell et al., 2005). In order to develop a robust simulation-based capability for the design of devices for such critical applications, one requires an underlying accurate thermo-mechanically-coupled constitutive theory and an attendant validated numerical implementation of the theory.

[1]Shape memory polymers which can recover from an imposed deformation by the application of other external stimuli such as light of a specific frequency also exist (e.g., Lendlein et al., 2005; Jiang et al., 2006); however, thermally-activated shape memory polymers are most common.

In the past few years several efforts at experimental characterization of the thermo-mechanical stress-strain response of a wide variety of shape-memory polymers have been published in the literature (e.g., Tobushi et al., 1996; Baer et al., 2007a; Gall et al., 2005; Yakacki et al., 2007; Safranski and Gall, 2008; Qi et al., 2008) In a typical thermo-mechanical shape memory cycle, the polymer transitions from a viscoelastic rubber-like material into an elastic-viscoplastic glassy solid during the fixation of the deformed shape, and again into a rubber-like material when the shape-recovery is actuated. Modeling this complex change in material behavior poses major challenges. Significant modeling efforts have also been published (e.g., Liu et al., 2006; Chen and Lagoudas, 2008; Qi et al., 2008; Nguyen et al., 2008). However, at this point in time, a thermo-mechanically-coupled large-deformation constitutive theory for modeling the response of thermally-actuated shape-memory polymers is not widely agreed upon — the field is still in its infancy. The purpose of this chapter is to present results from of our own recent research in this area.

Specifically, with the aim of developing a thermo-mechanically-coupled large-deformation constitutive theory and a numerical simulation capability for modeling the response of thermally-actuated shape-memory polymers, we have

- conducted large strain compression experiments on a representative shape-memory polymer to strains of approximately unity at strain rates of 10^{-3} s^{-1} and 10^{-1} s^{-1}, and at temperatures ranging from room temperature to approximately 30 °C above the glass transition temperature of the polymer;

- formulated a thermo-mechanically-coupled large deformation constitutive theory; and

- calibrated the material parameters appearing in the theory using the stress-strain data from the compression experiments.

Shawn A. Chester has numerically implemented our theory by writing a user-material subroutine for a widely-used finite element program ABAQUS/Standard (2009). In order to validate the predictive capability of our theory and its numerical implementaion, we have

- conducted representative experiments involving complex three-dimensional geometries. By comparing the numerically-predicted response in these validation simulations against measurements from corresponding experiments, we show that our theory is capable of reasonably accurately reproducing the experimental results.

The plan of this chapter is as follows. In §5.2 we describe results of our simple compression experiments on a chemically-crosslinked thermoset shape memory polymer — tert butyl acrylate monomer (tBA) with poly(ethylene glycol) dimethacrylate (PEGDMA) crosslinker. This polymer is chosen for study because the shape-memory actuation temperature for this polymer is close to that of body-temperature — the *nominal* glass transition temperature for this polymer is $\vartheta_g \approx 37\,\mathrm{C}$. In §5.3 we give specialized equations for our constitutive theory and show the quality of the fit of the constitutive theory to the experimentally-measured stress-strain curves.

In §5.5 we present results of representative thermo-mechanical cyclic experiments to validate the predictive capability of our theory and its numerical implementation in complex three-dimensional geometries. By comparing the numerically-predicted response in these validation simulations against measurements from corresponding experiments, we show that our theory is capable of reasonably accurately reproducing the experimental results. As a demonstration of the robustness of the three-dimensional numerical capability, in §5.6 we show results from a simulation of the shape-recovery response of a stent made from the polymer when it is inserted in an artery modeled as a compliant elastomeric tube.

5.2 Experimental characterization of the thermo-mechanical response

As a representative thermally-actuated shape-memory polymer we chose to characterize the mechanical response of a chemically-crosslinked thermoset polymer recently studied by Yakacki et al. (2007). Following a procedure described by these authors, the shape-memory polymer was synthesized via photopolymerization (UV curing) of the monomer tert-butyl acrylate (tBA) with the crosslinking agent poly(ethylene glycol) dimethacrylate (PEGDMA), in the following specific composition: tBA 90% by weight (mol. weight: 128 g/mol) with PEGDM 10% by weight (mol. weight: 550 g/mol).[2] This polymer is chosen for study because the shape-memory actuation temperature for this polymer is close to that of body-temperature — the *nominal* glass transition temperature for this polymer is $\vartheta_g \approx 37\,^{\circ}\mathrm{C}$ (Safranski and Gall, 2008).

We have conducted a set of simple compression experiments on this polymer. The cylindrical specimens were 6.3 mm diameter and 3.15 mm tall. The compression experiments were conducted at true-strain rates of 10^{-3} s^{-1} and 10^{-1} s^{-1} at 22 °C, 30 °C, 40 °C, 50 °C, and 65 °C, up to true strain-levels of $\approx$ 100%. Fig. 5-1 shows representative true stress-strain curves[3] for the shape memory polymer at strain rate of $10^{-3}\,\mathrm{s}^{-1}$ at temperatures ranging from 22 °C through 65 °C, while Fig. 5-2 shows a more extensive set of stress-strain curves at strain rates of $10^{-3}\,\mathrm{s}^{-1}$, and $10^{-1}\,\mathrm{s}^{-1}$, and at temperatures of 22 °C, 30 °C, 40 °C, 50 °C, and 65 °C. Referring to Fig. 5-2, the polymer exhibits two distinctly different responses at temperatures below and above ϑ_g:

- The stress-strain curves at 22 °C and 30 °C are below ϑ_g. At these temperatures the polymer exhibits a strain-rate and temperature-dependent response typical of a "glassy-

[2]The chemicals were mixed in a glass beaker for 2 minutes, and the mixed liquid solution was then degassed in a vacuum chamber for 10 minutes. The degassed mixture was then injected between two glass sheets that were separated with spacers. A UV-Lamp was used to photopolymerize the solution at an intensity of $\sim 30\,\mathrm{mW/cm^2}$ for 10 minutes. Finally, the polymer was heat-treated at 90 °C for 1 hour to complete the polymerization reaction.

[3]As is customary, in order to calculate the deformed cross-sectional area (and thence the true stress), we have assumed plastic incompressibility to estimate the stretch in the lateral direction of the compression specimens.

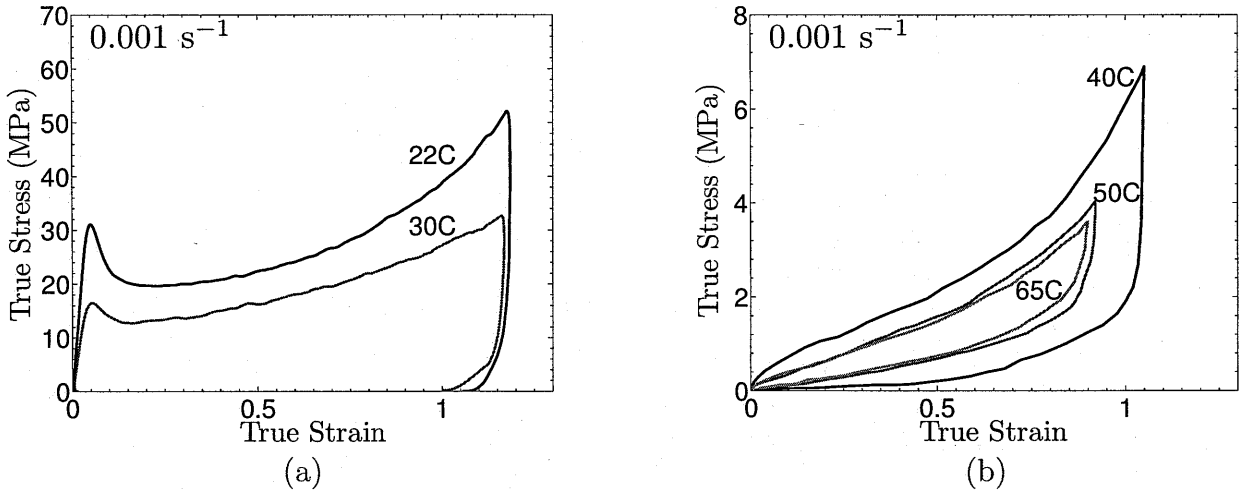

Figure 5-1: Stress-strain curves in simple compression for the shape memory polymer at various temperatures ranging from 22 °C to 65 °C, at a strain rate of $10^{-3}\,s^{-1}$: (a) for temperatures below $\vartheta_g \approx 37\,°C$; (b) for temperatures above ϑ_g. Note the change in scale for the stress axis between the two figures.

polymer". That is, a well-defined yield-peak, followed by strain-softening, and eventual rapid strain-hardening at large strains. Upon unloading after compression to a strain level of $\approx 100\%$, about 5% of the strain is recovered and the remainder is left as a "permanent-set" (as long as the temperature is held constant).

- The stress-strain curves at 50 °C and 65 °C are above ϑ_g. At these temperatures the material exhibits a "hysteretic-rubber"-like response. That is, the initial stiffness of the material drops dramatically from its value below ϑ_g, the yield-peak disappears, and upon unloading there is essentially no permanent set. However, there is significant hysteresis in the stress-strain response which is significantly rate- and temperature-dependent.

Of particular interest are the two stress-strain curves at 40 °C, a temperature which is in the vicinity of the *nominal* glass transition temperature of $\vartheta_g \approx 37\,°C$. At the lower strain rate of $10^{-3}\,s^{-1}$ the material responds like a "hysteretic-rubber", while at the higher strain rate of $10^{-1}\,s^{-1}$ the material responds like a "glassy-polymer." Thus, in accordance with the well-known result from frequency-dependent dynamic-mechanical-tests on amorphous polymers, this result shows that the "glass transition temperature" ϑ_g is *not a constant* for a material — it increases as the strain rate increases.

5.3 Constitutive theory

Amorphous polymers are called *thermoplastics* when they are not chemically-crosslinked, and are called *thermosets* when they are chemically-crosslinked. Both classes of amorphous

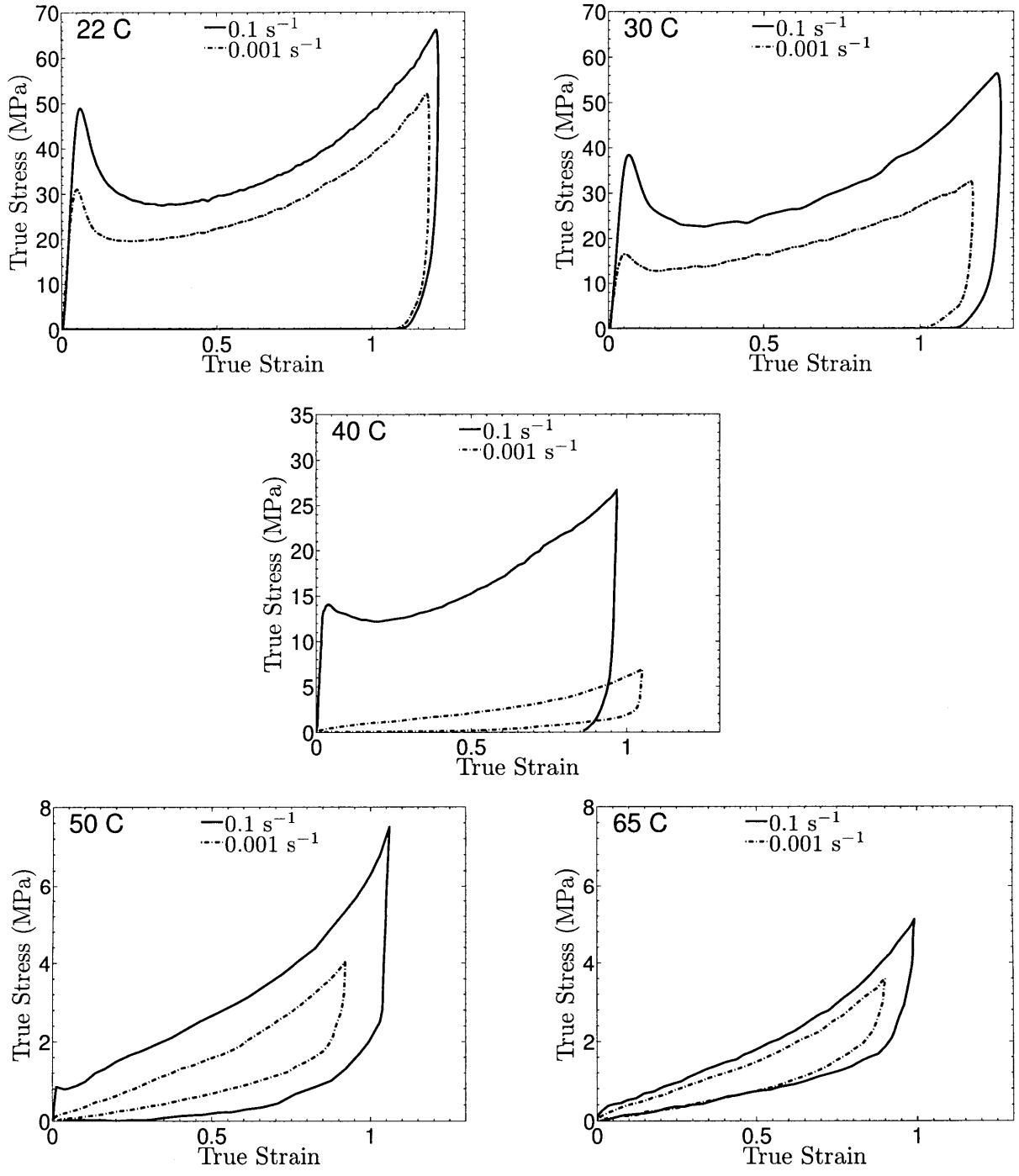

Figure 5-2: Stress-strain curves in simple compression for the shape memory polymer at strain rates of $10^{-3}\,s^{-1}$ and $10^{-1}\,s^{-1}$, and at temperatures of 22 °C, 30 °C, 40 °C, 50 °C, and 65 °C. Note the change in scale for the stress axis between various figures.

polymers behave in a qualitatively similar fashion when deformed below ϑ_g, but their response characteristics above ϑ_g are quite different. As shown in Fig. 5-2, at temperatures above ϑ_g, after a certain amount of deformation, the crosslinked thermoset material recovers almost fully upon reverse deformation – *a response essential to the shape-memory effect.* Unlike a crosslinked thermoset polymer, an amorphous polymer which is not crosslinked shows *permanent set* when subjected to a strain-cycle above ϑ_g, and is therefore said to be "thermoplastic" in character.

In Chapter 4 we have shown that a constitutive theory with $M = 3$ is able to reasonably accurately predict the thermo-mechanical response of thermoplastic amorphous polymers in a temperature regime which spans their glass transition temperature. For modeling the response of *amorphous thermoset shape-memory polymers*, we consider three micromechanisms and adopt and modify the constitutive theory presented in Chapter 4. For simplicity, we neglect the "defect energy" associated with plastic deformation which leads to a back-stress. The defect energy was used in Chapters 3 and 4 to allow for modeling the cyclic -loading and Bauschinger-like phenomena in polymers. Here, since we do not have any experimental data on cyclic loading for the tBA/PEGDMA shape-memory polymer, we consider a simpler theory which does not include defect energy. As a visual aid, Fig. 5-5 shows a schematic "spring-dashpot" representation of our three micromechanisms model for the shape-memory polymer. These three micromechanisms are intended to represent the following underlying physical phenomena:

- **The first micromechanism** ($\alpha = 1$): The nonlinear spring represents an "elastic" resistance due to intermolecular energetic bond-stretching. The dashpot represents thermally-activated plastic flow due to "inelastic mechanisms," such as chain-segment rotation and relative slippage of the polymer chains between neighboring cross-linkage points.

- **The second and third micromechanisms** ($\alpha = 2, 3$): In addition to the chemical-crosslinks which are present throughout the temperature range of interest in thermoset polymers, at temperatures below ϑ_g we expect that the polymer also exhibits a significant amount of mechanical-crosslinking. We conceptually distinguish molecular chains between mechanical-crosslinks and molecular chains between chemical-crosslinks by introducing two micromechanisms $\alpha = 2$ and $\alpha = 3$, respectively. The nonlinear springs in these two mechanisms represent resistances due to changes in the free energy upon stretching of the molecular chains between the crosslinks. The mechanical-crosslinks are expected to be destroyed when the temperature is increased through ϑ_g; the dashpot in micromechanism $\alpha = 2$ represents thermally-activated plastic flow resulting from such a phenomenon. The micromechanism $\alpha = 3$ represents chemically-crosslinked backbone of the thermoset polymer in which the crosslinks do not slip; accordingly we do not use a dashpot for this micromechanism, and we set $\mathbf{F}^{p(3)} = \mathbf{1}$, so that $\mathbf{F}^{e(3)} = \mathbf{F}$.

As in Chapter 4, our strategy to phenomenologically model the response of the material as the temperature traverses ϑ_g is as follows:

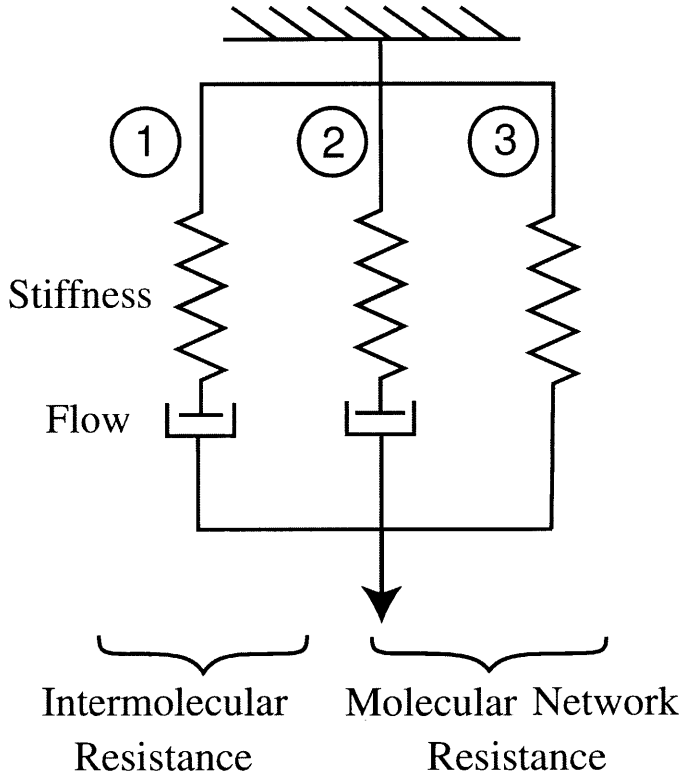

Figure 5-3: A schematic "spring-dashpot" representation of the constitutive model.

(i) For temperatures $\vartheta < \vartheta_g$, we do not allow any plastic flow in the dashpot associated with micromechanism $\alpha = 2$. Thus, since the springs in $\alpha = 2$ and $\alpha = 3$ are in parallel, the three-micromechanism model reduces to a simpler two-micromechanism model, which we have recently successfully used to model the response of amorphous polymers for temperatures below ϑ_g in Chapter 3.

(ii) For temperatures $\vartheta > \vartheta_g$, we allow for plastic flow in the dashpot associated with micromechanism $\alpha = 2$, but *quickly drop the plastic flow resistance in mechanism* $\alpha = 2$ *to a very small value*, so that for all practical purposes in this temperature range, only mechanisms $\alpha = 1$ and $\alpha = 3$ contribute to the macroscopic stress.

The theory relates the following basic fields:

$\mathbf{x} = \boldsymbol{\chi}(\mathbf{X}, t)$,	motion;
$\mathbf{F} = \nabla\boldsymbol{\chi}, \quad J = \det \mathbf{F} > 0$,	deformation gradient;
$\mathbf{F} = \mathbf{F}^{e\,(\alpha)}\mathbf{F}^{p\,(\alpha)}, \quad \alpha = 1, 2, 3$,	elastic-plastic decompositions of $\mathbf{F}$;
$\mathbf{F}^{e\,(\alpha)}, \quad J^{e\,(\alpha)} = \det \mathbf{F}^{e\,(\alpha)} = J > 0$,	elastic distortions;
$\mathbf{F}^{p\,(\alpha)}, \quad J^{p\,(\alpha)} = \det \mathbf{F}^{p\,(\alpha)} = 1$,	inelastic distortions;
$\mathbf{F}^{e\,(\alpha)} = \mathbf{R}^{e\,(\alpha)}\mathbf{U}^{e\,(\alpha)}$,	polar decomposition of $\mathbf{F}^{e\,(\alpha)}$;
$\mathbf{C}^{e\,(\alpha)} = \mathbf{F}^{e\,(\alpha)\top}\mathbf{F}^{e\,(\alpha)}$,	elastic right Cauchy-Green tensors;
$\mathbf{B}^{p\,(\alpha)} = \mathbf{F}^{p\,(\alpha)}\mathbf{F}^{p\,(\alpha)\top}$,	plastic left Cauchy-Green tensors;
$\mathbf{T} = \sum_{\alpha=1}^{3} \mathbf{T}^{(\alpha)}, \qquad \mathbf{T}^{(\alpha)} = \mathbf{T}^{(\alpha)\top}$,	Cauchy stress;
$\mathbf{T}_{\mathrm{R}} = J\mathbf{T}\mathbf{F}^{-\top}$,	Piola stress;
$\psi_{\mathrm{R}} = \sum_{\alpha=1}^{3} \bar{\psi}^{(\alpha)}$,	free energy density per unit reference volume;
$\boldsymbol{\xi}^{(\alpha)} = (\xi_1^{(\alpha)}, \xi_2^{(\alpha)}, \ldots, \xi_m^{(\alpha)})$,	scalar internal variables;
$\vartheta > 0$,	absolute temperature;
$\nabla\vartheta$,	referential temperature gradient;
$\mathbf{q}_{\mathrm{R}}$,	referential heat flux vector;
q_{R},	scalar heat supply.

Note that from our constitutive assumption, $\mathbf{F}^{p(3)} = \mathbf{1}$, such that $\mathbf{F}^{e(3)} = \mathbf{F}$ for all motions and all times.

As is well-known, the "glass transition" in amorphous polymers occurs over a narrow range of temperatures, and whatever the means that are used to define *a glass transition temperature*,[4] the glass transition temperature also depends on the strain rate to which the material is subjected. With $\mathbf{D}_0 = \mathrm{sym}_0(\dot{\mathbf{F}}\mathbf{F}^{-1})$ denoting the total deviatoric stretching tensor, let

$$\nu \stackrel{\text{def}}{=} \sqrt{2}|\mathbf{D}_0| \tag{5.1}$$

denote an *equivalent shear strain rate*. As a simple model for the variation of the glass transition temperature with strain rate, we assume that

$$\vartheta_g = \begin{cases} \vartheta_r & \text{if} \quad \nu \leq \nu_r, \\ \vartheta_r + n \log\left(\dfrac{\nu}{\nu_r}\right) & \text{if} \quad \nu > \nu_r, \end{cases} \tag{5.2}$$

where ϑ_r a *reference glass transition temperature* at a *reference strain rate* ν_r, and n is a material parameter.

In the following subsections we present constitutive equations for the three micromechanisms discussed above. For brevity we do not give a detailed development; the reader is

[4]Such as the peak in the tan-δ curve in a DMA experiment.

referred to Chapters 2, 3 and 4 for the intermediate steps of continuum-mechanical arguments and derivations.

5.3.1 Constitutive equations for micromechanism $\alpha = 1$

Free energy

We consider the free energy in the special form

$$\psi^{(1)} = \bar{\psi}^{(1)}(\mathcal{I}_{\mathbf{C}^{e(1)}}, \vartheta), \tag{5.3}$$

where $\mathcal{I}_{\mathbf{C}^{e(1)}}$ represents a list of the principle invariants of $\mathbf{C}^{e(1)}$ and $\tilde{\psi}^{(1)}$ is an energy associated with intermolecular interactions.

Let

$$\mathbf{C}^{e(1)} = \sum_{i=1}^{3} (\lambda_i^e)^2 \, \mathbf{r}_i^e \otimes \mathbf{r}_i^e, \tag{5.4}$$

denote the spectral representation of $\mathbf{C}^{e(1)}$, where $(\lambda_1^e, \lambda_2^e, \lambda_3^e)$ are the positive eigenvalues of $\mathbf{U}^{e(1)}$, and $(\mathbf{r}_1^e, \mathbf{r}_2^e, \mathbf{r}_3^e)$ are the orthonormal eigenvectors of $\mathbf{C}^{e(1)}$ and $\mathbf{U}^{e(1)}$. With

$$\mathbf{E}^{e(1)} = \sum_{i=1}^{3} E_i^e \, \mathbf{r}_i^e \otimes \mathbf{r}_i^e, \qquad E_i^e = \ln \lambda_i^e, \tag{5.5}$$

denoting an elastic logarithmic strain measure, we consider an elastic free energy of the form

$$\bar{\psi}^{(1)} = G|\mathbf{E}_0^{e\,(1)}|^2 + \tfrac{1}{2}K(\operatorname{tr}\mathbf{E}^{e(1)})^2 - 3\,K\,(\operatorname{tr}\mathbf{E}^{e(1)})\alpha^{\text{th}}(\vartheta - \vartheta_0) + \tilde{f}(\vartheta), \tag{5.6}$$

where $\tilde{f}(\vartheta)$ is an entropic contribution to the free energy related to the temperature-dependent specific heat of the material. The temperature-dependent parameters

$$G(\vartheta) > 0, \quad K(\vartheta) > 0, \quad \alpha^{\text{th}}(\vartheta) > 0, \tag{5.7}$$

are the shear modulus, bulk modulus, and coefficient of thermal expansion, respectively, and ϑ_0 is a reference temperature.

For polymeric materials the magnitude of the elastic shear modulus G decreases drastically as the temperature increases through the glass transition temperature ϑ_g of the material. Following Dupaix and Boyce (2007), we assume that the temperature dependence of the shear modulus may be adequately approximated by the following function:

$$G(\vartheta) = \tfrac{1}{2}(G_{gl} + G_r) - \tfrac{1}{2}(G_{gl} - G_r)\tanh\left(\frac{1}{\Delta}(\vartheta - \vartheta_g)\right) - M(\vartheta - \vartheta_g), \tag{5.8}$$

where ϑ_g is the glass transition temperature, G_{gl} and G_r ($< G_{gl}$) are values of the shear modulus in the glassy and rubbery regions, and Δ is a parameter related to the temperature

range across which the glass transition occurs. The parameter M represents the slope of the temperature variation of G outside the transition region, with

$$M = \begin{cases} M_{gl} & \vartheta \leq \vartheta_g, \\ M_r & \vartheta > \vartheta_g. \end{cases} \tag{5.9}$$

Next, the temperature dependence of Poisson's ratio ν^{poi} of the material is assumed to be

$$\nu^{\text{poi}}(\vartheta) = \frac{1}{2}(\nu_{gl}^{\text{poi}} + \nu_r^{\text{poi}}) - \frac{1}{2}(\nu_{gl}^{\text{poi}} - \nu_r^{\text{poi}}) \tanh\Big(\frac{1}{\Delta}(\vartheta - \vartheta_g)\Big), \tag{5.10}$$

with ν_{gl}^{poi} and ν_r^{poi} representing values below and above ϑ_g, respectively. The temperature dependence of the bulk modulus K is then obtained by using the standard relation for isotropic materials

$$K(\vartheta) = G(\vartheta) \times \frac{2(1 + \nu^{\text{poi}}(\vartheta))}{3(1 - 2\,\nu^{\text{poi}}(\vartheta))}. \tag{5.11}$$

The coefficient of thermal expansion is taken to have a bilinear temperature dependence, with the following contribution to the thermal expansion term $\alpha^{\text{th}}(\vartheta - \vartheta_0)$ in the free energy relation (5.6):

$$\alpha^{\text{th}}(\vartheta - \vartheta_0) = \begin{cases} \alpha_{gl}(\vartheta - \vartheta_0) & \text{if} \quad \vartheta \leq \vartheta_g, \\ \alpha_{gl}(\vartheta - \vartheta_0) + (\alpha_r - \alpha_{gl})(\vartheta - \vartheta_g) & \text{if} \quad \vartheta > \vartheta_g. \end{cases} \tag{5.12}$$

Cauchy stress. Mandel stress

Corresponding to the special free energy function considered above, the contribution $\mathbf{T}^{(1)}$ to the Cauchy stress is given by

$$\mathbf{T}^{(1)} \stackrel{\text{def}}{=} J^{-1}\,\mathbf{R}^{e\,(1)}\,\mathbf{M}^{e(1)}\,\mathbf{R}^{e\,(1)\top}, \tag{5.13}$$

where $\mathbf{M}^{e(1)}$, the Mandel stress, is obtained from the elastic free energy function by (5.6),

$$\mathbf{M}^{e(1)} = \frac{\partial \tilde{\psi}^{e\,(1)}(\mathbf{E}^{e(1)}, \vartheta)}{\partial \mathbf{E}^{e(1)}}, \tag{5.14}$$

which yields

$$\mathbf{M}^{e(1)} = 2G\mathbf{E}_0^{e\,(1)} + K\,(\operatorname{tr}\mathbf{E}^{e(1)})\mathbf{1} - 3K\alpha^{\text{th}}(\vartheta - \vartheta_0)\mathbf{1}; \tag{5.15}$$

note that $\mathbf{M}^{e(1)}$ is symmetric.

The Mandel stress is the driving stress for plastic flow in the theory. The corresponding *equivalent shear stress* and *mean normal pressure* are given by

$$\bar{\tau}^{(1)} \stackrel{\text{def}}{=} \frac{1}{\sqrt{2}} |\mathbf{M}_0^{e\,(1)}|, \quad \text{and} \quad \bar{p} \stackrel{\text{def}}{=} -\frac{1}{3}\text{tr}\mathbf{M}^{e(1)}, \tag{5.16}$$

respectively.

Internal variables

For the micromechanism $\alpha = 1$, we restrict the list $\boldsymbol{\xi}^{(1)}$ of internal variables to three positive-valued scalars

$$\boldsymbol{\xi}^{(1)} = \Big(\varphi, S_a, S_b\Big),$$

where

- The parameters $\varphi \geq 0$ and $S_a \geq 0$ are introduced to model the "yield-peak" which is widely-observed in the intrinsic stress-strain response of glassy polymers. A key microstructural feature controlling the strain-softening associated with the "yield-peak" in glassy polymers is the local change in molecular-packing due to deformation-induced disordering. The variable φ, a positive-valued dimensionless "order"-parameter, is introduced to represent such *deformation-induced disordering*; and a stress-dimensioned internal variable S_a which is coupled to the microstructural disordering of the material, represents the corresponding *transient resistance* to plastic flow.
- The internal variable $S_b \geq 0$ represents a dissipative resistance to plastic flow to model "isotropic hardening" at large strains as the chains are pulled taut between entanglements resulting in increasing interaction between the neighboring chains and pendant side-groups; this is in addition to any entropic or energetic contribution from network chain-stretching.

Flow rule

The evolution equation for $\mathbf{F}^{p(1)}$ is

$$\dot{\mathbf{F}}^{p\,(1)} = \mathbf{D}^{p(1)}\,\mathbf{F}^{p(1)}, \tag{5.17}$$

with $\mathbf{D}^{p(1)}$ given by

$$\mathbf{D}^{p(1)} = \nu^{p(1)} \left(\frac{\mathbf{M}_0^{e\,(1)}}{2\bar{\tau}^{(1)}} \right), \qquad \text{where} \qquad \nu^{p(1)} \stackrel{\text{def}}{=} \sqrt{2}|\mathbf{D}^{p(1)}|. \tag{5.18}$$

With the mean normal pressure defined by $(5.16)_2$ and an *effective stretch* defined by

$$\bar{\lambda} \stackrel{\text{def}}{=} \sqrt{\text{tr}\mathbf{C}/3} \equiv \sqrt{\mathbf{C}^{e(1)} : \mathbf{B}^{p\,(1)}/3}, \tag{5.19}$$

and following our work on amorphous polymers in Chapter 4, we choose a thermally-activated relation for the *equivalent plastic strain rate* in the specific form

$$\nu^{p(1)} = \begin{cases} 0 & \text{if} \quad \tau_{\mathrm{e}}^{(1)} \leq 0, \\ \nu_0^{(1)} \exp\Big(-\dfrac{1}{\zeta}\Big) \exp\Big(-\dfrac{Q}{k_B\,\vartheta}\Big) \left[\sinh\Big(\dfrac{\tau_{\mathrm{e}}^{(1)}\,V}{2k_B\vartheta}\Big)\right]^{1/m^{(1)}} & \text{if} \quad \tau_{\mathrm{e}}^{(1)} > 0, \end{cases} \tag{5.20}$$

where

$$\tau_{\mathrm{e}}^{(1)} \stackrel{\mathrm{def}}{=} \bar{\tau}^{(1)} - (S_a + S_b + \alpha_p\,\bar{p}), \tag{5.21}$$

denotes a *net shear stress for thermally-activated flow*; here $\alpha_p \geq 0$ is a parameter introduced to account for the *pressure sensitivity* of plastic flow. The parameter $\nu_0^{(1)}$ is a *pre-exponential factor* with units of 1/time, Q is an *activation energy*, k_B is Boltzmann's constant, V is an *activation volume*, and $m^{(1)}$ is a *strain rate sensitivity parameter*. The term $\exp(-1/\zeta)$ in (5.20) represents a *concentration of "flow defects,"* where ζ is a dimensionless parameter referred as *normalized equilibrium free-volume* in the literature on amorphous polymers (e.g., Spaepen, 1977).

Remark 1: The thermally activated form for the flow function (5.20) with $\left\{\nu_0^{(1)}, m^{(1)}, \zeta, Q, V\right\}$ *constants*, usually holds over a narrow range of temperature. Here, in order to model the plastic flow response over a range of temperature which spans the glass transition temperature of the material, ζ, and Q *are taken to be temperature dependent.*

With a linear temperature dependence of ζ, the term $\exp(-1/\zeta)$ represents the famous Vogel-Fulcher-Tamman (VFT) term, which is used widely to describe the temperature dependence of viscosity of polymeric liquids near their glass transition temperature (Vogel, 1921; Fulcher, 1925; Tammann and Hesse, 1926). Since the variation of ζ is expected to be small for temperatures below ϑ_g, we assume that $\zeta = \zeta_{gl} \equiv$ constant for $\vartheta < \vartheta_g$ and take the temperature dependence of ζ as

$$\zeta = \begin{cases} \zeta_{gl} & \text{for } \vartheta \leq \vartheta_g, \\ \zeta_{gl} + d(\vartheta - \vartheta_g) & \text{for } \vartheta > \vartheta_g. \end{cases} \tag{5.22}$$

The simple relation (5.22) is well-defined at temperatures lower than ϑ_g, and has a linear VFT-type form[5] at higher temperatures.

[5]Instead of the VFT form, Richeton et al. (2005a, 2006, 2007); Nguyen et al. (2008) have used Williams-Landel-Ferry (WLF)-type temperature-dependent expression for the plastic shear strain rate to extend to temperatures $\vartheta > \vartheta_g$. The WLF equation (Williams et al., 1955) can be written as

$$\exp\Big(-\frac{1}{\zeta}\Big) = \exp\Big(\frac{(\log_e 10) \times C_1\,(\vartheta - \vartheta_g)}{C_2 + \vartheta - \vartheta_g}\Big), \tag{5.23}$$

The temperature dependance of the activation energy Q is taken as

$$Q(\vartheta) = \frac{1}{2}(Q_{gl} + Q_r) - \frac{1}{2}(Q_{gl} - Q_r)\tanh\left(\frac{1}{\Delta}(\vartheta - \vartheta_g)\right), \tag{5.24}$$

where, $Q = Q_{gl}$ in the glassy regime, and $Q = Q_r (< Q_{gl})$ in the rubbery regime.

Evolution equations for internal variables

In a general form, the internal variables $\boldsymbol{\xi}^{(1)}$ can be presumed to evolve according to the differential equation

$$\dot{\xi}_i^{(1)} = \underbrace{h_i(\boldsymbol{\Lambda}^{(1)})\,\nu^{p(1)}}_{\text{dynamic evolution}} - \underbrace{\mathcal{R}_i(\boldsymbol{\Lambda}^{(1)})}_{\text{static recovery}}, \tag{5.25}$$

where the functions $h_i^{(1)}$ and $\mathcal{R}_i^{(1)}$ isotropic functions of their arguments and

$$\boldsymbol{\Lambda}^{(1)} \stackrel{\text{def}}{=} \left(\mathbf{C}^{e(1)}, \mathbf{B}^{p(1)}, \mathbf{A}, \boldsymbol{\xi}^{(1)}, \vartheta\right). \tag{5.26}$$

Remark 2: In (5.25), the functions $\mathcal{R}_i$ represent *static recovery* (or time recovery, or thermal recovery), since they do not depend on the plastic strain rate. The static recovery terms are important in *long time* situations such as creep experiments over a period of hours and days at high temperatures. Here, we focus our attention on thermal recovery processes that occur in relatively shorter periods of time (typically less than 10 minutes), in which case the slow static recovery effects may be neglected. Accordingly, in what follows, as a simplification, we neglect the effects of any static recovery in the evolution of the internal variables.

Further, the evolution equations for $\mathbf{F}^{p(1)}$ and $\boldsymbol{\xi}^{(1)}$ need to be accompanied by initial conditions. Typical initial conditions presume that the body is initially (at time $t = 0$, say) in a **virgin state** in the sense that

$$\mathbf{F}(\mathbf{X}, 0) = \mathbf{F}^{p(1)}(\mathbf{X}, 0) = \mathbf{1}, \qquad \xi_i^{(1)}(\mathbf{X}, 0) = \xi_{i0}^{(1)} \ (= \text{constant}), \tag{5.27}$$

so that by $\mathbf{F} = \mathbf{F}^{e(1)}\mathbf{F}^{p(1)}$ we also have $\mathbf{F}^{e(1)}(\mathbf{X}, 0) = \mathbf{1}$.

Evolution of φ and S_a:

We assume that the material disorders, and is accompanied by a microscale dilatation as plastic deformation occurs, resulting in an increase of the order-parameter φ,[6] and this increase in disorder leads to a change in the resistance S_a, causing a transient change in the flow stress of the material as plastic deformation proceeds. Accordingly, the evolution of the

where C_1 and C_2 are constants with dimensions of temperature. As is well-known, using suitable manipulations, the VFT and the WLF forms may be shown to be equivalent. Although the WLF and VFT equations are equivalent, the slightly simpler form of the VFT equation is often preferred.

[6]The microscale dilatation is extremely small, and at the macroscopic level we presume the plastic flow to be incompressible.

resistance S_a is coupled to the evolution of the order-parameter φ. Specifically, we take the evolution of S_a and φ to be governed by

$$\dot{S}_a = h_a \left(S_a^* - S_a\right) \nu^{p(1)}, \qquad \text{with initial value} \qquad S_a(\mathbf{X}, 0) = S_{a0}, \tag{5.28}$$

$$\dot{\varphi} = g \left(\varphi^* - \varphi\right) \nu^{p(1)} \qquad \text{with initial value} \qquad \varphi(\mathbf{X}, 0) = \varphi_0. \tag{5.29}$$

In the evolution equations for S_a and φ, the parameters h_a, g, S_{a0} and φ_0 are constants. During plastic flow, the resistance S_a increases (material hardens) if $S_a < S_a^*$, and it decreases (material softens) if $S_a > S_a^*$. The critical value S_a^* of S_a controlling such hardening/softening transitions is assumed to depend on the current values of the plastic strain rate, temperature, and the order-parameter φ. The function S_a^*, which controls the magnitude of the stress-overshoot, is taken as

$$S_a^* = b \left(\varphi^* - \varphi\right). \tag{5.30}$$

In (5.29), the parameter φ^* represents a strain-rate and temperature dependent critical value for the order-parameter: the material disorders when $\varphi < \varphi^*$, and becomes less disordered when $\varphi > \varphi^*$. We model the temperature and strain rate dependence of φ^* using the following phenomenological equation

$$\varphi^*(\nu^{p(1)}, \vartheta) = \begin{cases} z \left(1 - \dfrac{\vartheta}{\vartheta_g}\right)^r \left(\dfrac{\nu^{p(1)}}{\nu_r}\right)^s & \text{if } (\vartheta \leq \vartheta_g) \text{ and } (\nu^{p(1)} > 0), \\ 0 & \text{if } (\vartheta > \vartheta_g) \text{ or } (\nu^{p(1)} = 0), \end{cases} \tag{5.31}$$

with constants (z, r, s).

Thus, gathering the number of material parameters introduced to phenomenologically model the yield-peak, we have the following rather large list[7]

$$\left(h_a, b, S_{a0}, g, \varphi_0, z, r, s\right).$$

Evolution of S_b:

The experiments above ϑ_g indicate that the nonlinear stress response at large strains is not purely elastic as the unloading response shows significant hysteresis. It is for this reason that we have introduced the internal variable S_b to model a *dissipative* resistance to plastic flow which arises as the chains are pulled taut between entanglements, and there is increasing interaction between the long-chain molecules and pendant side-groups; this resistance is *in addition* to any entropic contribution from network chain-stretching. For the resistance S_b we assume

$$S_b = S_{b0} + H_b(\bar{\lambda} - 1)^{\ell}, \tag{5.32}$$

[7]Modeling the temperature and rate-sensitivity of the yield-peak over a wide-range of temperatures and strain rates is known to be complex. If a simpler theory with fewer material parameters is desired, and if it is deemed that modeling the yield-peak is not of interest, then there is no need to introduce the internal variables φ and S_a, and thereby also the attendant constants in their evolution equations.

where $\bar{\lambda}$ may be increasing or decreasing (i.e., loading or unloading). In (5.32) the material parameter H_b is temperature dependent and is assumed to have the following temperature dependence

$$H_b(\vartheta) = \frac{1}{2}(H_{gl} + H_r) - \frac{1}{2}(H_{gl} - H_r)\tanh\left(\frac{1}{\Delta}(\vartheta - \vartheta_g)\right) - L(\vartheta - \vartheta_g), \tag{5.33}$$

where H_{gl} and H_r ($< H_{gl}$) are values of H_b in the glassy and rubbery regions near the glass transition temperature ϑ_g, and L represents the slope of the temperature variation of H_b beyond the glass transition region, with

$$L = \begin{cases} L_{gl} & \vartheta \leq \vartheta_g, \\ L_r & \vartheta > \vartheta_g. \end{cases} \tag{5.34}$$

5.3.2 Constitutive equations for micromechanism $\alpha = 2$

Free energy

Let

$$\mathbf{F}^{e\,(2)}_{\text{dis}} \overset{\text{def}}{=} J^{-1/3}\,\mathbf{F}^{e(2)}, \quad \det \mathbf{F}^{e\,(2)}_{\text{dis}} = 1, \tag{5.35}$$

denote the distortional part of $\mathbf{F}^{e(2)}$. Correspondingly, let

$$\mathbf{C}^{e\,(2)}_{\text{dis}} \overset{\text{def}}{=} (\mathbf{F}^{e\,(2)}_{\text{dis}})^{\top}\mathbf{F}^{e\,(2)}_{\text{dis}} = J^{-2/3}\mathbf{C}^{e(2)}, \tag{5.36}$$

denote the elastic distortional right Cauchy-Green tensor and consider a free energy function in the special form[8]

$$\psi^{(2)} = \bar{\psi}^{(2)}(\mathbf{C}^{e\,(2)}_{\text{dis}}, \vartheta). \tag{5.37}$$

We use a simple phenomenological form for the free energy function $\psi^{(2)}$ proposed by Gent (1996):

$$\psi^{(2)} = -\tfrac{1}{2}\mu^{(2)}\, I_m^{(2)}\, \ln\left(1 - \frac{I_1^{(2)} - 3}{I_m^{(2)}}\right), \qquad \text{with} \qquad I_1^{(2)} \overset{\text{def}}{=} \operatorname{tr}\mathbf{C}^{e\,(2)}_{\text{dis}}, \tag{5.38}$$

where

$$\mu^{(2)}(\vartheta) > 0, \qquad \text{and} \qquad I_m^{(2)}(\vartheta) > 3 \tag{5.39}$$

are two temperature-dependent material constants, with $\mu^{(2)}$ representing the ground state rubbery shear modulus of the material, and $I_m^{(2)}$ representing maximum value of $(I_1^{(2)} - 3)$, associated with the limited extensibility of the polymer chains.

Experimental results indicate that the rubbery shear modulus $\mu^{(2)}$ *decreases* with increasing temperature; the empirical function chosen to fit the experimentally-observed tem-

[8]Since $J^{e\,(\alpha)} = J$, and we have already accounted for a volumetric elastic energy for $\psi^{(1)}$, we do not allow for a volumetric elastic energy for $\psi^{(2)}$ or $\psi^{(3)}$.

perature dependence of $\mu^{(2)}$ is

$$\mu^{(2)}(\vartheta) = \mu_g^{(2)} \exp\Big(- N(\vartheta - \vartheta_g)\Big), \tag{5.40}$$

where $\mu_g^{(2)}$ is the value of $\mu^{(2)}$ at the glass transition temperature, and N is a parameter that represents the slope of temperature variation on a logarithmic scale. The parameter $I_m^{(2)}$ is taken to be temperature-independent constant

$$I_m^{(2)}(\vartheta) \approx \text{constant}. \tag{5.41}$$

Cauchy stress. Mandel stress

Using the free energy (5.38) yields the corresponding second-Piola stress as

$$\mathbf{S}^{e(2)} = 2\frac{\partial \psi^{(2)}}{\partial \mathbf{C}^{e(2)}} = J^{-2/3}\mu^{(2)}\left(1 - \frac{I_1^{(2)} - 3}{I_m^{(2)}}\right)^{-1}\left[\mathbf{1} - \frac{1}{3}\left(\operatorname{tr}\mathbf{C}_{\text{dis}}^{e(2)}\right)\mathbf{C}_{\text{dis}}^{e(2)\,-1}\right], \tag{5.42}$$

which gives the contribution $\mathbf{T}^{(2)}$ to Cauchy stress as

$$\mathbf{T}^{(2)} = J^{-1}\mathbf{F}^{e(2)}\mathbf{S}^{e(2)}\mathbf{F}^{e(2)\top} = J^{-1}\left[\mu^{(2)}\left(1 - \frac{I_1^{(2)} - 3}{I_m^{(2)}}\right)^{-1}(\mathbf{B}_{\text{dis}}^{e(2)})_0\right], \tag{5.43}$$

where

$$\mathbf{B}_{\text{dis}}^{e(2)} \overset{\text{def}}{=} \mathbf{F}_{\text{dis}}^{e(2)}(\mathbf{F}_{\text{dis}}^{e(2)})^{\top} = J^{-2/3}\mathbf{B}^{e(2)} \tag{5.44}$$

denotes the elastic distortional left Cauchy-Green tensor.

The corresponding Mandel stress is

$$\mathbf{M}^{e(2)} = \mathbf{C}^{e(2)}\mathbf{S}^{e(2)} = \mu^{(2)}\left(1 - \frac{I_1^{(2)} - 3}{I_m^{(2)}}\right)^{-1}(\mathbf{C}_{\text{dis}}^{e(2)})_0, \tag{5.45}$$

and the *equivalent shear stress* for plastic flow is given by

$$\bar{\tau}^{(2)} \overset{\text{def}}{=} \frac{1}{\sqrt{2}}|\mathbf{M}^{e(2)}|. \tag{5.46}$$

Flow rule. Internal variables

The evolution equation for $\mathbf{F}^{p(2)}$ is

$$\dot{\mathbf{F}}^{p\,(2)} = \mathbf{D}^{p(2)}\,\mathbf{F}^{p(2)}, \tag{5.47}$$

with the plastic stretching $\mathbf{D}^{p(2)}$ given by

$$\mathbf{D}^{p(2)} = \nu^{p(2)} \left(\frac{\mathbf{M}^{e(2)}}{2\bar{\tau}^{(2)}} \right), \qquad \text{where} \quad \nu^{p(2)} \stackrel{\text{def}}{=} \sqrt{2}|\mathbf{D}^{p(2)}| \tag{5.48}$$

is the corresponding equivalent plastic shear strain rate. With $S^{(2)}(\vartheta)$ a positive-valued stress-dimensioned shear resistance, we take the equivalent plastic strain rate to be

$$\nu^{p(2)} = \nu_0^{(2)} \left(\frac{\bar{\tau}^{(2)}}{S^{(2)}} \right)^{1/m^{(2)}}, \tag{5.49}$$

where $\nu_0^{(2)}$ is a reference plastic shear strain rate with units of 1/time, and $m^{(2)}$ is a positive-valued strain-rate sensitivity parameter.

We assume that $S^{(2)}$ varies with temperature as

$$S^{(2)}(\vartheta) = \tfrac{1}{2}(S_{gl}^{(2)} + S_r^{(2)}) - \tfrac{1}{2}(S_{gl}^{(2)} - S_r^{(2)}) \tanh\left(\frac{1}{\Delta_2}(\vartheta - \vartheta_g) \right), \tag{5.50}$$

where, $S^{(2)} = S_{gl}^{(2)}$ in the glassy regime, and $S^{(2)} = S_r^{(2)} (\ll S_{gl}^{(2)})$ in the rubbery regime, and Δ_2 is a parameter related to the temperature range across which the transition occurs. A high value of $S^{(2)} = S_{gl}^{(2)}$ leads to $\nu^{p(2)} \approx 0$ when $\vartheta < \vartheta_g$, and as the temperature increases through the glass transition, the value of $S^{(2)}$ smoothly transitions to a very low value, allowing for plastic flow above ϑ_g. This assumption is meant to reflect the major effect of the rapid destruction of a *large fraction* of mechanical cross-links as the temperature increases beyond ϑ_g. To ensure a very rapid transition of $S^{(2)}$ near ϑ_g, we take $\Delta_2 = \Delta/20$. Thus, under a macroscopically-imposed deformation history at temperatures greater than a few degrees higher than ϑ_g, micromechanism $\alpha = 2$ freely deforms inelastically by relative chain-slippage, and there is no further increase in the corresponding elastic stretch $\mathbf{U}^{e(2)}$, and thereby the corresponding stress.

5.3.3 Constitutive equations for micromechanism $\alpha = 3$

Free energy

Let

$$\mathbf{F}_{\text{dis}} \stackrel{\text{def}}{=} J^{-1/3}\mathbf{F}, \quad \det \mathbf{F}_{\text{dis}} = 1, \tag{5.51}$$

denote the distortional part of $\mathbf{F}$. Correspondingly, let

$$\mathbf{C}_{\text{dis}} \stackrel{\text{def}}{=} (\mathbf{F}_{\text{dis}})^{\top}\mathbf{F}_{\text{dis}} = J^{-2/3}\mathbf{C}, \tag{5.52}$$

denote the distortional right Cauchy-Green tensor, and consider a free energy function in the special form

$$\psi^{(3)} = \bar{\psi}^{(3)}(\mathbf{C}_{\text{dis}}, \vartheta). \tag{5.53}$$

Similar to the case of micromechanism $\alpha = 2$, we assume the free energy in the Gent form as

$$\psi^{(3)} = -\tfrac{1}{2}\mu^{(3)}\, I_m^{(3)}\, \ln\Big(1 - \frac{I_1^{(3)} - 3}{I_m^{(3)}}\Big), \qquad \text{with} \qquad I_1^{(3)} \stackrel{\text{def}}{=} \operatorname{tr} \mathbf{C}_{\text{dis}}, \tag{5.54}$$

where

$$\mu^{(3)} > 0, \qquad \text{and} \qquad I_m^{(3)} > 3 \tag{5.55}$$

are two material constants. These two material constants are assumed to be *temperature-independent.*

Cauchy stress

Using the free energy (5.54) yields the corresponding second Piola stress as

$$\mathbf{S}^{e(3)} = J^{-2/3}\mu^{(3)} \Big(1 - \frac{I_1^{(3)} - 3}{I_m^{(3)}}\Big)^{-1} \Big[\mathbf{1} - \frac{1}{3}\Big(\operatorname{tr} \mathbf{C}_{\text{dis}}\Big)\mathbf{C}_{\text{dis}}^{-1}\Big], \tag{5.56}$$

and the contribution $\mathbf{T}^{(3)}$ to Cauchy stress as

$$\mathbf{T}^{(3)} = J^{-1}\left[\mu^{(3)} \Big(1 - \frac{I_1^{(3)} - 3}{I_m^{(3)}}\Big)^{-1} (\mathbf{B}_{\text{dis}})_0\right], \tag{5.57}$$

where

$$\mathbf{B}_{\text{dis}} \stackrel{\text{def}}{=} \mathbf{F}_{\text{dis}}(\mathbf{F}_{\text{dis}})^{\mathsf{T}} = J^{-2/3}\mathbf{B} \tag{5.58}$$

denotes the distortional left Cauchy-Green tensor.

5.3.4 Fourier's Law

The heat flux is taken to be given by Fourier's law

$$\mathbf{q}_{\text{R}} = -\kappa\, \nabla\vartheta, \tag{5.59}$$

with $\kappa(\vartheta) > 0$ the thermal conductivity.

5.3.5 Partial differential equations for the deformation and temperature fields

The partial differential equation for the deformation is obtained from the local force balance

$$\operatorname{Div} \mathbf{T}_{\text{R}} + \mathbf{b}_{0_{\text{R}}} = \rho_{\text{R}} \ddot{\boldsymbol{\chi}}, \tag{5.60}$$

where $\mathbf{b}_{0_R}$ is the non-inertial body force per unit volume of the reference body, $\rho_R > 0$ is the mass density, , and

$$\mathbf{T}_R = J\mathbf{T}\mathbf{F}^{-\top} \tag{5.61}$$

is the standard first Piola stress, with $\mathbf{T}$ given by $\mathbf{T} = \sum_{\alpha=1}^{3} \mathbf{T}^{(\alpha)}$.

Following the *approximations* considered in Chapters 3 and 4, (i) we assume that specific heat depends only on temperature, $c \approx \hat{c}(\vartheta)$; and (ii) we neglect the thermoelastic coupling terms, and assume instead that only a fraction $0 \lessapprox \omega \lessapprox 1$ of the rate of plastic dissipation contributes to the temperature changes. Under these approximate assumptions, the simplified partial differential equation for the temperature is

$$c\dot{\vartheta} = -\mathrm{Div}\,\mathbf{q}_R + q_R + \omega \left(\bar{\tau}^{(1)}\nu^{p\,(1)} + \bar{\tau}^{(2)}\nu^{p\,(2)}\right). \tag{5.62}$$

5.4 Fit of the stress-strain curves and material parameters

The material parameters appearing in the specialized model were calibrated by fitting the experimental stress-strain data for tBA/PEGDMA shown in Fig. 5-2 by following the procedure described in the Appendix A. These material parameters are listed in Table 5.1. The stress-strain curves calculated using the specialized model and the material parameters for tBA/PEGDMA are plotted in Fig. 5-4 as dashed lines. As shown in this figure, the constitutive model reasonably accurately reproduces all the major features of the macroscopic stress-strain response of the material both in the "glassy-polymer" regime below ϑ_g , and the "hysteretic-rubber" response above ϑ_g.

Remark 3: There are very few notable models for the time- and temperature-dependent response of elastomeric materials in the existing literature (e.g., Lion, 1997; Reese and Govindjee, 1998; Bergström and Boyce, 1998; Haupt and Sedlan, 2001; Bergström and Boyce, 2001). Considering the response of the tBA/PEGDMA thermoset shape memory polymer at temperatures above ϑ_g (cf. Fig. 5-4), we observe a behavior typical of a hysteretic elastomeric material; there is no yield-peak, and the polymer shows significant temperature- and rate-dependent nonlinear hysteretic behavior upon unloading after deformation to large strains. *The constitutive theory presented here may be used to phenomenologically model the temperature- and rate-dependent mechanical response of elastomeric materials.* In our constitutive theory, at temperatures above ϑ_g: (i) due to lack of yield-peak, the internal variables φ and S_a in micromechanism $\alpha = 1$ can be ignored; and (ii) the contribution from micromechanism $\alpha = 2$ to the overall stress-strain response is very small and it can be neglected. Therefore, for the special case of hysteretic elastomeric materials, our constitutive theory reduces from three micromechanisms to two, with only micromechanisms $\alpha = 1$ and $\alpha = 3$ contributing to the overall stress-strain response. This results in a reduced list of

material parameters

$$\{\, \vartheta_r, n, G_r, M_r, \nu_r^{\text{poi}}, \alpha_p, \nu_0^{(1)}, m^{(1)}, V, Q_r, \zeta_{gl}, d, S_{b0}, H_r, L_r, \mu^{(3)}, I_m^{(3)} \,\}$$

to phenomenologically model the mechanical response of elastomeric materials.[9]

Table 5.1: Material parameters for the tBA/PEGDMA shape memory polymer

Parameter	Value	Parameter	Value
ρ (kg m^{-3})	1020	b (MPa)	5850
α_{gl} (K^{-1})	13×10^{-5}	g	5.8
α_r (K^{-1})	25×10^{-5}	φ_0	0
ν_r (s^{-1})	5.2×10^{-4}	z	0.083
ϑ_r (K)	310	r	1.3
n (K)	2.1	s	0.005
Δ (K)	2.6	S_{b0} (MPa)	0
G_{gl} (MPa)	156	$H_{gl}(MPa)$	1.56
G_r (MPa)	13.4	L_{gl} (MPa K^{-1})	0.44
M_{gl} (MPa K^{-1})	7.4	H_r (MPa)	0.76
M_r (MPa K^{-1})	0.168	L_r (MPa K^{-1})	0.006
ν_{gl}^{poi}	0.35	l	0.5
ν_r^{poi}	0.49	$\mu_g^{(2)}$ (MPa)	1.38
α_p	0.058	N (K^{-1})	0.045
$\nu_0^{(1)}$ (s^{-1})	1.73×10^{13}	$I_m^{(2)}$	6.3
$m^{(1)}$	0.17	$\nu_0^{(2)}$ (s^{-1})	5.2×10^{-4}
V (m^3)	2.16×10^{-27}	$m^{(2)}$	0.19
Q_{gl} (J)	1.4×10^{-19}	$S_{gl}^{(2)}$ (MPa)	58
Q_r (J)	0.2×10^{-21}	$S_r^{(2)}$ (MPa)	3×10^{-4}
ζ_{gl}	0.14	$\mu^{(3)}$ (MPa)	0.75
d (K^{-1})	0.015	$I_m^{(3)}$	5.0
S_{a0} (MPa)	0	ω	0.7
h_a	230		

[9]The model does not account for the phenomenon of stress-softening (Mullins effect) commonly observed in certain elastomeric materials.

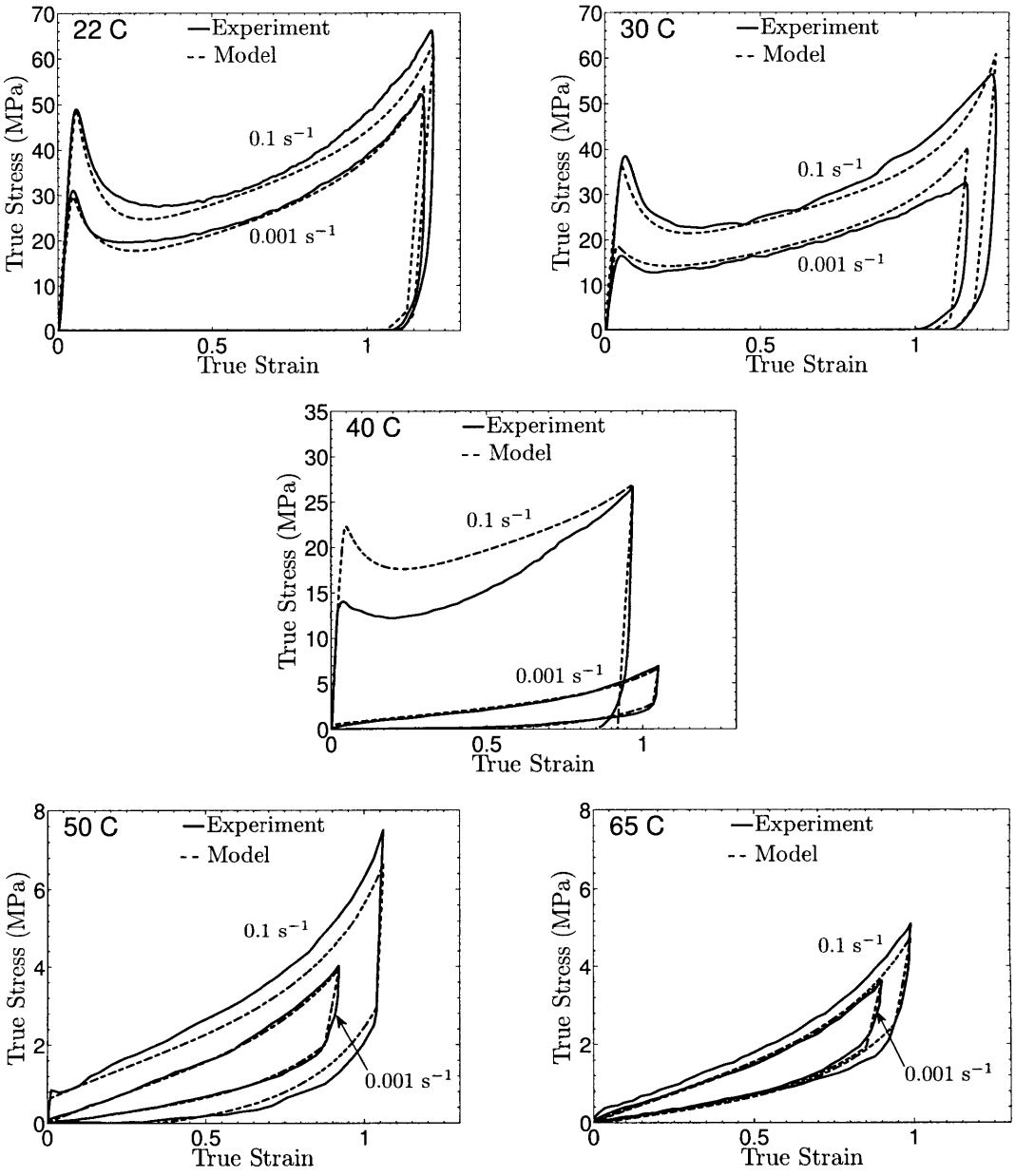

Figure 5-4: Fit of the model to experimental stress-strain curves for the shape memory polymer at strain rates of 10^{-3} s^{-1} and 3×10^{-3} s^{-1}, and at temperatures of 22 °C, 30 °C, 40 °C, 50 °C, and 65 °C. The experimental data is plotted as solid lines, while the fit is shown as dashed lines.

5.5 Validation experiments and simulations

Shawn A. Chester has numerically implemented the theory by writing a user-material subroutine for a widely-used finite element program ABAQUS/Standard (2009). In order to validate the predictive capabilities of our constitutive theory and its numerical implementation, in this section we show the results of two thermo-mechanical experiments that we have performed on the tBA/PEGDMA shape-memory polymer, and compare the results of macroscopic measurements from these experiments against results from corresponding numerical simulations. The validation experiments considered below are

(i) Measurement of the *force-versus-time* response of a ring-shaped specimen which was subjected to the following thermo-mechanical history: the specimen was heated to a temperature above ϑ_g of the material, the ring was then compressed into an oval shape, the compression grips were then held *fixed* while the specimen was first cooled to a temperature below ϑ_g, and then heated back to its initial temperature above ϑ_g. We call an experiment of this type a *constrained-recovery* experiment.

(ii) Measurement of the *displacement-versus-time* response of a planar specimen in the shape of a diamond-shaped lattice which was subjected to the following thermo-mechanical history: the specimen was compressed between two platens at temperature above ϑ_g of the material, the compression platens were then held *fixed* while the specimen was cooled to a temperature below ϑ_g. The constraint of the platens was then removed, and the specimen was heated to a temperature above ϑ_g and allowed to freely recover its shape. We call an experiment of this type an *unconstrained-recovery* or a *free-recovery* experiment.

Both thermo-mechanical experiments were conducted on an EnduraTEC Electroforce 3200 testing machine equipped with a furnace. The temperature of the polymer was measured by using a thermo-couple attached to the specimen. Transient heat conduction within the polymer was neglected since the effect was small. Consequently, in the numerical simulations we prescribed the measured temperature profile to all nodes in the finite element mesh.

5.5.1 Force-time response of a ring-shaped specimen subjected to a constrained-recovery experiment

The flat specimen, 3 mm thick, was ring-shaped with two extension arms which were used for gripping the specimen. The ring portion of the specimen had an outer diameter of 11.9 mm and an inner diameter of 6.3 mm, while the extension arms were each 12.7 mm long and 4.1 mm wide. The experimental set-up with the tBA/PEGDMA specimen mounted in place within the furnace of the EnduraTEC testing machine is shown in Fig. 5-5. The top and the bottom flat surfaces of the extension arms were rested against the base of the grips, and the vertical sides were securely tightened in the grips.

The specimen was subjected to the following thermo-mechanical history: (i) it was heated to 58 °C and gripped; (ii) the bottom grip was fixed in place while the top grip was moved

downwards at a velocity 0.01 mm s^{-1} for a total displacement of 2.5 mm to deform the ring; (iii) the grips were then held fixed in their positions and the specimen was first cooled to 32 °C and then heated back to 58 °C. The displacement and temperature histories for the experiment are shown in Fig. 5-6a. The reaction forces during the experiment were recorded using a load-cell, and the measured force-versus-time curve is shown in Fig. 5-6b.

For the finite element simulation of this constrained-recovery experiment we make use of the symmetry of the geometry, and only mesh one-eighth of the geometry using 537 ABAQUS-C3D8HT thermo-mechanically-coupled elements; Fig. 5-7a. Referring to this figure, all the nodes on the surface formed by CD extending into the 3-direction were prescribed displacement boundary conditions which enforced symmetry in the 1-direction, all the nodes on the surface formed by AB extending into the 3-direction were prescribed symmetry in the 2-direction, and all the nodes on the front surface defined by ABCD were prescribed symmetry in the 3-direction. A displacement history was prescribed to the highlighted nodes on the outer surface of the extension arm such that the displacement history for the complete geometry matched that of the experiment. The experimentally-measured temperature history was prescribed to the whole mesh. Fig. 5-7b shows the deformed mesh at the end of the compression step.

Fig. 5-6b compares the experimentally-measured and the numerically-predicted force-versus-time curves. The measurements from the experiment show that a compressive force was generated during the deformation at 58 °C. Subsequently, under the fixed-grip conditions, upon cooling to 32 °C the compressive force gradually reduces and transitions to a state of tension; and finally, upon heating back to 58 °C, the reaction force transitions back to a compressive state. As shown in Fig. 5-6b, the simulation is able to reasonably accurately predict the force-versus-time response for the constrained-recovery experiment.

5.5.2 Displacement-time response of a diamond-lattice-shaped specimen subjected to an unconstrained-recovery experiment

The flat diamond-lattice-shaped specimen, Fig. 5-8a, was 50 mm wide, 35 mm tall, and 3 mm thick. Each diamond-shaped cut-out was a square with 6.5 mm sides with a 1 mm fillet-radius at the corners; the width of the ligaments forming the lattice was 2.16 mm.

The specimen was subjected to the following thermo-mechanical history: (i) it was compressed between two platens at 60 °C at a relative platen velocity of 0.02 mm s^{-1}, and the height of the specimen was reduced from 35 mm to 20.5 mm — this resulted in an increase in its width from 50 mm to 59.5 mm; (ii) the platens were held in place and the specimen was cooled to 21 °C — the deformed shape is shown in Fig. 5-8b; (iii) the compression platens were then removed and the specimen was heated to 58 °C according to the temperature-versus-time history shown in Fig. 5-9. The dimensional changes in the specimen during this unconstrained-recovery phase were measured using a video-extensometer. The experimentally-measured stretches (L/L_0) in the 1- and 2-directions as functions of temperature and time during the unconstrained heating phase of the experiment are shown in Fig. 5-10 and Fig. 5-11, respectively.

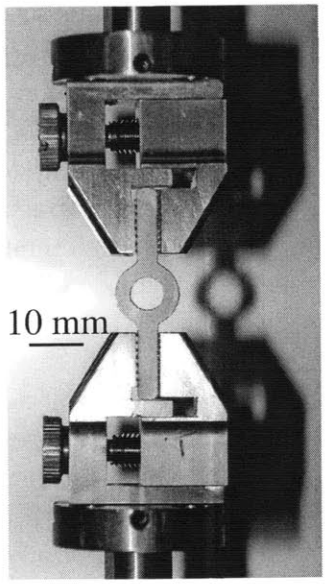

Figure 5-5: Experimental set-up for a thermo-mechanical constrained-recovery experiment on a ring-shaped specimen of tBA/PEGDMA.

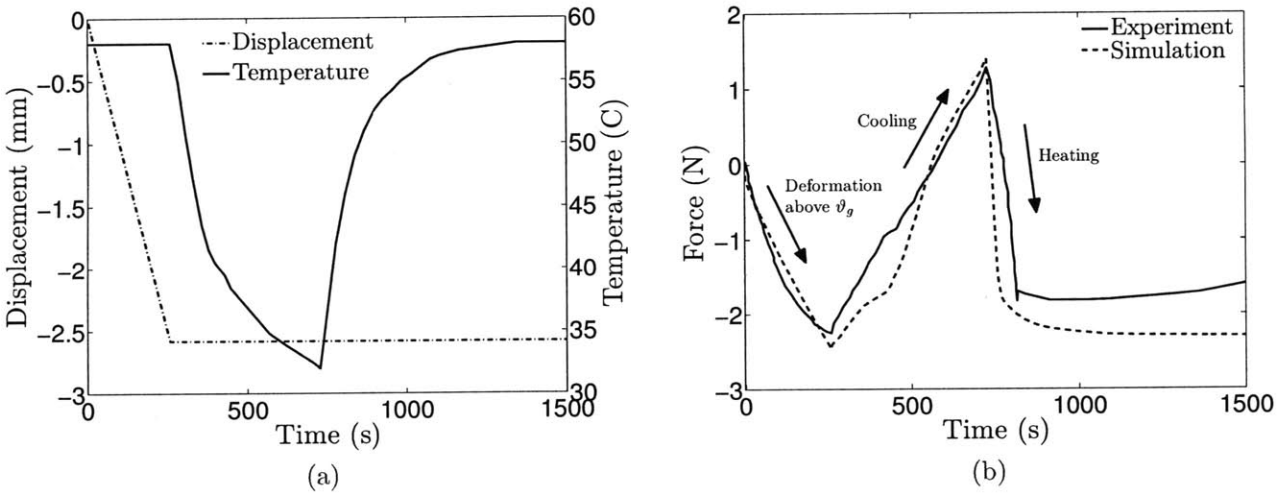

Figure 5-6: (a) Histories of the specimen-temperature and the relative-displacement of the grips: the specimen, initially at 58 °C, was compressed and the grips were then fixed in position while the specimen was first cooled to 32 °C and then heated back to 58 °C; corresponding reaction forces were measured by a load-cell. (b) The solid line shows the experimentally-measured force-versus-time curve for the constrained-recovery experiment. The corresponding numerically-predicted response is shown as a dashed line.

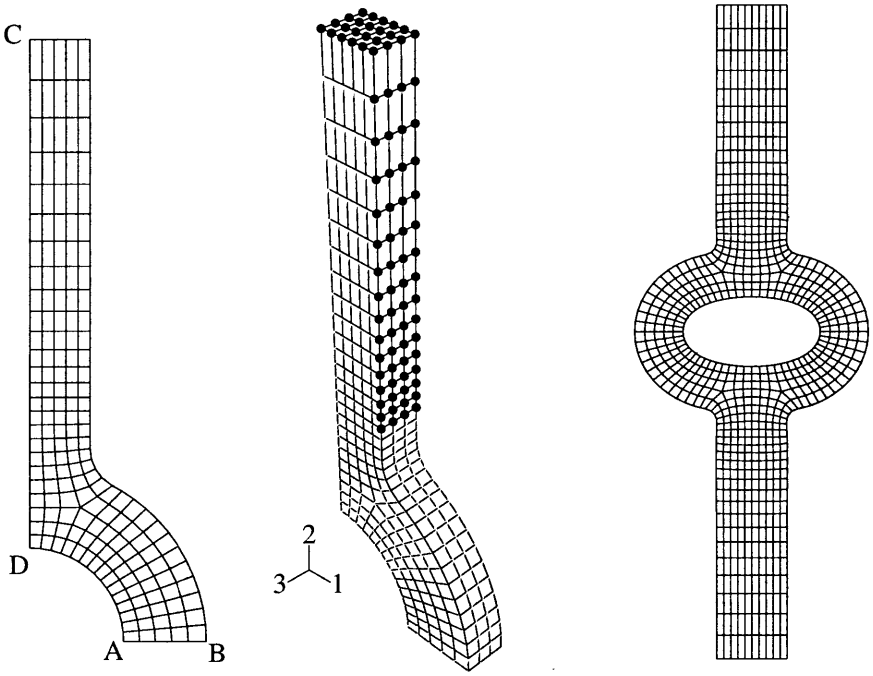

Figure 5-7: (a) One-eighth symmetry finite element mesh for the ring-shaped polymer. All the nodes on the surface formed by CD extending into the 3-direction were prescribed symmetry in the 1-direction, all the nodes on the surface formed by AB extending into the 3-direction were prescribed symmetry in the 2-direction, and all the nodes on the front surface defined by ABCD were prescribed symmetry in the 3-direction. A displacement history was prescribed to the highlighted nodes on the outer surface of the extension arm such that the displacement history for the complete geometry matched that of the experiment in Fig. 5-7b. (b) Deformed mesh.

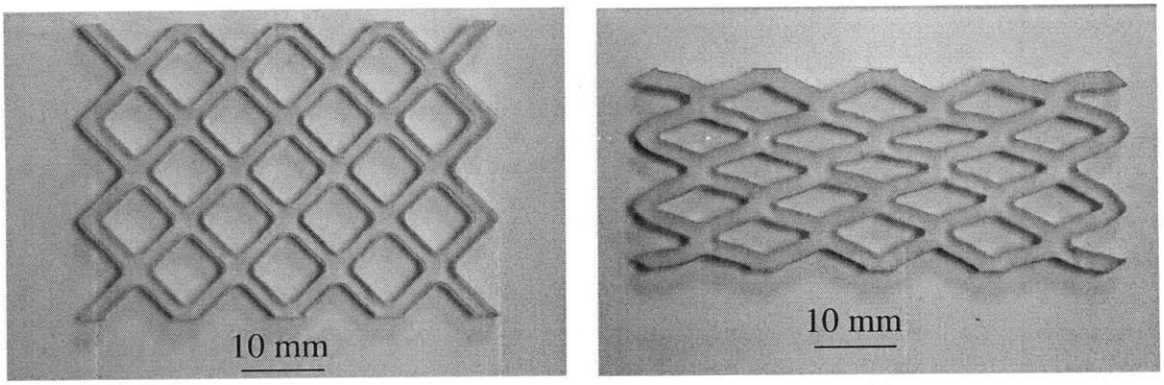

(a) (b)

Figure 5-8: Diamond-lattice-shaped specimen: (a) Undeformed specimen. (b) Deformed specimen in its "temporary shape" at room temperature — deformed at 60 °C, constrained cooling to 21 °C, and constraints removed.

For the finite element simulation of this experiment we make use of the symmetry of the geometry and only mesh one-eighth of the geometry, using 1962 ABAQUS-C3D8HT thermo-mechanically-coupled elements, Fig. 5-12. Referring to this figure, all the nodes on the 2-3 symmetry plane were prescribed symmetry displacement boundary conditions in the 1-direction, all the nodes on the 1-3 symmetry plane were prescribed symmetry boundary conditions in the 2-direction, and all the nodes on the front surface were prescribed symmetry boundary conditions in the 3-direction. The displacement history was prescribed to the highlighted nodes on the top surface during the hot-deformation and cooling steps. Our numerical simulation included all the steps described above for the thermo-mechanical history, including the initial hot-deformation, cooling, and finally the unconstrained shape-recovery with the applied temperature change. The results from the numerical simulation for the stretch in the 2-direction versus the temperature for the complete thermo-mechanical cycle are shown in Fig. 5-13. Fig. 5-10 and Fig. 5-11 compare the numerically-predicted and experimentally-measured stretches in the 1- and 2-directions versus temperature and time, respectively, during the unconstrained heating phase of the experiment. The numerically-predicted results are in good agreement with experimental measurements.

Finally, the left pane in Fig. 5-14 shows images of the specimen at various temperatures during unconstrained shape-recovery, while the right pane in this figure shows corresponding predictions from the numerical simulations.[10] The shapes at various temperatures predicted by the numerical simulation closely match those which were observed in the experiment.

[10]In Fig. 5-14, for ease of visualization, we have mirrored the simulation results along the symmetry planes.

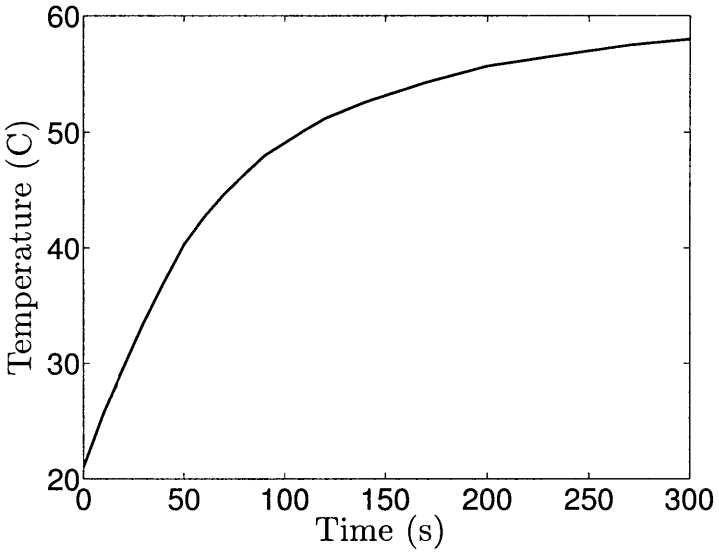

Figure 5-9: Time-temperature history for the diamond-lattice-shaped specimen during the unconstrained heating phase of the experiment.

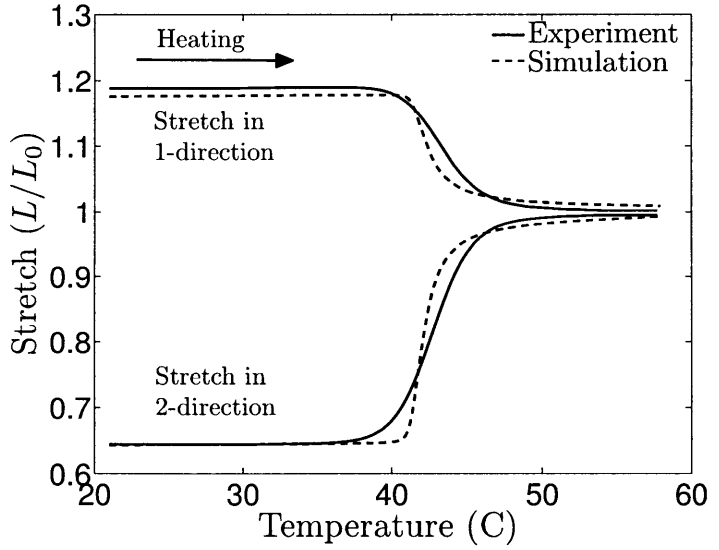

Figure 5-10: The solid lines show the experimentally-measured stretch-versus-temperature curves in the 1- and 2-direction during the unconstrained heating phase of the experiment. The dashed-lines are the corresponding numerically-predicted results.

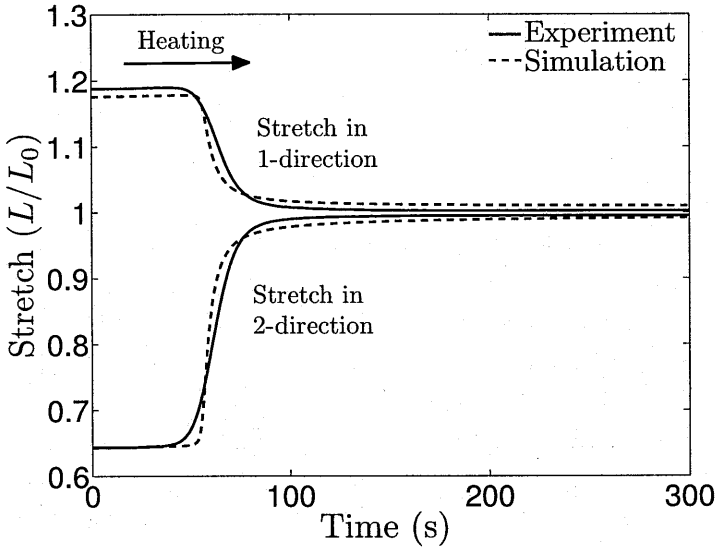

Figure 5-11: The solid lines show the experimentally-measured stretch-versus-time curves in the 1- and 2-direction during the unconstrained heating phase of the experiment. The dashed-lines are the corresponding numerically-predicted results.

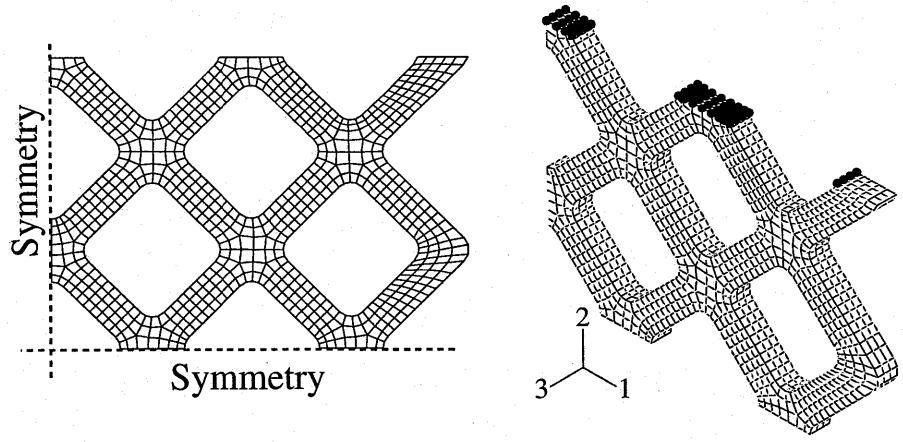

Figure 5-12: One-eighth symmetry finite element mesh for the diamond-shaped lattice geometry. All the nodes on the symmetry plane 2-3 were prescribed symmetry in the 1-direction, all the nodes on the symmetry plane 1-3 were prescribed symmetry in the 2-direction, and all the nodes on the front surface were prescribed symmetry in the 3-direction. A displacement history was prescribed to the highlighted nodes on the top surface to obtain a temporary shape that closely matches that from the experiment.

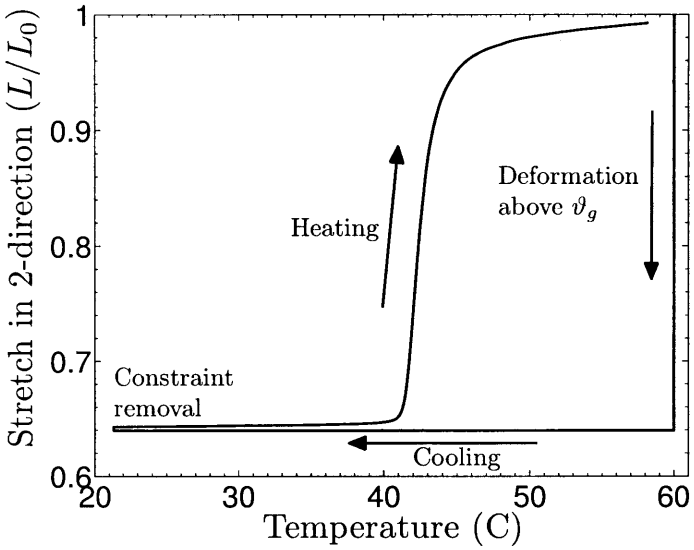

Figure 5-13: Numerical simulation results for the complete thermo-mechanical shape-recovery cycle of the lattice geometry. The lattice was deformed in the 2-direction at 60 °C; after which it was constrained in the 2-direction and was cooled to 21 °C; the constraints were then removed which resulted in a small elastic recovery; finally, the lattice was heated to 58 °C during which, it recovered almost to its original shape.

5.6 Numerical simulation of insertion of a stent in an artery

Shape-memory polymers have been proposed as potential materials for stents which expand and/or support blood vessels, and several experimental demonstrations of this concept have been published in the literature (e.g., Wache et al., 2003; Yakacki et al., 2007; Baer et al., 2007b). However, to the best of our knowledge, no reports of a numerical-simulation capability that can aid in understanding the performance of shape-memory-polymer-based stents exist in the current literature. As a demonstration of the robustness of our three-dimensional numerical-simulation capability in what follows we show results from a simulation of the shape-recovery response of a stent made from tBA/PEGDMA when it is inserted in an artery, with the latter modeled as a tube made from a nonlinear elastic material.

In our simulation we considered a cylindrical stent made from tBA/PEGDMA with diamond-shaped perforations, similar to those in the planar geometry considered in the previous subsection. The stent was modeled to have an initial length of 8 mm, and the outer and inner diameters of the stent were modeled as 8 mm and 7 mm, respectively. For the artery, we assumed a tubular geometry with an inner diameter of 5 mm, a wall thickness of 0.35 mm, and a length of 50 mm. The artery was modeled as an incompressible elastic Neo-Hookean material with a shear modulus of 33.33 kPa.

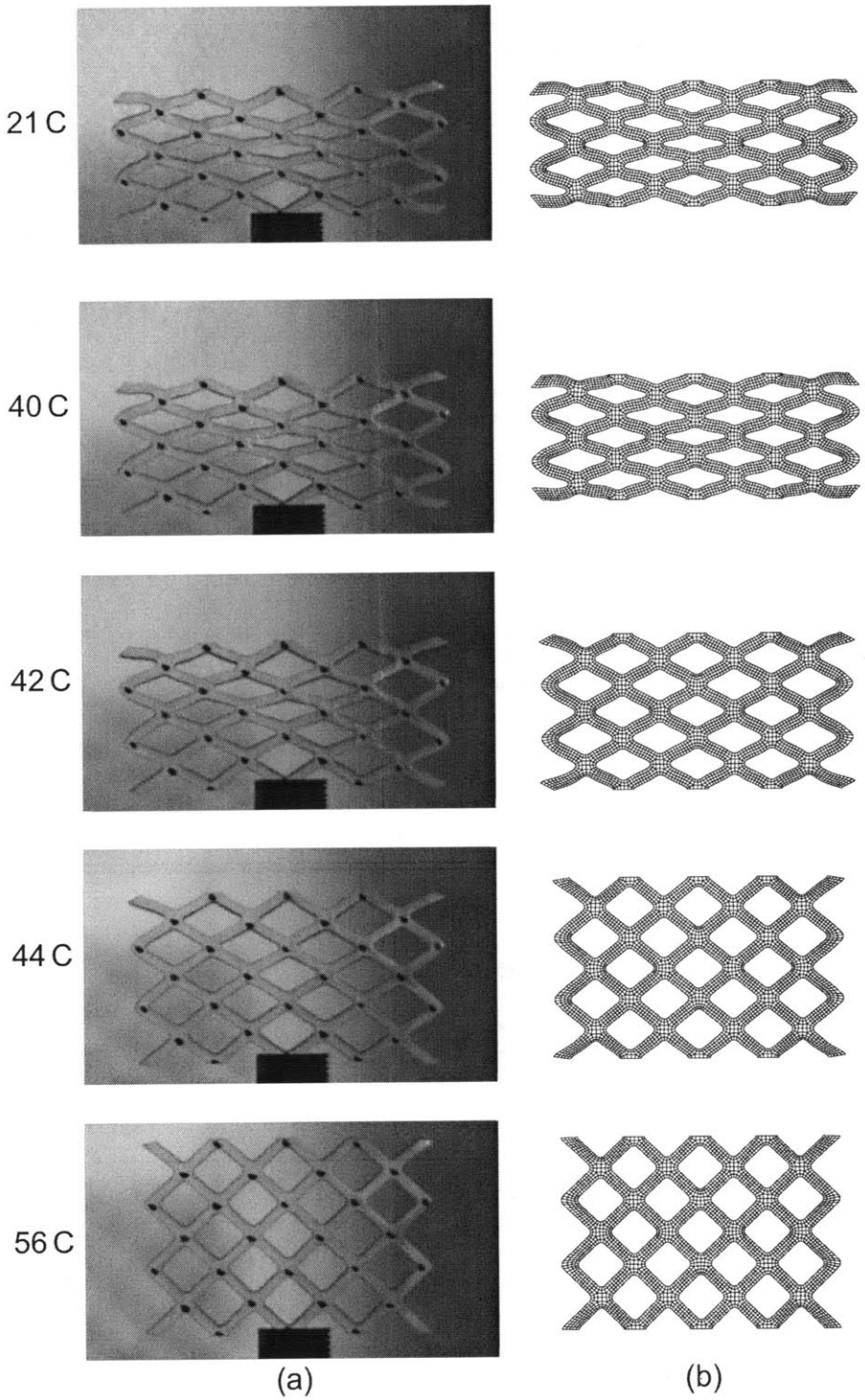

Figure 5-14: Comparison of (a) the experimentally-observed, and (b) the numerically-predicted recovered shapes at various temperatures during the unconstrained-recovery phase of the experiment.

The stent was subjected to the following thermo-mechanical history: (i) it was radially compressed above ϑ_g at 60 °C to reduce its outer diameter to 4.7 mm; (ii) cooled under kinematical constraints to 22 °C at a rate of 0.1 °C s^{-1} to fix its deformed shape; (iii) the constraints were removed; (iv) following which it was inserted into an arterial tube; and (v) was heated back to 60 °C at a rate of 0.1 °C s^{-1} to allow the stent to attempt to recover its initial shape under the constraints imposed by the artery.[11]

Due to the symmetry of the problem in our simulation we considered only one-eighth of the stent geometry, which was modeled using 1077 ABAQUS-C3D8HT thermo-mechanically-coupled elements, Fig. 5-15. The displacement boundary conditions prescribed to the stent were as follows: symmetry in the 1-direction for all the nodes on the surface defined by edge CD extending into the 3-direction; symmetry in the 2-direction for all the nodes on the surface defined by edge AB extending into the 3-direction; and symmetry in the 3-direction for all the highlighted nodes on the front surface. To apply the initial deformation above ϑ_g, all of the nodes at the outer diameter were given an inward radial displacement.

The finite element mesh for the artery consisted of 1500 ABAQUS-C3D8H elements: 2 elements through the thickness, 50 elements along the length, and 15 elements around the one-quarter circumference. For the artery, the displacement boundary conditions $u_1 = 0$, $u_2 = 0$ and $u_3 = 0$ were applied for all the nodes on the face perpendicular to the 3-direction and away from the stent; symmetry in the 3-direction was applied to all the nodes that were on the face perpendicular to the 3-direction and close to the stent. Contact between the stent and artery was modeled as frictionless.

Predictions from the numerical simulation for the outer-diameter of the stent at different temperatures during the imposed thermo-mechanical history of insertion of a stent in an artery are shown in Fig. 5-16. The simulation results in Fig. 5-16 show that the outer diameter of the stent recovered from 4.74 mm to 6.06 mm by the time the temperature reached 47 °C during heating; further heating to 60 °C only increased the outer diameter from 6.06 mm to 6.22 mm; that is, 90% of the total shape-recovery occurred by the time the stent was heated to 47 °C. Fig. 5-17a shows the initial undeformed stent, while Fig. 5-17b shows the deformed stent after radial compression at 60 °C. Fig. 5-17c shows snapshots of the stent inside the artery during shape-recovery at 22 °C, 42 °C, and 60 °C.

[11] We emphasize that this a purely numerical exercise; no actual stent for application in humans is expected to be heated to 60 °C!

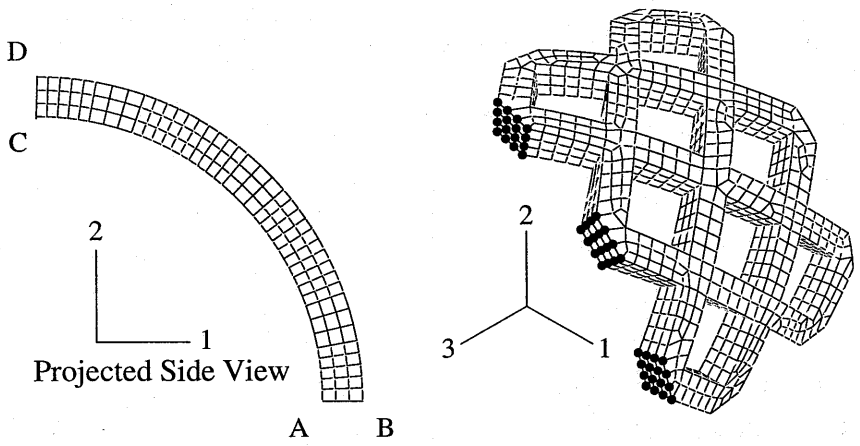

Figure 5-15: One-eighth symmetry finite element mesh for a vascular stent. The displacement boundary conditions prescribed were: symmetry in the 1-direction for the nodes on the surface formed by edge CD extending into the 3-direction; symmetry in the 2-direction for the nodes on the surface defined by edge AB extending into the 3-direction; and symmetry in the 3-direction for the highlighted nodes on the front surface.

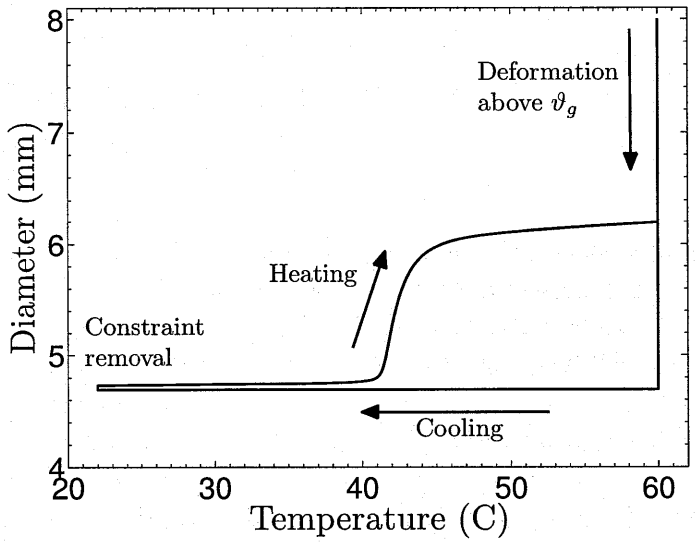

Figure 5-16: Predictions from the numerical simulation for the outer-diameter of the stent at different temperatures during the imposed thermo-mechanical history of insertion of a stent in an artery: (i) the tBA/PEGDMA stent was radially compressed at 60 °C to reduce its outer diameter from its initial 8 mm value to 4.7 mm; (ii) the compressed stent was cooled to 22 °C; (iii) the constraints were then removed and the stent recovered to a diameter of 4.74 mm at 22 °C; finally (iv) the stent was inserted into an artery and was heated to 60 °C during which its outer diameter recovered to a value of 6.22 mm.

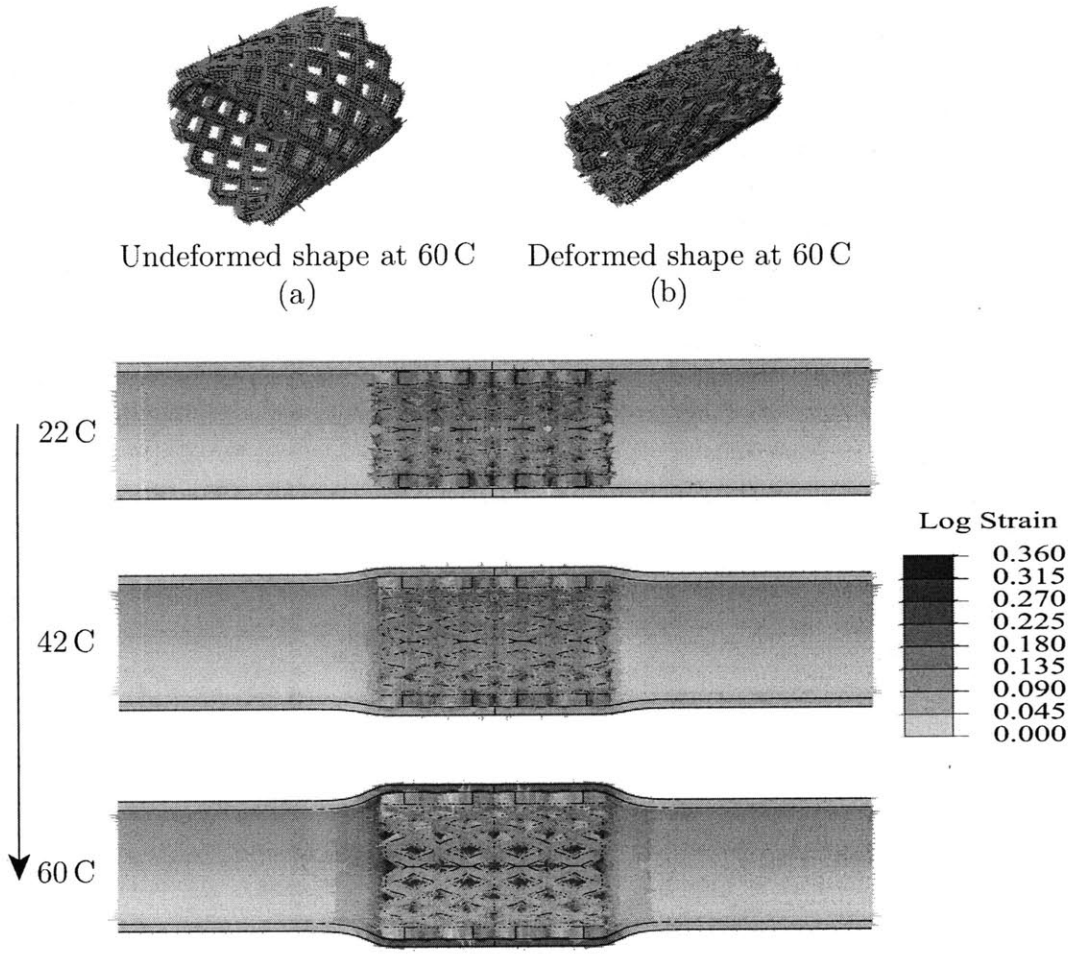

Figure 5-17: Numerically-predicted thermo-mechanical shape-recovery cycle for the vascular stent; for clarity the mesh has been mirrored along relevant symmetry planes to show the full stent and artery. (a) Undeformed original stent. (b) Deformed stent. (c) Shape-recovery of the stent inside the artery with temperature.

Chapter 6

Concluding remarks

We have presented a thermo-mechanically coupled large-deformation isotropic elastic-viscoplastic theory for amorphous polymers for the purpose of simulation and design of important polymer processing operations, and for predicting the relationship between processing methods and the subsequent mechanical properties of polymeric products. In this thesis:

- We have developed the following specialized thermo-mechanically coupled, large-deformation constitutive theories: (i) a constitutive theory for amorphous polymers below their glass transition temperature for a wide range of strain-rates; (ii) a constitutive theory for amorphous polymers in a temperature range which spans their glass transition; and (iii) a constitutive theory to model the shape memory response of shape memory polymers.

- We have generated a relatively complete set of stress-strain data for a technologically important amorphous thermoplastic cyclo-olefin copolymer Zeonex-690R by conducting a suite of simple compression experiments on Zeonex-690R to large strains exceeding 130%, including loading and unloading; at strain rates of $3 \times 10^{-4}\,\mathrm{s}^{-1}$, $3 \times 10^{-3}\,\mathrm{s}^{-1}$, $3 \times 10^{-2}\,\mathrm{s}^{-1}$, and $3 \times 10^{-1}\,\mathrm{s}^{-1}$, in a temperature range from room temperature to $\approx 40\,^{\circ}\mathrm{C}$ above the glass transition temperature of the material. Stress-strain data for a chemically cross-linked shape memory polymer has also been generated for strains $\sim 100\%$, at strain rates of $10^{-3}\,\mathrm{s}^{-1}$, and $10^{-1}\,\mathrm{s}^{-1}$, in a temperature range from room temperature to $\approx 30\,^{\circ}\mathrm{C}$ above the glass transition temperature of the material. The polymer was fabricated via photopolymerization of a tert-butyl acrylate (tBA) monomer with the cross-linking agent poly(ethylene glycol) dimethacrylate (PEGDMA).

- Detailed calibration procedures for the material parameters that appear in our theories have also been presented. Following these procedures, we have obtained material parameter values for (i) three technologically important thermoplastic amorphous polymers Zeonex-690R, PC and PMMA, and (ii) a tBA/PEGDMA thermoset shape memory polymer.

- An implicit time-integration procedure for our thermo-mechanically coupled theory was developed and implemented by Shawn A. Chester to create a numerical simulation capability for the finite element program ABAQUS/Standard (2009). Using this simulation capability, polymer processing operations such as micro-hot-embossing, thermoforming, and blow-molding as well as thermo-mechanical shape-recovery response of shape memory polymers have been successfully simulated.

- Results for the following macro-scale validation experiments which involved inhomogeneous deformations are presented: (i) isothermal fixed-end reversed torsion test on PC; (ii) high-speed normal-impact of a circular plate of PC; (iii) isothermal plane-strain cold- and hot-forming operations on PC; (iv) isothermal, axi-symmetric hot-forming operations on Zeonex-690R; (v) blow-forming of thin-walled semi-spherical shapes in PC; (vi) force-time response of a ring-shaped tBA/PEGDMA shape memory polymer specimen subjected to a constrained-recovery experiment; and (vii) unconstrained-recovery response of a diamond-lattice-shaped specimen of tBA/PEGDMA shape memory polymer. In addition to validating the accuracy of our models and their numerical implementations, these experimental results could also serve the purpose of verifying the predictive capability of other models.

- We have used numerical simulations to successfully determine suitable temperature, pressure and hold-time process conditions for micro-hot-embossing of various features in Zeonex-690R. We have also conducted corresponding micro-hot-embossing experiments on Zeonex-690R to verify the predictive capability of our theory and its numerical simulation capability. Numerical simulation approaches such as the ones demonstrated in this thesis can be used to determine optimum processing conditions for micro-hot-embossing without a need for costly experimentation.

6.1 Future directions

While much has been accomplished, there are several important areas in which further research should be conducted. Some of the future research could include:

- An important extension of our theory will be to account for crazing and cavitation and to include suitable damage and failure criteria for amorphous polymers to model the fracture initiation from cracks and notches.

- Our constitutive theory does not contain any intrinsic material length-scale and therefore cannot capture length-scale dependent phenomenon such as increase of hardness with decreasing indentation depth at nano-length-scales. For such applications, our theory will need to be extended; maybe following the approaches which are recently being developed for metallic materials where material length-scale phenomena are modeled via dependencies on plastic strain gradients (e.g., Anand et al., 2005; Lele and

Anand, 2009; Gurtin and Anand, 2009). It is important to note that at this point the physical origins of "gradient effects" in polymers are not clear.

- Classical plasticity theories for amorphous polymers such as the one used here assume a flow rule in which the direction of plastic flow is co-directional with the stress deviator (a Mises-type flow rule). Although this is a reasonable approximation at the macro-scale, it is not able to accurately predict the shear-yielding micromechanism of plastic flow in which plasticity occurs by closely spaced shear-bands. Modified flow-rules such as "double-shearing" (cf. Anand and Gu (2000); Anand and Su (2005); Henann and Anand (2008)) instead of Mises-type flow rule may be considered to more accurately predict the shear-bands.

- The important physical micromechanisms need to be investigated at the molecular level. Tools such as Molecular Dynamics simulations could be used to investigate the effects of evolving polymer micro-structure at the molecular level on the macroscopic mechanical response.

- Actual use of shape-memory polymers in devices is still quite limited. The major reason for this is that due to the low stiffness of these polymers above their glass transition temperature, very small forces are generated during constrained-shape-recovery. This prevents use of these polymers in numerous applications in which reasonably high actuation forces are required. In the future, our study can be extended to model and simulate the response of composites made from shape-memory polymers and superelastic alloys (e.g. Nitinol wires) to achieve desired, application-specific, recovery/actuation forces from components made from these materials.

Bibliography

ABAQUS/Explicit, 2009. Documentaion. SIMULIA, Providence, RI.

ABAQUS/Standard, 2009. Documentaion. SIMULIA, Providence, RI.

Ames, N. M., 2007. A thermo-mechanical finite deformation theory of plasticity for amorphous polymers: application to micro-hot-embossing of poly(methyl methacrylate). Phd thesis, Massachusetts Institute of Technology, Cambridge, MA.

Anand, L., 1979. On h. hencky's approximate strain-energy function for moderate deformations. ASME Journal of Applied Mechanics 46, 78–82.

Anand, L., 1986. Moderate deformations in extension-torsion of incompressible isotropic elastic materials. Journal of the Mechanics and Physics of Solids 34, 293–304.

Anand, L., Ames, N. M., 2006. On modeling the micro-indentation response of an amorphous polymer. International Journal of Plasticity 22, 1123–1170.

Anand, L., Ames, N. M., Srivastava, V., Chester, S. A., 2009. A thermo-mechanically coupled theory for large deformations of amorphous polymers. Part I: formulation. International Journal of Plasticity 25, 1474–1494.

Anand, L., Gu, C., 2000. Granular materials: constitutive equations and strain localization. Journal of the Mechanics and Physics of Solids 48, 1710–1733.

Anand, L., Gurtin, M. E., 2003a. A theory of amorphous solid undergoing large deformations, with applications to polymeric glasses. International Journal of Solids and Structures 40, 1465–1487.

Anand, L., Gurtin, M. E., Lele, S. P., Gething, C., 2005. A one-dimensional theory of strain-gradient plasticity: Formulation, analysis, numerical results. Journal of the Mechanics and Physics of Solids 53 (8), 1789–1826.

Anand, L., Su, C., 2005. A theory for amorphous viscoplastic materials undergoing finite deformations, with application to metallic glasses. Journal of the Mechanics and Physics of Solids 53, 1362–1396.

Argon, A. S., 1973. A theory for the low temperature plastic deformation of glassy polymers. Philosophical Magazine 28, 839–865.

Argon, A. S., Demkowicz, M. J., 2008. What can plasticity of amorphous silicon tell us about plasticity of metallic glasses? Metallurgical and Materials Transactions A 39A, 1762–1778.

Armstrong, P. J., Frederick, C. O., 1966. A mathematical representation of the multiaxial bauschinger effect. Tech. rep., Report RD/B/N731, CEGB, Central Electricity Generating Board, Berkeley, UK.

Arruda, E. M., Boyce, M. C., 1993a. A three-dimensional constitutive model for the large stretch behavior of rubber elastic materials. Journal of the Mechanics and Physics of Solids 41, 389–412.

Arruda, E. M., Boyce, M. C., 1993b. Evolution of plastic anisotropy in amorphous polymers during finite straining. International Journal of Plasticity 9, 697–720.

Arruda, E. M., Boyce, M. C., Jayachandran, R., 1995. Effects of strain rate, temperature and thermomechanical coupling on the finite strain deformation of glassy polymers. Mechanics of Materials 19, 193–212.

Baer, G. M., Small, W., Wilson, T. S., Benett, W. J., Matthews, D. L., Hartman, J., Maitland, D. J., 2007b. Fabrication and in vitro deployment of a laser-activated shape memory vascular stent. Biomedical Engineering Online 6.

Baer, G. M., Wilson, T. S., Matthews, D. L., Maitland, D. J., 2007a. Shape memory behavior of thermally stimulated polyurethane for medical applications. Journal of Applied Polymer Science 103, 3882–3892.

Bagepalli, B. S., 1984. Finite strain elastic-plastic deformation of glassy polymers. Phd thesis, Massachusetts Institute of Technology, Cambridge, MA.

Basu, S., Van der Giessen, E., 2002. A thermo-mechanical study of mode I, small-scale yielding crack-tip fields in glassy polymers. International Journal of Plasticity 18, 1395–1423.

Bauschinger, J., 1886. über die veränderungder position der elastizitätsgrenze des eisens und stahls durchstrecken und quetschen und durch erwärmen und abkühlen und durchoftmals wiederholte beanspruchungen. Mitteilung aus demMechanisch-technischen Laboratorium der Königlichen polytechnischenHochschule in München 13, 1–115.

Bauwens, J. C., 1972. Relation between the compression yield stress and the mechanical loss peak of bisphenol-a-polycarbonate in the β transition range. Journal of Materials Science 7, 577–584.

Bauwens, J. C., Bauwens-Crowet, C., Homeś, G., 1969. Tensile yield-stress behavior of poly(vinyl chloride) and polycarbonate in the glass transition region. Journal of Polymer Science: Part A-2 7, 1745–1754.

Bauwens-Crowet, C., 1973. The compression yield behaviour of polymethyl methacrylate over a wide range of temperatures and strain-rates. Journal of Materials Science 8, 968 979.

Bauwens-Crowet, C., Bauwens, J. C., Homeś, G., 1969. Tensile yield-stress behavior of glassy polymers. Journal of Polymer Science: Part A-2 7, 735–742.

Behl, M., Lendlein, A., 2007. Shape memory polymers. Materials Today 10, 20–28.

Bergström, J. S., Boyce, M. C., 1998. Constitutive modeling of the large strain time-dependent behavior of elastomers. Journal of Mechanics and Physics of Solids 46, 931–954.

Bergström, J. S., Boyce, M. C., 2001. Constitutive modeling of the time-dependent and cyclic loading of elastomers and application to soft biological tissues. Mechanics of Materials 33, 523–530.

Bicerano, J., 1993. Prediction of Polymer Properties. Marcel Dekker Inc., New York.

Bilenberg, B., Hansen, M., Johansen, D., Özkapici, V., Jeppesen, C., Szabo, P., Obieta, I. M., Arroyo, O., Tegenfeldt, J. O., Kristensen, A., 2005. Topas-based lab-on-a-chip microsystems fabricated by thermal nanoimprint lithography. Journal of Vacuum Science and Technology B 23, 2944–2949.

Bjerke, T., Li, Z., Lambros, J., 2002. Role of plasticity in heat generation during high rate deformation and fracture of polycarbonate. International Journal of Plasticity 18, 549–567.

Boyce, M. C., 1996. Direct comparison of the Gent and the Arruda-Boyce constitutive models of rubber elasticity. Rubber Chemistry and Technology 69, 781–785.

Boyce, M. C., Parks, D. M., Argon, A. S., 1988. Large inelastic deformation of glassy polymers. part 1: rate-dependent constitutive model. Mechanics of Materials 7, 15–33.

Boyce, M. C., Socrate, S., Llana, P. G., 2000. Constitutive model for the finite deformation stress strain behavior of poly(ethylene terephthalate) above the glass transition. Polymer 41, 2183–2201.

Boyce, M. C., Weber, G. G., Parks, D. M., 1989. On the kinematics of finite strain plasticity. Journal of the Mechanics and Physics of Solids 37, 647–665.

Bronkhorst, C. A., Kalidindi, S. R., L., Anand, 1992. Polycrystalline plasticity and the evolution of crystallographic texture in fcc metals. Philosophical Transactions of The Royal Society of London A 341, 443–477.

Buckley, C. P., Jones, D. C., 1995. Glass-rubber constitutive model for amorphous polymers near the glass transition. Polymer 36, 3301–3312.

Campbell, D., Lake, M. S., Scherbarth, M. R., Nelson, E., Six, R. W., 2005. Elastic memory composite material: an enabling technology for future furlable space structures. In: 46th AIAA/ASME/ASCE/AHS/ASC Structures, Structural Dynamics and Materials Conference. Austin, Texas.

Chaboche, J. L., 2008. A review of some plasticity and viscoplasticity constitutive theories. International Journal of Plasticity 24, 1642–1693.

Chen, Y. C., Lagoudas, D. C., 2008. A constitutive theory for shape memory polymers. Part I: Large deformations. Journal of the Mechanics and Physics of Solids 56, 1752–1765.

Chou, S. Y., 2001. Nanoimprint lithography and lithographically induced self-assembly. MRS Bulletin 26, 512–517.

Cohen, M. H., Grest, G. S., 1979. Liquid-glass transition, a free volume approach. Physical Review B 20, 1077–1098.

Crist, B., 1997. Yield processes in glassy polymers. In: Haward, R. N., Young, R. J. (Eds.), The Physics of Glassy Polymers. Chapman & Hall, London.

Dooling, P. J., Buckley, C. P., Rostami, C. P., Zahlan, N., 2002. Hot-drawing of poly(methyl metahcrylate) and simulation using a glass-rubber consitutive model. Polymer 43, 2451–2465.

Dupaix, R. B., 2003. Temperature and rate dependent finite strain behavior of poly(ethylene terephthalate) and poly(ethylene terephthalate)-glycol above the glass transition temperature. Phd thesis, Massachusetts Institute of Technology, Cambridge, MA.

Dupaix, R. B., Boyce, M. C., 2007. Constitutive modeling of the finite strain behavior of amorphous polymers in and above the glass transition. Mechanics of Materials 39, 39–52.

Estevez, R., Basu, S., 2008. On the importance of thermo-elastic cooling in the fracture of glassy polymers at high rates. International Journal of Solids and Structures 45, 3449–3465.

Estevez, R., Basu, S., Van der Giessen, E., 2005. Analysis of temperature effects near mode I cracks in glassy polymers. International Journal of Fracture 132, 249–273.

Eyring, H., 1936. Viscosity, plasticity, and diffusion as examples of absolute reaction rates. Journal of Chemical Physics 4, 283–291.

Fotheringham, D. G., Cherry, B. W., 1978. The role of recovery forces in the deformation of linear polyethylene. Journal of Materials Science 13, 951–964.

Fotheringham, D. G., Cherry, B. W., Bauwens-Crowet, C., 1976. Comment on "the compression yield behaviour of polymethyl methacrylate over a wide range of temperatures and strain-rates". Journal of Materials Science 11, 1368–1371.

Fulcher, G. S., 1925. Analysis of recent measurements of the viscosity of glasses. Journal of the American Ceramic Society 8, 339–355.

Gall, K., Kreiner, P., Turner, D., Hulse, M., 2004. Shape-memory polymers for microelectromechanical systems. Journal of Microelectromechanical Systems 13, 472–483.

Gall, K., Yakacki, C. M., Liu, R., Shandas, R., Willett, N., Anseth, K. S., 2005. Thermomechanics of the shape memory effect in polymers for biomedical applications. Journal of Biomedical Materials Research Part A 73A, 339–348.

Garg, M., Mulliken, A. D., Boyce, M., 2008. Temperature rise in polymeric materials during high rate deformation. Journal of Applied Mechanics 75, 011009 (8 pages).

Gent, A. N., 1996. A new constitutive relation for rubber. Rubber Chemistry and Technology 69, 59–61.

Govaert, L. E., Timmermans, P. H. M., Brekelmans, W. A. M., 2000. The influence of intrinsic strain softening on strain localization in polycarbonate: modeling and experimental validation. Journal of Engineering Materials and Technology 122, 177–185.

Gurtin, M. E., 2002. A gradient theory of single-crystal viscoplasticity that accounts for geometrically necessary dislocations. Journal of the Mechanics and Physics of Solids 50, 5–32.

Gurtin, M. E., Anand, L., 2005. The decomposition $\mathbf{F} = \mathbf{F}^e\mathbf{F}^p$, material symmetry, and plastic irrotationality for solids that are isotropic-viscoplastic or amorphous. International Journal of Plasticity 21, 1686–1719.

Gurtin, M. E., Anand, L., 2009. Thermodynamics applied to gradient theories involving the accumulated plastic strain: The theories of Aifantis and Fleck and Hutchinson and their generalization. Journal of the Mechanics and Physics of Solids 57, 405–421.

Gurtin, M. E., Fried, E., Anand, L., 2009. The Mechanics and Thermodynamics of Continua, (forthcoming) Edition. Cambridge University Press, New York.

Hardt, D. E., Anthony, B., Tor, S. B., 2008. A teaching factory for polymer microfabrication - μFac. In: Proceedings of the 6th International Symposium on Nano-Manufacturing. Vouliagmeni, Athens, Greece.

Hasan, O. A., Boyce, M. C., 1995. A constitutive model for the nonlinear viscoelastic viscoplastic behavior of glassy polymers. Polymer Engineering and Science 35, 331–344.

Haupt, P., Sedlan, K., 2001. Viscoplasticity of elastomeric materials. experimental facts and constitutive modelling. Archive of Applied Mechanics 71, 89–109.

Haward, R. N., Thackray, G., 1968. The use of a mathematical model to describe isothermal stress-strain curves in glassy polymers. Proceedings of the Royal Society, London A 302, 453–472.

Henann, D. L., Anand, L., 2008. A constitutive theory for the mechanical response of amorphous metals at high temperatures spanning the glass transition temperature: application to microscale thermoplastic forming. Acta Materialia 56, 3290–3305.

Jiang, H. Y., Kelch, S., Lendlein, A., 2006. Polymers move in response to light. Advanced Materials 18, 1471–1475.

Juang, Y. J., Lee, L. J., Koelling, K. W., 2002. Hot embossing in microfabrication; Part II: Rheological characterization and process analysis. Polymer Engineering and Science 42, 551–566.

Kröner, E., 1960. Allgemeine kontinuumstheorie der versetzungen und eigenspannungen. Archive for Rational Mechanics and Analysis 4, 273–334.

Lee, E. H., 1969. Elastic plastic deformation at finite strain. ASME Journal of Applied Mechanics 36, 1–6.

Lele, S. P., Anand, L., 2009. A large-deformation strain-gradient theory for isotropic viscoplastic materials. International Journal of Plasticity 25, 420–453.

Lendlein, A., Jiang, H., Jünger, O., Langer, R., 2005. Light-induced shape memory polymers. Nature 434, 879–882.

Lendlein, A., Langer, R., 2002. Biodegradable, elastic shape-memory polymers for potential biomedical applications. Science 296, 1673–1676.

Lion, A., 1997. On the large deformation behavior of reinforced rubber at different tempeartures. Journal of the Mechanics and Physics of Solids 45, 1805–1834.

Liu, Y., Gall, K., Dunn, M. L., Greenberg, A. R., Diani, J., 2006. Thermomechanics of shape memory polymers: Uniaxial experiments and constitutive modeling. International Journal of Plasticity 22, 279–313.

Maitland, D. J., Metzger, M. F., Schumann, D., Lee, A., Wilson, T. S., 2002. Photothermal properties of shape memory polymer micro-actuators for treating stroke. Lasers in Surgery and Medicine 30, 1–11.

Maitland, D. J., Metzger, M. F., Schumann, D., Lee, A., Wilson, T. S., 2003. Cold hibernated elastic memory foams for endovascular interventions. Biomaterials 24, 491–497.

Metzger, M. F., Wilson, T. S., Schumann, D., Matthews, D. L., Maitland, D. J., 2002. Mechanical properties of mechanical actuator for treating ischemic stroke. Biomedical Microdevices 4, 89–96.

Mulliken, A. D., Boyce, M. C., 2006. Mechanics of the rate-dependent elasticplastic deformation of glassy polymers from low to high strain rates. International Journal of Solids and Structures 43, 1331–1356.

Nguyen, T. D., Qi, H. J., Castro, F., Long, K. N., 2008. A thermoviscoelastic model for amorphous shape memory polymers: Incorporating structural and stress relaxation. Journal of the Mechanics and Physics of Solids 56, 2792–2814.

Ota, S., 1981. A current status of irradiated heat-shrinkable tubing in Japan. Radiation Physics and Chemistry 18, 81–87.

Parks, D. M., Argon, A. S., Bagepalli, B., 1985. Large elastic-plastic deformation of glassy polymers, part 1: Constitutive modelling. Tech. rep., MIT, Program in Polymer Science and Technology Report.

Povolo, F., Hermida, E. B., 1995. Phenomenlogical description of strain rate and temperature-dependent yield stress of PMMA. Journal of Applied Polymer Science 58, 55–68.

Povolo, F., Schwartz, G., Hermida, E. B., 1996. Temperature and strain rate dependence of the tensile yield stress of PVC. Journal of Applied Polymer Science 61, 109–117.

Qi, H. J., Nguyen, T. D., Castro, F., Yakacki, C. M., Shandas, R., 2008. Finite deformation thermo-mechanical behavior of thermally induced shape memory polymers. Journal of the Mechanics and Physics of Solids 56, 1730 – 1751.

Ratna, D., Kocsis, J. K., 2008. Recent advances in shape memory polymers and composites: a review. Journal of Materials Science 43, 254–269.

Reese, S., Govindjee, S., 1998. A theory of finite viscoelasticity and numerical aspects. International Journal of Solids and Structures 35, 3455–3482.

Richeton, J., Ahzi, S., Daridon, L., Rémond, Y., 2005a. A formulation of the cooperative model for the yield stress of amorphous polymers for a wide range of strain rates and temperatures. Polymer 46, 6035–6043.

Richeton, J., Ahzi, S., Vecchio, K. S., Jiang, F. C., Adharapurapu, R. R., 2006. Influence of temperature and strain rate on the mechanical behavior of three amorphous polymers: Characterization and modeling of the compressive yield stress. InternationalJournal of Solids and Structures 43, 2318–2335.

Richeton, J., Ahzi, S., Vecchio, K. S., Jiang, F. C., Makradi, A., 2007. Modeling and validation of the large deformation inelastic response of amorphous polymers over a wide range of temperatures and strain rates. International Journal of Solids and Structures 44, 7938–7954.

Robertson, R. E., 1966. Theory for the plasticity of glassy polymers. The Journal of Chemical Physics 44, 3950–3956.

Safranski, D., Gall, K., 2008. Effect of chemical structure and crosslinking density on the thermo-mechanical properties and toughness of (meth)acrylate shape memory polymer networks. Polymer 49, 4446–4455.

Shah, V. M., Stern, S. A., Ludovice, P. J., 1989. Estimation of the free volume in polymers by means of a Monte Carlo technique. Macromolecules 22, 4660–4662.

Spaepen, F., 1977. A microscopic mechanism for steady state inhomogeneous flow in metallic glasses. Acta Metallurgica 25, 407–415.

Swift, H. W., 1947. Length changes in metals under torsional overstrain. Engineering 163, 253–257.

Tammann, V. G., Hesse, W., 1926. Die abhängigkeit der viscosität von der temperatur bei unterkühlten flüssigkeiten. Zeitschrift für anorganische und allgemeine Chemie 156, 245–257.

Tobushi, H., Hara, H., Yamada, E., Hayashi, S., 1996. Thermomechanical properties in a thin film of shape memory polymer of polyurethane series. Smart Materials and Structures 5, 483–491.

Van Krevelen, D. W., 1990. Properties of Polymers, third ed. Edition. Elsevier, Amsterdam.

Vettiger, P., Cross, G., Despont, M., Drechsler, U., Dürig, U., Gotsmann, B., Häberle, W., Lantz, M. A., Rothuizen, H. E., Stutz, R., Binning, G. K., 2002. The "millipede"—nanotechnology entering data storage. IEEE Transactions on Nanotechnology 1, 39–55.

Vogel, H., 1921. Das temperaturabhängigkeitsgesetz der viskosität von flüssigkeiten. Physikalische Zeitschrift 22, 645–646.

Wache, H. M., Tartakowska, D. J., Hentrich, A., Wagner, M. H., 2003. Development of a polymer stent with shape memory effect as a drug delivery system. Journal of Materials Science: Materials in Medicine 14, 109–112.

Williams, M. L., Landel, R. F., Ferry, J. D., 1955. The temperature dependence of relaxation mechanisms in amorphous polymers and other glass-forming liquids. Journal of the American Chemical Society 77, 3701–3707.

Wornyo, E., Gall, K., Yang, F., King, W., 2007. Nanoindention of shape memory polymer networks. Polymer 48, 3213–3225.

Wu, P. D., Van der Giessen, E., 1993a. On improved network models for rubber elasticity and their applications to orientation hardening of glassy polymers. Journal of the Mechanics and Physics of Solids 41, 427–456.

Wu, P. D., Van der Giessen, E., 1993b. On large strain inelastic torsion of glassy polymers. Journal of the Mechanics and Physics of Solids 35, 935–951.

Yakacki, C. M., Shandas, R., Lanning, C., Rech, B., Eckstein, A., Gall, K., 2007. Unconstrained recovery characterization of shape-memory polymer networks for cardiovascular applications. Biomaterials 28, 2255–2263.

Appendix A

Material parameter estimation procedure for temperatures below the glass transition

A.1 Introduction

In this appendix we briefly outline a procedure for estimating values of the material parameters in the constitutive model described in Chapter 3. For an isotropic theory such as the one presented in Chapter 3, it is most convenient to use an implementation of a one-dimensional version of our model in the computer program MATLAB to conduct appropriate simulations to estimate the material parameters. We illustrate our material parameter calibration procedure for Zeonex-690R; the procedure for PC and PMMA is essentially identical.

A.2 One-dimensional version of the constitutive theory

In this section we present an *approximate* one-dimensional version of the model described in chapter 3, which substantially aids in the calibration of material properties from experimental data. The approximation is primarily in that we cannot account for Poisson's type lateral contractions, and attendant volume changes, in a one-dimensional setting. The underlying constitutive equations relate the following basic fields:

$U > 0$,	stretch,
U^p,	plastic stretch,
$U^e = UU^{p-1}$,	elastic part of the stretch,
$\epsilon = \ln U$,	logarithmic strain,
$\epsilon^e = \ln U^e$,	logarithmic elastic strain,

$\boldsymbol{\xi} = (\varphi, S_a, S_b)$	scalar internal variables,
$A > 0,$	squared stretch-like internal variable,
$\vartheta > 0,$	absolute temperature,
$\psi = \psi^{e\,(1)}\big(U^e, \vartheta\big) + \psi^{(2)}\big(U, \vartheta\big) + \psi^{p\,(1)}\big(A, \vartheta\big),$	free energy density,
σ	Cauchy stress.

A.2.1 Free energy. Stress

For $\psi^{(1)}$ we use a simple linear elastic form for the free energy

$$\psi^{e\,(1)} = \frac{1}{2}\,E\,(\epsilon^e)^2 - E\,\alpha\,(\vartheta - \vartheta_0)\epsilon^e + \tilde{f}(\vartheta), \tag{A.1}$$

where $E(\vartheta) > 0$ is Young's modulus, α is the coefficient of thermal expansion, ϑ_0 is a reference temperature, and $\tilde{f}(\vartheta)$ is an entropic contribution to the free energy related to the specific heat of the material. This free energy contributes a component

$$\sigma^{(1)} = E\,\epsilon^e - E\alpha(\vartheta - \vartheta_0), \tag{A.2}$$

to the total Cauchy stress σ.

Next, for $\psi^{p\,(1)}$, consider a symmetric positive definite squared-stretch-like tensor $\mathbf{A}$ which satisfies $\det \mathbf{A} = 1$. Let (a_1, a_2, a_3) denote the set of principal values of $\mathbf{A}$, with $a_1 a_2 a_3 = 1$. We assume a plastic energy of the form

$$\psi^{p\,(1)} = \tfrac{1}{4}\,B\,\big[(\ln a_1)^2 + (\ln a_2)^2 + (\ln a_3)^2\big], \tag{A.3}$$

where $B(\vartheta) \geq 0$ is a back-stress modulus. With $\boldsymbol{\sigma}^{(\text{back})}$ denoting a stress from this free energy, standard relations of finite deformation incompressible elasticity give the corresponding principal values of the back-stress as

$$\sigma_i^{(\text{back})} = 2a_i \frac{\partial \psi^{p\,(1)}}{\partial a_i} - P, \tag{A.4}$$

with P an arbitrary "pressure," so that in a simple tension/compression, with $\sigma_1^{(\text{back})} \equiv \sigma_{\text{back}}$, $\sigma_2^{(\text{back})} = \sigma_3^{(\text{back})} = 0$,

$$\sigma_{\text{back}} = 2a_1 \frac{\partial \psi^{p\,(1)}}{\partial a_1} - 2a_2 \frac{\partial \psi^{p\,(1)}}{\partial a_2}. \tag{A.5}$$

When the free energy is given by (A.3), (A.5) reduces to

$$\sigma_{\text{back}} = B\,(\ln a_1 - \ln a_2)\,, \tag{A.6}$$

or equivalently, with $a_1 = A$, and $a_2 = a_2 = A^{-1/2}$,

$$\sigma_{\text{back}} = \frac{3}{2} B \ln A. \tag{A.7}$$

In a one-dimensional setting, the driving stress for plastic flow is the effective stress given by

$$\sigma_{\text{eff}}^{(1)} = \sigma^{(1)} - \sigma_{\text{back}}, \tag{A.8}$$

and the *equivalent tensile stress* and the *mean normal pressure* are

$$\bar{\sigma} \stackrel{\text{def}}{=} |\sigma_{\text{eff}}^{(1)}| \qquad \text{and} \qquad \bar{p} = -\frac{1}{3}\sigma^{(1)}, \tag{A.9}$$

respectively.

For $\psi^{(2)}$, consider first a symmetric positive definite stretch tensor $\mathbf{U}$ which satisfies $\det \mathbf{U} = 1$. Let (U_1, U_2, U_3) denote the set of principal stretches, with $U_1 U_2 U_3 = 1$. The first invariant I_1 of the squared-stretch tensor $\mathbf{U}^2$ in three-dimensions is defined by

$$I_1 \stackrel{\text{def}}{=} U_1^2 + U_2^2 + U_3^2. \tag{A.10}$$

In terms of I_1, the Gent (1996) free energy is

$$\psi^{(2)} = -\frac{1}{2}\mu I_m \ln\left(1 - \frac{I_1 - 3}{I_m}\right), \tag{A.11}$$

where $\mu(\vartheta) > 0$ and $I_m > 3$ are two material parameters, with μ representing the ground state rubbery shear modulus of the material, and I_m representing the upper limit of $(I_1 - 3)$, associated with limited chain extensibility. With $\sigma^{(2)}$ denoting the contribution to the Cauchy stress from this free energy, standard relations of finite deformation incompressible elasticity give the the principal values of the corresponding stress as

$$\sigma_i^{(2)} = U_i \frac{\partial \psi^{(2)}}{\partial U_i} - P, \tag{A.12}$$

with P an arbitrary "pressure." In simple tension/compression, with $\sigma_1^{(2)} \equiv \sigma^{(2)}$ and $\sigma_2^{(2)} = \sigma_3^{(2)} = 0$, we get

$$\sigma^{(2)} = U_1 \frac{\partial \psi^{(2)}}{\partial U_1} - U_2 \frac{\partial \psi^{(2)}}{\partial U_2} = \frac{\partial \psi^{(2)}}{\partial I_1}\left(U_1 \frac{\partial I_1}{\partial U_1} - U_2 \frac{\partial I_1}{\partial U_2}\right) = 2\frac{\partial \psi^{(2)}}{\partial I_1}\left(U_1^2 - U_2^2\right), \tag{A.13}$$

or equivalently, with $U_1 \equiv U$ and $U_2 = U_3 = U^{-1/2}$,

$$\sigma^{(2)} = 2\frac{\partial \psi^{(2)}}{\partial I_1}\left(U^2 - U^{-1}\right), \tag{A.14}$$

and hence, for the Gent free energy (A.11),

$$\sigma^{(2)} = \mu \left(1 - \frac{I_1 - 3}{I_m}\right)^{-1} \left(U^2 - U^{-1}\right). \tag{A.15}$$

The total Cauchy stress in simple tension/compression is

$$\sigma = \sigma^{(1)} + \sigma^{(2)}. \tag{A.16}$$

A.2.2 Flow rule

The evolution equation for U^p is

$$\left.\begin{aligned} &\dot{U}^p = D^p U^p \qquad U^p(0) = 1, \\ &D^p = \dot{\epsilon}^p \mathrm{sign}(\sigma^{(1)}), \qquad \dot{\epsilon}^p \geq 0, \\ &\sigma_e \stackrel{\text{def}}{=} \bar{\sigma} - (S_a + S_b + \alpha_p \bar{p}), \\ &\dot{\epsilon}^p = \begin{cases} 0 & \text{if} \quad \sigma_e \leq 0, \\ \dot{\epsilon}_0 \exp\left(-\dfrac{Q}{k_B \vartheta}\right) \left[\sinh\left(\dfrac{\sigma_e V}{2\, k_B \vartheta}\right)\right]^{1/m} & \text{if} \quad \sigma_e > 0. \end{cases} \end{aligned}\right\} \tag{A.17}$$

Here $\dot{\epsilon}^p$ is the *equivalent tensile plastic strain-rate*, and σ_e denotes a *net equivalent tensile stress for thermally activated flow*; α_p is a pressure-sensitivity parameter; $\dot{\epsilon}_0$ is a *pre-exponential factor* with units of s^{-1}; Q is an *activation energy*; k_B is Boltzmann's constant; V is an activation volume; and m is a *strain rate sensitivity parameter.*

When $\dot{\epsilon}^p > 0$, (A.17), using (A.8) and (A.9), may be inverted to give

$$|\sigma^{(1)} - \sigma_{\text{back}}| + \frac{1}{3}\alpha_p\, \sigma^{(1)} = S_a + S_b + \frac{2k_b\vartheta}{V} \sinh^{-1}\left[\left(\frac{\dot{\epsilon}^p}{\dot{\epsilon}^*(\vartheta)}\right)^m\right], \tag{A.18}$$

with

$$\dot{\epsilon}^*(\vartheta) \stackrel{\text{def}}{=} \dot{\epsilon}_0 \exp\left(-\frac{Q}{k_B \vartheta}\right). \tag{A.19}$$

A.2.3 Evolution equations for the internal variables S_a, φ, S_b, and A

The internal variables S_1 and φ are taken to obey the coupled evolution equations:

$$\dot{S}_a = h_a \left(S_a^* - S_a\right) \dot{\epsilon}^p, \quad \text{with} \quad S_a^* = b\left(\varphi^* - \varphi\right), \quad \text{and} \quad S_a(0) = S_{a0}; \tag{A.20}$$

and

$$\left.\begin{aligned} &\dot{\varphi} = g\,(\varphi^* - \varphi)\,\dot{\epsilon}^p, \qquad \text{with} \qquad \varphi(0) = \varphi_0, \\ \text{and} \qquad &\varphi^*(\dot{\epsilon}^p, \vartheta) = \begin{cases} z\Big(1 - \dfrac{\vartheta}{\vartheta_c}\Big)^r \left(\dfrac{\dot{\epsilon}^p}{\dot{\epsilon}_r}\right)^s & \text{if } (\vartheta < \vartheta_c) \text{ and } (\dot{\epsilon}^p > 0), \\ 0 & \text{if } (\vartheta \geq \vartheta_c) \text{ or } (\dot{\epsilon}^p = 0), \end{cases} \\ \text{where} \qquad &\vartheta_c = \begin{cases} \vartheta_g + n \ln\left(\dfrac{\dot{\epsilon}^p}{\dot{\epsilon}_r}\right) & \text{for } \dot{\epsilon}^p > \dot{\epsilon}_r, \\ \vartheta_g & \text{for } \dot{\epsilon}^p \leq \dot{\epsilon}_r, \end{cases} \end{aligned}\right\} \tag{A.21}$$

with $\{h_a, b, S_{a0}, \varphi_0, z, r, s, \dot{\epsilon}_r, n\}$ constants, and g temperature-dependent.

The evolution of S_b is taken to be governed by

$$\dot{S}_b = h_b\,(\bar{\lambda} - 1)\,(S_b^* - S_b)\,\dot{\epsilon}^p, \quad \text{with initial value} \quad S_b(0) = S_{b0} \geq 0, \tag{A.22}$$

where

$$\bar{\lambda} \stackrel{\text{def}}{=} \sqrt{(U^2 + 2U^{-1})/3} \tag{A.23}$$

is an effective plastic stretch, h_b a constant, and S_b^* temperature-dependent.

Also, the evolution equation for A is taken as

$$\dot{A} = 2\,A\,D^p - \gamma(A \ln A)\,\dot{\epsilon}^p, \qquad A(0) = 1, \tag{A.24}$$

where $\gamma \geq 0$ is a constitutive parameter which governs the dynamic recovery of A.

A.2.4 Evolution equation for temperature

For one-dimensional tests at the highest strain rates, which may be approximated as adiabatic, the temperature is taken to evolve according to

$$c\,\dot{\vartheta} = \omega \left(\sigma_e + \frac{1}{2} B\,\gamma\,|\ln A|^2\right) \dot{\epsilon}^p. \tag{A.25}$$

A.3 Material parameter calibration

With the full three-dimensional and simplified one-dimensional version of the theory in place, we are in position to estimate the material parameters/functions appearing in the theory by fitting the experimental data. We illustrate our material parameter calibration procedure for Zeonex-690R; the procedure for PMMA and PC is essentially identical.

We have implemented the one-dimensional model of Section A.2 in MATLAB using an explicit integration scheme, and we use it to calibrate the material parameters from the experiments described in Chapter 3. The one-dimensional calibration process consists of four sequential steps which are outlined in this section. The four steps cover calibration

of the following aspects of the stress-strain response: (1) elastic modulus; (2) initial yield stress; (3) large strain behavior; and (4) yield-peak and back-stress.

A.3.1 Elastic modulus

For polymeric materials the magnitude of the Young's modulus E decreases as the temperature increases. We assume that the temperature dependence of the Young's modulus may be adequately approximated by (cf. (3.77))[1]

$$E(\vartheta) = E_0 - M_E(\vartheta - \vartheta_g),$$

where E_0 and M_E are constants. Using the experimental data for the E versus ϑ, we estimate

$$E_0 = 1350 \text{ MPa}, \qquad M_E = 0.45 \text{ MPa K}^{-1}.$$

A.3.2 Initial yield stress

Most previous models for amorphous polymers have identified the *peak stress* in a stress-strain curve from a simple compression test as a "yield stress" for the material. Since the stress-peak is associated with the transient disordering of the material, and the actual level of a peak is very dependent on the initial thermal history of the material, here we follow a different approach. We identify a "yield stress" in a compression experiment as a back-extrapolated value of the intersection of the initial elastic slope with the tangent to the stress-strain curve at a strain of, say, 0.4, a strain level by which all transients of the yield-peak have died out, and the chain-locking effects giving rise to the stress-strain curve are minimal. Accordingly, at this point in the calibration procedure we ignore the effects of the yield-peak and define the "yield stress" as the intersection of the pre-peak stress-strain curve with the back-extrapolated tangent to the stress-strain curve at approximately 0.4 strain; this is shown schematically in Fig. A-1.[2]

Since

$$|\sigma^{(1)} - \sigma_{\text{back}}| = (\sigma^{(1)} - \sigma_{\text{back}}) \operatorname{sign}(\sigma^{(1)} - \sigma_{\text{back}})$$

and since in a monotonic compression test

$$\operatorname{sign}(\sigma^{(1)} - \sigma_{\text{back}}) = \operatorname{sign}(\sigma^{(1)}) = \operatorname{sign}(\sigma_{\text{back}}),$$

we have

$$|\sigma^{(1)} - \sigma_{\text{back}}| = |\sigma^{(1)}| - |\sigma_{\text{back}}|,$$

[1] We ignore all rate-sensitivity of the initial stiffness.

[2] This is a non-standard definition of the yield stress for polymeric materials.

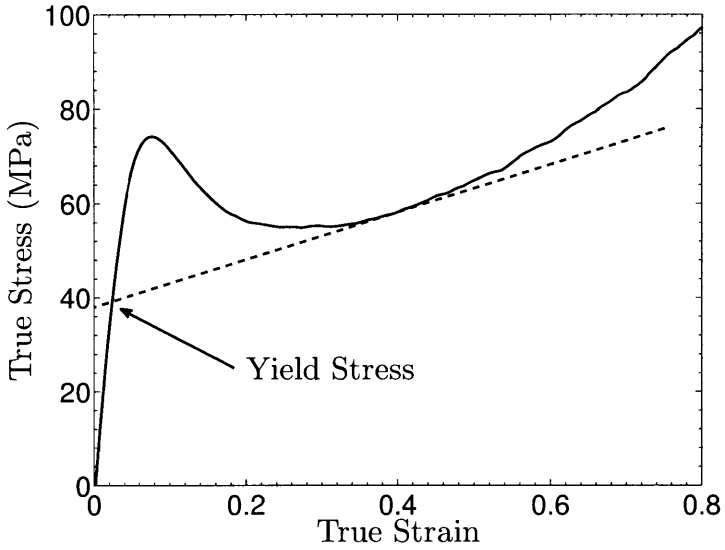

Figure A-1: Schematic showing the "yield stress" defined as the intersection of the pre-peak stress-strain curve with the back-extrapolated tangent to the stress-stain curve at a strain of 0.4.

and hence, from (A.18),

$$\left(1-\frac{\alpha_p}{3}\right)|\sigma^{(1)}| = S_a + S_b + |\sigma_{\text{back}}| + \frac{2k_b\vartheta}{V}\sinh^{-1}\left[\left(\frac{\dot{\epsilon}^p}{\dot{\epsilon}^*(\vartheta)}\right)^m\right]. \tag{A.26}$$

Thus, neglecting the contribution from the internal variables S_a(which is associated with the transient yield peak) and the contribution from S_b (since this only manifests itself at large stretches), for fully-developed flows when $\dot{\epsilon}^p \approx \dot{\epsilon}$ (taken to be positive in compression) and with $|\sigma^{(1)}| = \sigma_y$, (A.26) gives the following approximate expression for yield stress σ_y as a function of temperature ϑ and strain rate $\dot{\epsilon}$:

$$\left(1-\frac{\alpha_p}{3}\right)\sigma_y \approx \sigma^*_{\text{back}}(\vartheta) + \frac{2k_B\vartheta}{V}\sinh^{-1}\left[\left(\frac{\dot{\epsilon}}{\dot{\epsilon}^*(\vartheta)}\right)^m\right], \tag{A.27}$$

where we have introduced the notation

$$\sigma^*_{\text{back}}(\vartheta) \stackrel{\text{def}}{=} |\sigma_{\text{back}}(\vartheta)|. \tag{A.28}$$

Here, $\sigma^*_{\text{back}}(\vartheta)$ represents a temperature-dependent *saturation value* of the back-stress in compression.[3] is always a positive valued scalar internal stress which leads to isotropic

[3] For the purpose of obtaining material parameters associated with the "yield stress," we ignore the evolution of the back-stress and use the temperature-dependent *saturation* value for the back-stress as an internal stress in the one-dimensional theory. In order to make connection with the work of Richeton et al. (2005a, 2006, 2007), one may identify $\sigma^*_{\text{back}}(\vartheta)$ with their internal stress $\sigma_i(\vartheta)$. Note, however, that in the work of Richeton et al., $\sigma_i(\vartheta)$

hardening, whereas in our more general theory the back-stress may in general be positive or negative, and is not only temperature dependent, but also evolves with strain to give rise to kinematic hardening. Because of the assumed temperature dependence (3.79) of the back-stress modulus, σ^*_{back} decreases linearly with temperature,

$$\sigma^*_{\text{back}} = R(\vartheta_g - \vartheta) \quad \text{for} \quad \vartheta \leq \vartheta_g, \tag{A.29}$$

where R is a material parameter. Finally, recalling (A.19),

$$\dot{\epsilon}^*(\vartheta) \stackrel{\text{def}}{=} \dot{\epsilon}_0 \exp\left(-\frac{Q}{k_B \vartheta}\right). \tag{A.30}$$

To summarize, from (A.27), (A.29), and (A.30), there is a list of six material parameters

$$\{\, \alpha_p, V, m, R,\ \dot{\epsilon}_0, Q \,\} \tag{A.31}$$

that must be calibrated from the experimental data for σ_y as a function of strain rate $\dot{\epsilon}$ and temperature ϑ. The value of the pressure-sensitivity parameter α_p is not determinable from simple compression experiments alone. As reviewed by Crist (1997), for amorphous polymers the pressure-sensitivity parameter α_p in simple tension/compression for PMMA is ≈ 0.35, that for PC is ≈ 0.2, and for amorphous polymers is generally in the range 0.1 to 0.4. We are not aware of any data for the pressure sensitivity of yield for Zeonex in the literature. Here, we assume that

$$\alpha_p \approx 0.2 \tag{A.32}$$

for Zeonex. This reduces the list (A.31) to

$$\{\, V, m, R, \dot{\epsilon}_0, Q \,\}, \tag{A.33}$$

which need to be calibrated from the experimental data for σ_y as a function of strain rate $\dot{\epsilon}$ and temperature ϑ.

Following the back-extrapolation method of Fig. A-1, values of the yield stress σ_y as a function of temperature ϑ and strain rate $\dot{\epsilon}$ have been estimated from the compression stress-strain curves for Zeonex in the temperature range 25 °C to 130 °C at four strain-rates. The ratio of these yield stresses to test temperatures, σ_y/ϑ, as a function of the logarithm of strain-rate, $\log_{10} \dot{\epsilon}$ are shown in the Eyring-plot of Fig. A-2a. Estimated isotherms have been drawn to visually connect the yield points for a given test temperature. For a given temperature we have only four data points spanning a relatively narrow strain-rate range, which makes fitting the flow function (A.27) difficult. However, by utilizing the shifting and superposition ideas of Richeton et al. (2005a, 2006), we can form a master curve of all 16 data points at a single reference temperature that covers a much wider range of strain rates. To obtain the master curve, the experimental data is shifted along both axes by

temperature-dependent shift factors defined below:

$$\left.\begin{aligned} \text{Horizontal shift:} \qquad \Delta(\log_{10}\dot{\epsilon}) &= H_h\left(\frac{1}{\vartheta}-\frac{1}{\vartheta_{\text{shift}}}\right), \\ \text{Vertical shift:} \qquad \Delta\left(\frac{\sigma_y}{\vartheta}\right) &= H_v\left(\frac{1}{\vartheta}-\frac{1}{\vartheta_{\text{shift}}}\right), \end{aligned}\right\} \tag{A.34}$$

where ϑ is the temperature of the experiment, ϑ_{shift} is the temperature that the data is shifted to, and H_h and H_v are shift parameters. Richeton et al. (2005a, 2006) have argued that these shift factors may be equated with the material parameters appearing in the cooperative flow model such that

$$\left.\begin{aligned} H_h &= \frac{Q}{k_B \ln 10}, \\ H_v &= -\sigma^*_{\text{back}}(\vartheta=0) = -R\theta_g. \end{aligned}\right\} \tag{A.35}$$

The master curve constructed at $\vartheta_{\text{shift}} = \vartheta_g = 408\,\text{K}$ using the shift factors

$$H_h = 5.7\times10^3\ \text{K}, \qquad H_v = -70\ \text{MPa},$$

is shown in Fig. A-2b, and the values of Q and R, calculated using (A.35), are

$$Q = 1.81\times10^{-19}\ \text{J}, \qquad \text{and} \qquad R = 0.172\ \text{MPa K}^{-1}.$$

For a master curve constructed at $\vartheta_{\text{shift}} = \vartheta_g$, the back-stress term from the flow function (A.27) vanishes, and (A.27) simplifies to

$$\frac{\sigma_y}{\vartheta_g} = \frac{2k_B}{V}\left(1-\frac{\alpha_p}{3}\right)^{-1}\sinh^{-1}\left[\left(\frac{\dot{\epsilon}}{\dot{\epsilon}^*(\vartheta_g)}\right)^m\right], \tag{A.36}$$

with the list of unknown parameters reduced to $\{\dot{\epsilon}_0,\, V,\, m\}$. A non-linear least-squares fitting method was used in MATLAB to obtain these parameters from the shifted experimental data. This gives

$$\dot{\epsilon}_0 = 1.8\times10^{11}\,\text{s}^{-1}, \qquad V = 1.14\times10^{-27}\,\text{m}^3, \qquad \text{and} \qquad m = 0.16,$$

and the resulting fit of (A.36) to the shifted data at 408K is shown in Fig. A-2b as a solid line.

A.3.3 Stress-strain response at large strains

Here, we focus on estimating the material parameters: (1) μ and I_m in the expression (A.15), together with the temperature dependence of μ given in (3.82); and (2) h_b and S_b^*, together with the temperature dependence of S_b^* given in (3.81) — parameters which account for the stress increase associated with chain-locking at large stretches.

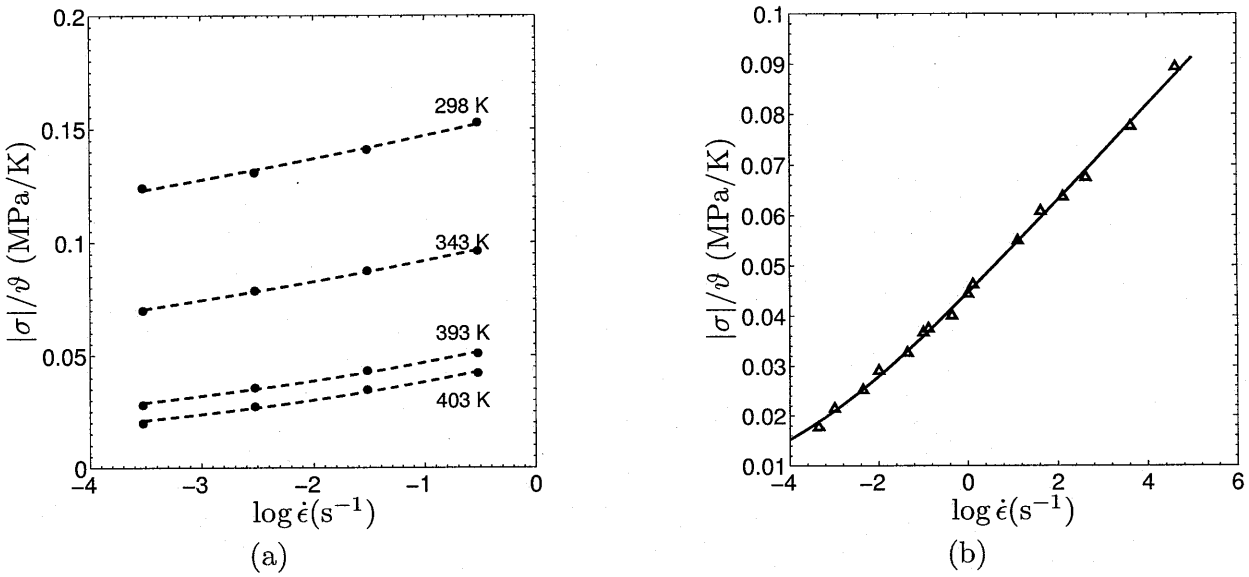

Figure A-2: (a) Ratio of compressive yield stress to temperature as a function of logarithm of strain rate. The data plotted as bullets (•) are the yield stress values estimated from the compression experiments, and the dashed lines are estimated isotherms. (b) Master curve constructed at 408 K by shifting the yield stress data. The shifted experimental data is plotted as triangles (△), and the solid line indicates a fit of flow function to the master curve.

To begin, we neglect the transient response associated with the yield-peak and set $\varphi_0 = S_{a0} = 0$, and correspondingly ignore the evolution equations (A.20) and (A.21) for φ and S_a; we return to determining the material parameters appearing in these coupled evolution equations later. We also ignore the evolution of the back-stress, and set it constant, using the temperature-dependent saturation value, such that

$$\sigma_{\text{back}}(\vartheta) = \sigma^*_{\text{back}}(\vartheta)\,\text{sign}(\sigma_{\text{back}}) = -R(\vartheta_g - \vartheta) \quad \text{for} \quad \vartheta < \vartheta_g, \tag{A.37}$$

and determine material parameters associated with the evolution of the back-stress later.

Below the glass transition temperature, the parameter I_m is presumed to be temperature-independent, as is the parameter h_2 in the evolution equation (A.22), while the temperature-dependence of $\mu(\vartheta)$ and $S^*_b(\vartheta)$ is presumed to follow

$$\mu(\vartheta) = \mu_0 - N(\vartheta - \vartheta_g) \quad \text{for} \quad \vartheta < \vartheta_g, \tag{A.38}$$

and

$$S^*_b(\vartheta) = l_1 - l_2\vartheta \quad \text{for} \quad \vartheta < \vartheta_g, \tag{A.39}$$

(cf., (3.82) and (3.81)). Using the one-dimensional MATLAB implementation of the model, together with the material parameters estimated to this point, estimates for the desired parameter list

$$\{\, \mu_0,\ N,\ I_m,\ S_{b0},\ h_b,\ l_1,\ l_2 \,\}$$

are relatively easily obtained by curve-fitting both the loading as well as the unloading response at large strains for the stress-strain data at the lowest strain rate.[4] A few trials give the estimates as

$$\mu_0 = 3 \text{ MPa}, \qquad N = 6.2 \times 10^{-2} \text{ MPa K}^{-1}, \qquad I_m = 6.2,$$
$$h_2 = 6.24, \qquad l_1 = 130 \text{ MPa}, \qquad l_2 = 0.27 \text{ MPa K}^{-1}.$$

A.3.4 Yield-peak and back-stress evolution

Finally we calibrate material parameters associated with the yield-peak and the back-stress evolution. This last step in the calibration procedure is an iterative process, and requires fitting the transient stress-overshoot in the simple compression stress-strain response together with the creep response, iteratively, several times in order to get a good fit. The steps in the iterative procedure are listed below.

Step 1:

The parameters related to the change of back-stress σ_{back} with strain and temperature are γ and X (cf. (A.24), (3.79)). To begin, we note that for compression

$$D^p = -\dot{\epsilon}^p, \tag{A.40}$$

and we may then rewrite the evolution equation for A (A.24) as

$$\dot{A} = -(2 + \gamma \ln A)\, A\, \dot{\epsilon}^p. \tag{A.41}$$

It follows then that the saturation value of A in compression is

$$A^* = \exp\left(-\frac{2}{\gamma}\right). \tag{A.42}$$

Combining this result with the equation for the back-stress (A.7) gives the saturation value of the back-stress as a function of the material parameters $B(\vartheta)$ and γ

$$\sigma^*_{\text{back}}(\vartheta) = 3\,\frac{B(\vartheta)}{\gamma}. \tag{A.43}$$

Equating the saturation value for the back-stress using (3.79) and $(A.29)_1$ we obtain

$$3\,\frac{X(\vartheta_g - \vartheta)}{\gamma} = R(\vartheta_g - \vartheta) \quad \Rightarrow \quad X = \frac{R}{3}\gamma, \tag{A.44}$$

[4]The internal variable S_b, together with its evolution (A.22), is essential for a proper modeling of the unloading response of the material after large strains. We assume that the material begins in a well-annealed, "ground" state and take S_{b0} to be zero. For PMMA the experimental data, to which the model is fit, to does not include data at very large strains, therefore we ignore the material parameters associated with the isotropic hardening at large strains and set h_b, l_1, l_2 to be zero for this material.

and since R has already been determined, we obtain the fixed value for the ratio X/γ.

Step 2:

In this step we estimate a value for γ, and calculate the corresponding value for X from (A.44) to get an estimate for the parameters involved in the evolution of the back-stress. This leaves one with a list of parameters $\{S_{a0}, h_a, b, \varphi_0, g, \varphi^*\}$ in the evolution equations (A.20) and (A.21) for φ and S_a to calibrate the yield-peak.

We assume the material begins in a well-annealed "ground-state," so that we may take the initial value of the order parameter φ and stress like internal resistance S_a to be zero,

$$\varphi_0 = 0 \quad \text{and} \quad S_{a0} = 0.$$

To find $\{h_a, b, g, \varphi^*\}$, several simulations are performed using different values of parameters to approximately match the shape of the yield peak at the various strain rates and temperatures. As an aid to the iterative curve-fitting procedure, Fig. A-3 shows how the parameters $\{h_a, b, g, \varphi^*\}$ affect the shape of the yield-peak. The parameter h_a controls the initial slope of the yield peak, the parameters b and φ^* control the height of the yield peak, while the parameter g controls the width of the yield-peak.

Step 3:

With the parameters for yield-peak estimated, one returns to refining the values of the material parameters in the back-stress evolution. To get refined estimates for the recovery parameter γ and the temperature sensitivity parameter X for the back-stress modulus B, we first note that γ controls the rate of saturation of the back-stress. This is shown in Fig. A-4a, where the back-stress versus axial strain response is shown for varying values of γ at a constant ratio of B/γ: as γ increases, the back-stress approaches its saturation value more rapidly.

The parameters γ and B significantly affect the creep response of the material.[5] In order to get more refined estimates for these parameters, we turn to a limited set of available data for room-temperature creep of Zeonex shown in Fig. A-4b as solid lines. The value of γ is chosen such that that the creep response is adequately represented, as shown by the dashed lines in Fig. A-4b.

Steps 2 and 3 are iteratively repeated until the yield-peaks in the total stress-strain response of the material, as well as the creep response are satisfactorily calibrated.

Once $\{h_a, b, g, \varphi^*\}$ are determined for each stress-strain curve, we have found that to a good approximation, the parameters h_a and b may be taken as constants; g as temperature dependent, and φ^* as both temperature and strain rate dependent. The temperature dependence of g was then fit to the functional form (3.80), while the temperature and strain rate dependence of φ^* was fit to the functional form (A.21); Fig. A-5 shows a schematic of the variation of φ^* with temperature and strain rate.

[5]Cyclic tension-compression stress-strain curves at different temperatures may also be used to fit the back-stress parameters, but we have not conducted the necessary extensive set of such experiments.

The material parameters for Zeonex that give a reasonable fit for the yield peak for the range of temperatures and strain rates under consideration, and also adequately reproduce the limited creep data, are

$$
\begin{array}{llll}
h_a = 300, & b = 10.13 \times 10^3 \text{ MPa}, & g_1 = -28, & g_2 = 0.12, \\
z = 0.0055, & r = 0.24, & s = 0.042, & \nu_r = 3 \times 10^{-4} \text{ s}^{-1} \\
n = 1.6, & \gamma = 12, & X = 0.7 \text{ MPa K}^{-1}, &
\end{array}
$$

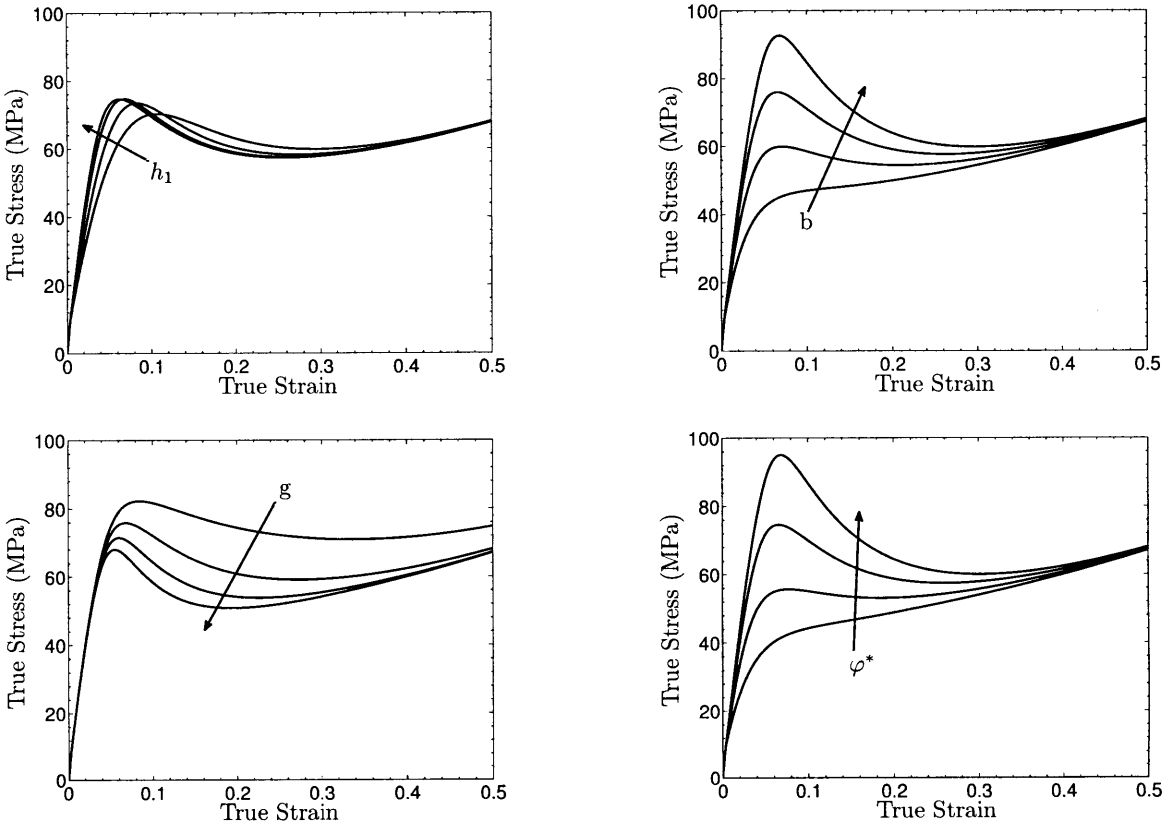

Figure A-3: Schematics of the effects of the material parameters $\{h_1, b, g, \varphi^*\}$ on the shape of the yield-peak. Arrows indicate changes as the values of the respective parameters are increased.

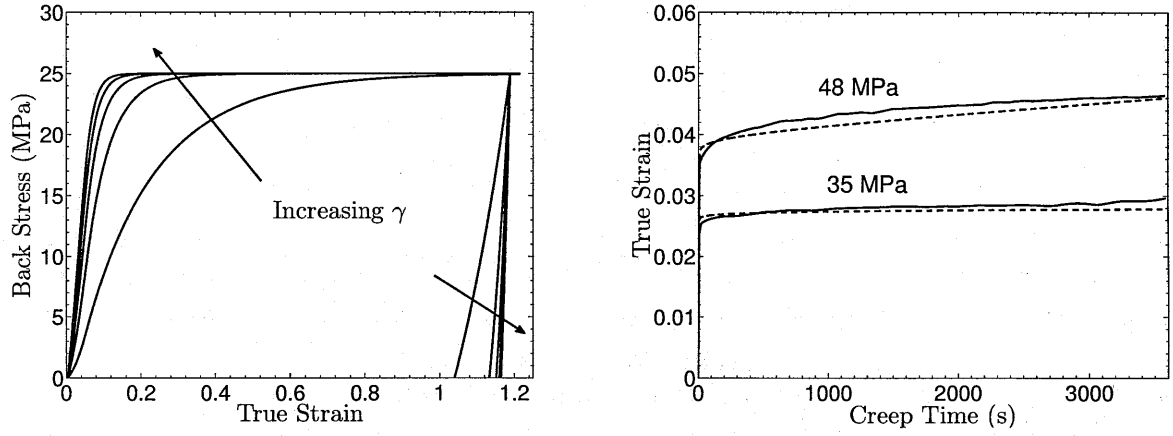

Figure A-4: (a) The dependence of the evolution of back-stress on the material parameter γ: effect of sequentially doubling the material parameter γ from 5 to 160 on the back-stress for a constant ratio of B/γ. (b) Creep test results under simple compression at two stress levels below the yield-peak (solid lines), together with one-dimensional MATLAB simulations (dashed lines).

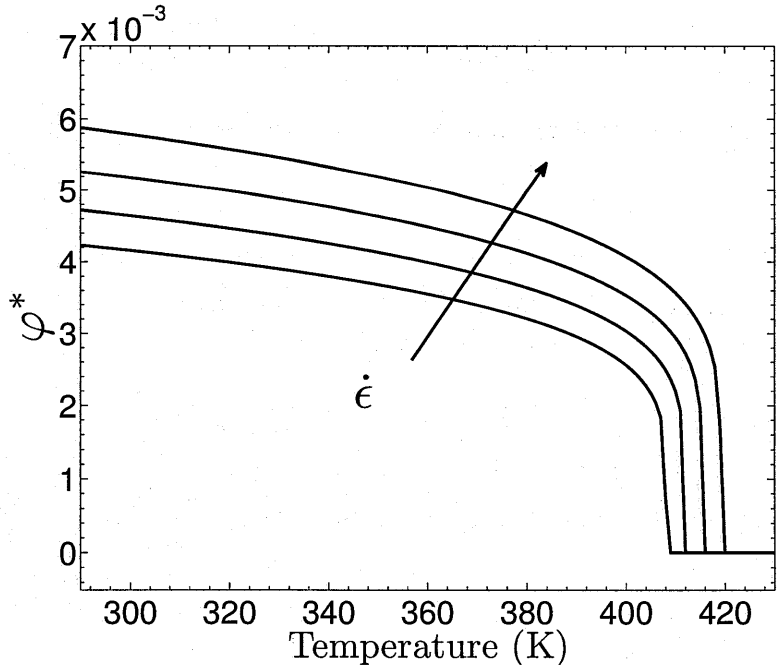

Figure A-5: Temperature and rate dependance of φ^*. The arrow indicates an increase in the strain rate.

A.4 Parameters for the three-dimensional model

Except for the list of parameters $\{\nu_0, \alpha_p, V, S_{a0}, h_a, b, g_1, g_2, S_{b0}, h_b, l_1, l_2, \nu_r, \gamma\}$, the values of the one-dimensional material parameters are unchanged when used in the three-dimensional equations. Noting that

$$\tau\nu = \sigma\dot{\epsilon}, \quad \sigma = \sqrt{3}\tau, \quad \dot{\epsilon} = \frac{\nu}{\sqrt{3}}, \tag{A.45}$$

the list of parameters $\{\nu_0, \alpha_p, V, S_{a0}, h_a, b, g_1, g_2, S_{b0}, h_b, l_1, l_2, \nu_r, \gamma\}$ may be converted from the one-dimensional compression form to the three-dimensional shear form using

$$\left.\begin{array}{lll}
\dot{\epsilon}_0 = \frac{1}{\sqrt{3}}\nu_0\,, & \alpha_p^{(\text{comp})} = \sqrt{3}\,\alpha_p^{(\text{shear})}\,, & V^{(\text{comp})} = \frac{1}{\sqrt{3}}\,V^{(\text{shear})}\,, \\
S_{a0}^{(\text{comp})} = \sqrt{3}\,S_{a0}^{(\text{shear})}\,, & h_a^{(\text{comp})} = \sqrt{3}\,h_a^{(\text{shear})}\,, & b^{(\text{comp})} = \sqrt{3}\,b^{(\text{shear})}\,, \\
g_1^{(\text{comp})} = \sqrt{3}\,g_1^{(\text{shear})}\,, & g_2^{(\text{comp})} = \sqrt{3}\,g_2^{(\text{shear})}\,, & S_{b0}^{(\text{comp})} = \sqrt{3}\,S_{b0}^{(\text{shear})}\,, \\
h_b^{(\text{comp})} = \sqrt{3}\,h_b^{(\text{shear})}\,, & l_1^{(\text{comp})} = \sqrt{3}\,l_1^{(\text{shear})}\,, & l_2^{(\text{comp})} = \sqrt{3}\,l_2^{(\text{shear})}\,, \\
\gamma^{(\text{comp})} = \sqrt{3}\,\gamma^{(\text{shear})}\,, & \dot{\epsilon}_r = \frac{1}{\sqrt{3}}\,\nu_r\,. &
\end{array}\right\} \tag{A.46}$$

Further, to convert the temperature dependence parameters for the Young's modulus E to those for the shear modulus G, we use the standard relations

$$G_0 = \frac{E_0}{2\,(1+\nu_{\text{poi}})}\,, \quad M = \frac{M_E}{2\,(1+\nu_{\text{poi}})}\,, \tag{A.47}$$

with ν_{poi} assumed to be temperature-independent in the temperature range under consideration.

The material parameters for the three-dimensional theory that were determined by following the procedure described in this Appendix are listed for Zeonex-690R, PC, and PMMA in Table 3.1 of Chapter 3.

Appendix B

Material parameter estimation procedure for a temperature range which spans the glass transition

B.1 Introduction

In this appendix we briefly outline our procedure for estimating values of the material parameters in the constitutive model described in Chapter 4. For an isotropic theory such as the one presented in Chapter 4, it is most convenient to use an implementation of a one-dimensional version of our model in the computer program MATLAB to conduct appropriate simulations to estimate the material parameters. We illustrate our material parameter calibration procedure for Zeonex-690R; the procedure for PC and PMMA is essentially identical.

From the outset we acknowledge that for any given material, the list of material parameters is rather long, and that the parameter values that we determine are *not unique.* However, having apologized for these features of our list of material parameters in advance, we know of no other theory which is able to phenomenologically (or otherwise) reproduce the complicated response of these materials over the ranges of strains, strain-rates, and temperatures considered in Chapter 4.

B.2 One-dimensional version of the constitutive theory

In this section we present an *approximate* one-dimensional version of the model, which substantially aids in the calibration of material properties from experimental data. The approximation is primarily in that we cannot account for Poisson's-type lateral contractions, and attendant volume changes, in a one-dimensional setting. The underlying constitutive equations relate the following basic fields:

$U > 0$,		stretch,
$U = U^{e(\alpha)} U^{p(\alpha)}$,	$\alpha = 1, 2, 3$	elastic-plastic decomposition of U,
$U^{e(\alpha)}$		elastic part of the stretch for each α,
$U^{p(\alpha)}$,		plastic part of the stretch for each α,
$\vartheta > 0$,		absolute temperature,
$\psi = \sum_\alpha \psi^{(\alpha)}$		free energy density,
$\sigma = \sum_\alpha \sigma^{(\alpha)}$,		Cauchy stress.

B.2.1 Variation of the glass transition temperature ϑ_g with strain rate

Let

$$\dot{\epsilon} \stackrel{\text{def}}{=} |\dot{U} U^{-1}| \tag{B.1}$$

denote an *equivalent tensile strain rate.* We assume that

$$\vartheta_g = \begin{cases} \vartheta_r & \text{if } \dot{\epsilon} \leq \dot{\epsilon}_r, \\ \vartheta_r + n \log \dfrac{\dot{\epsilon}}{\dot{\epsilon}_r} & \text{if } \dot{\epsilon} > \dot{\epsilon}_r, \end{cases} \tag{B.2}$$

where ϑ_r a *reference glass transition temperature* at a *reference strain rate* $\dot{\epsilon}_r$, and n is a material parameter.

B.2.2 Constitutive equations for $\alpha = 1$

1. **Free energy. Cauchy stress. Back-stress. Effective stress**

   With

   $$\epsilon^{e(1)} = \ln U^{e(1)} \tag{B.3}$$

   denoting a logarithmic elastic strain, we assume that

   $$\psi^{(1)} = \psi^{e(1)}(\epsilon^{e(1)}, \vartheta) + \psi^{p(1)}(A, \vartheta), \tag{B.4}$$

   where $A > 0$, is a squared stretch-like internal variable. For $\psi^{e(1)}$ we use a simple linear elastic form for the free energy

   $$\psi^{e(1)} = \frac{1}{2} E (\epsilon^{e(1)})^2 - E \alpha^{\text{th}} (\vartheta - \vartheta_0) \epsilon^{e(1)} + \tilde{f}(\vartheta), \tag{B.5}$$

   where $E(\vartheta) > 0$ is a Young's modulus, $\alpha^{\text{th}}(\vartheta)$ is a coefficient of thermal expansion, ϑ_0 is a reference temperature, and $\tilde{f}(\vartheta)$ is an entropic contribution to the free energy related to the specific heat of the material. The temperature dependence of the Young's modulus E is taken in the same form as that for the shear modulus G in (5.8), while

the temperature dependence of the coefficient of thermal expansion is as in (4.14). This free energy contributes a component

$$\sigma^{(1)} = E\,\epsilon^{e\,(1)} - E\alpha^{\text{th}}(\vartheta - \vartheta_0), \tag{B.6}$$

to the total Cauchy stress σ.

Next, for $\psi^{p\,(1)}$, first consider a symmetric positive definite squared-stretch-like tensor $\mathbf{A}$ which satisfies $\det \mathbf{A} = 1$. Let (a_1, a_2, a_3) denote the set of principal values of $\mathbf{A}$, with $a_1 a_2 a_3 = 1$. Then as in (4.17), the defect energy is

$$\psi^{p\,(1)} = \tfrac{1}{4} B \left[(\ln a_1)^2 + (\ln a_2)^2 + (\ln a_3)^2\right], \tag{B.7}$$

where $B(\vartheta) \geq 0$ is a back-stress modulus, with temperature dependence given in (4.19). With $\boldsymbol{\sigma}^{(\text{back})}$ denoting a stress from this free energy, standard relations of finite deformation incompressible elasticity give the corresponding principal values of the back-stress as

$$\sigma_i^{(\text{back})} = 2a_i \frac{\partial \psi^{p\,(1)}}{\partial a_i} - P, \tag{B.8}$$

with P an arbitrary "pressure." In simple tension/compression, $\sigma_1^{(\text{back})} \equiv \sigma_{\text{back}}$ and $\sigma_2^{(\text{back})} = \sigma_3^{(\text{back})} = 0$, and hence

$$\sigma_{\text{back}} = 2a_1 \frac{\partial \psi^{p\,(1)}}{\partial a_1} - 2a_2 \frac{\partial \psi^{p\,(1)}}{\partial a_2} = B\left(\ln a_1 - \ln a_2\right), \tag{B.9}$$

or equivalently, with $a_1 = A$, and $a_2 = a_3 = A^{-1/2}$,

$$\sigma_{\text{back}} = \frac{3}{2} B \ln A. \tag{B.10}$$

In a one-dimensional setting, the driving stress for plastic flow is the effective stress given by

$$\sigma_{\text{eff}}^{(1)} = \sigma^{(1)} - \sigma_{\text{back}}, \tag{B.11}$$

and the *equivalent tensile stress* and the *mean normal pressure* are

$$\bar{\sigma}^{(1)} \stackrel{\text{def}}{=} |\sigma_{\text{eff}}^{(1)}| \qquad \text{and} \qquad \bar{p} = -\frac{1}{3}\sigma^{(1)}, \tag{B.12}$$

respectively.

2. Flow rule

The one-dimensional version of the flow rule (4.26) is that

$$\dot{U}^{p\,(1)} = D^{p\,(1)} U^{p\,(1)}, \qquad D^{p\,(1)} = \dot{\epsilon}^{p(1)} \text{sign}(\sigma^{(1)}), \qquad \text{with} \qquad \dot{\epsilon}^{p(1)} \geq 0. \tag{B.13}$$

With (S_a, S_b) two positive-valued stress-dimensioned internal variables, and α_p a pressure-sensitivity parameter, let

$$\sigma_e \stackrel{\text{def}}{=} \bar{\sigma}^{(1)} - (S_a + S_b + \alpha_p \bar{p}) \tag{B.14}$$

define a net equivalent tensile stress, then equivalent tensile plastic strain rate $\dot{\epsilon}^{p(1)}$ is taken to be given by

$$\dot{\epsilon}^{p(1)} = \begin{cases} 0 & \text{if} \quad \sigma_e \leq 0, \\ \dot{\epsilon}_0^{(1)} \exp\left(-\dfrac{1}{\zeta}\right) \exp\left(-\dfrac{Q}{k_B \vartheta}\right) \left[\sinh\left(\dfrac{\sigma_e V}{2\, k_B \vartheta}\right)\right]^{1/m^{(1)}} & \text{if} \quad \sigma_e > 0. \end{cases} \tag{B.15}$$

In the scalar flow rule (B.15), $(\dot{\epsilon}_0^{(1)}, V, m^{(1)}, \alpha_p)$ are taken to be constants, while (ζ, Q) are assumed to be temperature- dependent, with the dependencies given in (5.22) and (4.45), respectively. When $\dot{\epsilon}^{p(1)} > 0$, the scalar flow rule (B.15), using (B.11) and (B.12), may be inverted to give the strength relation

$$|\sigma^{(1)} - \sigma_{\text{back}}| + \frac{1}{3}\alpha_p\, \sigma^{(1)} = S_a + S_b + \frac{2k_b\vartheta}{V} \sinh^{-1}\left[\left(\frac{\dot{\epsilon}^{p(1)}}{\dot{\epsilon}^*(\vartheta)}\right)^{m^{(1)}}\right], \tag{B.16}$$

where

$$\dot{\epsilon}^*(\vartheta) \stackrel{\text{def}}{=} \dot{\epsilon}_0^{(1)} \exp\left(-\frac{1}{\zeta}\right) \exp\left(-\frac{Q}{k_B \vartheta}\right). \tag{B.17}$$

3. Evolution equations for the internal variables φ, S_a, S_b, and A

Together with (S_a, S_b, A), we introduce another internal variable φ. The internal variables S_a and φ are taken to obey the coupled evolution equations:

$$\dot{S}_a = h_a\, (S_a^* - S_a)\, \dot{\epsilon}^{p(1)}, \quad \text{with} \quad S_a^* = b\,(\varphi^* - \varphi)\,, \quad \text{and} \quad S_a(0) = S_{a0}; \tag{B.18}$$

where

$$\left.\begin{aligned} &\dot{\varphi} = g\, (\varphi^* - \varphi)\, \dot{\epsilon}^{p(1)}, \qquad \text{with} \qquad \varphi(0) = \varphi_0, \qquad \text{where} \\ &\varphi^*(\dot{\epsilon}^{p(1)}, \vartheta) = \begin{cases} z\left(1 - \dfrac{\vartheta}{\vartheta_g}\right)^r \left(\dfrac{\dot{\epsilon}^{p(1)}}{\dot{\epsilon}_r}\right)^s & \text{for} \quad (\vartheta \leq \vartheta_g) \ \text{ and } \ (\dot{\epsilon}^{p(1)} > 0), \\ 0 & \text{for} \quad (\vartheta > \vartheta_g) \ \text{ or } \ (\dot{\epsilon}^{p(1)} = 0). \end{cases} \end{aligned}\right\} \tag{B.19}$$

Here $(h_a, b, S_{a0}, \varphi_0, z, r, s)$ are taken to be constants, and g is taken to be temperature-dependent, cf. (4.51).

The evolution of S_b is taken to be governed by

$$\dot{S}_b = h_b\, (\bar{\lambda} - 1)\, (S_b^* - S_b)\, \dot{\epsilon}^{p(1)}, \quad \text{with initial value} \quad S_b(0) = S_{b0} \geq 0, \tag{B.20}$$

where

$$\bar{\lambda} \stackrel{\text{def}}{=} \sqrt{(U+2U)/3} \tag{B.21}$$

is an effective stretch, h_b a constant, and S_b^* temperature-dependent, cf. (4.52).

The one-dimensional form of (4.55) is the following evolution equation for A:

$$\dot{A} = 2\,A\,D^{p\,(1)} - \gamma(A \ln A)\,\dot{\epsilon}^{p(1)}, \qquad A(0) = 1, \tag{B.22}$$

where $\gamma \geq 0$ is a constitutive parameter which governs the dynamic recovery of A.

B.2.3 Constitutive equations for $\alpha = 2$

1. Free energy. Cauchy stress

For ease of notation, suppress for the time being the superscript $\alpha = 2$. For ψ, consider first a symmetric positive definite, unimodular stretch tensor $\mathbf{U}^e$. Let (U_1^e, U_2^e, U_3^e) denote the set of principal stretches of $\mathbf{U}^e$, with $U_1^e U_2^e U_3^e = 1$. The first invariant I_1 of $(\mathbf{U}^e)^2$ is

$$I_1 \stackrel{\text{def}}{=} U_1^{e\,2} + U_2^{e\,2} + U_3^{e\,2}. \tag{B.23}$$

With $\boldsymbol{\sigma}$ denoting the contribution to the Cauchy stress from free energy ψ, which is presumed to be a function of I_1, standard relations of finite-deformation incompressible elasticity give the principal values of $\boldsymbol{\sigma}$ as

$$\sigma_i = U_i^e \frac{\partial \psi}{\partial U_i^e} - P, \tag{B.24}$$

with P an arbitrary "pressure." In simple tension/compression, with $\sigma_1 \equiv \sigma$ and $\sigma_2 = \sigma_3 = 0$, we get

$$\sigma = U_1^e \frac{\partial \psi}{\partial U_1^e} - U_2^e \frac{\partial \psi}{\partial U_2^e} = \frac{\partial \psi}{\partial I_1}\left(U_1^e \frac{\partial I_1}{\partial U_1^e} - U_2^e \frac{\partial I_1}{\partial U_2^e}\right) = 2\,\frac{\partial \psi}{\partial I_1}\left(U_1^{e\,2} - U_2^{e\,2}\right), \tag{B.25}$$

or equivalently, with $U_1^e \equiv U^e$ and $U_2^e = U_3^e = U^{e\,-1/2}$,

$$\sigma = 2\,\frac{\partial \psi}{\partial I_1}\left(U^{e\,2} - U^{e\,-1}\right). \tag{B.26}$$

Reinstating the superscript (2) for micromechanism $\alpha = 2$, the Gent (1996) free energy in terms of $I_1^{(2)} \stackrel{\text{def}}{=} \left(U_1^{e(2)}\right)^2 + \left(U_2^{e(2)}\right)^2 + \left(U_3^{e(2)}\right)^2$ is

$$\psi^{(2)} = -\frac{1}{2}\,\mu^{(2)}\,I_m^{(2)} \ln\left(1 - \frac{I_1^{(2)} - 3}{I_m^{(2)}}\right), \tag{B.27}$$

which with (B.26) gives the contribution $\sigma^{(2)}$ to total one-dimensional Cauchy stress σ as

$$\sigma^{(2)} = \mu^{(2)} \left(1 - \frac{I_1^{(2)} - 3}{I_m^{(2)}}\right)^{-1} \left((U^{e(2)})^2 - (U^{e(2)})^{-1}\right), \tag{B.28}$$

where $\mu^{(2)}(\vartheta) > 0$ and $I_m^{(2)} > 3$ are two material parameters, with the temperature dependency of $\mu^{(2)}$ given in (5.40).

2. Flow rule

The evolution equation for $U^{p\,(2)}$ is

$$\left.\begin{aligned} \dot{U}^{p\,(2)} &= D^{p\,(2)} U^{p\,(2)}, \qquad D^{p\,(2)} = \dot{\epsilon}^{p(2)} \mathrm{sign}(\sigma^{(2)}), \\ \dot{\epsilon}^{p(2)} &= \dot{\epsilon}_0^{(2)} \left(\frac{|\sigma^{(2)}|}{S^{(2)}}\right)^{1/m^{(2)}}, \end{aligned}\right\} \tag{B.29}$$

with $\dot{\epsilon}^{p(2)}$ the equivalent tensile plastic strain-rate. The parameters $(\dot{\epsilon}_0^{(2)}, m^{(2)})$ are constants, and $S^{(2)}$ temperature-dependent, cf. (5.50).

B.2.4 Constitutive equations for $\alpha = 3$

1. Free energy. Cauchy stress

For a free energy function of the form

$$\psi^{(3)} = -\frac{1}{2} \mu^{(3)} I_m^{(3)} \ln\left(1 - \frac{I_1^{(3)} - 3}{I_m^{(3)}}\right), \tag{B.30}$$

where $I_1^{(3)} \stackrel{\text{def}}{=} (U_1^{e(3)})^2 + (U_2^{e(3)})^2 + (U_3^{e(3)})^2$, analogous to the case $\alpha = 2$, we have the contribution

$$\sigma^{(3)} = \mu^{(3)} \left(1 - \frac{I_1^{(3)} - 3}{I_m^{(3)}}\right)^{-1} \left((U^{e(3)})^2 - (U^{e(3)})^{-1}\right) \tag{B.31}$$

to the total one-dimensional Cauchy stress σ. Here $\mu^{(3)} > 0$ and $I_m^{(3)} > 3$ are two temperature-independent material parameters.

2. Flow rule

The evolution equation for $U^{p\,(3)}$ is

$$\left.\begin{aligned} \dot{U}^{p\,(3)} &= D^{p\,(3)} U^{p\,(3)} \qquad D^{p\,(3)} = \dot{\epsilon}^{p(3)} \mathrm{sign}(\sigma^{(3)}), \\ \dot{\epsilon}^{p(3)} &= \begin{cases} 0 & \text{if} \quad \vartheta < \vartheta_g, \\ \dot{\epsilon}_0^{(3)} \left(\dfrac{|\sigma^{(3)}|}{S^{(3)}}\right)^{1/m^{(3)}} & \text{if} \quad \vartheta \geq \vartheta_g, \end{cases} \end{aligned}\right\} \tag{B.32}$$

where $\dot{\epsilon}^{p(3)}$ is the equivalent tensile plastic strain-rate, and the parameters $(\dot{\epsilon}_0^{(3)}, m^{(3)})$ are constants, while $S^{(3)}$ evolves, as discussed below.

3. **Evolution equations for internal variable $S^{(3)}$:**

   The evolution of $S^{(3)}$ is taken to be governed by

$$\dot{S}^{(3)} = h_3\,(\bar{\lambda} - 1)\,\dot{\epsilon}^{p(3)} \quad \text{with initial value} \quad S^{(3)}(0) = S_0^{(3)} \geq 0, \tag{B.33}$$

   where

$$\bar{\lambda} \stackrel{\text{def}}{=} \sqrt{(U + 2U)/3}, \tag{B.34}$$

   is an effective stretch, and $h_3(\vartheta)$ and $S_0^{(3)}(\vartheta)$ are temperature-dependent material parameters, (4.88).

B.2.5 Evolution equation for temperature

For one-dimensional tests at the highest strain rates, *which may be approximated as adiabatic*, the temperature is taken to evolve according to

$$c\dot{\vartheta} = \omega\,\left(\bar{\sigma}^{(1)}\,\dot{\epsilon}^{p(1)} + \tfrac{1}{2}\,B\,\gamma\,|\ln A|^2\,\dot{\epsilon}^{p(1)} + |\sigma^{(2)}|\,\dot{\epsilon}^{p(2)} + |\sigma^{(3)}|\,\dot{\epsilon}^{p(3)}\right). \tag{B.35}$$

B.3 Material parameter calibration

We have implemented the one-dimensional version of the constitutive theory in MATLAB using an explicit integration scheme, and we use it to calibrate the material parameters from the experiments described in Chapter 4. The one-dimensional calibration process consists of four sequential steps which are outlined in this section. The four steps cover calibration of the following aspects of the stress-strain response: (1) elastic modulus and rate dependence of ϑ_g; (2) initial yield stress; (3) large-strain behavior; and (4) yield-peak and back-stress.

B.3.1 Temperature dependence of E and strain rate dependence of ϑ_g

The temperature dependence of the modulus E is taken in the same form as that for G in (5.8):

$$E(\vartheta) = \tfrac{1}{2}(E_{gl} + E_r) - \tfrac{1}{2}(E_{gl} - E_r)\tanh\left(\frac{1}{\Delta}(\vartheta - \vartheta_g)\right) - M_E(\vartheta - \vartheta_g), \tag{B.36}$$

where

$$M_E = \begin{cases} M_{Egl} & \vartheta \leq \vartheta_g, \\ M_{Er} & \vartheta > \vartheta_g, \end{cases} \tag{B.37}$$

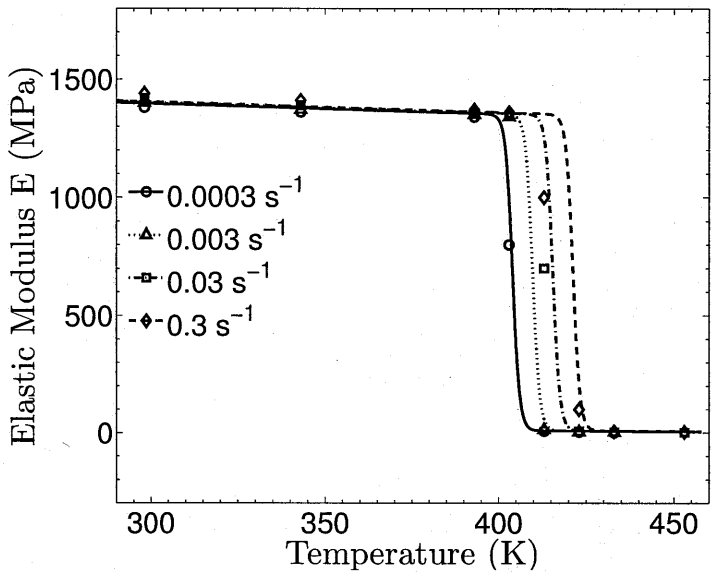

Figure B-1: Fit of elastic modulus E to phenomenological function (B.36).

and ϑ_g is the *rate-dependent* glass transition temperature, cf. (B.2). Experimental values of E were estimated from the initial slopes of the experimentally-measured stress-strain curves at small strains, at the various different temperatures and the four different strain ratees. The reference strain rate $\dot{\epsilon}_r$ in (B.2) was chosen as the slowest rate 3×10^{-4} s^{-1} in our experiments, and the elastic modulus data was fit to (B.36) and (B.2). The resulting material parameters for the fit shown in Fig. B-1 are

$$\dot{\epsilon}_r = 3 \times 10^{-4}\ \text{s}^{-1}, \quad \vartheta_r = 404\ \text{K}, \quad n = 2.5\ \text{K},$$
$$E_{gl} = 1350\ \text{MPa}, \quad E_r = 10\ \text{MPa}, \quad \Delta = 2.0\ \text{K}, \quad M_{Egl} = 0.45\ \text{MPa K}^{-1}, \quad M_{Er} = 0.1\ \text{MPa K}^{-1}.$$

B.3.2 Initial yield stress

1. Initial yield at temperatures below ϑ_g

First we consider the material parameters related to the flow stress at temperatures below ϑ_g. Since the stress-peak is associated with the transient disordering of the material, and the actual level of a peak is very dependent on the initial thermal history of the material, here we follow a different approach. We identify a "yield stress" in a compression experiment as a back-extrapolated value of the intersection of the initial elastic slope with the tangent to the stress-strain curve at a strain of, say, 0.4, a strain level by which all transients of the yield-peak have died out, and the chain-locking effects giving rise to the stress-strain curve are minimal. Accordingly, at this point in the calibration procedure we ignore the effects of the yield-peak and define the

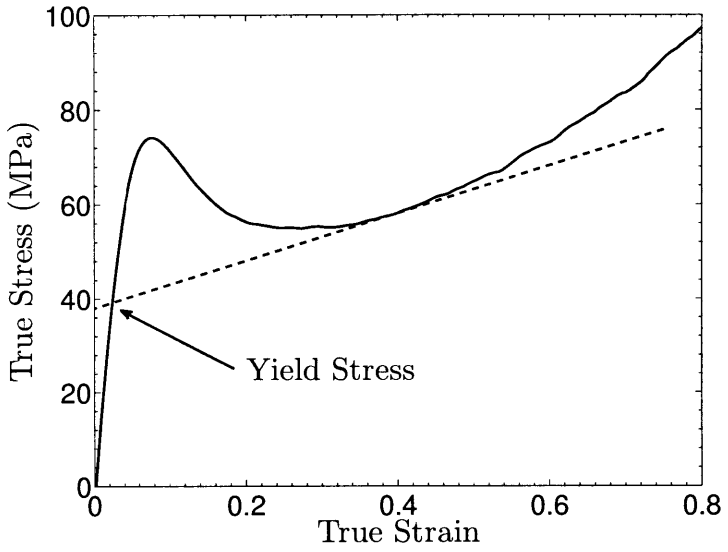

Figure B-2: Schematic showing the "yield stress" defined as the intersection of the pre-peak stress-strain curve with the back-extrapolated tangent to the stress-stain curve at 0.4 strain.

"yield stress" as the intersection of the pre-peak stress-strain curve with the back-extrapolated tangent to the stress-strain curve at approximately 0.4 strain; this is shown schematically in Fig. B-2.

Since

$$|\sigma^{(1)} - \sigma_{\text{back}}| = (\sigma^{(1)} - \sigma_{\text{back}})\,\text{sign}(\sigma^{(1)} - \sigma_{\text{back}})$$

and since in a monotonic compression test

$$\text{sign}(\sigma^{(1)} - \sigma_{\text{back}}) = \text{sign}(\sigma^{(1)}) = \text{sign}(\sigma_{\text{back}}),$$

we have

$$|\sigma^{(1)} - \sigma_{\text{back}}| = |\sigma^{(1)}| - |\sigma_{\text{back}}|,$$

and hence, from (B.16),

$$\left(1 - \frac{\alpha_p}{3}\right)|\sigma^{(1)}| = S_a + S_b + |\sigma_{\text{back}}| + \frac{2k_b\vartheta}{V}\sinh^{-1}\left[\left(\frac{\dot{\epsilon}^{p(1)}}{\dot{\epsilon}^*(\vartheta)}\right)^{m^{(1)}}\right]. \tag{B.38}$$

Thus, neglecting the contribution from the internal variables S_a(which is associated with the transient yield peak) and the contribution from S_b (since this only manifests itself at large stretches), for fully-developed flows when $\dot{\epsilon}^{p(1)} \approx \dot{\epsilon}$ (taken to be positive in compression) and with $|\sigma^{(1)}| = \sigma_y$, (B.38) gives the following approximate expression

for yield stress σ_y as a function of temperature ϑ and strain rate $\dot{\epsilon}$:

$$\left(1-\frac{\alpha_p}{3}\right)\sigma_y \approx \sigma^*_{\text{back}}(\vartheta) + \frac{2k_B\vartheta}{V}\sinh^{-1}\left[\left(\frac{\dot{\epsilon}}{\dot{\epsilon}^*(\vartheta)}\right)^{m^{(1)}}\right], \tag{B.39}$$

where we have introduced the notation

$$\sigma^*_{\text{back}}(\vartheta) \stackrel{\text{def}}{=} |\sigma_{\text{back}}(\vartheta)|. \tag{B.40}$$

Here, $\sigma^*_{\text{back}}(\vartheta)$ represents a temperature-dependent *saturation value* of the back-stress in compression.[1] Because of the assumed temperature dependence (4.19) of the back-stress modulus, σ^*_{back} decreases linearly with temperature,

$$\sigma^*_{\text{back}} = R(\vartheta_g - \vartheta) \quad \text{for} \quad \vartheta \leq \vartheta_g, \tag{B.41}$$

where R is a material parameter.[2]

Finally, recalling (B.17), (5.22), and (4.45),

$$\dot{\epsilon}^*(\vartheta) = \dot{\epsilon}_0^{(1)} \exp\left(-\frac{1}{\zeta_{gl}}\right)\exp\left(-\frac{Q_{gl}}{k_B\vartheta}\right) \quad \text{for} \quad \vartheta \leq \vartheta_g. \tag{B.42}$$

To summarize, from (B.39), (B.41), and (B.42), there is a list of seven material parameters

$$\{\alpha_p,\ \dot{\epsilon}_0^{(1)},\ m^{(1)},\ V,\ \zeta_{gl},\ Q_{gl},\ R\}$$

that must be calibrated from the experimental data for σ_y as a function of strain rate $\dot{\epsilon}$ and temperature ϑ for temperatures below ϑ_g. The value of the pressure-sensitivity parameter α_p is not determinable from simple compression experiments alone. As reviewed by Crist (1997), for amorphous polymers the pressure-sensitivity parameter α_p in simple tension/compression for PMMA is ≈ 0.35, that for PC is ≈ 0.2, and for amorphous polymers is generally in the range 0.1 to 0.4. We are not aware of any data for the pressure sensitivity of yield for Zeonex in the literature. Here, we assume that $\alpha_p \approx 0.2$ for Zeonex. The parameter $\dot{\epsilon}_0^{(1)}$, represents an attempt frequency for

[1] For the purpose of obtaining material parameters associated with the "yield stress," we ignore the evolution of the back-stress and use the temperature-dependent *saturation* value for the back-stress as an internal stress in the one-dimensional theory. In order to make connection with the work of Richeton et al. (2005a, 2006, 2007), one may identify $\sigma^*_{\text{back}}(\vartheta)$ with their internal stress $\sigma_i(\vartheta)$. Note, however, that in the work of Richeton et al., $\sigma_i(\vartheta)$ is always a positive valued scalar internal stress which leads to isotropic hardening, whereas in our more general theory the back-stress may in general be positive or negative, and is not only temperature dependent, but also evolves with strain to give rise to kinematic hardening.

[2] For the purpose of fitting the parameters associated with the yield points in the glassy regime, the rate dependence of the glass transition temperature is neglected and for this step of material parameter calibration procedure, we assume the glass transition temperature to be constant and assume $\vartheta_g = \vartheta_r = 404$ K for Zeonex.

the plastic flow, and we assume that it has the classical value 10^{13} s^{-1} for the three polymers.

Following the back-extrapolation method of Fig. B-2, values of the yield stress σ_y as a function of temperature ϑ and strain rate $\dot{\epsilon}$ have been estimated from the compression stress-strain curves for Zeonex in the temperature range 25 °C to 130 °C at four strain-rates. The ratio of these yield stresses to test temperatures, σ_y/ϑ, as a function of the logarithm of strain-rate, $\log_{10}\dot{\epsilon}$ are shown in the Eyring-plot of Fig. B-3a. Estimated isotherms have been drawn to visually connect the yield points for a given test temperature. For a given temperature we have only four data points spanning a relatively narrow strain-rate range, which makes fitting the flow function (B.39) difficult. However, by utilizing the shifting and superposition ideas of Richeton et al. (2005a, 2006), we can form a master curve of all 16 data points at a single reference temperature that covers a much wider range of strain rates. To obtain the master curve, the experimental data is shifted along both axes by temperature-dependent shift factors defined below:

$$\left.\begin{aligned} \text{Horizontal shift:} \quad & \Delta(\log_{10}\dot{\epsilon}) = H_h\left(\frac{1}{\vartheta}-\frac{1}{\vartheta_{\text{shift}}}\right), \\ \text{Vertical shift:} \quad & \Delta\left(\frac{\sigma_y}{\vartheta}\right) = H_v\left(\frac{1}{\vartheta}-\frac{1}{\vartheta_{\text{shift}}}\right), \end{aligned}\right\} \tag{B.43}$$

where ϑ is the temperature of the experiment, ϑ_{shift} is the temperature that the data is shifted to, and H_h and H_v are shift parameters. Richeton et al. (2005a, 2006) have argued that these shift factors may be equated with the material parameters appearing in the cooperative flow model such that

$$\left.\begin{aligned} H_h &= \frac{Q_{gl}}{k_B \ln 10}, \\ H_v &= -\sigma^*_{\text{back}}(\vartheta=0) = -R\theta_g. \end{aligned}\right\} \tag{B.44}$$

The master curve constructed at $\vartheta_{\text{shift}} = \vartheta_r = 404$ K $\approx \vartheta_g$ using the shift factors

$$H_h = 4.91\times10^3 \text{ K}, \qquad H_v = -69.5 \text{ MPa},$$

is shown in Fig. B-3b, and the values of Q_{gl} and R, calculated using (B.44), are

$$Q_{gl} = 1.56\times10^{-19} \text{ J}, \qquad \text{and} \qquad R = 0.172 \text{ MPa K}^{-1}.$$

For a master curve constructed at $\vartheta_{\text{shift}} = 404$ K $\approx \vartheta_g$, the back-stress term from the flow function (B.39) vanishes, and (B.39) simplifies to

$$\frac{\sigma_y}{\vartheta_g} = \frac{2k_B}{V}\left(1-\frac{\alpha_p}{3}\right)^{-1}\sinh^{-1}\left[\left(\frac{\dot{\epsilon}}{\dot{\epsilon}^*(\vartheta_g)}\right)^{m^{(1)}}\right], \tag{B.45}$$

with the list of unknown parameters reduced to $\{\zeta_{gl}, V, m^{(1)}\}$. A non-linear least-squares fitting method was used in MATLAB to obtain these parameters from the shifted experimental data. This gives

$$\zeta_{gl} = 0.135 \qquad V = 0.98 \times 10^{-27}\,\mathrm{m}^3, \qquad \text{and} \qquad m^{(1)} = 0.16,$$

and the resulting fit of (B.45) to the shifted data at 404 K is shown in Fig. B-3b as a solid line.

2. Initial yield at temperatures above ϑ_g

As the temperature is increased through the glass transition region, the yield stress drops off very rapidly to negligibly small values. In our model, as the temperature increases through the glass transition, the characteristic strain rate $\dot{\epsilon}^*$ rapidly increases, leading to a relatively fast drop in the yield stress. At temperatures above ϑ_g, the values for the yield stress σ_y were estimated to be the stress value at ≈ 0.04 strain. For the estimated values of the yield stress, corresponding values for characteristic strain rate $\dot{\epsilon}^*$ were calculated using relation (B.39) for each experiment above ϑ_g. With $\dot{\epsilon}^*$ defined as

$$\dot{\epsilon}^*(\vartheta) \stackrel{\text{def}}{=} \dot{\epsilon}_0^{(1)} \exp\left(-\frac{1}{\zeta}\right) \exp\left(-\frac{Q}{k_B\vartheta}\right), \tag{B.46}$$

where the additional temperature dependence of ζ and Q govern the change in characteristic strain-rate $\dot{\epsilon}^*(\vartheta)$ through the glass transition. With (5.22) and (4.45) representing temperature dependence of ζ and Q, we are left to determine (Q_r, d). To determine these two material parameters, values of $\dot{\epsilon}^*$ that were obtained from the experiments were fit for temperatures above ϑ_g. The selected values of $\dot{\epsilon}^*$ along with a fit of function (B.46) are shown in Fig. B-4 for following values of material parameters

$$Q_r = 1.0 \times 10^{-20}\ \mathrm{J}, \qquad \text{and} \qquad d = 0.015\ \mathrm{K}^{-1}.$$

B.3.3 Stress-strain response at large strains

This part of the calibration procedure was divided into two steps: (i) material parameter calibration for temperatures above ϑ_g; and (ii) material parameter calibration for temperatures below ϑ_g.

1. Large strain response above ϑ_g

For temperatures above ϑ_g, we allow for network slippage corresponding to micromechanism $\alpha = 2$ and select material parameters $(S_r^{(2)}, \dot{\epsilon}_0^{(2)}, m^{(2)})$, such that the flow stress

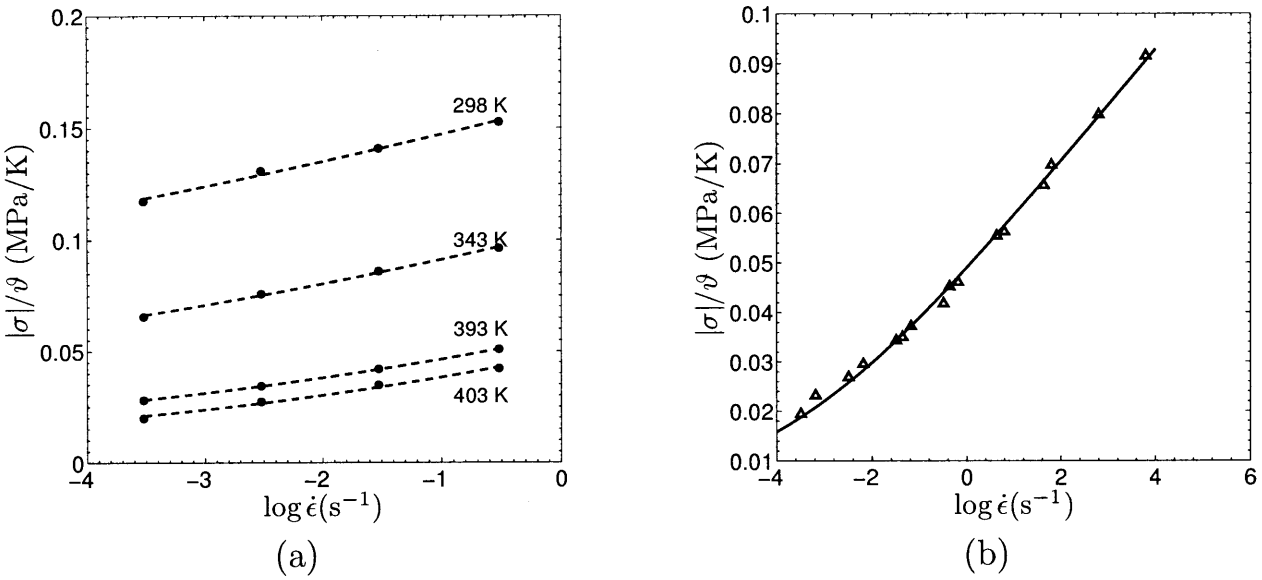

Figure B-3: (a) Ratio of compressive yield stress to temperature as a function of logarithm of strain rate. The data plotted as bullets (•) are the yield stress values estimated from the compression experiments, and the dashed lines are estimated isotherms. (b) Master curve constructed at 404 K by shifting the yield stress data. The shifted experimental data is plotted as triangles (△), and the solid line indicates a fit of flow function to the master curve.

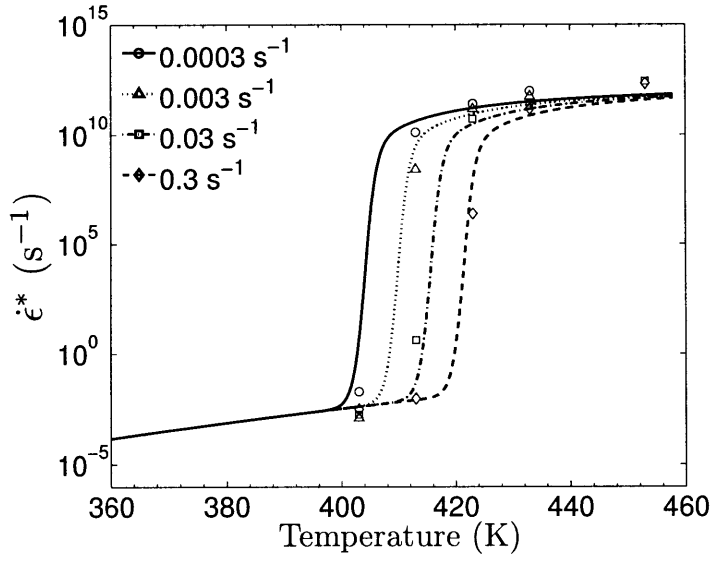

Figure B-4: Fit of characteristic strain-rate $\dot{\epsilon}^*$ versus temperature above the glass transition temperature ϑ_g. Symbols indicate selected value for fitting and lines indicate fit of function given in (B.46).

associated with (B.29) is negligibly small. We accomplish this by taking

$$S_r^{(2)} = 0.02 \text{ MPa}, \qquad \dot{\epsilon}_0^{(2)} = 3 \times 10^{-4} \text{ s}^{-1}, \qquad m^{(2)} = 0.18,$$

where the value of $\dot{\epsilon}_0^{(2)}$ is the slowest strain rate of our experiments, and the value of $m^{(2)}$ is a suitably large value at these high temperatures. Thus, in the calibration procedure above ϑ_g, we may neglect the small contribution from $\sigma^{(2)}$ and set

$$\sigma \approx \sigma^{(1)} + \sigma^{(3)}.$$

Thus, for $\vartheta > \vartheta_g$ the nonlinear increase in stress at large stretches depends primarily on (i) the evolution of the internal variable S_b in micromechanism $\alpha = 1$ according to (B.20); and (ii) the values of the elastic parameters ($\mu^{(3)}$, $I_m^{(3)}$), the values of the flow parameters ($\dot{\epsilon}_0^{(3)}$, $m^{(3)}$), and the evolution of the internal variable $S^{(3)}$ in micromechanism $\alpha = 3$.

Using the one-dimensional MATLAB implementation of the model, together with the material parameters estimated up to this point, the stress-strain response *at a given strain rate and temperature*, can be fit by adjusting values of (h_b, S_{b0}, S_b^*) for $\alpha = 1$, and the values ($\mu^{(3)}$, $I_m^{(3)}$, $\dot{\epsilon}_0^{(3)}$, $m^{(3)}$, h_3, $S_0^{(3)}$) for $\alpha = 3$. In the lists above (h_b, S_{b0}) and ($\mu^{(3)}$, $I_m^{(3)}$, $\dot{\epsilon}_0^{(3)}$, $m^{(3)}$) are presumed to be temperature-independent, the initial value of the internal variable S_b is set to $S_{b0} = 0$, the reference plastic strain rate $\dot{\epsilon}_0^{(3)}$ is taken as 3×10^{-4} s^{-1} (the slowest strain rate of our experiments), while the temperature-dependence of $S_b^*(\vartheta)$, $S_0^{(3)}(\vartheta)$, and $h_3(\vartheta)$ is presumed to follow

$$S_b^*(\vartheta) = S_r - L_r\Big(\vartheta - (\vartheta_g + 2.5\Delta)\Big) \quad \text{for} \quad \vartheta > \vartheta_g, \tag{B.47}$$

$$S_0^{(3)}(\vartheta) = S_g^{(3)} \exp\Big(-Y(\vartheta - \vartheta_g)\Big), \tag{B.48}$$

$$\text{and} \quad h_3(\vartheta) = h_{3g} \exp\Big(-Z(\vartheta - \vartheta_g)\Big). \tag{B.49}$$

Estimates of the values of the desired material parameter lists

$$(h_b,\, S_r,\, L_r)$$

for $\alpha = 1$, and

$$(\mu^{(3)},\, I_m^{(3)},\, m^{(3)},\, S_g^{(3)},\, Y,\, h_{3g},\, Z)$$

for $\alpha = 3$ are obtained by *trial-and-error curve-fitting* both the loading and unloading response at large strains for the stress-strain data at temperatures above ϑ_g. A few

trials give the estimate as

$$h_b = 1.0, \qquad S_r = 2.0 \text{ MPa}, \qquad L_r = 0.05 \text{ MPa K}^{-1},$$
$$\mu^{(3)} = 0.75 \text{ MPa}, \quad I_m^{(3)} = 6.5, \qquad m^{(3)} = 0.18,$$
$$S_g^{(3)} = 5.3 \text{ MPa} \qquad Y = 0.19 \text{ K}^{-1}, \quad h_{3g} = 52.0 \text{ MPa}, \qquad Z = 0.178 \text{ K}^{-1}.$$

2. Large strain response below ϑ_g

Here, we focus on estimating the material parameters: (i) $\mu^{(2)}$ and $I_m^{(2)}$ in the expression (B.28), together with the temperature dependence of $\mu^{(2)}$ given in (5.40); and (ii) S_b^*, together with the temperature dependence of S_b^* given in (4.53) — parameters which account for the stress increase associated with chain-locking at large stretches.

To begin, we neglect the transient response associated with the yield-peak and set $\varphi_0 = S_{a0} = 0$, and correspondingly ignore the evolution equations (B.18) and (B.19) for φ and S_a; we return to determining the material parameters appearing in these coupled evolution equations later. We ignore the evolution of the back-stress, and set it constant, using the temperature-dependent saturation value, such that

$$\sigma_{\text{back}}(\vartheta) = \sigma^*_{\text{back}}(\vartheta)\,\text{sign}(\sigma_{\text{back}}) = \begin{cases} -R(\vartheta_g - \vartheta) & \text{if } \vartheta \leq \vartheta_g, \\ 0 & \text{if } \vartheta > \vartheta_g, \end{cases} \tag{B.50}$$

and determine material parameters associated with the evolution of the back-stress later. Also we select a large value for the material parameter $S_{gl}^{(2)} = 150\,\text{MPa}$ to allow for the assumption $\dot{\epsilon}^{(2)} \approx 0$. The parameter $I_m^{(2)}$ is presumed to be temperature-independent while the temperature dependence of $\mu^{(2)}(\vartheta)$ and $S_b^*(\vartheta)$ is presumed to follow

$$\mu^{(2)}(\vartheta) = \mu_g^{(2)} \exp\Big(- N(\vartheta - \vartheta_g)\Big), \tag{B.51}$$

and

$$S_b^*(\vartheta) = S_{gl} - L_{gl}\Big(\vartheta - (\vartheta_g + 2.5\Delta)\Big) \quad \text{for} \quad \vartheta < \vartheta_g, \tag{B.52}$$

(cf., (5.40) and (4.53)). Using the one-dimensional MATLAB implementation of the model, together with the material parameters estimated to this point, estimates for the desired parameter list

$$(\mu_g^{(2)},\, N,\, I_m^{(2)},\, S_{gl},\, L_{gl})$$

are relatively easily obtained by curve-fitting both the loading and unloading response at large strains for the stress-strain data at the lowest strain rate. A few trials give the estimates as

$$\mu_g^{(2)} = 2.8 \text{ MPa}, \qquad N = 11.1 \times 10^{-3} \text{ K}^{-1}, \qquad I_m^{(2)} = 6.2,$$
$$S_{gl} = 74 \text{ MPa}, \qquad L_{gl} = 1.13 \text{ MPa K}^{-1}.$$

B.3.4 Yield-peak and back-stress evolution

Finally, we calibrate material parameters associated with the yield-peak and the back-stress evolution for temperatures below ϑ_g. Both the back-stress and yield-peak are observed to vanish above the glass transition temperature of the material. This step in the calibration procedure is an iterative process, and requires fitting the transient stress-overshoot in the simple compression stress-strain response together with the creep response, iteratively, several times in order to get a good fit. The steps in the iterative procedure are listed below.

Step 1:

The parameters related to the change of back-stress σ_{back} with strain and temperature are γ and X (cf. (B.22), (4.19)). To begin, we note that for compression

$$D^{p(1)} = -\dot{\epsilon}^{p(1)}, \tag{B.53}$$

and we may then rewrite the evolution equation for A (B.22) as

$$\dot{A} = -(2 + \gamma \ln A)\, A\, \dot{\epsilon}^{p(1)}. \tag{B.54}$$

It follows then that the saturation value of A in compression is

$$A^* = \exp\left(-\frac{2}{\gamma}\right). \tag{B.55}$$

Combining this result with the equation for the back-stress (B.10) gives the saturation value of the back-stress as a function of the material parameters $B(\vartheta)$ and γ

$$\sigma^*_{\text{back}}(\vartheta) = 3\,\frac{B(\vartheta)}{\gamma}. \tag{B.56}$$

Equating the saturation value for the back-stress using (4.19) and (B.41) we obtain

$$3\,\frac{X(\vartheta_g - \vartheta)}{\gamma} = R(\vartheta_g - \vartheta) \quad \Rightarrow \quad X = \frac{R}{3}\gamma, \tag{B.57}$$

and since R has already been determined, we obtain the fixed value for the ratio X/γ.

Step 2:

In this step we estimate a value for γ, and calculate the corresponding value for X from (B.57) to get an estimate for the parameters involved in the evolution of the back-stress. This leaves one with a list of parameters $\{S_{a0}, h_a, b, \varphi_0, g, \varphi^*\}$ in the evolution equations (B.18) and (B.19) for φ and S_a to calibrate the yield-peak.

We assume the material begins in a well-annealed "ground-state," so that we may take the initial value of the order parameter φ and stress-like internal resistance S_a to be zero,

$$\varphi_0 = 0 \quad \text{and} \quad S_{a0} = 0.$$

To find $\{ h_a, b, g, \varphi^* \}$, several simulations are performed using different values of parameters to approximately match the shape of the yield-peak at the various strain rates and temperatures. The parameter h_a controls the initial slope of the yield peak, the parameters b and φ^* control the height of the yield peak, while the parameter g controls the width of the yield-peak.

Step 3:

With the parameters for yield-peak estimated, one returns to refining the values of the material parameters in the back-stress evolution. To get refined estimates for the recovery parameter γ and the temperature sensitivity parameter X for the back-stress modulus B, we first note that γ controls the rate of saturation of the back-stress. As γ increases, the back-stress approaches its saturation value more rapidly.

The parameters γ and B significantly affect the creep response of the material.[3] In order to get more refined estimates for these parameters, we turn to a limited set of available data for room-temperature creep of Zeonex shown in Fig. B-5 as solid lines. The value of γ is chosen such that the creep response is adequately represented, as shown by the dashed lines in Fig. B-5.

Steps 2 and 3 are iteratively repeated until the yield-peaks in the total stress-strain response of the material, as well as the creep response, are satisfactorily calibrated. Once $\{ h_a, b, g, \varphi^* \}$ are determined for each stress-strain curve, we have found that to a good approximation, the parameters h_a and b may be taken as constants; g as temperature dependent, and φ^* as both temperature and strain-rate dependent. The temperature dependence of g was then fit to the functional form (4.51), while the temperature and strain rate dependence of φ^* was fit to the functional form (B.19).

The material parameters for Zeonex that give a reasonable fit for the yield-peak for the range of temperatures and strain rates under consideration, and also adequately reproduce the limited creep data, are

$$\begin{aligned} &h_a = 300, && b = 10.13 \times 10^3 \text{ MPa}, && g_1 = -28, && g_2 = 0.12, \\ &z = 0.0055, && r = 0.24, && s = 0.042, && \gamma = 12, \\ &X = 0.7 \text{ MPa K}^{-1}. \end{aligned}$$

[3]Cyclic tension-compression stress-strain curves at different temperatures may also be used to fit the back-stress parameters, but we have not conducted the necessary extensive set of such experiments.

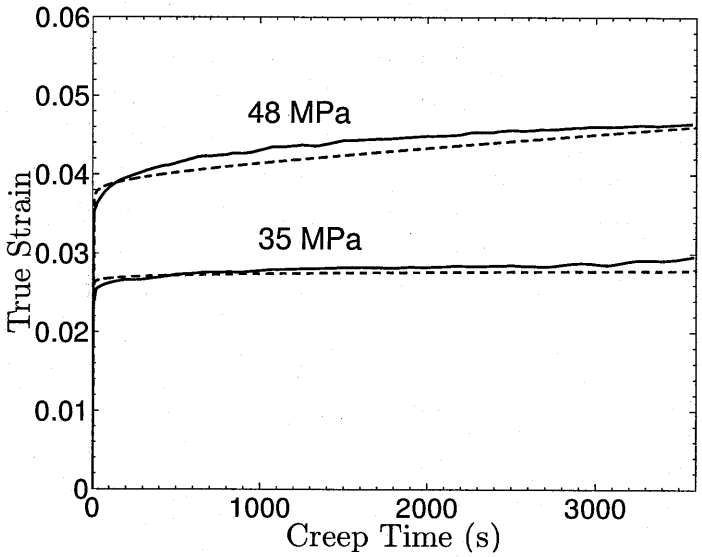

Figure B-5: Creep test results under simple compression at two stress levels below the yield-peak (solid lines), together with one-dimensional MATLAB simulations (dashed lines).

B.4 Parameters for the three-dimensional model

Except for the list of parameters

$$\{\nu_r,\ \nu_0^{(1)},\ \alpha_p,\ V,\ S_{a0},\ h_a,\ b,\ g_1,\ g_2,\ \gamma,\ S_{b0},\ h_b,\ S_{gl}, L_{gl},\ S_r,\ L_r,\ \nu_0^{(2)},\ S_{gl}^{(2)},\ S_r^{(2)},\ \nu_0^{(3)},\ S_g^{(3)},\ h_{3g}\}, \tag{B.58}$$

the values of the one-dimensional material parameters are unchanged when used in the three-dimensional equations. Noting that

$$\tau\nu = \sigma\dot{\epsilon}, \quad \sigma = \sqrt{3}\tau, \quad \dot{\epsilon} = \frac{\nu}{\sqrt{3}} \tag{B.59}$$

the parameters listed in (B.58) may be converted from the one-dimensional compression form to the three-dimensional shear form using

$$\left.\begin{array}{lll}
\nu_r = \sqrt{3}\,\dot{\epsilon}_r\,, & \nu_0^{(1)} = \sqrt{3}\,\dot{\epsilon}_0^{(1)}\,, & \alpha_p^{(\text{shear})} = \frac{1}{\sqrt{3}}\,\alpha_p^{(\text{comp})}\,, \\
V^{(\text{shear})} = \sqrt{3}\,V^{(\text{comp})}\,, & S_{a0}^{(\text{shear})} = \frac{1}{\sqrt{3}}\,S_{a0}^{(\text{comp})}\,, & h_a^{(\text{shear})} = \frac{1}{\sqrt{3}}\,h_a^{(\text{comp})}\,, \\
b^{(\text{shear})} = \frac{1}{\sqrt{3}}\,b^{(\text{comp})}\,, & g_1^{(\text{shear})} = \frac{1}{\sqrt{3}}\,g_1^{(\text{comp})}\,, & g_2^{(\text{shear})} = \frac{1}{\sqrt{3}}\,g_2^{(\text{comp})}\,, \\
\gamma^{(\text{shear})} = \frac{1}{\sqrt{3}}\,\gamma^{(\text{comp})} & S_{b0}^{(\text{shear})} = \frac{1}{\sqrt{3}}\,S_{b0}^{(\text{comp})}\,, & h_b^{(\text{shear})} = \frac{1}{\sqrt{3}}\,h_b^{(\text{comp})}\,, \\
S_{gl}^{(\text{shear})} = \frac{1}{\sqrt{3}}\,S_{gl}^{(\text{comp})}\,, & L_{gl}^{(\text{shear})} = \frac{1}{\sqrt{3}}\,L_{gl}^{(\text{comp})}\,, & S_r^{(\text{shear})} = \frac{1}{\sqrt{3}}\,S_r^{(\text{comp})}\,, \\
L_r^{(\text{shear})} = \frac{1}{\sqrt{3}}\,L_r^{(\text{comp})}\,, & \nu_0^{(2)} = \sqrt{3}\,\dot{\epsilon}_0^{(2)}\,, & S_{gl}^{(2)(\text{shear})} = \frac{1}{\sqrt{3}}S_{gl}^{(2)(\text{comp})}\,, \\
S_r^{(2)(\text{shear})} = \frac{1}{\sqrt{3}}S_r^{(2)(\text{comp})}\,, & \nu_0^{(3)} = \sqrt{3}\,\dot{\epsilon}_0^{(3)}\,, & S_g^{(3)(\text{shear})} = \frac{1}{\sqrt{3}}S_g^{(3)(\text{comp})}\,, \\
h_{3g}^{(\text{shear})} = \frac{1}{3}h_{3g}^{(\text{comp})}\,. & &
\end{array}\right\} \tag{B.60}$$

Further, to convert the temperature dependence parameters for the elastic modulus E to those of the shear modulus G, we use the following standard relations

$$\begin{aligned}
G_{gl} &= \frac{E_{gl}}{2\,(1+\nu_{gl}^{\text{poi}})}\,, \qquad M_{gl} = \frac{M_{Egl}}{2\,(1+\nu_{gl}^{\text{poi}})}\,, \\
G_r &= \frac{E_r}{2\,(1+\nu_r^{\text{poi}})}\,, \qquad M_r = \frac{M_{Er}}{2\,(1+\nu_r^{\text{poi}})}\,.
\end{aligned} \tag{B.61}$$

The material parameters for the three-dimensional theory that were determined by following the procedure described in this Appendix are listed for Zeonex-690R, PC, and PMMA in Table 4.1 of Chapter 4.

Appendix C

Matlab code for the one dimensional model

```
%%% 1D Matlab code
%%% Model for amorphous polymers which spans their glass transition
%%% Micromechanism based model: 3 micromechanisms
%%% Material parameters in this file are for Zeonex-690R
%%% Note this code also uses following two matlab source codes:
%%% (i)  plotxy.m file for creating stress-strain plots
%%% (ii) cycle.m file that returns vectors of [x and time] for cyclic x
%%% Created: July 2009 by Vikas Srivastava
%%%%%%%%%%%%%%%%%%%%%%%%%%%%%%%%%%%%%%%%%%%%%%%%%%%%%%%%%%%%%%%%%%%%%%%%%%%%

function []=amorphous_final()
clc
clear all
close all
%
% Select options for simulation options
%
nreversals = 1;          % number of reversals
nincr      = 2000;       % increments per reversal
peak_flag  = 1;          % yield-peak or not
isothermal = 0;          % adiabatic or isothermnal
thermocycle= 0;          % thermocycle or pure mechanical deformation
CTE_Flag   = 0;          % include coefficient of thermal expansion
%
% Select option for load control of displacement control simulation
%
% control  = 'load';     % stress control
control = 'disp';        % strain control
%
```

```
% Plot options
%
%color_case = 'color';
color_case = 'bw';

fig_format = 'other';
%fig_format = 'paper';

fig_case   = 'rate';    % puts selected temperatures in one figure for each rate
%fig_case   = 'theta';  % puts strain rates in one figure for each temperature

experiments = 1;        % 1 to plot experiments
simulations = 1;        % 1 to run and plot simulations

%               1    2    3    4
edot        = [3e-1 3e-2 3e-3 3e-4]; % 1/s
min_edot    = 1;
max_edot    = 1;

%             1   2   3   4   5   6   7   8
theta0      = [25 70 120 130 140 150 160 180] + 273; % matrix of test temperatures
min_theta   = 1;
max_theta   = 4;

mystrain    = 0;   % for simulations to desired strain, 0: max strain in experiment
maxx        = 1.3; % desired maximum strain for simulation

% This is to override the max y-axis of the plots.
% leave it commented to set it automatically
switch fig_case
    case 'theta'
           maxy_axis = [260; 160; 120; 120; 120; 25; 6; 3]
    case 'rate'
        if (max_theta > 5)
           maxy_axis  = [6; 6; 3; 3];
        else
           maxy_axis = [260; 260; 260; 260];
        end
end

maxx_axis   = 1.6;
minx_axis   = 0;
miny_axis   = 0;

% This is to load experimental stress-strain data
load('Zeonex690R_Comp_Strain_Stress_Time2.mat');
exp{1,:} = {c25_3e1 c70_3e1 c120_3e1 c130_3e1 c140_3e1 c150_3e1 c160_3e1 c180_3e1};
exp{2,:} = {c25_3e2 c70_3e2 c120_3e2 c130_3e2 c140_3e2 c150_3e2 c160_3e2 c180_3e2};
exp{3,:} = {c25_3e3 c70_3e3 c120_3e3 c130_3e3 c140_3e3 c150_3e3 c160_3e3};
exp{4,:} = {c25_3e4 c70_3e4 c120_3e4 c130_3e4 c140_3e4 c150_3e4 c160_3e4};
```

```
x = [0.9  0.9  0.9  0.9  .7  .9  1.32  1.32;
     0.85  0.85  0.85  0.85   0.85  1.32  1.32  1.32;
     1  1  1  1   0.7  1.32  1.32  .2;
     1  1  1  1   1.32  1.32  1.32  .2];

 y = [180 95 64  35  18  10  5.5  2.3;
     120 80 50  30  10  4.9  2.7  0.7;
     170 103 67  28  13  2.8  0.9  0.1;
     146 100 57  15  2.8  0.85  0.43  0.1];

% Set color of plot lines
% Aold = get(gca,'ColorOrder');
switch fig_case
    case 'rate'
        switch color_case
            case 'color'
                A=[ 0 0 0;  0.6 0 0.6;  0 0.2 0.6;  0 0.6 0.8;
                    0 0.6 0.4;  1 0 0; 0.2 0.8 0.2;
                    1 0.6 0;  0.8 0.2 0;  0 0 0];
                A=A(min_theta:max_theta,:);
            case 'bw'
                A=[ 0 0 0; 0 0 0; 0 0 0; 0 0 0; 0 0 0; 0 0 0];
                A=A(1:(max_theta-min_theta+1),:);
        end
        figstart = min_edot-1;
        maxy = zeros(max_edot-figstart,1);
    case 'theta'
        switch color_case
            case 'color'
                A = [ .85 .16 0; 0 .5 0; 0 0 1;0 0 0;
                    .85 .16 0; 0 .5 0; 0 0 1;0 0 0;];
                A=A(min_edot:max_edot,:);
            case 'bw'
                A=[ 0 0 0; ] ;
                set(0,'DefaultAxesLineStyleOrder','-|--|:|---');
        end
        figstart = min_theta-1;
        maxy = zeros(max_theta-figstart,1);
end

set(0,'DefaultAxesColorOrder',A)

if experiments
%
% PLOT EXPERIMENTS
%
    for j=min_theta:max_theta
        for i=min_edot:max_edot
         switch fig_case
              case 'theta'
                  fig_num = j;
```

```
            case 'rate'
                fig_num = i;
        end

        figure(fig_num);
        plotXY(exp{i}{j})
        hold all
        maxy(fig_num-figstart)=max(max(exp{i}{j}(:,2)),maxy(fig_num-figstart));

        if exist('maxy_axis', 'var')
            axis([minx_axis maxx_axis miny_axis maxy_axis(fig_num)])
        else
            axis([minx_axis maxx_axis miny_axis maxy(fig_num-figstart)])
        end
      end
    end

else
end

if simulations
%
% PLOT 1D SIMULATIONS
%
    for j=min_theta:max_theta
      for i=min_edot:max_edot
        switch fig_case
            case 'theta'
                fig_num = j;
            case 'rate'
                fig_num = i;
        end

        if mystrain
                    % simulation to maxx if mystrain is 1
        else
            maxx = max(exp{i}{j}(:,1)); % simulation to max strain in experiment
        end

        matsim{i}{j}=amorphous_general(theta0(j),edot(i),maxx,nreversals,...
        nincr,peak_flag,isothermal,thermocycle,CTE_Flag,control);

        figure(fig_num)
        plotXY(matsim{i}{j},'--')  % plot function for stress vs. strain
        hold all
        maxy(fig_num-figstart)=max(max(matsim{i}{j}(:,2)),maxy(fig_num-figstart));
        if exist('maxy_axis', 'var')
            axis([minx_axis maxx_axis miny_axis maxy_axis(fig_num)])
        else
            axis([minx_axis maxx_axis miny_axis maxy(fig_num-figstart)])
        end
```

```
      end
    end

else
end

% Add plot decorations
for i=(figstart+1):(figstart+length(maxy))
    figure(i)
    switch fig_case
       case 'theta'
         text(0.05,0.95*maxy_axis(fig_num),[num2str(theta0(i)-273),' C'],...
                'FontSize',48,'Interpreter','tex')

         for j=1:(max_edot-min_edot+1)
                legend_text{j} = [num2str(edot(j+min_edot-1)),' 1/s'];
         end
         legend(legend_text,'FontSize',38,'Location','north')
         legend boxoff

       case 'rate'
         filename_eps = ['e_zeonex_' strrep(num2str(edot(i),'%1.0e'),'-00','')...
                '_' num2str(theta0(min_theta)-273) 'c_' ...
                num2str(theta0(max_theta)-273) 'c_' color_case '.eps'];
         filename_png = ['m_zeonex_' strrep(num2str(edot(i),'%1.0e'),'-00','')...
                '_' num2str(theta0(min_theta)-273) 'c_' ...
                num2str(theta0(max_theta)-273) 'c_' color_case '.png'];
         text(0.05,0.95*maxy_axis(fig_num),[num2str(edot(i)),' 1/s'],...
                'FontSize',42,'Interpreter','tex')
         for j=1:(max_theta-min_theta+1)
                k = j+min_theta-1;
                legend_text{j} = [num2str(theta0(k)-273),' C'];
         end
    end

    set(gca,'Position',[0.1300    0.1100    0.7750    0.8150]);
    set(gca,'XMinorTick','On')
    set(gca,'YMinorTick','On')

    switch (fig_format)
    % Formatiing types for the stress-strain plots
        case 'other'
        % general format
           set(gcf,'Units','Inches');
           set(gca,'FontSize',28)
           xlabel('True Strain','FontSize',28)
           ylabel('True Stress, MPa','FontSize',28)
           set( get( gca, 'XLabel' ), 'Interpreter', 'latex' );
           set( get( gca, 'YLabel' ), 'Interpreter', 'latex' );
           set(gcf,'PaperSize',[15 8.25]);
```

```
    set(gcf,'PaperPosition',[1.75 4.25 5 2.5])
    set(gcf,'Position',[2.5 2.0 10 7.5])

case 'paper'
% formatting for manuscripts
  set(gca,'FontSize',42)
  set(gcf,'Units','Inches');
  set(gcf,'Position',[2 0.2 1.5*10. 1.37*7.5])
  xlabel('True Strain','Interpreter','latex','FontSize',48)
  ylabel('True Stress (MPa)','Interpreter','latex','FontSize',48)

  if (simulations==1)
      if(strcmp(fig_case,'theta')==1)
          h = legend(legend_text,'FontSize',40,'Location','North');
          set(h, 'Box', 'off')
      else
          legend_text = 'Experiment';
          h = legend(legend_text,'Location','North');
          set(h, 'Box', 'off')

          if (max_theta > 4)
            if (max_edot < 3)
              text(.5265,5.2,'-- Model','FontSize',42);
            else
              text(.5265,2.6,'-- Model','FontSize',42);
            end
          else
            text(.5265,222,'-- Model','FontSize',42);
          end
      end
  else
  end

  if (strcmp(fig_case,'rate')==1)
      if (max_theta > 4)
            switch (max_edot)
               case 4
                    text(.87*maxx_axis,2.7,'140C','FontSize',38)
                    text(.87*maxx_axis,0.8,'150C','FontSize',38)
                    text(.87*maxx_axis,0.3,'160C','FontSize',38)
                case 3
                    text(.87*maxx_axis,2.5,'150C','FontSize',38)
                    text(.87*maxx_axis,0.8,'160C','FontSize',38)
                case 2
                    text(.87*maxx_axis,4.6,'150C','FontSize',38)
                    text(.87*maxx_axis,2.1,'160C','FontSize',38)
                    text(.87*maxx_axis,0.5,'180C','FontSize',38)
                case 1
                    text(.87*maxx_axis,5.4,'160C','FontSize',38)
                    text(.87*maxx_axis,1.8,'180C','FontSize',38)
            end
```

```
            else
                    switch (max_edot)
                      case 4
                          text(.87*maxx_axis,210,'25C','FontSize',38)
                          text(.87*maxx_axis,150,'70C','FontSize',38)
                          text(.87*maxx_axis,90,'120C','FontSize',38)
                          text(.87*maxx_axis,50,'130C','FontSize',38)
                       case 3
                          text(.87*maxx_axis,230,'25C','FontSize',38)
                          text(.87*maxx_axis,160,'70C','FontSize',38)
                          text(.87*maxx_axis,125,'120C','FontSize',38)
                          text(.87*maxx_axis,70,'130C','FontSize',38)
                       case 2
                          text(.87*maxx_axis,240,'25C','FontSize',38)
                          text(.87*maxx_axis,160,'70C','FontSize',38)
                          text(.87*maxx_axis,125,'120C','FontSize',38)
                          text(.87*maxx_axis,70,'130C','FontSize',38)
                       case 1
                         text(.87*maxx_axis,200,'25C','FontSize',38)
                         text(.87*maxx_axis,150,'70C','FontSize',38)
                         text(.87*maxx_axis,110,'120C','FontSize',38)
                         text(.87*maxx_axis,80,'130C','FontSize',38)
                    end
            end

        end
    end

end

% Reset color order
Aold=[         0         0    1.0000;
         0    0.5000         0;
    1.0000         0         0;
         0    0.7500    0.7500;
    0.7500         0    0.7500;
    0.7500    0.7500         0;
    0.2500    0.2500    0.2500];
set(0,'DefaultAxesColorOrder',Aold);
set(0,'DefaultAxesLineStyleOrder','-');

%%%%%%%%%%%%%%%%%%%%%%%%%%%%%%%%%%%%%%%%%%%%%%%%%%%%%%%%%%%%%%%%%%%%%%%%%%%%%%%
function [stress_strain] = amorphous_general(theta0,edot,maxx,nreversals,...
    nincr,peak_flag,isothermal,thermocycle,CTE_flag,control)

switch (control)
    case 'load'
    % For stress control analysis

      if (thermocycle==1)
          sigmamax  = -0.43e6;  % Pa
```

```
        loadtime  = 500;       % s
        sigmadot  = abs(sigmamax/loadtime);   % Pa /s
        theta0    = 155 + 273; % K
        thetaCold = 50 + 273;  % K
        thetaHot  = 160 + 273; % K
        thetaDotC = 1;         % K/s
        thetaDotH = 1;         % K/s
        Nstep1    = 2000;
        Nstep2    = 1000;
        Nstep3    = 1000;
        reheating = 0;

    [sigma,t,theta] = ThermoMechCycle_lc(sigmamax,sigmadot,theta0,thetaCold,...
                thetaHot,thetaDotC,thetaDotH,Nstep1,Nstep2,Nstep3,reheating);
    else
        sigmadot = 2.4e6;          % stress rate
        sigmamax = -48e6;          % max stress
        sigmamin = 0;
        tcreep   = 3600;

    [sigma,t]= creep([sigmamax],[sigmadot],[tcreep],[nincr],[nincr]);
    end

    N        = length(sigma);
    e        = zeros(N-1,1);   % strain history

case 'disp'
% For strain control analysis

      if (thermocycle==1)
        emax      = -0.5;
        edot      = 3e-3;
        theta0    = 160 + 273; % K
        thetaCold = 50 + 273;  % K
        thetaHot  = 160 + 273; % K
        thetaDotC = 1;         % K/s
        thetaDotH = 1;         % K/s
        Nstep1    = 2000;
        Nstep2    = 1000;
        Nstep3    = 1000;
        reheating = 0;

      [e,t,theta] = ThermoMechCycle(emax,edot,theta0,thetaCold,thetaHot,...
                    thetaDotC,thetaDotH,Nstep1,Nstep2,Nstep3,reheating);
      else
        emax     = -maxx;          % max strain
        emin     = 0;              % min strain
        [e,t]    = cycle(emax,emin,edot,nreversals,nincr);
      end
      N        = length(e);      % maximum number of strain points
      sigma    = zeros(N-1,1);   % stress history set up
```

```
end

%%%%%%%%%%%%%%%%%%%%%%%%%%%%%%%%%%%%%%%%%%%%%%%%%%%%%%%%%%%%%%%%%%%%%%%%
%%% 1D MODEL FOR AMORPHOUS POLYMERS STARTS HERE
%%%%%%%%%%%%%%%%%%%%%%%%%%%%%%%%%%%%%%%%%%%%%%%%%%%%%%%%%%%%%%%%%%%%%%%%
% Branch 1 has linear elastic behavior with a dashpot that provides yield
% stresses below Tg as well above Tg. Dashpot slips easily above Tg.
%
% Branch 2 has non-linear elastic behavior with a dashpot which is rigid
% below Tg but slips easily above Tg to account for network slippage.
%
% Branch 3 has non-linear elastic behavior with a dashpot which is rigid
% below Tg but slips above Tg.
%
% Static recovery is neglected.
%%%%%%%%%%%%%%%%%%%%%%%%%%%%%%%%%%%%%%%%%%%%%%%%%%%%%%%%%%%%%%%%%%%%%%%%
%
% Material properties
%
alpha      = 3;            % number of micro mechanisms
kB         = 1.3807e-23;   % Joules/Kelvin

% Reference rate and reference glass transition temperature
edot_r     = 3e-4;         % reference strain rate
Tg_r       = 273 + 131;    % Tg in K for 3e-4 /s strain rate

% Rate dependence of Glass Transition Temperature
n          = 2.5;          % K
if (edot<edot_r)
    Tg = Tg_r;
else
    Tg = Tg_r+ n*log(edot/edot_r);
end

% Young's Modulus parameters for branch 1
E_gl       = 1.35e9;       % glassy value at Tg, Pa
E_r        = 10e6;         % rubbery value, Pa
M_gl       = 0.45e6;       % slope in glassy region, Pa/K
M_r        = 0.1e6;        % slope in rubbery region, Pa/K
Del        = 10/5;         % width of transition, K

% Back Stress for branch 1
gamma      = 12;           % recovery term
r1         = 1.72e5;
X          = r1*gamma/3;   % Pa/K

% Pressure sensitivity of branch 1
alpha_p    = 0.2;

% Flow parameters for branch 1
edot1_0    = 1.0e13;       % pre-exponential factor, /s
```

```
m1          = 0.16;
Q1_gl       = 1.56e-019;    % glassy activation energy, Joules
Q1_r        = 1e-20;        % rubbery activation energy, Joules
V1          = 9.8e-28;      % glassy activation volume, m^3
zeta_gl     = 0.135;
dd          = 0.015;

% Stress like internal resistances for branch 1
Sa_0        = 0;            % Pa
Sb_0        = 0;            % Pa
ha          = 300;
hb          = 1;

% Order parameter for branch 1
phi0        = 0;            % initial value of order parameter

% Parameters for saturation value of order parameter for branch 1
z         = 0.0055;
r           = 0.24;
s           = 0.042;
b           = 10.13e9;      % Pa
g1          = -28;
g2          = 0.12;         % /K

% Parameters for saturation value of Sb for branch 1
Sbstar_gl   = 74.0e6;       % Pa
L_gl        = 1.13e6;       % Pa/K
Sbstar_r    = 2.0e6;        % Pa
L_r         = 0.05e6;       % Pa/K

% Elastic parameters for the Gent Spring in branch 2
mu0_2       = 2.8e6;        % Pa
NN          = 11.1e-3;      % 1/K
I_m2        = 6.2;

% Flow parameters for branch 2
edot2_0     = 3e-4;         % pre-exponential factor, /s
S2_gl       = 150e6;        % Pa
S2_r        = 0.02e6;       % Pa
m2          = 0.18;

% Elastic parameters for the Gent Spring in branch 3
mu3         = 0.75e6;
I_m3        = 6.5;

% Flow parameters for branch 3
edot3_0 = 3e-4;             % /s
m3 = 0.18;
S3_g = 5.3e6;               % Pa
hS3_g = 52e6;               % Pa
YY = .19;                   % /K
```

```
ZZ = 0.178;                % /K

% Specific heat
c1         = 2120;         % J/(kg-C)
c2         = 8;            % J/(kg-C^2)

% Fraction of the total heat dissipated that gives temperature rise
omega      = 0.8;

% Density
rho        = 1010;         % kg/m^3

% coefficient of thermal expansion
alpha_gl   = 7e-5;         % /K
alpha_r    = 12e-5;        % /K

%%%%%%%%%%%%%%%%%%%%%%%%%%%%%%%%%%%%%%%%%%%%%%%%%%%%%%%%%%%%%%%%%%%%%%%%%%%
%
% Initialization of variables
%
Ue         = zeros(N,alpha); % elastic stretch history. N rows and alpha columns
Ue(1,:)    = 1;              % Set the first element of the elastic stretch to 1
Up         = zeros(N,alpha); % plastic stretch history
Up(1,:)    = 1;              % Set the first element of the plastic stretch to 1

A          = zeros(N,1);     % stretch-like internal variable history
A(1)       = 1;              % Set the first element of A to unity

T          = zeros(N,alpha); % T history, matrix of N rows and alpha columns
Teff       = zeros(1,alpha); % Teff history, matrix of N rows and alpha columns
Tback      = zeros(N,alpha); % Teff history, matrix of N rows and alpha columns
edot_p     = zeros(N,alpha);

Dp         = zeros(1,alpha);
sigma_bar= zeros(N,alpha);

phi        = zeros(N,1);
phi(1)     = phi0;

Sa(1)      = Sa_0;
Sb(1)      = Sb_0;

gamma_p    = zeros(1,alpha);

if (thermocycle==1)
else
    theta      = zeros(N,1);
    theta(1)   = theta0;
end
%%%%%%%%%%%%%%%%%%%%%%%%%%%%%%%%%%%%%%%%%%%%%%%%%%%%%%%%%%%%%%%%%%%%%%%%%%%
%
```

```
%  Begin computation
%
%%%%%%%%%%%%%%%%%%%%%%%%%%%%%%%%%%%%%%%%%%%%%%%%%%%%%%%%%%%%%%%%%%%%%%%%%%%%%%%
for n=1:N-1

%%%%%%%%%%%%%%%%%%%%%%%%%%%%%%%%%%%%%%%%%%%%%%%%%%%%%%%%%%%%%%%%%%%%%%%%%%%%%%%
% Temperature dependence of material parameters
%%%%%%%%%%%%%%%%%%%%%%%%%%%%%%%%%%%%%%%%%%%%%%%%%%%%%%%%%%%%%%%%%%%%%%%%%%%%%%%
    if theta(n)≤Tg
      Me       = M_gl;
      B        = -X*(theta(n)- Tg);
      L        = L_gl;
      CTE_delTheta(n) = alpha_gl*(theta(n)-298);
    else
      Me       = M_r;
      B        = 0;
      L        = L_r;
      CTE_delTheta(n) = alpha_gl*(theta(n)-298) + (alpha_r-alpha_gl)*(theta(n)-Tg);
    end

    if (CTE_flag==1)
                                % if CTE_flag=1 then include CTE effect
    else
        CTE_delTheta(n) = 0;    % No CTE effect
    end

    Eyoung = 0.5*(E_gl+E_r)-0.5*(E_gl-E_r)*tanh((theta(n)-Tg)/Del)-Me*(theta(n)-Tg);
    Q1     = 0.5*(Q1_gl + Q1_r) - 0.5*(Q1_gl - Q1_r)*tanh((theta(n)-Tg)/Del);
    zeta   = zeta_gl+ 0.5*dd*(theta(n) - Tg + sqrt((theta(n)-Tg)^2));

    g      = g1 + g2*theta(n);
    Sb_star = 0.5*(Sbstar_g +Sbstar_r)-0.5*(Sbstar_gl-Sbstar_r)...
              *tanh((theta(n)-Tg)/Del) - L*(theta(n)-Tg);

    mu2    = mu0_2*exp(-NN*(theta(n)-Tg));
    S2     = 0.5*(S2_gl + S2_r) - 0.5*(S2_gl - S2_r)*tanh((theta(n)-Tg)/Del);

    S3_0   = S3_g*exp(-YY*(theta(n)-Tg));
    hS3    = hS3_g*exp(-ZZ*(theta(n)-Tg));
    S3(1)  = S3_0;

    Cp     = c1 + c2*(theta(n)-Tg);
%%%%%%%%%%%%%%%%%%%%%%%%%%%%%%%%%%%%%%%%%%%%%%%%%%%%%%%%%%%%%%%%%%%%%%%%%%%%%%%

    delt   = t(n+1) - t(n);
    U      = exp(e(n));
    Ue(n,:) = U./Up(n,:);
%
% Calculate stress in branch 3
%
    I1_3           = Ue(n,3)^2 + 2/Ue(n,3);
```

```
    eff_stretch3(n) = (I1_3 - 3)/I_m3;

    T(n,3)          = (mu3/(1-eff_stretch3(n)))*(Ue(n,3)^2 - 1/Ue(n,3));
    Teff(3)         = T(n,3);
    sigma_bar(3)    = abs(Teff(3));
%
% Calculate stress in branch 2
%
    I1_2            = Ue(n,2)^2 + 2/Ue(n,2);
    eff_stretch2(n) = (I1_2 - 3)/I_m2;

    % assume chain breakage at eff_stretch of 0.85 at room temperature
    if (eff_stretch2(n) < 0.85)
    else
        eff_stretch2(n) = 0.85;
    end

    T(n,2)          = (mu2/(1-eff_stretch2(n)))*(Ue(n,2)^2 - 1/Ue(n,2));
    Teff(2)         = T(n,2);
    sigma_bar(2)    = abs(Teff(2)) ;
%
% Calculate stress in branch 1
%
    Tback(n,1)      = 3/2*B*log(A(n,1));
    Teff(1)         = T(n,1) - Tback(n,1);
    p_bar(1)        = -(1/3)*T(n,1);

    sigma_bar(1)    = abs(Teff(1)) - alpha_p*p_bar(1) - Sa(n) - Sb(n);
%
% Calculate the plastic flow in branch 1
%
    estar1         = edot1_0 *exp(-1/zeta)*exp(-Q1/(kB*theta(n)));

    if (sigma_bar(1) > 0)
     edot_p(n+1,1)= estar1*( sinh(sigma_bar(1)*V1/(2*kB*theta(n))) )^(1/m1);
    else
     edot_p(n+1,1)= 0;
    end
%
% Calculate the plastic flow in branch 2
%
    if (sigma_bar(2) > 0)
       edot_p(n+1,2) = edot2_0 *(sigma_bar(2)/S2)^(1/m2);
    else
       edot_p(n+1,2) = 0;
    end
%
% Calculate the flow in branch 3
%
    if (sigma_bar(3) > 0)
        edot_p(n+1,3) = edot3_0 *(sigma_bar(3)/S3(n))^(1/m3);
```

```
    else
        edot_p(n+1,3) = 0;
    end
%
% Calculate plastic stretching
%
    Dp  = (sign(Teff) .* edot_p(n+1,:));
%
% Update Up
%
    Up(n+1,:) = Up(n,:) + delt*Dp .* Up(n,:);
%
% Update total plastic strain
%
    gamma_p(n+1,:) = gamma_p(n,:) + delt*edot_p(n+1,:);
%
% Update stress/strain
%
    switch (control)
        case 'load'
            T(n+1,1)    = sigma(n) - T(n,2)- T(n,3);
            e_e1        = T(n+1,1)/Eyoung + CTE_delTheta(n);
            Ue(n+1,1)   = exp(e_e1);
            U           = Ue(n+1,1)*Up(n+1,1);
            e(n+1)      = log(U);
        case 'disp'
            U           = exp(e(n+1));
            Ue(n+1,:)   = U./Up(n+1,:);
            e_e(1)      = log(Ue(n+1,1));
            T(n+1,1)    = Eyoung*e_e(1) - Eyoung*CTE_delTheta(n);
            sigma(n+1)  = T(n+1,1) + T(n,2) + T(n,3);
    end

%%%%%%%%%%%%%%%%%%%%%%%%%%%%%%%%%%%%%%%%%%%%%%%%%%%%%%%%%%%%%%%%%%%%%%%
% Update internal variables
%%%%%%%%%%%%%%%%%%%%%%%%%%%%%%%%%%%%%%%%%%%%%%%%%%%%%%%%%%%%%%%%%%%%%%%
% update A
%
    Adot    = 2*Dp(1)*A(n,1) - gamma*A(n,1)*log(A(n,1))*edot_p(n+1,1);
    A(n+1) = A(n,1) + delt*Adot;
%
% evolution of order parameter
%
    if theta(n)> Tg
        phi_star(n) = 0;
    else
      if edot_p(n+1,1)≤0
           phi_star(n) = phi(n);
      else
           phi_star(n) = z*((1-theta(n)/Tg)^r)*(edot_p(n+1,1)/edot_r)^s;
      end
```

```
    end

    phi_dot  = g * (phi_star(n) - phi(n)) * edot_p(n+1,1);
    phi(n+1) = phi(n) + phi_dot * delt;
%
% evolution of Sa and Sb for branch 1
%
    Sa_star(n+1) = Sa_0 + b*(phi_star(n) - phi(n+1));

    if (peak_flag==1)
         Sadot = ha *(Sa_star(n+1) - Sa(n)) * edot_p(n+1,1);
    else
         Sadot = 0;
    end

    trace_C =  U^2 + 2/U;
    lambda(n+1) = sqrt(trace_C/3);

    DynamicEvolution = hb*(lambda(n+1)-1)*(Sb_star - Sb(n))* edot_p(n+1,1);
    StaticEvolution = 0;
    Sbdot   =  DynamicEvolution + StaticEvolution;

    Sa(n+1) = Sa(n) + Sadot * delt;
    Sb(n+1) = Sb(n) + Sbdot * delt;
%
% evolution of S3 for branch 3
%
    S3dot = hS3*(lambda(n+1)-1)* edot_p(n+1,3);
    S3(n+1) = S3(n) + S3dot * delt;

%%%%%%%%%%%%%%%%%%%%%%%%%%%%%%%%%%%%%%%%%%%%%%%%%%%%%%%%%%%%%%%%%%%%%%%
% Calculate temperature rise due to dissipation
%%%%%%%%%%%%%%%%%%%%%%%%%%%%%%%%%%%%%%%%%%%%%%%%%%%%%%%%%%%%%%%%%%%%%%%
    if (thermocycle==1)
        % do nothing temperature comes from the temprature profile
    else
        %
        % Calculate temperature rise for adiabatic case
        %
        if isothermal
           theta_dot = 0;
        else
           arg1(n) = edot_p(n,1)*(abs(Teff(1)));
           arg2(n) = edot_p(n,2)*(abs(Teff(2)));
           arg3(n) = edot_p(n,3)*(abs(Teff(3)));
           arg4(n) = edot_p(n,1)*(0.5*B*gamma*(log(A(n,1)))^2);

           if (edot > 0.09)   % only highest rate is treated as adiabatic
             if ((theta(n) >410)&&(theta(n)<430))
               theta_dot = 0;
             else
```

```
            theta_dot = omega*(arg1(n)+arg2(n)+arg3(n)+arg4(n))/(Cp*rho);
          end
        elseif (edot > 0.009)
          theta_dot = 0.25*omega*(arg1(n)+arg2(n)+arg3(n)+arg4(n))/(Cp*rho);
        else
          theta_dot=0;
        end
      end
     theta(n+1) = theta(n) + theta_dot * delt;
  end

end
%%%%%%%%%%%%%%%%%%%%%%%%%%%%%%%%%%%%%%%%%%%%%%%%%%%%%%%%%%%%%%%%%%%%%%%%%%%%
%  End computation
%%%%%%%%%%%%%%%%%%%%%%%%%%%%%%%%%%%%%%%%%%%%%%%%%%%%%%%%%%%%%%%%%%%%%%%%%%%%

stress_strain=[-e -sigma/1e6 t];
hold all

return
```

Appendix D

Micro-hot-embossing experimental set-up

D.1 Introduction

We have designed and fabricated an experimental set-up to carry out micro-hot-embossing experiments. In this appendix we present details of our micro-hot-embossing set-up. The schematic Fig. D-1 of micro-hot-embossing assembly fits with our servo-hydraulic Instron testing machine and a high-temperature furnace as shown in Fig. D-2. Amorphous polymers are poor thermal conductors; accordingly, in order to heat the polymer substrate uniformly, we also used heated steel platens in addition to the furnace. During hot-embossing, the bottom platen and collar used in the micro-hot-embossing assembly were heated with cartridge heaters, and thermocouples inserted into the platen and the collar were used to control the temperature. To maintain a good alignment between the embossing tool and the polymer substrate during the embossing, the embossing tool was attached to a cylindrical base with a spherical backing at the upper end. A tight clearance was maintained between the cylindrical base and the heated tool collar. For micro-hot-embossing, the polymer substrate was placed between a polished surface at the bottom and a metallic glass embossing tool on the top. The area near the periphery of the polymer substrate was vertically clamped by the heated collar.

D.2 Component drawings

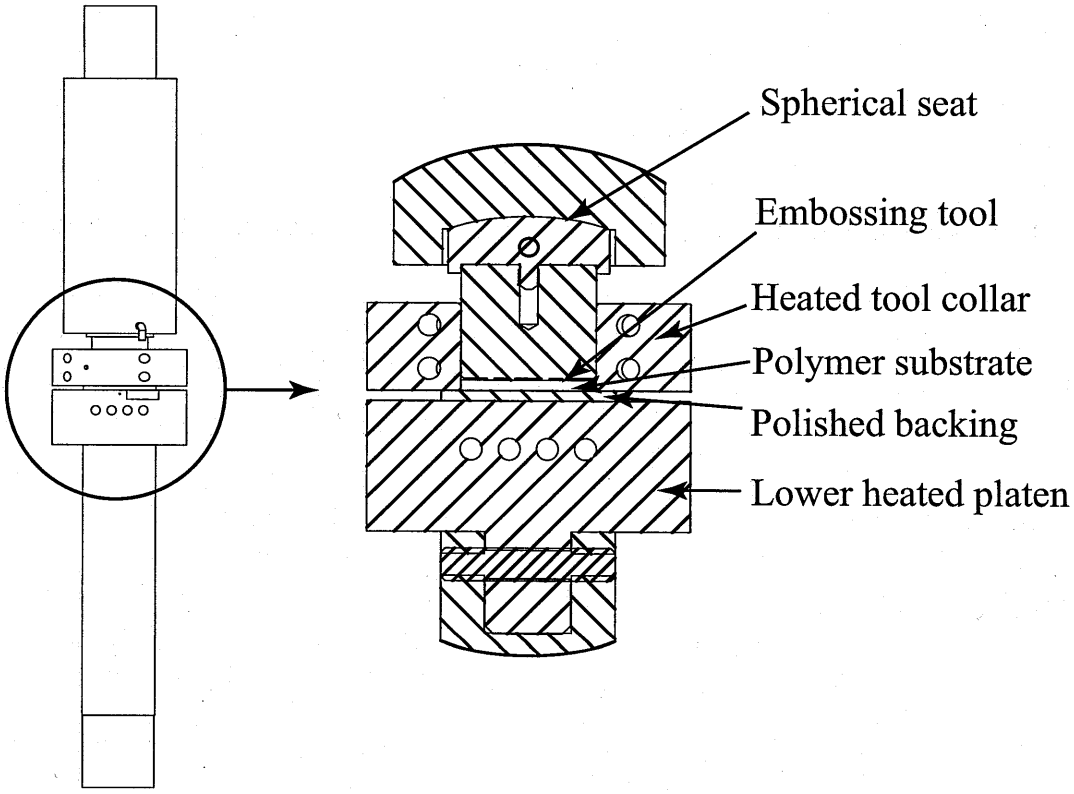

Figure D-1: Schematic of the micro-hot-embossing test set-up.

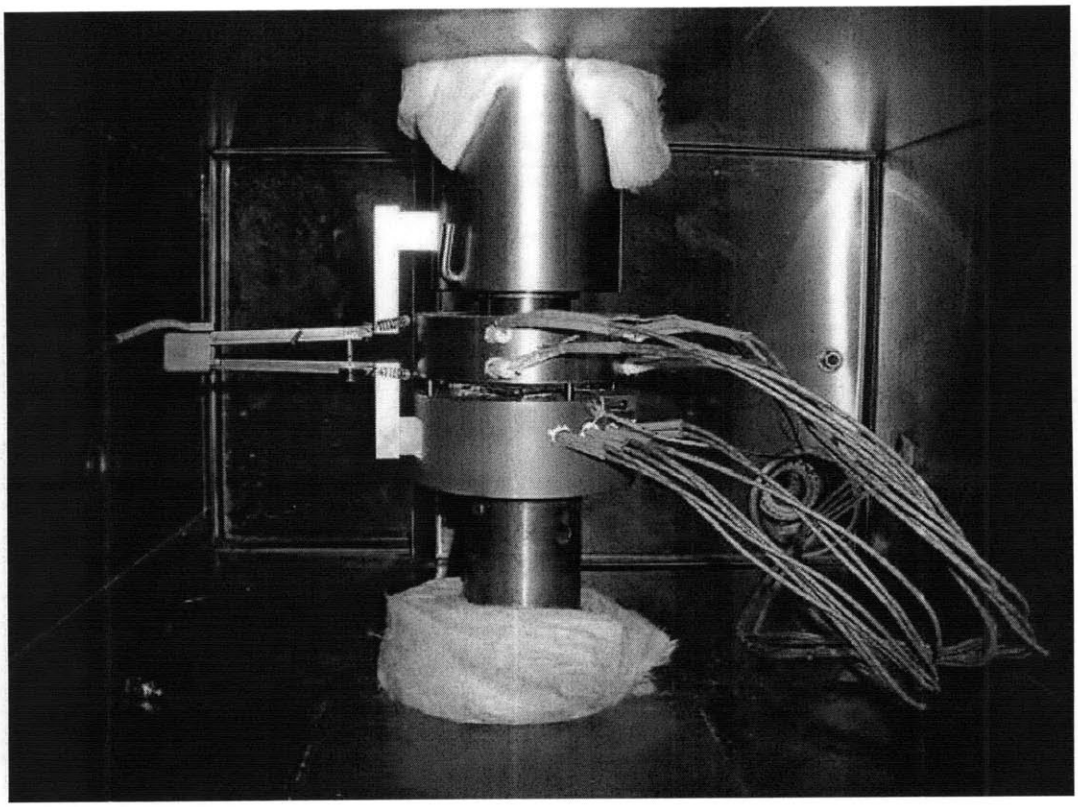

Figure D-2: Image of the experimental set-up used for micro-hot-embossing.

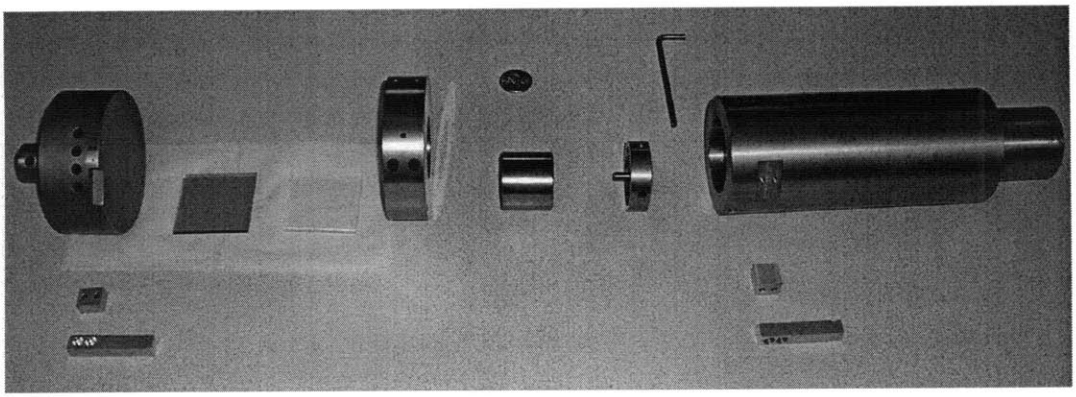

Figure D-3: Image of various micro-hot-embossing set-up components.

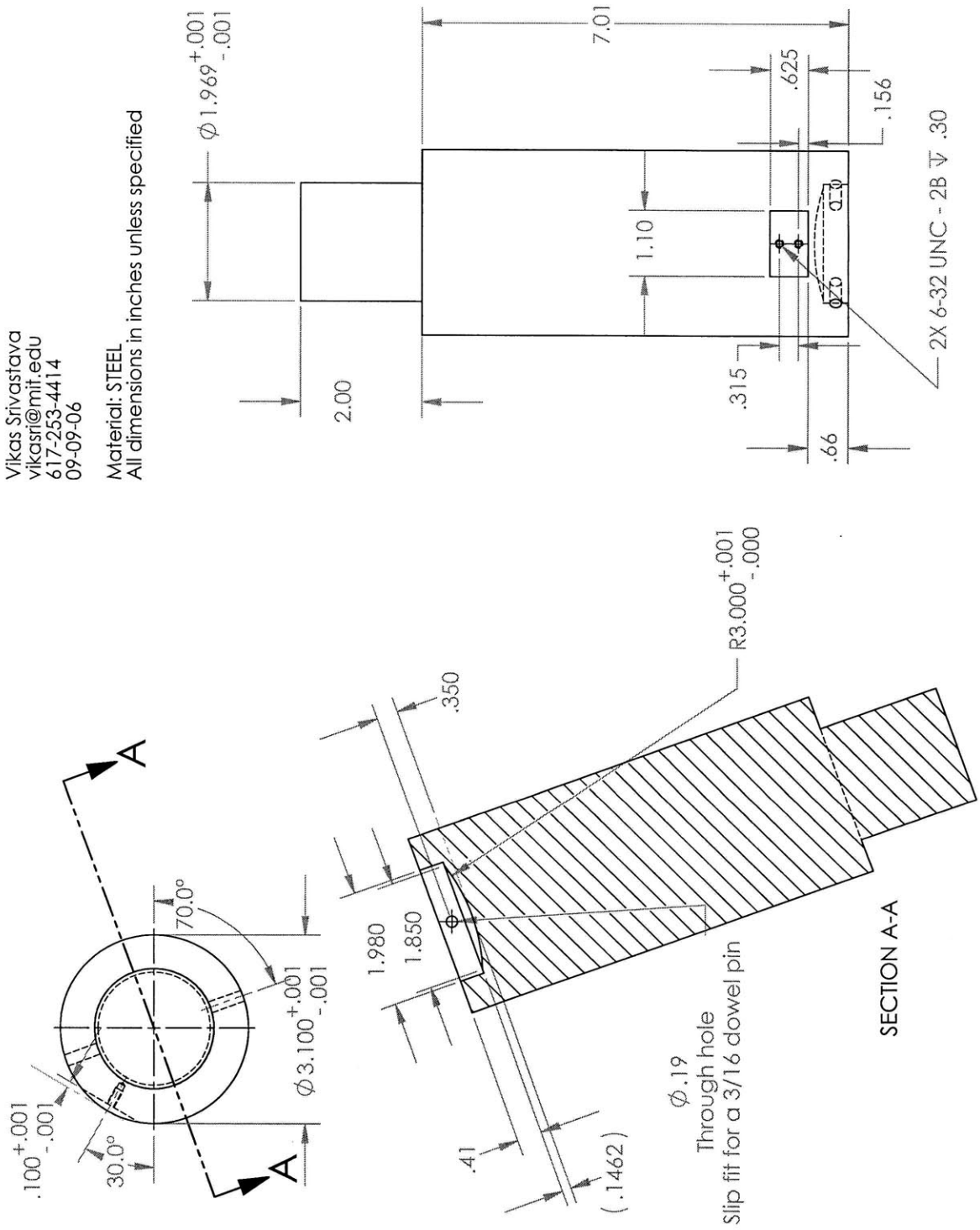

Figure D-4: Top connector.

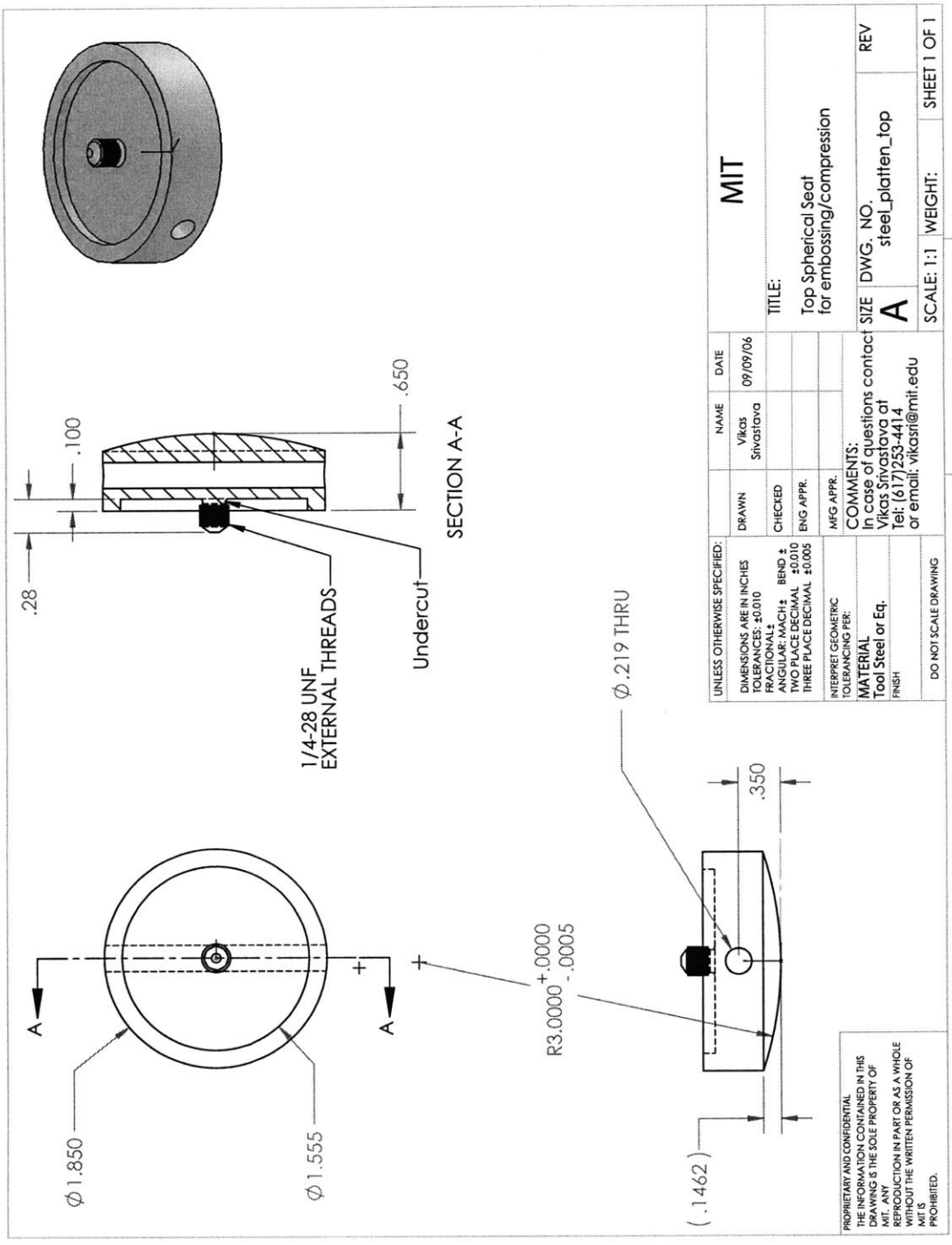

Figure D-5: Spherical seat for the embossing tool base.

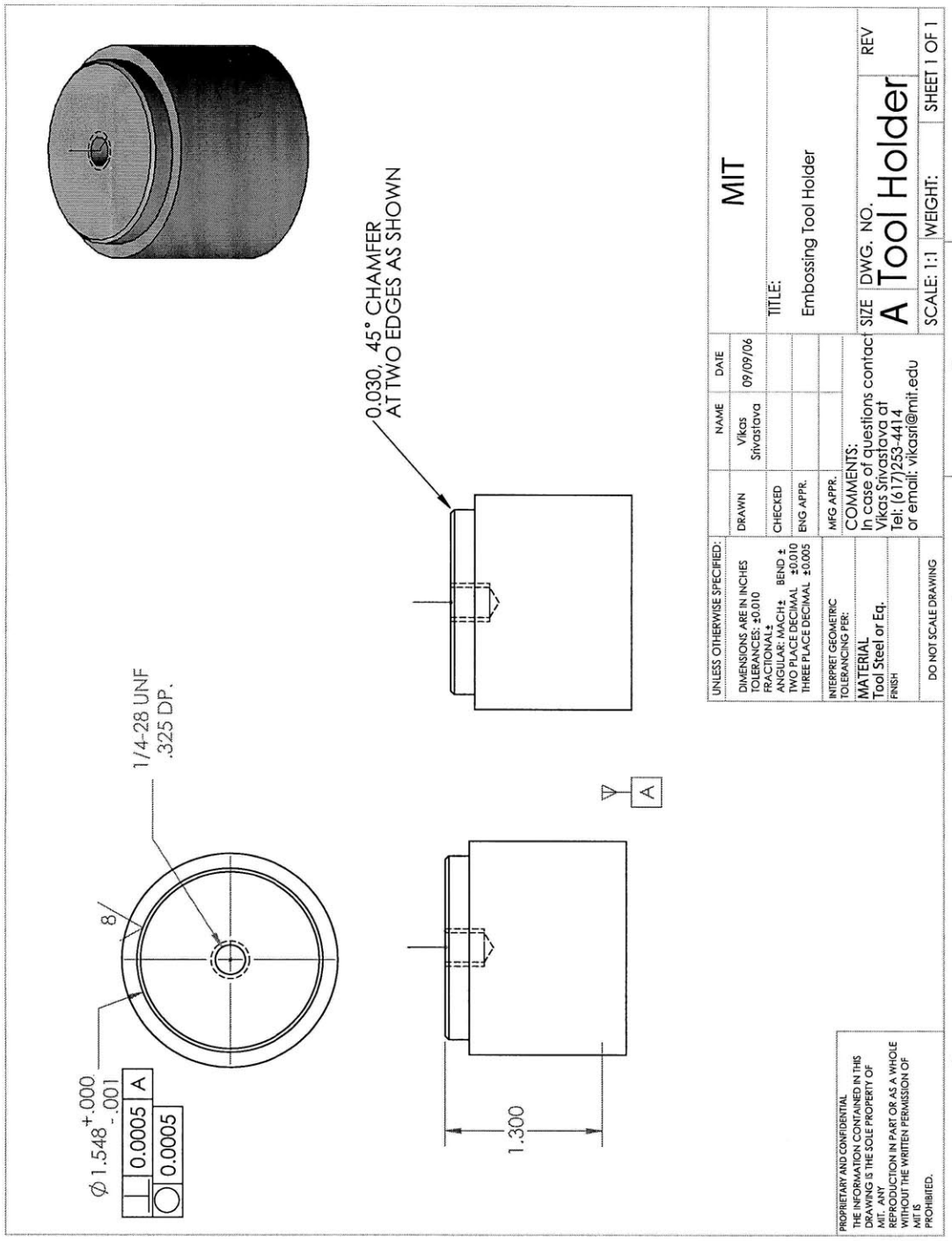

Figure D-6: Cylindrical embossing tool base.

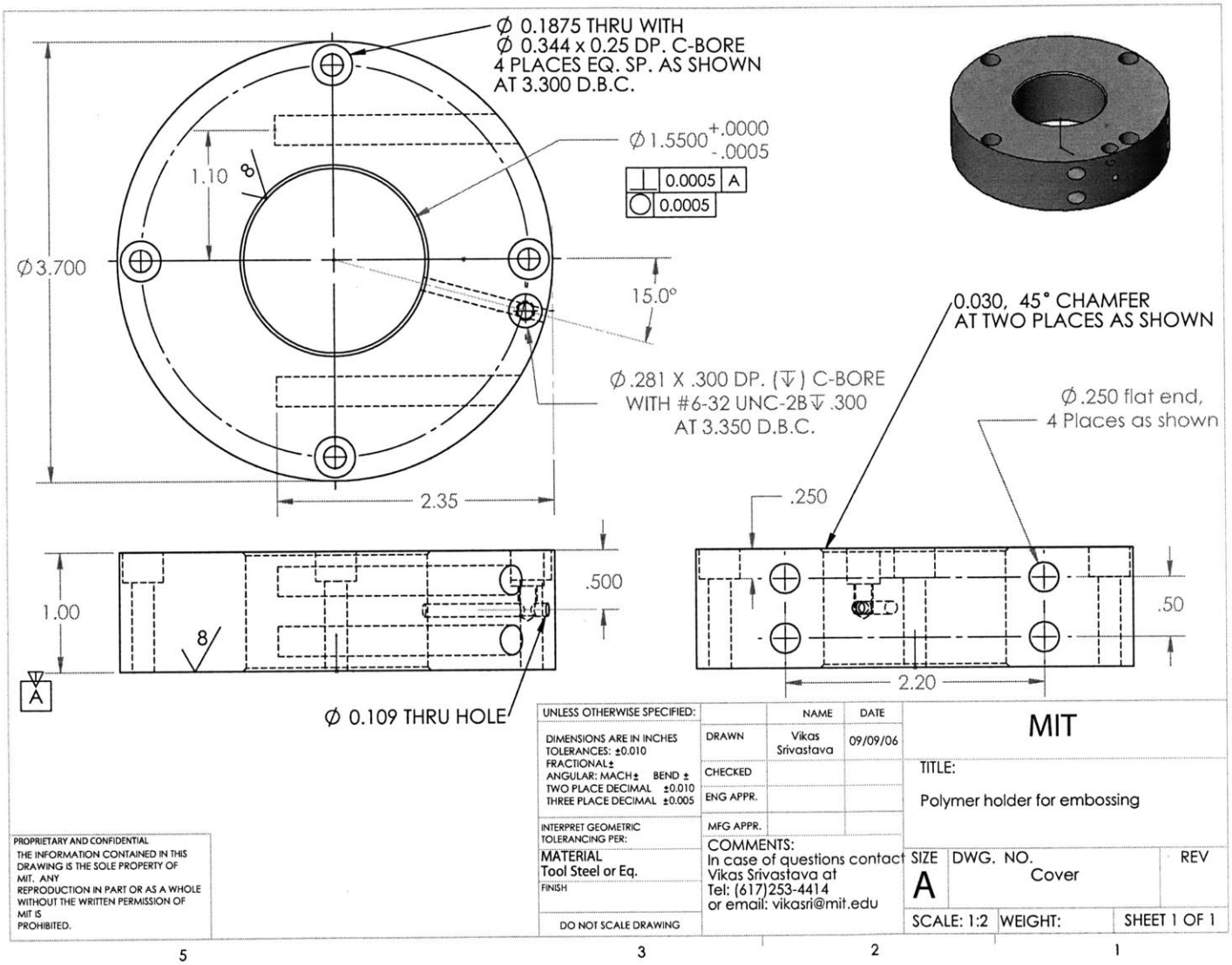

Figure D-7: Heated collar.

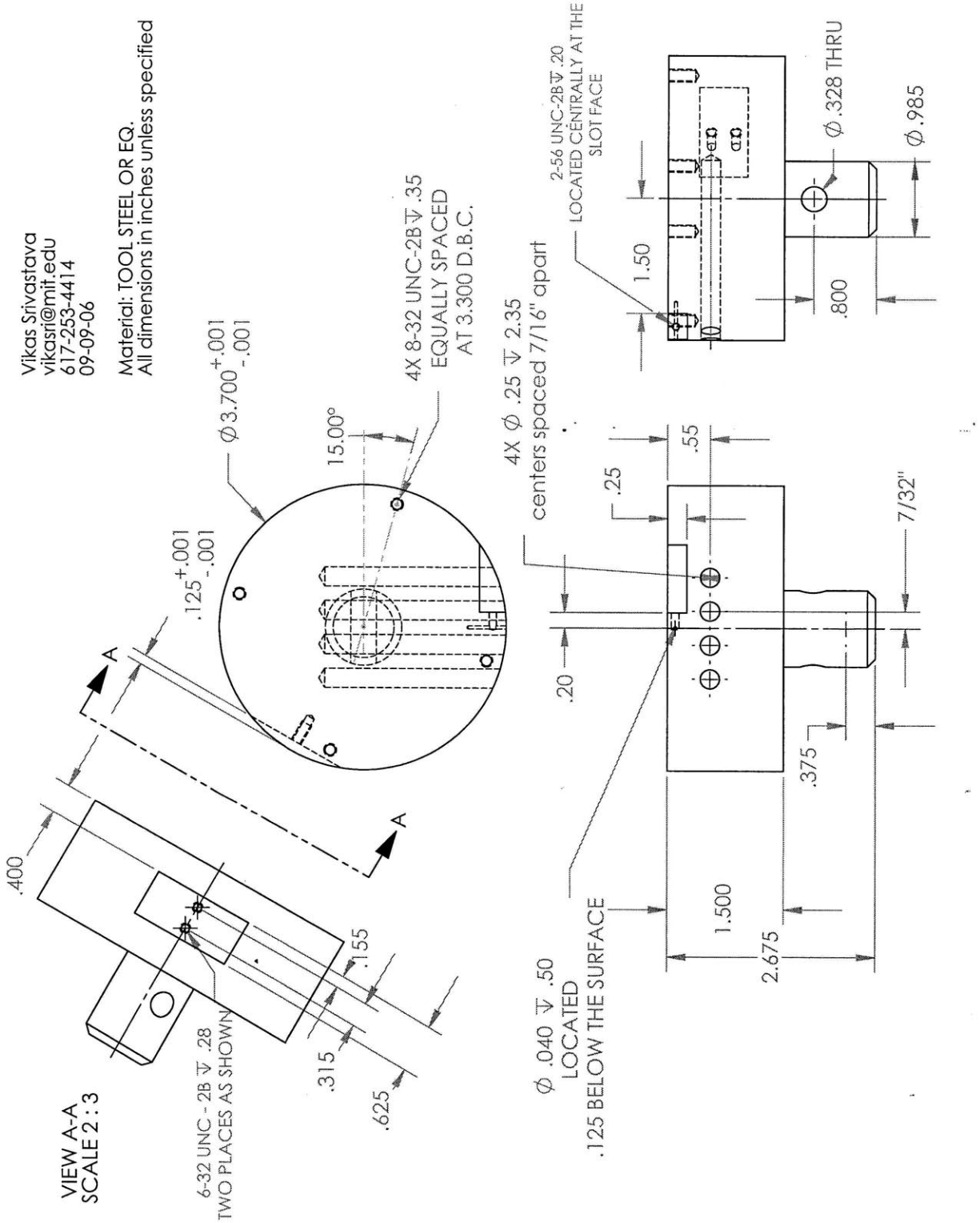

Figure D-8: Bottom steel platen.

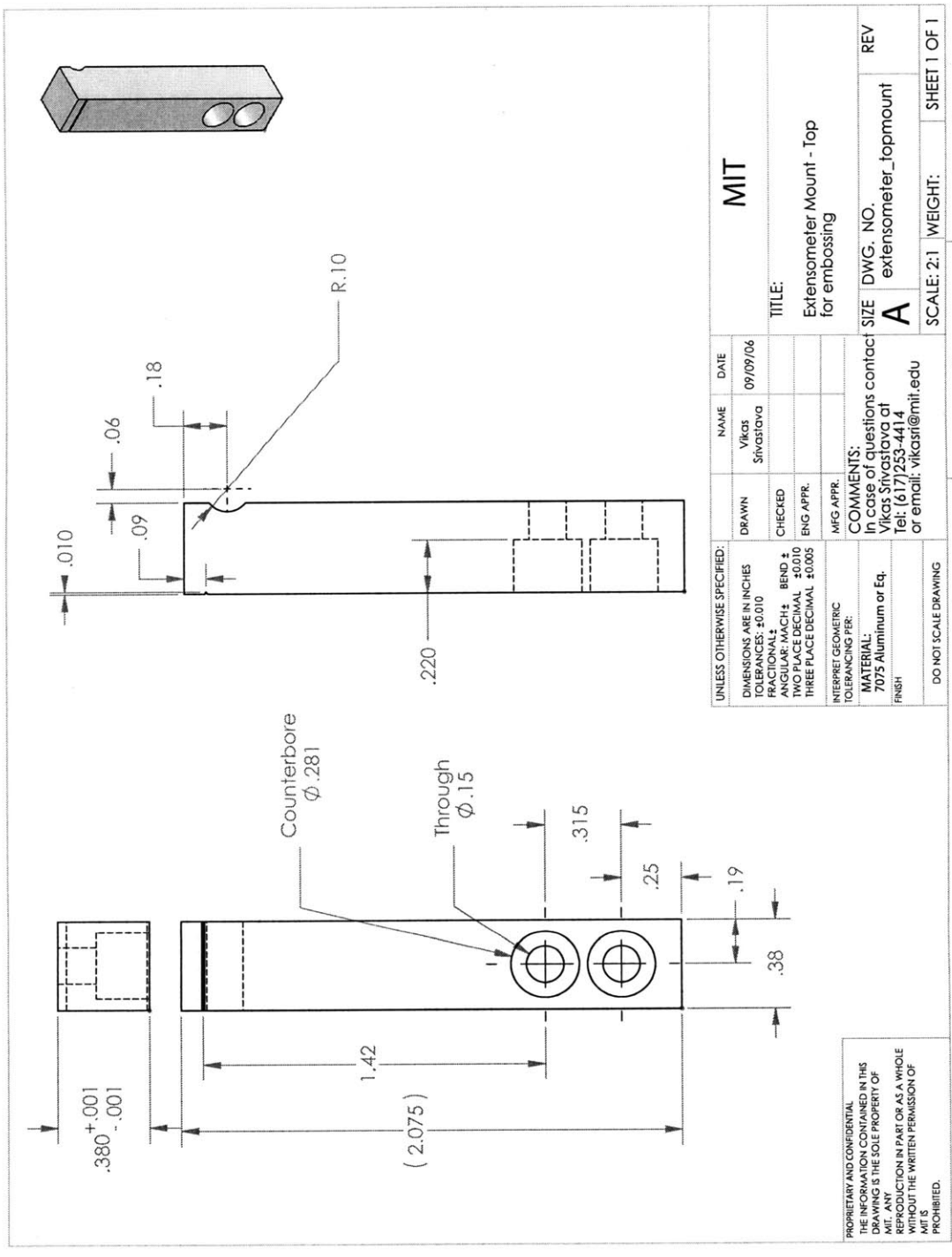

Figure D-9: Top extensometer mount.

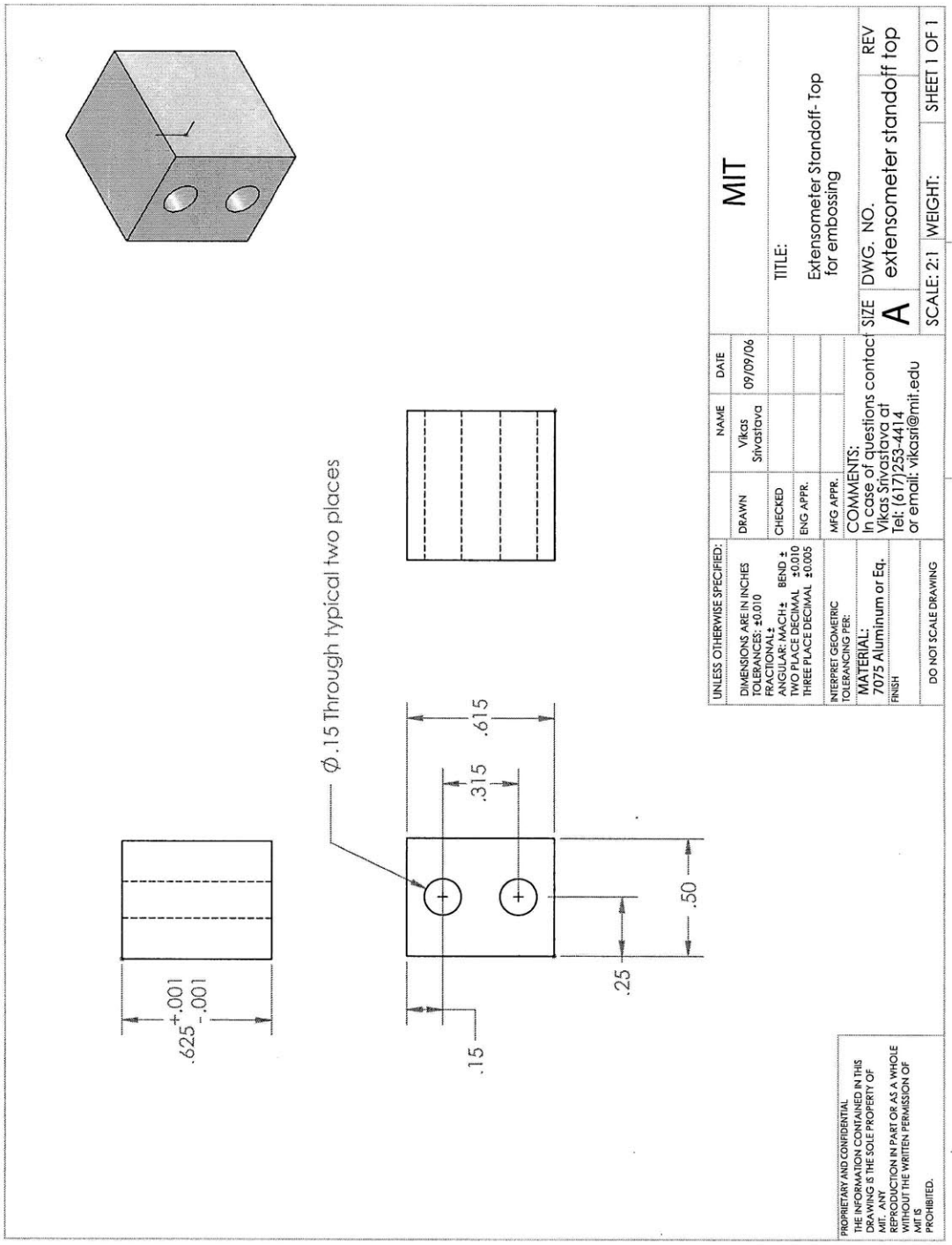

Figure D-10: Standoff for the top extensometer mount.

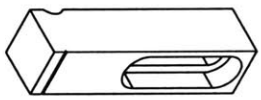

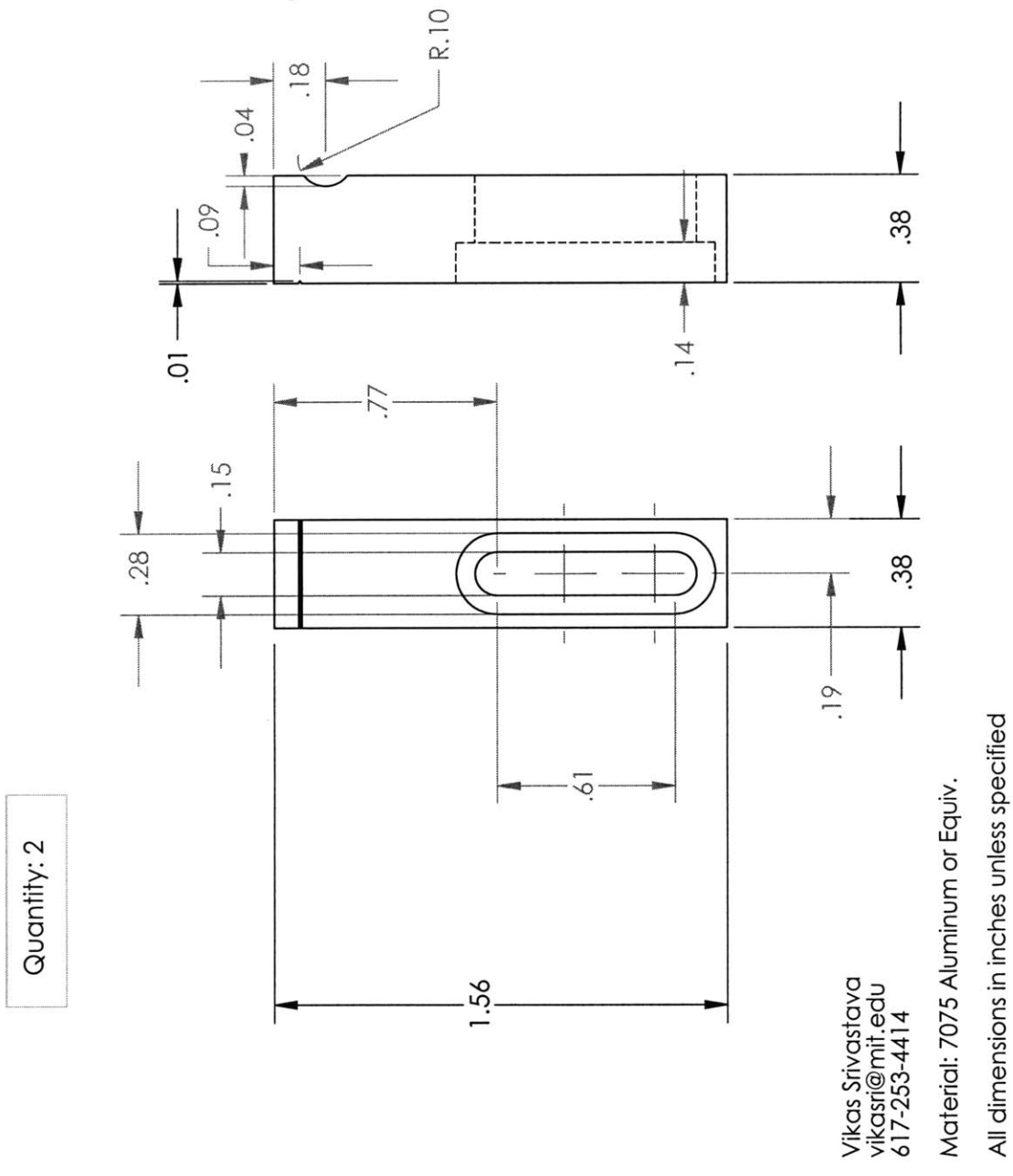

Figure D-11: Bottom extensometer mount.

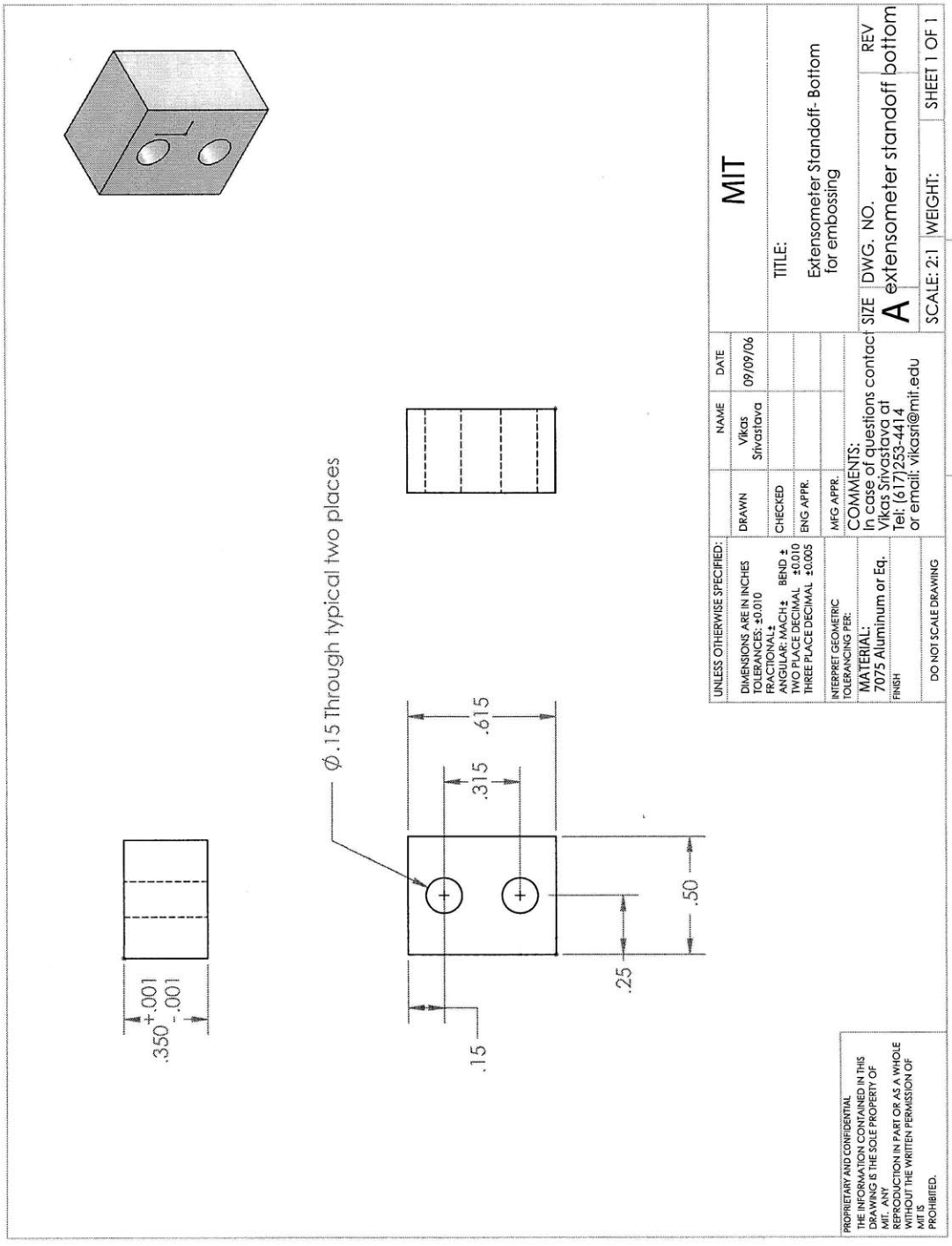

Figure D-12: Standoff for the bottom extensometer mount.